Analogy and Incongruity Between Classical and Quantum Turbulence in Isotropic and Anisotropic Turbulent Systems: A Numerical Study

Daniel Harris Wacks

Thesis submitted for the degree of
Doctor of Philosophy

School of Mathematics & Statistics
Newcastle University
Newcastle upon Tyne
United Kingdom

February 2013

To S, E, YA, CR, B, M, NB and Y.

Acknowledgements

I am very grateful to many people for their support and help. First and foremost, I would like to thank my PhD supervisor, Prof. Carlo Barenghi for his genuine interest in my work, his invaluable guidance and his useful suggestions. His bubbling enthusiasm played no small part in the progress of my research. I would also like to thank him for his 'open door' policy and his rapid feedback.

I thank Dr Andrew Baggaley for providing me with the Qvort code along with much helpful advice on its use. For technical assistance, I would like to thank Dr Anthony Youd. His expertise benefits all of the PhD students in the department.

I would like to thank the other members of staff of the Department of Mathematics and Statistics at Newcastle University for making me welcome and providing a suitable environment in which to conduct my research. I especially wish to thank the members of the Newcastle University branch of the Joint Quantum Centre for providing a forum to discuss all matters quantum and superfluid. I would like to express my gratitude to all of the postgraduate students, past and present, from Newcastle University who created a pleasant atmosphere and helped me during the three and a half years of my PhD.

Financial support was provided by The Engineering and Physical Sciences Research Council.

My final thanks go to my wife and children in recognition of their support, encouragement and understanding.

Abstract

This thesis is a study of quantum turbulence in superfluid helium. Superfluid helium consists of two interpenetrating fluids, a viscous normal fluid and an inviscid superfluid, coupled by a mutual friction. The thesis is divided in two parts. The first part deals with fully developed turbulence. In analogy to classical turbulence theory, I develop a two-fluid shell model to study superfluid turbulence. I investigate the energy spectra and the balance of fluxes between the two fluids as a function of temperature in continuously forced turbulence and show how both fluids generate the classical $k^{-5/3}$ Kolmogorov scaling law within the inertial subrange, whilst simultaneously exhibiting deviations from this law outside the subrange due to the mutual friction force. I furthermore investigate the decay of turbulence in the absence of forcing. I compare my results with experiments and existing calculations. I find that, at sufficiently low temperatures a build-up of energy develops at high wavenumbers suggesting the need for a further dissipative effect, such as the Kelvin wave cascade and phonon emission.

The second part of this thesis is concerned with complex vortex flows. It is well known that two coaxial vortex rings can leapfrog about each other. By direct numerical simulation, I show that in superfluid helium the effect can be generalised to a large number of vortex rings, which form a toroidal bundle. The bundle is shown to be robust, travelling a significant distance compared to its diameter, whilst at the same time becoming linked and turbulent. I also discuss the effects of friction at non-zero temperatures, and show how in this case the presence of normal fluid rotation is necessary for the stability of the bundle. Although I am unable to model numerically the number of rings realised in experiments, I compare my results with those of experiments both qualitatively and by extending the equations for a single quantised vortex ring.

Contents

List of Figures

List of Tables

Chapter 1

Introduction

1.1 A brief introduction to two-fluids hydrodynamics

Helium II (the low temperature, quantum phase of liquid ^{4}He) consists of two interpenetrating fluid components (Donnelly, 1991): the inviscid superfluid (associated with the quantum ground state) and the viscous normal fluid (consisting of thermal excitations). Each fluid component has its own density and velocity field, ρ^s, $\mathbf{u}^s$ for the superfluid and ρ^n, $\mathbf{u}^n$ for the normal fluid, where $\rho = \rho^s + \rho^n$ is helium's density and the relative proportion of superfluid and normal fluid depends on the absolute temperature T: $\rho^n/\rho \to 1$ ($T \to T_\lambda$) and $\rho^s/\rho \to 1$ ($T \to 0$ K) (see Figure 1.1).

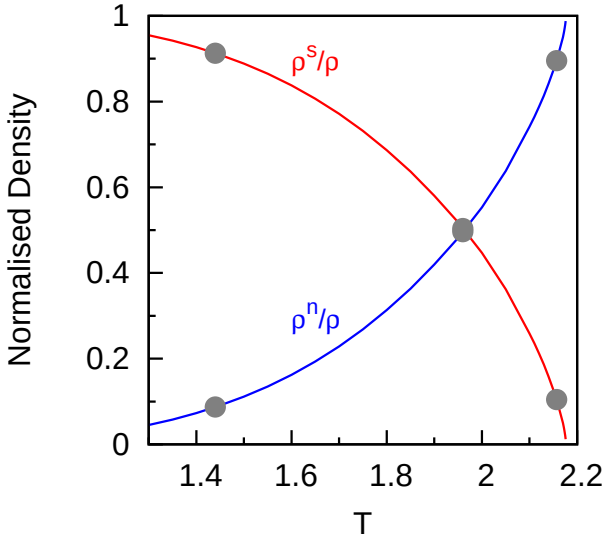

Figure 1.1: Normalised densities ρ^s/ρ and ρ^n/ρ vs T (K). Grey dots show T at which ratio $\rho^n/\rho^s = 0.1$, 1 and 10, used for analysis of two-fluids shell model (Part I).

What makes helium II particularly interesting is that the superfluid vorticity is concentrated in thin, discrete vortex filaments of fixed (quantised) circulation $\kappa = h/m = 9.97 \times 10^{-4}$ cm^2/s, where h is Planck's constant and m the mass of one ^{4}He atom. The vortex filaments interact with the thermal excitations, causing a mutual friction between superfluid and normal fluid (Barenghi *et al.*, 1983).

Turbulence in helium II (quantum turbulence) is easily generated in the laboratory by stirring or pushing liquid helium with grids and propellers (Smith *et al.*, 1993; Roche *et al.*, 2007; Salort *et al.*, 2010), vibrating forks (Schmoranzer *et al.*, 2010) or other means. Quantum turbulence is a complex state (Vinen & Niemela, 2002) in which normal fluid eddies of arbitrary shapes and strengths interact with a tangle of discrete vortex filaments of fixed strength. Despite the two-fluids nature of quantum turbulence, experiments have shown remarkable similarities with turbulence in ordinary fluids (classical turbulence), for example the same pressure drops along pipes and channels (Walstrom *et al.*, 1988), drag crisis behind a sphere (Smith *et al.*, 1999), and Kolmogorov energy spectrum (Maurer & Tabeling, 1998). The last property, which is my particular concern in Part I of this thesis, describes how the energy of the flow is distributed over the length scales in homogeneous isotropic turbulence.

Whereas turbulence in ordinary fluids is studied on the firm ground of the Navier-Stokes equation, there is no such established equation for turbulent helium II. Existing numerical simulations (Baggaley & Barenghi, 2011*b*; Adachi *et al.*, 2010) of quantum turbulence follow the approach of Schwarz (Schwarz, 1988), who calculated the properties of the vortex tangle by integrating in time the motion of a great number of individual vortex filaments in the presence of a prescribed normal fluid, neglecting the back reaction of the superfluid onto the normal fluid.

The aim of Part I of this work is to gain insight into self-consistent turbulent two-fluids hydrodynamics using a shell model (Biferale, 2003). In classical fluid dynamics (Frisch, 1995) shell models are idealised truncated models of the Navier-Stokes equation which neglect any geometry of the flow but describe the Richardson cascade and its properties (e.g. the Kolmogorov energy spectrum) over a wide range of scales and times. In the less-understood context of helium II, shell models allow us to explore the interaction of normal fluid and superfluid in the inertial and dissipative ranges in a relatively simple way. What happens at very large length scales (Adzhemyan *et al.*, 1998) where finite-size effects may affect the dynamics of the energy-containing eddies is beyond the scope of this work.

1.2 A discussion of the two-fluids equations

The two-fluids equations of helium II are (Donnelly, 1991)

$$\rho^s(\frac{\partial \mathbf{u}^s}{\partial t} + \mathbf{u}^s \cdot \nabla \mathbf{u}^s) = -\frac{\rho^s}{\rho}\nabla p + \rho^s s \nabla T - \mathbf{F}_{ns} \tag{1.1}$$

$$\rho^n(\frac{\partial \mathbf{u}^n}{\partial t} + \mathbf{u}^n \cdot \nabla \mathbf{u}^n) = -\frac{\rho^n}{\rho}\nabla p - \rho^s s \nabla T + \mu \nabla^2 \mathbf{u}^n + \mathbf{F}_{ns} \tag{1.2}$$

with $\nabla \cdot \mathbf{u}^s = \nabla \cdot \mathbf{u}^n = 0$, where s is the specific entropy. Hereafter I denote by $\nu^n = \mu/\rho^n$ the kinematic viscosity of helium II. If $\mathbf{F}_{ns} = 0$ and $\nabla \times \mathbf{u}^s = \boldsymbol{\omega}^s = 0$, Equations 1.1 and 1.2 reduce to Landau's two-fluids equations, which describe the well-known mechanical and thermal behaviour of helium II in the absence of vortex lines.

In the presence of vortices, the mutual friction $\mathbf{F}_{ns}$ which couples the two fluids depends on the vortex line density L (vortex length per unit volume), or, more precisely, on some suitably defined coarse-grained vorticity field $\boldsymbol{\omega}^s$. Unfortunately the form of $\mathbf{F}_{ns}$ is uncertain. The form given by Hall & Vinen (Hall & Vinen, 1956*a*,*b*) accounts for experiments in rotating cylinders and Taylor-Couette flow (Barenghi, 1992), in which vortices are either straight or curved, but still polarised in the same direction. That is to say that there is a laminar vortex flow. In this case the mutual friction term takes the following form

$$\mathbf{F}_{ns} = -\frac{B\rho^s\rho^n}{\rho}\hat{\boldsymbol{\omega}} \times (\boldsymbol{\omega} \times \mathbf{q}) - \frac{B'\rho^s\rho^n}{\rho}\hat{\boldsymbol{\omega}} \times \mathbf{q}, \tag{1.3}$$

where $\hat{\boldsymbol{\omega}} = \boldsymbol{\omega}/|\omega|$, $\mathbf{q} = \mathbf{v}_s - \mathbf{v}_n$ and B and B' are known temperature dependent mutual friction coefficients, $\alpha = B\rho^n/(2\rho)$ and $\alpha' = B'\rho^n/(2\rho)$. This form of the mutual friction implies that there is no mutual friction if $\mathbf{q}$ is in the same direction as the vortex lines.

In Part I for the sake of simplicity, I assume the Gorter-Mellink (Gorter & Mellink, 1949) form

$$\mathbf{F}_{ns} = \frac{B\rho^s\rho^n}{2\rho}\kappa L(\mathbf{u}^s - \mathbf{u}^n). \tag{1.4}$$

This form for the mutual friction is motivated by dimensional arguments and is consistent with the method employed to measure vortex line density in experiments. It has been widely used in the quantum turbulence literature (Tough, 1982; Barenghi *et al.*, 1983; Melotte & Barenghi, 1998; Vinen & Niemela, 2002; Vinen, 2005; Roche *et al.*, 2009).

In the case of turbulent flow, vortex filaments may be random or partially polarised, so the relation between the coarse-grained vorticity $\boldsymbol{\omega}^s$ and the vortex line density L is not clear. There is nonzero vortex line density, but the coarse-grained superfluid vorticity may be zero. For this reason one must resort to numerical simulations, such as the Biot-Savart Law (see Section 8.1), which integrate each point of the vortex filaments independently. This is the approach used in Part II of the thesis

to evolve multiple vortex rings simultaneously. Although initially laminar, and as such a possible candidate for the Hall-Vinen form of the mutual friction, the vortex rings develop instabilities such that the laminar description is no longer valid.

1.3 Overview of Part I

The first part of my thesis deals with fully developed homogeneous isotropic turbulence. In Chapter 2, I introduce the GOY shell model for a (single) classical turbulent fluid, explaining the motivation for its development, its advantages and disadvantages, and its conservation laws in 2D and 3D. I use the classical GOY model to test my code by showing that it is capable of reproducing the scaling laws predicted by Kolmogorov for a turbulent fluid. In Chapter 3, I develop the two-fluids GOY shell model by incorporating the mutual friction term into the governing equations of the classical shell model. I show how both the two-fluids equations (Equations 1.1 and 1.2) and the two-fluids GOY model conserve energy and helicity. In Chapter 4, I report results on a range of topics. Sections 4.1 and 4.2 focus on the two-fluids energy spectra in continuously forced turbulence and examine the balance of fluxes between the fluids for a range of temperatures. In Section 4.3, I discuss deviations from the classical $k^{-5/3}$ Kolmogorov spectrum in the inertial subrange predicted by L'vov *et al.* (L'vov *et al.*, 2006) and show that these deviations are present in the spectra of the two-fluids GOY model. Section 4.4 shows the need for energy sinks, such as the Kelvin wave cascade and phonon emission, at low temperature (in the absence of a significant normal fluid fraction). In Section 4.5, I introduce the concept of a quantum Reynolds number which reflects the ratio of inertial to general dissipative terms and discuss the scaling law that it is expected to obey. Section 4.6 deals with the decay of the energy spectra and the scaling laws which the vortex line density and energy obey during decay. Finally, in Section 4.7, by switching off the normal fluid velocity, I investigate the much more viscous case of superfluid ^{3}He-B, thereby confirming Vinen's prediction (Vinen, 2005) that the inertial and dissipative subranges exchange places. Chapter 5 contains a discussion of the results of Part I of the thesis and suggests possible avenues for further work.

A full list of variables used in Part I can be found in Appendix A.

1.4 Overview of Part II

The second part of my thesis is concerned with complex vortex flows, specifically with a system of N initially coaxial superfluid vortex rings which take the form of a toroidal bundle. In Chapter 6, I introduce the concept of thin-cored vortex rings, first in classical hydrodynamics and then in superfluid hydrodynamics. Chapter 7 gives details of experiments which have examined properties of such systems in

superfluid helium II. The results of these experiments point to the presence of $N = O(10^3)$ individual vortex rings and show that the system is capable of travelling a considerable distance without undergoing a turbulent transformation. In Chapter 8, I give details of the vortex filament method by means of which the evolution of the system is studied. I test the numerical code for the relatively simple cases of $N = 1$ and $N = 2$ and show that the stability and instability of the system are independent of the choice of time and space discretisation which is employed. I develop a normal fluid velocity field which I impose to include finite temperature effects in my model. Chapter 9 explains how the self-induced velocity and vortex energy can be quantitatively modelled by the numerical code, although the full evolution of a system of $N = O(10^3)$ vortex rings is at present too computationally expensive to consider. I also suggest a mathematical model which can be used to predict these results. I compare the numerical and mathematical models with the experimental results and discuss the level of agreement between them. In Chapter 10, I use Schwarz's vortex filament method to qualitatively model systems of vortex rings for $N \leq 19$. I show that these systems of rings are capable of travelling considerable distances whilst retaining a toroidal formation. I discuss the need for a normal fluid velocity field at finite temperatures and show how the velocity field described in Chapter 8 is extremely successful in prolonging the lifetime of the system. I also discuss the generalised leapfrogging phenomenon which occurs for $N \geq 2$, the trajectories taken by individual vortex rings in the frame of reference of the centre of vorticity and the existence of a critical value for a parameter which controls the occurrence of leapfrogging. Chapter 11 examines the dependence of the velocity, period of leapfrog, shape of trajectories and general stability of the system on two parameters: the intervortex spacing and the ratio R/a. In Chapter 12, I briefly discuss the agreement between numerical results and the mathematical model at finite temperature in the absence of a normal fluid velocity field. Chapter 13 returns to the point at which Chapter 10 finished, with an investigation of the development of instabilities in systems of multiple coaxial vortex rings. I investigate the development of instabilities at zero and finite temperature (with a prescribed normal fluid velocity field) of systems of 7 and 19 rings, particular attention is paid to the two types of reconnections that occur: parallel and antiparallel reconnections. I conclude this Part of my thesis with Chapter 14 in which I use the Tree Algorithm to evolve a system of 91 rings. Where appropriate I conclude each Chapter with a brief summary of the main results of that Chapter. Chapter 15 contains a discussion of the results of Part II of the thesis and suggests possible avenues for further work.

I include here a note on nomenclature. In this Part, I study the evolution of a system of coaxial vortex rings which assume a toroidal configuration, as described in detail in Section 8.3. A general term for such a collection of vortex rings would be a 'vortex bundle'. However, this term can also refer, for example, to a collection of

vortex lines. It is not a term used specifically to refer to vortex rings. Borner *et al.* (Borner *et al.*, 1981, 1983; Borner & Schmidt, 1985) and Murakami *et al.* (Murakami *et al.*, 1987) referred to their piston-induced system of vortex rings as a 'large-scale vortex ring'. Stamm *et al.* (Stamm *et al.*, 1994*a*,*b*) called their counterflow-induced system a 'macroscopic vortex ring'. I will use this latter term when referring to the entire system of vortex rings and will call a single vortex ring simply 'a (vortex) ring'.

In the overview of Part II, I have described how I study macroscopic vortex rings under three different conditions: (1) $T = 0$ K for which there is no normal fluid fraction and hence no mutual friction, (2) $T > 0$ K with no normal fluid velocity field, and (3) $T > 0$ K with an imposed normal fluid velocity field. For the sake of brevity, I will often refer to case (1) as the T0 case, to case (2) as the T1 case and to case (3) as the T2 case.

A full list of variables used in Part II can be found in Appendix D.

Many of the 3D figures of vortex rings in Part II were produced using the Knotplot package (http://www.KnotPlot.com/). Some KnotPlot related issues are discussed in more detail in Appendix E.

1.5 Collaborations

The Fortran code Qvort including the application of the Tree Algorithm to the vortex filament method (http://www.staff.ncl.ac.uk/a.w.baggaley/doxy/html/index.html) used in Part II of this thesis was written by Dr Andrew Baggaley. My input was limited to developing the subroutines specific to the macroscopic vortex ring and its analysis and to the imposed normal fluid velocity field appropriate to a normal fluid vortex ring.

1.6 Publications

- A.C. White, C.F. Barenghi, N. P. Proukakis, A. J. Youd, and **D. H. Wacks**, "Nonclassical Velocity Statistics in a Turbulent Atomic Bose-Einstein Condensate", Phys. Rev. Lett., **104**, 075301 (2010).
  My contribution to this paper involved the use of a 2D point vortex model to investigate the effect of changing the core size of the vortices on the shape of the PDF of the velocity.

- **D. H. Wacks** and C.F. Barenghi, "Shell model of superfluid turbulence", Phys. Rev. B, **84**, 184505 (2011).
  This paper discusses some of the main results appearing in Part I. Subsequent numerical results using the alternative Sabra shell model have been investigated by L'vov, Procaccia *et al.* (Boue *et al.*, 2012).

- **D. H. Wacks** and C.F. Barenghi, "Generalised leapfrogging of robust macroscopic vortex rings" (*in preparation*).
- **D. H. Wacks** and C.F. Barenghi, "Finite temperature effects on macroscopic vortex rings in superfluid He II" (*in preparation*).

Part I

Fully developed isotropic turbulence

Chapter 2

The classical GOY shell model

2.1 Motivation for the development of shell models

The classical Navier-Stokes equation is

$$\rho \frac{D\mathbf{u}}{Dt} = \rho \left(\frac{\partial \mathbf{u}}{\partial t} + \mathbf{u} \cdot \nabla \mathbf{u} \right) = -\nabla p + \mu \nabla^2 \mathbf{u}, \tag{2.1}$$

with the incompressibility condition $\nabla \cdot \mathbf{u} = 0$ (for constant density), where $\mathbf{u}$ is the velocity, p the pressure, ρ the density and μ the viscosity. In the inviscid, unforced limit the Navier-Stokes equation reduces to the Euler equation

$$\rho \frac{D\mathbf{u}}{Dt} = \rho \left(\frac{\partial \mathbf{u}}{\partial t} + \mathbf{u} \cdot \nabla \mathbf{u} \right) = -\nabla p, \tag{2.2}$$

which conserves both energy and helicity for a 3D turbulent fluid.

One of the most fundamental properties of fully developed turbulence is the inertial subrange: the range of wavenumbers where each statistical quantity has a definite scaling law. These are the scaling laws proposed by Kolmogorov in his K41 theory (Kolmogorov, 1941). In an attempt to understand these scaling laws, scalar models called shell models were introduced. Although computationally inexpensive, shell models share many important properties of the Navier-Stokes equation. They are deterministic, quadratically nonlinear, energy conserving and scale invariant. They proved to be tractable, scalar models with which to study classical turbulence, but being scalar and not vector models, geometry is lost.

Starting from the works of Gledzer (Gledzer, 1973), who used his shell model to study two-dimensional Navier-Stokes turbulence, and Yamada & Ohkitani (Yamada & Ohkitani, 1987), who extended Gledzer's model to include three-dimensional turbulence, a variety of shell models have been developed (L'vov *et al.*, 1998) to study turbulent solutions of Equation 2.1. The GOY model, named after the pioneering authors (Gledzer-Ohkitani-Yamada), is a finite-dimensional dynamical system

which describes the dynamics of idealised (complex) Fourier components of the velocity field, u_m corresponding to wavenumber k_m; the index m ($m = 1, \cdots, M$) is called the shell index. The wavenumbers are geometrically distributed in k-space, $k_m = k_0\lambda^m$, where k_0 is a reference wavenumber and $\lambda > 1$ is the aspect ratio (the ratio between the wavenumbers of successive shells). It is these wavenumbers which give rise to the name 'shell' model. This construction gives rise to a set of complex variables $\{u_m\}$, where u_m represents the velocity of those eddies in the turbulent cascade whose wavenumber, k, lies between k_m and k_{m+1}. The velocity evolution is followed over this set of values only. This leads to a much reduced phase space and allows access to a large range of wavenumbers, which correspond to large Reynolds numbers. A model with M shells means that there are $2M$ degrees of freedom. In this sense shell models may be viewed as severe truncations of the Navier-Stokes equation, retaining only one complex (or real) mode u_m as a representative of all the Fourier modes in the shell of wavenumbers k between k_m and k_{m+1} (Pisarenko *et al.*, 1993).

This model realises the Kolmogorov similarity law and $k^{-5/3}$-form of the energy spectrum in the inertial subrange. My aim is to use an adapted form of the GOY model to investigate properties of superfluids, such as the energy-cascade, scale-by-scale energy budget and relaxation of turbulence.

2.2 Governing equation of shell models in k-space

The general form of the equations of motion of shell models is (Biferale, 2003)

$$\left(\frac{d}{dt} + \nu k_m^2\right) u_m = G_m[u] + f\delta_{m,m'}, \tag{2.3}$$

for $m = 1, \cdots M$, where $\nu = \mu/\rho$ is the kinematic viscosity, $\delta_{m,m'}$ is Kronecker's delta, k_m^2 is the Laplacian in k-space, and f is the amplitude of external, steady forcing applied on a particular shell $m = m'$. The inertial term $G_m[u]$ is quadratically nonlinear and local in k-space, coupling u_m with its nearest neighbouring shells u_{m-2}, u_{m-1}, u_{m+2}, and u_{m+1}. It represents the nonlinear wave interaction or advection, associated with the shell index m and corresponds to the nonlinear term in the Navier-Stokes equation (Equation 2.1). More precisely in the case of the GOY model

$$G_m[u] = i(c_m^{(1)}\bar{u}_{m+1}\bar{u}_{m+2} + c_m^{(2)}\bar{u}_{m-1}\bar{u}_{m+1} + c_m^{(3)}\bar{u}_{m-1}\bar{u}_{m-2}), \tag{2.4}$$

where $\bar{u}$ denotes the complex conjugate of u, and

$$c_m^{(1)} = ak_m, \qquad c_m^{(2)} = bk_{m-1}, \qquad c_m^{(3)} = ck_{m-2} \tag{2.5}$$

are real constants. The form of the shell model equation (Equation 2.3) is readily

comparable to that of the Navier-Stokes equation (Equation 2.1). The boundary conditions are $u_m = 0$ for $m \leq 0$, $m > M$ and

$$c_1^{(2)} = c_1^{(3)} = c_2^{(3)} = c_{M-1}^{(1)} = c_M^{(1)} = c_M^{(2)} = 0. \tag{2.6}$$

2.3 Conservation laws for shell models

The quadratic form of the nonlinear term of the GOY shell model allows for the conservation of two quantities (i.e. conserved integrals or summations) in the inviscid and unforced limit (Ditlevsen & Mogensen, 1996; Biferale, 2003). The coefficients $a = 1$, $b = -1/2$, $c = -1/2$ and $\lambda = 2$ are chosen so that in the steady ($d/dt = 0$), unforced ($f = 0$), inviscid ($\nu = 0$) case the nonlinear interaction conserves the two quadratic invariants of the 3-dimensional Euler equation (Equation 2.2), energy and helicity,

$$E = \frac{1}{V} \int \frac{1}{2} \mathbf{u} \cdot \mathbf{u} \, dV, \tag{2.7}$$

$$H = \frac{1}{V} \int \mathbf{u} \cdot \boldsymbol{\omega} \, dV, \tag{2.8}$$

(where $\boldsymbol{\omega} = \nabla \times \mathbf{u}$ and V is volume) which are identified as

$$E = \frac{1}{2} \sum_{m=1}^{M} |u_m|^2 = \sum_{m=1}^{M} E_m k_m, \tag{2.9}$$

where

$$E_m = \frac{|u_m|^2}{2k_m}, \tag{2.10}$$

is the spectral energy associated with shell m, and

$$H = \frac{1}{2} \sum_{m=1}^{M} (-1)^m \lambda^m |u_m|^2. \tag{2.11}$$

2.4 Conservation of energy and helicity in Euler's equation

2.4.1 Energy

Consider the total kinetic energy per unit mass, E, in a volume, V, bounded by a simply-connected surface, S,

$$E = \int_V \frac{1}{2} \mathbf{u} \cdot \mathbf{u} \, dV, \tag{2.12}$$

then substituting Euler's equation, using continuity and the divergence theorem and requiring no flow through S,

$$\begin{aligned}\frac{dE}{dt} &= \int_V \frac{1}{2}\frac{D}{Dt}(\mathbf{u}.\mathbf{u})\ dV = \int_V \mathbf{u}\cdot\left(-\frac{1}{\rho}\nabla p\right)\ dV \\ &= -\int_V \left(\mathbf{u}\cdot\frac{1}{\rho}\nabla p + \frac{p}{\rho}\nabla\cdot\mathbf{u}\right)\ dV = -\oint_S p\mathbf{u}\cdot\mathbf{n}\ dS = 0,\end{aligned}$$

showing that energy is conserved.

2.4.2 Helicity

Helicity is the extent to which corkscrew-like motion occurs in a fluid. Consider a fluid element dV, which undergoes a uniform velocity $\mathbf{u}$ and a rigid body rotation $\boldsymbol{\omega}$. The contribution to the helicity, H, of the fluid is then given by $\mathbf{u}\cdot\boldsymbol{\omega}dV$. Hence, the integral over the entire volume of fluid, V, gives the total helicity of the fluid. The conservation of helicity in 3D turbulence was proven by Moffatt (Moffatt, 1969). Moffatt's method is essentially the same as for the energy, only now involving the vorticity, $\boldsymbol{\omega} = \nabla\times\mathbf{u}$. The vorticity equation is

$$\frac{D\boldsymbol{\omega}}{Dt} = \frac{\partial\boldsymbol{\omega}}{\partial t} + \mathbf{u}\cdot\nabla\boldsymbol{\omega} = (\boldsymbol{\omega}\cdot\nabla)\,\mathbf{u}. \tag{2.13}$$

Consider the quantity $\mathbf{u}\cdot\boldsymbol{\omega}$, then

$$\begin{aligned}\frac{D}{Dt}(\mathbf{u}\cdot\boldsymbol{\omega}) &= \boldsymbol{\omega}\cdot\left(-\frac{1}{\rho}\nabla p\right) + \mathbf{u}\cdot(\boldsymbol{\omega}\cdot\nabla)\,\mathbf{u} \\ &= (\boldsymbol{\omega}\cdot\nabla)\left(-\frac{p}{\rho} + \frac{1}{2}\mathbf{u}\cdot\mathbf{u}\right)\end{aligned}$$

Consider the total helicity per unit mass, H, in a volume, V, bounded by a simply-connected surface, S,

$$H = \int_V \mathbf{u}\cdot\boldsymbol{\omega}\ dV. \tag{2.14}$$

Substituting $\frac{D}{Dt}(\mathbf{u}\cdot\boldsymbol{\omega})$, using the divergence theorem and requiring no flow of vorticity through S,

$$\begin{aligned}\frac{dH}{dt} &= \int_V \frac{D}{Dt}(\mathbf{u}\cdot\boldsymbol{\omega})\ dV = \int_V (\boldsymbol{\omega}\cdot\nabla)\left(-\frac{p}{\rho} + \frac{1}{2}\mathbf{u}\cdot\mathbf{u}\right)\ dV \\ &= \oint_S (\mathbf{n}\cdot\boldsymbol{\omega})\left(-\frac{p}{\rho} + \frac{1}{2}\mathbf{u}\cdot\mathbf{u}\right)\ dS = 0,\end{aligned}$$

showing that helicity is conserved.

2.5 Conservation of energy for the inviscid, unforced GOY shell model

The inviscid, unforced GOY shell model evolution equation reduces to the following

$$\frac{du_m}{dt} = i[c_m^{(1)} u_{m+1}^* u_{m+2}^* + c_m^{(2)} u_{m-1}^* u_{m+1}^* + c_m^{(3)} u_{m-1}^* u_{m-2}^*]. \tag{2.15}$$

Conversely,

$$\frac{du_m^*}{dt} = i[c_m^{(1)} u_{m+1} u_{m+2} + c_m^{(2)} u_{m-1} u_{m+1} + c_m^{(3)} u_{m-1} u_{m-2}]. \tag{2.16}$$

If one multiplies the first equation by u_m^* and the second by u_m, adds the two together, and sums over all m, the LHS becomes

$$\begin{aligned}\sum_m \left(\frac{du_m}{dt}u_m^* + u_m\frac{du_m^*}{dt}\right) &= \sum_m \left(\frac{d}{dt}(u_m u_m^*)\right) = \sum_m \left(\frac{d}{dt}(|u_m|^2)\right) \\ &= \sum_m \left(2k_m\frac{dE_m}{dt}\right) = 2k_m\frac{d}{dt}\left(\sum_m E_m\right) = 2k_m\frac{dE}{dt} = 0,\end{aligned}$$

when energy is conserved. The RHS (before summation) becomes

$$\begin{aligned}RHS &= i[c_m^{(1)} u_{m+1}^* u_{m+2}^* + c_m^{(2)} u_{m-1}^* u_{m+1}^* + c_m^{(3)} u_{m-1}^* u_{m-2}^*]u_m^* \\ &+ i[c_m^{(1)} u_{m+1} u_{m+2} + c_m^{(2)} u_{m-1} u_{m+1} + c_m^{(3)} u_{m-1} u_{m-2}]u_m \\ &= i[c_m^{(1)}(u_m^* u_{m+1}^* u_{m+2}^* + u_m u_{m+1} u_{m+2}) \\ &+ c_m^{(2)}(u_{m-1}^* u_m^* u_{m+1}^* + u_{m-1} u_m u_{m+1}) \\ &+ c_m^{(3)}(u_m^* u_{m-1}^* u_{m-2}^* + u_m u_{m-1} u_{m-2})] \\ &= i[ak_m(u_m^* u_{m+1}^* u_{m+2}^* + u_m u_{m+1} u_{m+2}) \\ &+ bk_{m-1}(u_{m-1}^* u_m^* u_{m+1}^* + u_{m-1} u_m u_{m+1}) \\ &+ ck_{m-2}(u_m^* u_{m-1}^* u_{m-2}^* + u_m u_{m-1} u_{m-2})]\end{aligned}$$

Summing over any three consecutive values of m, such as m, $m+1$ and $m+2$, one gets the following expression

$$k_m(a+b+c)\cdot(u_m^* u_{m+1}^* u_{m+2}^* + u_m u_{m+1} u_{m+2}). \tag{2.17}$$

Hence, in order to conserve energy, one must satisfy $a+b+c=0$. Summing over all m and employing this condition leads to the cancellation of almost all terms. The only terms that remain are those containing the boundary conditions for $c_m^{(i)}, (1 \leq i \leq 3)$, which are all zero by construction (Equation 2.6).

2.6 The second conserved quantity

Ditlevsen *et al.* (Ditlevsen & Mogensen, 1996) give a more rigorous derivation of the two conserved quantities. One first denotes the two conserved quantities as follows:

$$E^{(1),(2)} = \sum_{M=1}^{M} E_m^{(1),(2)} = \frac{1}{2}\sum_{m=1}^{M} k_m^{\alpha_{1,2}} |u_m|^2 = \frac{1}{2}\sum_{m=1}^{M} \lambda^{m\alpha_{1,2}} |u_m|^2 \tag{2.18}$$

One then uses $\dot{u}_m$ from the GOY model evolution equation in the inviscid, unforced limit (Equation 2.15) to evaluate $\dot{E}^{(1),(2)}$ in the same way as I did for the energy conservation. Cancelling and gathering terms gives the following condition for the conserved quantities:

$$a + b\lambda^{\alpha_{1,2}} + c\lambda^{2\alpha_{1,2}} = 0 \tag{2.19}$$

One immediately recognises that for $\alpha = 0$ the condition for the conservation of energy is recovered. In general this equation will have two roots z_1 and z_2, corresponding to α_1 and α_2 respectively (i.e. $\lambda^{\alpha_{1,2}} = z_{1,2}$), which are the generators of the conserved integrals. In the case of negative z the complex formulation $\alpha = (ln|z| + i\pi)/ln\lambda$ is used. Traditionally the value of a is rescaled so as to be 1. The condition $a+b+c=0$ then reduces to $c=-(1+b)$. In which case there remains one free variable, b. Using this convention the quadratic in λ^α becomes

$$1 + b\lambda^\alpha - (1+b)\lambda^{2\alpha} = 0, \tag{2.20}$$

which has roots $\alpha = 0$ (as expected) and $\alpha = log_\lambda\left(\frac{-1}{1+b}\right)$, depending on the free variable b.

For $b > -1$ the second conserved quantity is not positive definite. It takes the form:

$$E^{(2)} = H = \frac{1}{2}\sum_{m=1}^{M}(-1)^m \left|\frac{-1}{1+b}\right|^m |u_m|^2, \tag{2.21}$$

which is interpreted as a generalised helicity. The typical choices for b and λ in 3D

shell models of turbulence are $b = -1/2$ and $\frac{-1}{1+b} = -2 = -\lambda$, in which case the conserved quantity reduces to

$$E^{(2)} = \frac{1}{2}\sum_{m=1}^{M}(-1)^m \lambda^m |u_m|^2, \tag{2.22}$$

which was identified by Kadanoff *et al.* (Kadanoff *et al.*, 1995) as the proper form for the helicity in the GOY shell model. In this case $E^{(2)}$ has dimensions cms^{-2}, which is in agreement with the dimensions of the definition of helicity (per unit volume) given by Equation 2.8

$$H = \frac{1}{V}\int_V \mathbf{u}\cdot\boldsymbol{\omega}\; dV = \frac{1}{V}\int_V \mathbf{u}\cdot(\nabla\times\mathbf{u})\; dV.$$

Since helicity is conserved in 3D turbulence, it is understood why these values of b and λ are chosen for the GOY shell model for 3D turbulence.

For $b < -1$ the second conserved quantity is positive definite. It takes the form:

$$E^{(2)} = Q = \frac{1}{2}\sum_{m=1}^{M}\left(\frac{-1}{1+b}\right)^m |u_m|^2, \tag{2.23}$$

which is interpreted as a generalised enstrophy. The typical choices for b and λ in 2D shell models of turbulence are $b = -5/4$ and $\frac{-1}{1+b} = 4 = \lambda^2$, in which case the conserved quantity reduces to

$$E^{(2)} = \frac{1}{2}\sum_{m=1}^{M}\lambda^{2m}|u_m|^2, \tag{2.24}$$

which was identified by Aurell (Aurell *et al.*, 1994) as the proper form for the enstrophy in the GOY shell model. In this case $E^{(2)}$ has dimensions s^{-2}, which is in agreement with the dimensions of the definition of enstrophy (per unit area) given by

$$Q = \frac{1}{S}\int_S \boldsymbol{\omega}^2\; dS = \frac{1}{S}\int_S (\nabla\times\mathbf{u})^2\; dS. \tag{2.25}$$

Once again since enstrophy is conserved in 2D turbulence, it is understood why these values of b and λ are chosen for the GOY shell model for 2D turbulence.

The only other possibility is for $b = -1$ in which case the second conserved quantity is singular (Ditlevsen & Mogensen, 1996).

2.7 Summary of invariants with reference to differences between 2D and 3D cases

In summary, the GOY model has 2 invariants (symmetries and conserved integrals) in the inviscid and unforced limit. These invariants govern the dynamical behaviour of the system. They depend on the choice of interaction coefficients (coupling parameters). When both invariants are positive definite they are identified with energy and enstrophy and the case is therefore analogous to 2D turbulence. On the other hand, when only one invariant is positive definite, that invariant is identified with energy and the other, which is not positive definite, with helicity. In this case the model is analogous to 3D turbulence.

2.8 Numerical test of classical GOY model

I have shown analytically that in the inviscid, unforced limit energy and helicity are conserved in the 3D-like GOY model and that energy and enstrophy in the 2D-like GOY model. Before adapting the GOY shell model code with the addition of a mutual friction term, which effectively couples the normal fluid and superfluid components, I test the classical GOY model equations to confirm that these quantities are indeed conserved numerically by my code. I use the following parameters $(M, \lambda, k_0) = (18, 2, 2^{-4})$, and as shown above in the 3D case the shell coefficients are taken as $(a, b, c) = (1, -0.5, -0.5)$ and in the 2D case $(a, b, c) = (1, -5/4, 1/4)$.

I find that the value of the timestep, Δt, has a great effect on the ability of the GOY shell code to conserve the required quantities. I observe an increase in the accuracy of the conservation as Δt was decreased. Notice that the 2D GOY shell model is much better at conserving both quantities than the 3D model. Also notice that in the 3D model energy is more readily conserved than helicity. This is probably due to the variable sign of the helicity-like term in the GOY shell model. I record the percentage variation of E, Q and H in Table 2.1, where I define the variation as

$$\delta_{err} = 100 \times \frac{|\hat{E}(t) - \hat{E}(0)|}{\hat{E}(0)} \tag{2.26}$$

for $\hat{E} = E$, H and Q.

2.9 Scaling properties of the GOY shell model

Review of Kolmogorov K41 theory

Kolmogorov's second similarity hypothesis states that the statistical properties of eddies within the inertial subrange (the range in which viscous effects are negligible)

	2D		3D	
Δt (s)	E (%)	Q (%)	E (%)	H (%)
$5 \cdot 10^{-2}$	$O(10^{-3})$	$O(10^{-2})$	–	–
$5 \cdot 10^{-3}$	$O(10^{-5})$	$O(10^{-4})$	–	–
$5 \cdot 10^{-4}$	$O(10^{-7})$	$O(10^{-6})$	–	–
$5 \cdot 10^{-5}$	–	–	–	–
$5 \cdot 10^{-6}$	–	–	$O(10^{-1})$	$O(10^{3})$
$5 \cdot 10^{-7}$	–	–	$O(10^{-4})$	$O(10^{0})$
$5 \cdot 10^{-8}$	–	–	$O(10^{-7})$	$O(10^{-3})$

Table 2.1: Time-averaged percentage error in conserved quantities in inviscid, unforced 2D and 3D classical GOY models for different size timesteps, Δt.

are uniquely determined by $\epsilon = -dE/dt$, the rate at which kinetic energy is passed to smaller eddies, and the eddy size $l = 1/k$. If one then writes $v(l) \sim \epsilon^{\alpha} l^{\beta}$ and $\tau(l) \sim \epsilon^{\alpha'} l^{\beta'}$, this gives $v(l) \sim (\epsilon l)^{1/3}$ and $\tau(l) \sim (l^2/\epsilon)^{1/3}$. Now, if eddies decay on a timescale dependent on their size, $\tau(l)$, then the rate at which kinetic energy (per unit mass) passes to smaller eddies is $dE/dt \sim v^2(l)/\tau(l) = \epsilon$. In other words, energy cascades at a constant rate ϵ down the scales and is independent of eddy size l.

The kinetic energy in a volume V is given by

$$E = \frac{1}{V} \int \frac{1}{2} u^2 \, dV = \int E_k dk \tag{2.27}$$

Since $[E] = cm^2 s^{-2}$ and $[k] = cm^{-1}$, then $[E_k] = \frac{[E]}{[k]} = cm^3 s^{-2}$ (or, equivalently, $[E_k dk] = cm^2 s^{-2}$). Also since $\epsilon = -dE/dt$, then $[\epsilon] = cm^2 s^{-3}$. Assuming that $E_k = \epsilon^{\alpha''} k^{\beta''}$, then $\alpha'' = 2/3$ and $\beta'' = -5/3$, giving an expression for the energy spectrum in the inertial subrange

$$E_k \sim \epsilon^{2/3} k^{-5/3}, \tag{2.28}$$

which for constant ϵ (in the inertial subrange) becomes

$$E(k) \sim k^{-5/3}. \tag{2.29}$$

2.9.1 K41 theory in shell model k-space

Equation 2.29 gives an expression for a continuum in k-space. Define the equivalent expression for the truncated k-space of the GOY shell model

$$E(k_m) = E_m \sim k_m^{-5/3}. \tag{2.30}$$

Recall Equation 2.10 for the spectral energy associated with the shell m

$$E(k_m) = \frac{|u_m|^2}{2k_m}.$$

This has dimensions cm^3s^{-2} the same as that of E_k. Substituting Equation 2.10 into Equation 2.30 gives the scaling law for $|u_m|$

$$u_m \sim k_m^{-1/3}. \tag{2.31}$$

From Equation 2.24 and $k_m = k_0\lambda^m$, it is apparent that the enstrophy associated with shell m is $Q_m = |\omega_m|^2 = |u_m|^2k_m^2$, and that it has (correct) dimensions $[\omega_m^2] = s^{-2}$. This gives a scaling law for the vorticity $|\omega_m|$

$$\omega_m \sim k_m^{2/3}. \tag{2.32}$$

Finally, define the turnover time of eddies of wavenumber k_m as $\tau_m = 1/\omega_m = 1/(u_mk_m)$ (with correct dimensions in seconds). Then the scaling law for τ_m is

$$\tau_m \sim k_m^{-2/3}. \tag{2.33}$$

In summary the scaling laws of the GOY model are $E_m \sim k_m^{-5/3}$, $u_m \sim k_m^{-1/3}$, $\omega_m \sim k_m^{2/3}$ and $\tau_m \sim k_m^{-2/3}$. The GOY variables have dimensions $[E_m] = cm^3s^{-2}$, $[u_m] = cms^{-1}$, $[\omega_m] = s^{-1}$ and $[\tau_m] = s$.

2.9.2 Kolmogorov spectrum satisfies the GOY shell model evolution equation

I will now show that the Kolmogorov spectrum satisfies the GOY shell model evolution equation in the steady, inviscid and unforced limit. In the steady, inviscid and unforced limit the GOY shell model evolution equation reduces to the following

$$0 = c_m^{(1)}u_{m+1}^*u_{m+2}^* + c_m^{(2)}u_{m-1}^*u_{m+1}^* + c_m^{(3)}u_{m-1}^*u_{m-2}^*. \tag{2.34}$$

Substituting Equation 2.31 into this equation gives for shell m

$$\begin{aligned} 0 = \;& ak_{m+1}\,(k_{m+1})^{-1/3}(k_{m+2})^{-1/3} \\ + \;& bk_m\,(k_{m-1})^{-1/3}(k_{m+1})^{-1/3} \\ + \;& ck_{m-1}\,(k_{m-1})^{-1/3}(k_{m+2})^{-1/3} \end{aligned}$$

Replacing k_m with $k_0\lambda^m$ and cancelling k_0^3 gives

$$\begin{aligned} 0 = \quad & a\lambda^{m+1}\ \lambda^{(m+1)(-1/3)}\lambda^{(m+2)(-1/3)} \\ + \quad & b\lambda^{m}\ \lambda^{(m-1)(-1/3)}\lambda^{(m+1)(-1/3)} \\ + \quad & c\lambda^{m-1}\ \lambda^{(m-1)(-1/3)}\lambda^{(m+2)(-1/3)} \end{aligned}$$

which simplifies to

$$0 = (a + b + c)\lambda^{m/3} \tag{2.35}$$

but by definition of the GOY model $a + b + c = 0$.

2.10 Results of classical GOY model

The energy spectra that result from the implementation of the GOY model are subject to severe oscillations (orders of magnitude), necessitating time and/or ensemble averaging (Yamada & Ohkitani, 1987; Pisarenko *et al.*, 1993). There follows good agreement between the averaged energy spectra from the GOY model and the $k^{-5/3}$ spectrum predicted by K41 theory over 3 decades of inertial subrange, comparable to an impressive 1000^3 spatial resolution.

I have reproduced the results of the classical turbulence with my (two-fluids) GOY code by decoupling the two-fluids equations (i.e. setting the mutual friction term to zero). I show the results of these numerical calculations in Figures 2.1 to 2.3. The parameters used are standard ones $(M, \lambda, m') = (18, 2, 4)$ (Yamada & Ohkitani, 1987). I use a timestep $\Delta t = 5 \times 10^{-6}$ seconds and run the code for an initial period of 500 seconds, equivalent to approximately 10 big eddy turnover times, to allow the spectrum to develop fully. I then run the code for further 500 seconds and take 10 snapshots of the data to produce time-averaged spectra and the scale-by-scale energy budget. I run the code at a 'high' temperature $T = 2.157$ K, although in the absence of mutual friction, this only has an effect on the value of ν^n, the normal fluid viscosity.

All figures show good agreement with K41 predictions for inertial subrange, which seems to stretch over 3 decades from 10^{-1} to 10^2. Figure 2.3 shows the scale-by-scale energy budget in which the flux of energy due to the inertial term and viscous term balance each other in the inertial subrange (see Section 4.1 for further details).

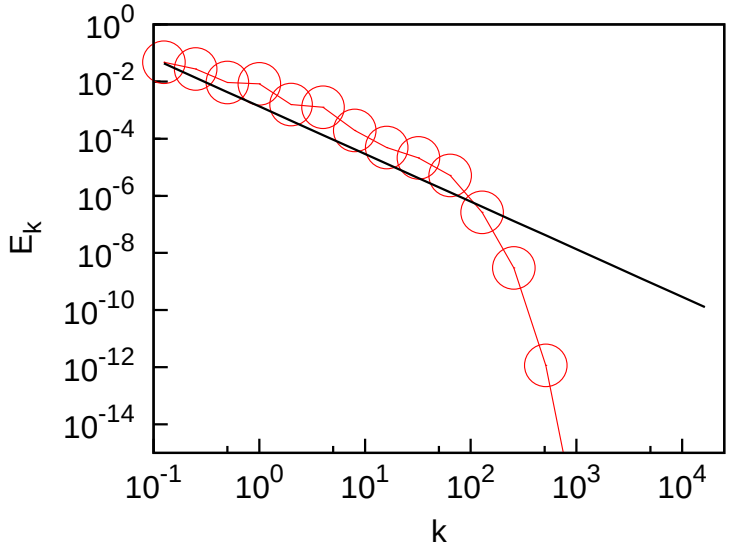

(a)

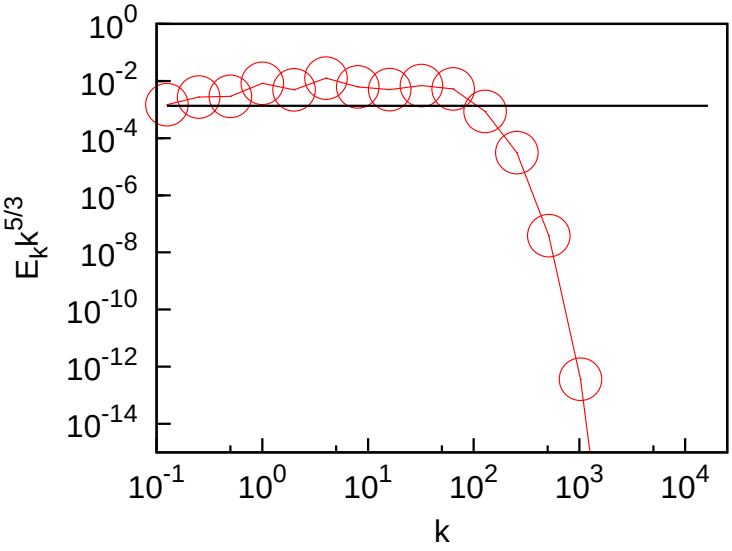

(b)

Figure 2.1: Log-log plot of time-averaged (a) energy spectrum E_k ($\mathrm{cm}^2\mathrm{s}^{-2}$) vs wavenumber k (cm^{-1}) (red circles) and (b) compensated energy spectrum $E_k k^{5/3}$ vs k (red circles) for classical turbulence. The solid black line denotes the $k^{-5/3}$ power law predicted by the K41 theory.

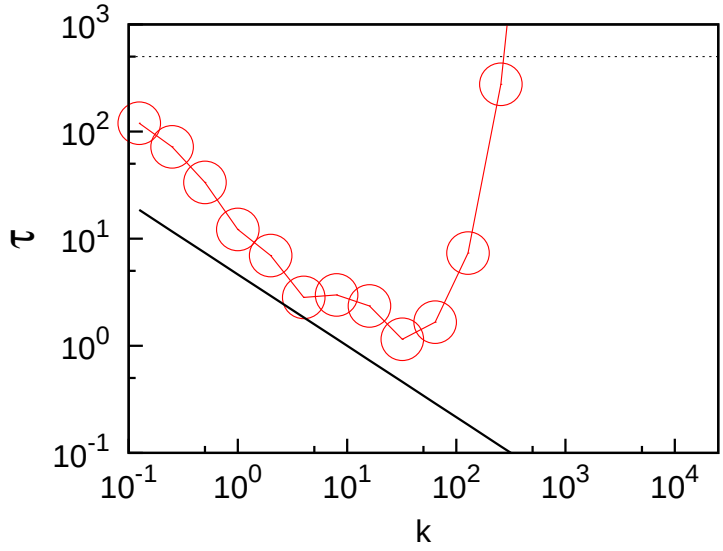

(a)

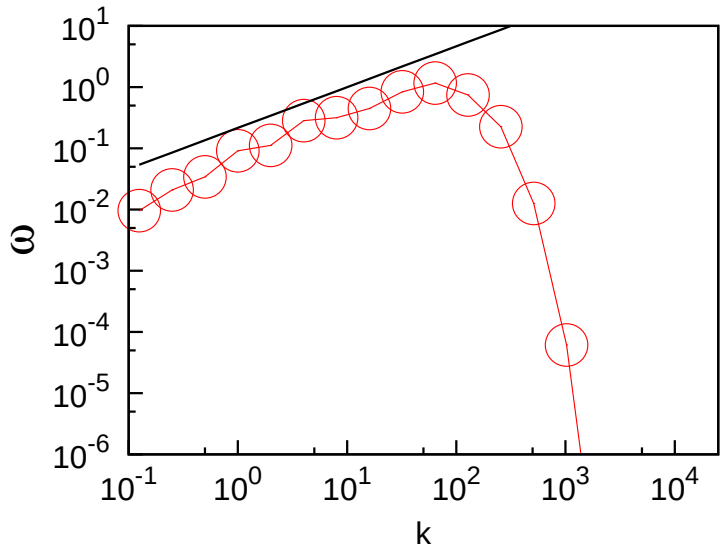

(b)

Figure 2.2: Log-log plot of time-averaged (a) turnover time τ (s) vs k (cm^{-1}) (red circles) and (b) vorticity spectrum ω (s^{-1}) vs k (cm^{-1}) (red circles) for classical turbulence. The solid black line in (a) denotes the $k^{-2/3}$ power law and in (b) the $k^{2/3}$ power law predicted by the K41 theory. The dashed black line in (a) denotes the final time, 500 seconds.

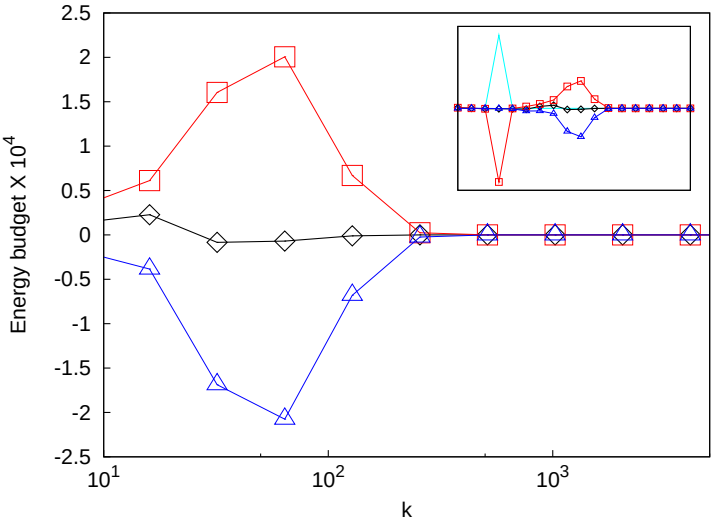

Figure 2.3: Log-lin plots of scale-by-scale time-averaged energy budget dE_m/dt ($\mathrm{cm}^{-2}\mathrm{s}^{-3}$) vs k (cm^{-1}) for classical turbulence. Main plot: focus on the balance between energy flux due to inertial term (red squares) and viscous term (blue triangles). I also show the scale-by-scale total energy flux (black diamonds). Inset: shows scale-by-scale energy budgets over all m, including that due to the external forcing (light blue line) which is nonzero only at shell $m = 4$.

Chapter 3

A two-fluids GOY shell model

3.1 Two-fluids equations

Recall the two-fluids equations (Equations 1.1 and 1.2) of helium II (Donnelly, 1991)

$$\rho^s(\frac{\partial \mathbf{u}^s}{\partial t} + \mathbf{u}^s \cdot \nabla \mathbf{u}^s) = -\frac{\rho^s}{\rho}\nabla p + \rho^s s \nabla T - \mathbf{F}_{ns}$$

$$\rho^n(\frac{\partial \mathbf{u}^n}{\partial t} + \mathbf{u}^n \cdot \nabla \mathbf{u}^n) = -\frac{\rho^n}{\rho}\nabla p - \rho^s s \nabla T + \mu \nabla^2 \mathbf{u}^n + \mathbf{F}_{ns}$$

with $\nabla \cdot \mathbf{u}^s = \nabla \cdot \mathbf{u}^n = 0$, where s is the specific entropy. Hereafter I denote by $\nu^n = \mu/\rho^n$ the kinematic viscosity of helium II. If $\mathbf{F}_{ns} = 0$ and $\nabla \times \mathbf{u}^s = \boldsymbol{\omega}^s = 0$, Equations 1.1 and 1.2 reduce to Landau's two-fluids equations, which describe the well-known mechanical and thermal behaviour of helium II in the absence of vortex lines. In the presence of vortices, the mutual friction $\mathbf{F}_{ns}$ which couples the two fluids depends on the vortex line density L (vortex length per unit volume), or, more precisely, on some suitably defined coarse-grained vorticity field $\boldsymbol{\omega}^s$. Unfortunately the form of $\mathbf{F}_{ns}$ is uncertain. The form given by Hall & Vinen (Hall & Vinen, 1956*a*,*b*) accounts for experiments in rotating cylinders and Taylor-Couette flow (Barenghi, 1992), in which vortices are either straight or curved, but still polarised in the same direction. In the case of turbulent flow, vortex filaments may be random or partially polarised, so the relation between the coarse-grained vorticity $\boldsymbol{\omega}^s$ and the vortex line density L is not clear. Hereafter for the sake of simplicity, I assume the Gorter-Mellink (Gorter & Mellink, 1949) form

$$\mathbf{F}_{ns} = \frac{B\rho^s\rho^n}{2\rho}\kappa L(\mathbf{u}^s - \mathbf{u}^n), \tag{3.1}$$

where B is a known temperature dependent mutual friction coefficient $\alpha = B\rho^n/(2\rho)$. This form for the mutual friction is motivated by dimensional arguments and is consistent with the method employed to measure vortex line density in experiments. It has been widely used in the quantum turbulence literature (Tough, 1982; Barenghi

et al., 1983; Melotte & Barenghi, 1998; Vinen & Niemela, 2002; Vinen, 2005; Roche *et al.*, 2009).

3.2 Conservation laws for the two-fluids model

I now consider the conservation of energy and helicity in the two-fluids model in the unforced, inviscid limit. In other words, I consider the effect of the mutual friction term on the conservation laws. It is not sufficient to consider each fluid independently of the other, since the mutual friction term couples the two equations. One must instead consider the conservation of total energy,

$$E^t = E^s + E^n + E^c, \tag{3.2}$$

and total helicity,

$$H^t = H^s + H^n + H^c, \tag{3.3}$$

which include a contribution from the superfluid, normal fluid and cross terms. In order to evaluate the total energy, I define the total velocity

$$\mathbf{u}^t = \left(\frac{\rho^n}{\rho}\mathbf{u}^n + \frac{\rho^s}{\rho}\mathbf{u}^s\right), \tag{3.4}$$

and in order to evaluate the total helicity, I define the total vorticity

$$\boldsymbol{\omega}^t = \nabla \times \mathbf{u}^t = \left(\frac{\rho^n}{\rho}\boldsymbol{\omega}^n + \frac{\rho^s}{\rho}\boldsymbol{\omega}^s\right). \tag{3.5}$$

3.2.1 Conservation of total energy

Equations 1.1 and 1.2 in the inviscid, unforced limit at fixed temperature become

$$\frac{D}{Dt}\mathbf{u}^n = -\frac{1}{\rho^n}\nabla p^n + \frac{\rho^s}{\rho}\frac{B}{2}|\boldsymbol{\omega}^s|\left(\mathbf{u}^s - \mathbf{u}^n\right) \tag{3.6}$$

$$\frac{D}{Dt}\mathbf{u}^s = -\frac{1}{\rho^s}\nabla p^s - \frac{\rho^n}{\rho}\frac{B}{2}|\boldsymbol{\omega}^s|\left(\mathbf{u}^s - \mathbf{u}^n\right). \tag{3.7}$$

The total kinetic energy, using Equation 3.4, is

$$\begin{aligned} E^t &= \int_V \frac{1}{2}\mathbf{u}^t \cdot \mathbf{u}^t \, dV \\ &= \int_V \frac{1}{2}\left(\frac{(\rho^n)^2}{\rho^2}\mathbf{u}^n \cdot \mathbf{u}^n + \frac{(\rho^s)^2}{\rho^2}\mathbf{u}^s \cdot \mathbf{u}^s + 2\frac{\rho^n\rho^s}{\rho^2}\mathbf{u}^n \cdot \mathbf{u}^s\right) dV, \end{aligned}$$

the 3 terms in the integrand being the normal fluid contribution, the superfluid contribution and a contribution from the cross terms. Now differentiating with

respect to t gives

$$\begin{aligned}
\frac{dE^t}{dt} &= \int_V \frac{1}{2}\frac{D}{Dt}\left(\mathbf{u}^t \cdot \mathbf{u}^t\right) \\
&= \int_V \left(\frac{(\rho^n)^2}{\rho^2}\frac{D\mathbf{u}^n}{Dt}\cdot\mathbf{u}^n + \frac{(\rho^s)^2}{\rho^2}\frac{D\mathbf{u}^s}{Dt}\cdot\mathbf{u}^s + \frac{\rho^n\rho^s}{\rho^2}\left(\frac{D\mathbf{u}^n}{Dt}\cdot\mathbf{u}^s + \mathbf{u}^n\cdot\frac{D\mathbf{u}^s}{Dt}\right)\right) dV \\
&= \int_V \frac{(\rho^n)^2}{\rho^2}\left(-\frac{1}{\rho^n}\nabla p^n + \frac{\rho^s}{\rho}\frac{B}{2}|\boldsymbol{\omega^s}|\left(\mathbf{u}^s - \mathbf{u}^n\right)\right)\cdot\mathbf{u}^n \\
&\quad + \frac{(\rho^s)^2}{\rho^2}\left(-\frac{1}{\rho^s}\nabla p^s - \frac{\rho^n}{\rho}\frac{B}{2}|\boldsymbol{\omega^s}|\left(\mathbf{u}^s - \mathbf{u}^n\right)\right)\cdot\mathbf{u}^s \\
&\quad + \frac{\rho^n\rho^s}{\rho^2}\left(-\frac{1}{\rho^n}\nabla p^n + \frac{\rho^s}{\rho}\frac{B}{2}|\boldsymbol{\omega^s}|\left(\mathbf{u}^s - \mathbf{u}^n\right)\right)\cdot\mathbf{u}^s \\
&\quad + \frac{\rho^n\rho^s}{\rho^2}\left(-\frac{1}{\rho^s}\nabla p^s - \frac{\rho^n}{\rho}\frac{B}{2}|\boldsymbol{\omega^s}|\left(\mathbf{u}^s - \mathbf{u}^n\right)\right)\cdot\mathbf{u}^n \; dV
\end{aligned}$$

The mutual friction terms all cancel (the first with the fourth and the second with the third), leaving the pressure terms which are dealt with as in the case of a single fluid. I conclude that the addition of a mutual friction term coupling the normal fluid and superfluid does not affect the conservation of energy. It is also clear that the cross terms are indispensable in maintaining the conservation of energy i.e. the friction terms in the normal fluid and superfluid components alone do not cancel.

3.2.2 Conservation of total helicity

Using the definitions for total velocity (Equation 3.4) and total vorticity (Equation 3.5), the total helicity is then

$$\begin{aligned}
H^t &= \int_V \mathbf{u}^t\cdot\boldsymbol{\omega}^t \; dV \\
&= \int_V \left(\frac{\rho^n}{\rho}\mathbf{u}^n + \frac{\rho^s}{\rho}\mathbf{u}^s\right)\cdot\left(\frac{\rho^n}{\rho}\boldsymbol{\omega}^n + \frac{\rho^s}{\rho}\boldsymbol{\omega}^s\right) \; dV \\
&= \int_V \left(\frac{(\rho^n)^2}{\rho^2}\mathbf{u}^n\cdot\boldsymbol{\omega}^n + \frac{(\rho^s)^2}{\rho^2}\mathbf{u}^s\cdot\boldsymbol{\omega}^s + \frac{\rho^n\rho^s}{\rho^2}\left(\mathbf{u}^n\cdot\boldsymbol{\omega}^s + \mathbf{u}^s\cdot\boldsymbol{\omega}^n\right)\right) \; dV
\end{aligned}$$

Differentiating with respect to t gives

$$
\begin{aligned}
\frac{dH^t}{dt} &= \int_V \frac{(\rho^n)^2}{\rho}\left(\frac{D\mathbf{u}^n}{Dt}\cdot\boldsymbol{\omega}^n + \mathbf{u}^n\cdot\frac{D\boldsymbol{\omega}^n}{Dt}\right) \\
&+ \frac{(\rho^s)^2}{\rho}\left(\frac{D\mathbf{u}^s}{Dt}\cdot\boldsymbol{\omega}^s + \mathbf{u}^s\cdot\frac{D\boldsymbol{\omega}^s}{Dt}\right) \\
&+ \frac{\rho^n\rho^s}{\rho^2}\left(\frac{D\mathbf{u}^n}{Dt}\cdot\boldsymbol{\omega}^s + \mathbf{u}^n\cdot\frac{D\boldsymbol{\omega}^s}{Dt} + \frac{D\mathbf{u}^s}{Dt}\cdot\boldsymbol{\omega}^n + \mathbf{u}^s\cdot\frac{D\boldsymbol{\omega}^n}{Dt}\right)\,dV \\
&= \int_V \frac{(\rho^n)^2}{\rho^2}\left(\left(-\frac{1}{\rho^n}\nabla p^n + \frac{\rho^s}{\rho}\frac{B}{2}|\boldsymbol{\omega}^s|\left(\mathbf{u}^s-\mathbf{u}^n\right)\right)\cdot\boldsymbol{\omega}^n + \mathbf{u}^n\cdot\left(\boldsymbol{\omega}^n\cdot\nabla\right)\mathbf{u}^n\right) \\
&+ \frac{(\rho^s)^2}{\rho^2}\left(\left(-\frac{1}{\rho^s}\nabla p^s - \frac{\rho^n}{\rho}\frac{B}{2}|\boldsymbol{\omega}^s|\left(\mathbf{u}^s-\mathbf{u}^n\right)\right)\cdot\boldsymbol{\omega}^s + \mathbf{u}^s\cdot\left(\boldsymbol{\omega}^s\cdot\nabla\right)\mathbf{u}^s\right) \\
&+ \frac{\rho^n\rho^s}{\rho^2}\left[\left(-\frac{1}{\rho^n}\nabla p^n + \frac{\rho^s}{\rho}\frac{B}{2}|\boldsymbol{\omega}^s|\left(\mathbf{u}^s-\mathbf{u}^n\right)\right)\cdot\boldsymbol{\omega}^s + \mathbf{u}^n\cdot\left(\boldsymbol{\omega}^s\cdot\nabla\right)\mathbf{u}^s\right. \\
&\qquad \left. + \left(-\frac{1}{\rho^s}\nabla p^s - \frac{\rho^n}{\rho}\frac{B}{2}|\boldsymbol{\omega}^s|\left(\mathbf{u}^s-\mathbf{u}^n\right)\right)\cdot\boldsymbol{\omega}^n + \mathbf{u}^s\cdot\left(\boldsymbol{\omega}^n\cdot\nabla\right)\mathbf{u}^n\right]\,dV
\end{aligned}
$$

Once again, as with the total energy, the friction terms cancel: the first with the fourth and the second with the third. The remaining terms are identically zero by Moffatt's method (cf. Section 2.4).

3.3 Two-fluids GOY model

The natural generalisation of Equation 2.3 to two fluids is

$$\frac{d}{dt}u_m^s = G_m[u^s] - F_m + f^s\delta_{m,m'}, \tag{3.8}$$

$$\left(\frac{d}{dt} + \nu^n k_m^2\right) u_m^n = G_m[u^n] + \frac{\rho^s}{\rho^n}F_m + f^n\delta_{m,m'}, \tag{3.9}$$

where the nonlinear term for each fluid is as in Equation 2.4, and the mutual friction is

$$F_m = \alpha\kappa L(u_m^s - u_m^n). \tag{3.10}$$

The temperature dependence of the friction coefficient $\alpha = B\rho^n/(2\rho)$ is well-known (Donnelly & Barenghi, 1998). For consistency, the vortex line density L is not an arbitrary parameter, but is identified as $L = Q^{1/2}/\kappa$ where the superfluid enstrophy Q is

$$Q = \sum_{m=1}^{M} \frac{1}{2}k_m^2|u_m^s|^2. \tag{3.11}$$

Clearly this model, which describes superfluid vorticity as a continuum, is meaningful only for length scales bigger than the average intervortex spacing $\ell \approx L^{-1/2}$, that is to say for wavenumbers $k_m < k_\ell = 1/\ell = L^{1/2}$.

In a recent paper, Roche *et al.* (Roche *et al.*, 2009) solved equations similar to my Equations 1.1 and 1.2 in the presence of continuous forcing applied to the fluid with the greater density, thus performing the first Direct Numerical Simulations (DNS) of two-fluids hydrodynamics. Unlike my two-fluids shell model, their two-fluids DNS contained an artificial superfluid viscous force $\nu^s\rho^s\nabla^2\mathbf{u}^s$ at the right hand side of Equation 1.1. The introduction of this unphysical term was motivated by numerical analysis. They set the ratio $\nu^n/\nu^s = 4$ to minimise the effect of the artificial viscosity while preserving the stability of the calculation. I stress that my two-fluids shell model (see Equation 3.8) does not need such an artificial term. Another related model is the large-eddy calculation of Merahi *et al.* (Merahi *et al.*, 2006)

3.3.1 Conservation of total energy in the GOY shell model

I now consider the conservation of total energy in the two-fluids GOY shell model in the unforced, inviscid limit. I define the total spectral energy (per unit mass), E^t, as

$$E^t = \sum_{m=1}^{M} \frac{1}{2}|u_m^t|^2 = \sum_{m=1}^{M} E_m^t k_m \tag{3.12}$$

where

$$\begin{aligned}
E_m^t &= \frac{1}{2}\frac{1}{k_m}|u_m^t|^2 \\
&= \frac{1}{2}\frac{1}{k_m}u_m^t \bar{u}_m^t \\
&= \frac{1}{2}\frac{1}{k_m}\left(\frac{\rho^n}{\rho}u_m^n + \frac{\rho^s}{\rho}u_m^s\right)\left(\frac{\rho^n}{\rho}\bar{u}_m^n + \frac{\rho^s}{\rho}\bar{u}_m^s\right) \\
&= \frac{1}{2}\frac{1}{k_m}\left[\frac{(\rho^n)^2}{\rho^2}|u_m^n|^2 + \frac{(\rho^s)^2}{\rho^2}|u_m^s|^2 + \frac{\rho^n\rho^s}{\rho^2}\left(u_m^n\bar{u}_m^s + \bar{u}_m^n u_m^s\right)\right]
\end{aligned}$$

such that the total energy is the sum of the energy contained in the normal fluid, the superfluid and the cross terms. Now differentiating with respect to t gives

$$\begin{aligned}
\frac{dE_m^t}{dt} = \frac{1}{2}\frac{1}{k_m} \quad & \left[\frac{(\rho^n)^2}{\rho^2}\left(\frac{du_m^n}{dt}\bar{u}_m^n + u_m^n\frac{d\bar{u}_m^n}{dt}\right)\right. \\
& + \frac{(\rho^s)^2}{\rho^2}\left(\frac{du_m^s}{dt}\bar{u}_m^s + u_m^s\frac{d\bar{u}_m^s}{dt}\right) \\
& \left. + \frac{\rho^n\rho^s}{\rho^2}\left(\frac{du_m^n}{dt}\bar{u}_m^s + u_m^n\frac{d\bar{u}_m^s}{dt} + \frac{d\bar{u}_m^n}{dt}u_m^s + \bar{u}_m^n\frac{du_m^s}{dt}\right)\right] \\
= \frac{1}{2}\frac{1}{k_m} \quad & \left[\frac{(\rho^n)^2}{\rho^2}\left(G_m^n\bar{u}_m^n + \alpha\kappa L\frac{\rho^s}{\rho^n}\left(u_m^s - u_m^n\right)\bar{u}_m^n\right.\right. \\
& \qquad \left.\left. + \bar{G}_m^n u_m^n + \alpha\kappa L\frac{\rho^s}{\rho^n}\left(\bar{u}_m^s - \bar{u}_m^n\right)u_m^n\right)\right. \\
& + \frac{(\rho^s)^2}{\rho^2}\left(G_m^s\bar{u}_m^s - \alpha\kappa L\left(u_m^s - u_m^n\right)\bar{u}_m^s\right. \\
& \qquad \left. + \bar{G}_m^n u_m^s - \alpha\kappa L\left(\bar{u}_m^s - \bar{u}_m^n\right)u_m^s\right) \\
& + \frac{\rho^n\rho^s}{\rho^2}\left(G_m^n\bar{u}_m^s + \alpha\kappa L\frac{\rho^s}{\rho^n}\left(u_m^s - u_m^n\right)\bar{u}_m^s\right. \\
& \qquad + \bar{G}_m^s u_m^n + \alpha\kappa L\frac{\rho^s}{\rho^n}\left(\bar{u}_m^s - \bar{u}_m^n\right)u_m^s \\
& \qquad + \bar{G}_m^n u_m^s - \alpha\kappa L\left(\bar{u}_m^s - \bar{u}_m^n\right)u_m^n \\
& \qquad \left. + G_m^s\bar{u}_m^n - \alpha\kappa L\left(u_m^s - u_m^n\right)\bar{u}_m^n\right)]
\end{aligned}$$

where

$$G_m^j = G_m[u^j, u^j] = i\left[c_m^{(1)} u_{m+1}^j u_{m+2}^j + c_m^{(2)} u_{m-1}^j u_{m+1}^j + c_m^{(3)} u_{m-1}^j u_{m-2}^j\right]^*, \qquad (j = n, s)$$

and

$$\bar{G}_m^j = G_m[\bar{u}^j, \bar{u}^j].$$

I have used the "‾" symbol, instead of the "*" symbol, to denote complex conjugation since in many cases there is already a superscript symbol in use. Comparing coefficients of the mutual friction terms in this last expression for $\frac{dE_m^t}{dt}$, it is evident that pairs of mutual friction terms cancel: the first with the eighth, the second with the seventh, the third with the sixth and the fourth with the fifth. This means that at each shell the mutual friction terms cancel with each other, unlike the remaining nonlinear terms which only cancel when summed over three consecutive shells due to the properties of the shell coefficients, a, b and c (as shown in Section 2.5).

3.3.2 Conservation of total helicity in the GOY shell model

Define the total spectral helicity (per unit mass), H^t, as

$$H^t = \sum_{m=1}^{M} \frac{1}{2}(-1)^m k_m |u_m^t|^2 \tag{3.13}$$

where $u_m^t = \left(\frac{\rho^n}{\rho} u_m^n + \frac{\rho^s}{\rho} u_m^s\right)$ as in the case of total energy. Now differentiating with respect to t, I find that

$$\frac{dH^t}{dt} = \sum_{m=1}^{M} \frac{1}{2}(-1)^m k_m \frac{d}{dt}\left(|u_m^t|^2\right). \tag{3.14}$$

I have already shown (Section 3.3.1) that the contribution of the mutual friction terms in the expression $\frac{d}{dt}\left(|u_m^t|^2\right)$ is zero since all of the terms cancel out for each shell independently of the other shells (unlike the contribution from the nonlinear terms). Hence I conclude that the conservation of helicity is unchanged by the inclusion of the mutual friction terms to the GOY shell model equation and helicity is conserved in the inviscid, unforced limit of the two-fluids GOY shell model.

3.3.3 Note on the effect of the addition of the mutual friction term to the GOY shell model with respect to the level of numerical error in the conservation of helicity

If the relatively poor numerical conservation of helicity (in comparison to the conservation of energy) in the 3D turbulence shell model is due to the non-positive-definite nature of the shell model representation of the helicity, then the mutual friction terms

should not contribute to this effect because they cancel out at each shell and do not rely on summation over three consecutive shells for cancellation as is the case with the nonlinear term.

Chapter 4

Results

4.1 Forced Turbulence

Unless stated otherwise, the results which I present are obtained by numerically integrating in time Equations 3.8 and 3.9 for $M = 18$, $k_0 = 2^{-4}$, $b = -1/2$ and $\lambda = 2$. The same forcing (typically $f^s = f^n = (1 + i) \times 5 \times 10^{-3}$) is applied to shell $m = 4$ for both superfluid and normal fluid. In theory, forcing can take place at any shell number whose complex velocity u_m is not identically zero (e.g. not at $m = 0$). Experience has shown that forcing at some shell numbers tends to lead to a steadier spectrum than at others. I found that shell number $m = 4$ produces the smoothest spectrum (closely followed by $m = 2$) and also produces a suitably long inertial subrange. These choices for k_0 and m' are commonly found in the literature (Yamada & Ohkitani, 1987, 1988; Pisarenko *et al.*, 1993; Biferale *et al.*, 1995; Kadanoff *et al.*, 1995; Okkels, 2001). A typical initial condition is $u_m^j = (1 + i)k_m \exp(-k_m^2/2)$, $(j = n, s)$, for which $E_m^j = k_m \exp(-k_m^2)$. The time stepping combines the Crank-Nicolson method for the diffusion term and the Adams-Bashforth method for the other terms; the typical time step is $\Delta t = 5 \times 10^{-6}$ seconds. I stop the time integration after the spectrum saturates, making sure that the elapsed time is of the order of 10 large eddy turnover times (about 100 turnover times of the forcing wavenumber), which is typically of the order of 500 s. I find that, once saturation is achieved, time averaged spectra are the same as ensemble averaged spectra (obtained using randomly phase shifted realisations). Further details are included in Appendix B.

To study the temperature dependence of the results, I consider three temperatures $T = 2.157$ K, 1.96 K and 1.44 K which hereafter I refer to as high, medium and low temperatures (Roche *et al.*, 2009). The values of ρ^s, ρ^n, ρ, ν and α corresponding to these temperatures are shown in Table 4.1. The resulting normal fluid fractions, ρ^n/ρ^s, are approximately 10, 1 and 0.1 for high, medium and low temperatures respectively.

Figure 4.1 (top) shows superfluid and normal fluid spectra at high temperature.

T (K)	ρ^s (g/cm^3)	ρ^n (g/cm^3)	ρ (g/cm^3)	ν (cm^2/s)	α
2.157	0.01510	0.12939	0.14449	1.526×10^{-4}	1.045
1.96	0.07335	0.07221	0.14556	9.694×10^{-5}	0.245
1.44	0.13251	0.01264	0.14515	9.538×10^{-5}	0.059

Table 4.1: Helium parameters used in my calculations.

It is apparent that superfluid and normal fluid velocities are locked onto each other by the mutual friction over many length scales as envisaged by Vinen and Niemela (Vinen & Niemela, 2002) and Barenghi *et al.* (C.F. Barenghi *et al.*, 2002). Furthermore a closer inspection of the complex u_m throughout the inertial subrange reveals that $\Re\left(u_m^n\right) = \Re\left(u_m^s\right)$ and $\Im\left(u_m^n\right) = \Im\left(u_m^s\right)$ to at least 4 decimal places. Both spectra are consistent with the Kolmogorov scaling $k^{-5/3}$ (denoted by the solid line) over a wide inertial range $k_0 \ll k \ll k_\ell$, as observed in experiments (Maurer & Tabeling, 1998) and DNS of two-fluids hydrodynamics (Roche *et al.*, 2009). The vertical dotted line denotes the wavenumber k_ℓ which corresponds to the intervortex spacing. To make the Kolmogorov scaling more evident, I plot the compensated spectra $k^{5/3}\ E_k$ (see Figure 4.1 (top, inset)). It is apparent that the superfluid spectrum extends to higher wavenumbers than the normal fluid's: this is because there are no viscous forces acting on the superfluid; nevertheless, the superfluid spectrum decays at large k because superfluid motion is damped by mutual friction. I confirmed that the development of a $k^{-5/3}$ spectrum is dependent neither on my choice of initial condition nor on the fact that I force both fluids.

It is instructive to consider the scale-by-scale energy budget per unit mass. Using Equations 3.8 and 3.9 and the fact that

$$\frac{dE_m}{dt} = \frac{1}{2}\left(\frac{du_m}{dt}\ \bar{u}_m + u_m\ \frac{d\bar{u}_m}{dt}\right)$$

I obtain

$$\frac{dE_m^n}{dt} = T_m^n + D_m^n + M_m^n + \epsilon_{inj}^n \delta_{m,4}, \tag{4.1}$$

$$\frac{dE_m^s}{dt} = T_m^s + M_m^s + \epsilon_{inj}^s \delta_{m,4}, \tag{4.2}$$

where

$$T_m^j = -\Im\left(G_m[u^j] u_m^j\right) \tag{4.3}$$

are the energy transfer rates arising from the triadic interactions between Fourier modes within each fluid,

$$D_m^n = -2\nu^n\ k_m^2 E_m^n \tag{4.4}$$

is the rate of viscous dissipation in the normal fluid,

$$M_m^n = \frac{\rho^s}{\rho^n} \Re \left(F_m \bar{u}_m^n \right) \tag{4.5}$$

and

$$M_m^s = -\Re \left(F_m \bar{u}_m^s \right) \tag{4.6}$$

are the rates of exchange of kinetic energy between the two fluids due to mutual friction (M_m^n being the flow of energy from the normal fluid to the superfluid and M_n^s the flow from the superfluid to the normal fluid) and

$$\epsilon_{inj}^j = f^n \delta_{m,m'} \Re \left(u_m^j \right) \tag{4.7}$$

are the rate of influx of energy due to the forcing terms, where $\Re$ and $\Im$ denote real and imaginary parts respectively. The nonlinear triadic interaction T_m^j is defined such that the energy flux at shell m^* is given by

$$\begin{aligned} \Pi_m^j &= \sum_{m \leq\ m^*} T_m^j & (4.8) \\ &= \Delta_{m+1}^j - (-b-1)\Delta_m^j, & (4.9) \end{aligned}$$

where I define the correlator

$$\Delta_m^j = k_{m-1} \Im \left(u_{m-1}^j u_m^j u_{m+1}^j \right), \tag{4.10}$$

all other terms cancelling due to the conservation of energy.

Figure 4.1 (bottom) shows the energy balance in the inertial range. It is apparent that the total energy flux in each shell is zero (solid black diamond). I find that the normal fluid's inertial term (hollow red squares) is balanced by the viscous term (blue hollow triangles), as in ordinary turbulence (see Figure 2.3). On the other hand, the superfluid's inertial term (solid red squares) is balanced by the mutual friction (solid grey circles), in agreement with Roche *et al.* (Roche *et al.*, 2009). The inset of Figure 4.1 (bottom) shows the energy balance over the all m, including the contribution of the forcing on the shell $m = 4$. I observe that M_m^n and M_m^s are always of opposite signs, as expected from their definitions, and, almost without exception, $M_m^n > 0$ and $M_m^s < 0$. Furthermore $D_m^n < 0$ for all m.

The basic picture did not change when I reduced the temperature to $T = 1.96$ K (Figure 4.2), and then to $T = 1.44$ K (Figure 4.3), again in agreement with experiments (Maurer & Tabeling, 1998). There are however noticeable differences which develop as the temperature is lowered. At high temperature viscous forces provide a sufficient energy sink for normal fluid and, indirectly, for superfluid. As the temperature drops the normal fluid fraction decreases and the superfluid fraction increases.

This reduces the ability of the normal fluid viscosity to adequately dissipate the energy. As T is decreased, both the normal fluid and superfluid spectra extend to the right, towards higher wavenumbers, and the wavenumber, k_ℓ, corresponding to the intervortex spacing, moves progressively to the right. Furthermore at low T in the normal fluid the viscous dissipation is no longer balanced by the inertial term, but by the mutual friction term (see Figure 4.3 bottom).

Finally, I include 2 figures (Figure 4.4) which show the predicted scaling laws for the eddy turnover time τ and vorticity ω. Both can be seen to conform to the scaling laws for classical turbulence, $\tau \sim k^{-2/3}$ and $\omega \sim k^{2/3}$. These figures show all temperatures and once again the superfluid spectra extend further than the normal fluid spectra and the lower temperature cases extend further than the higher temperature cases.

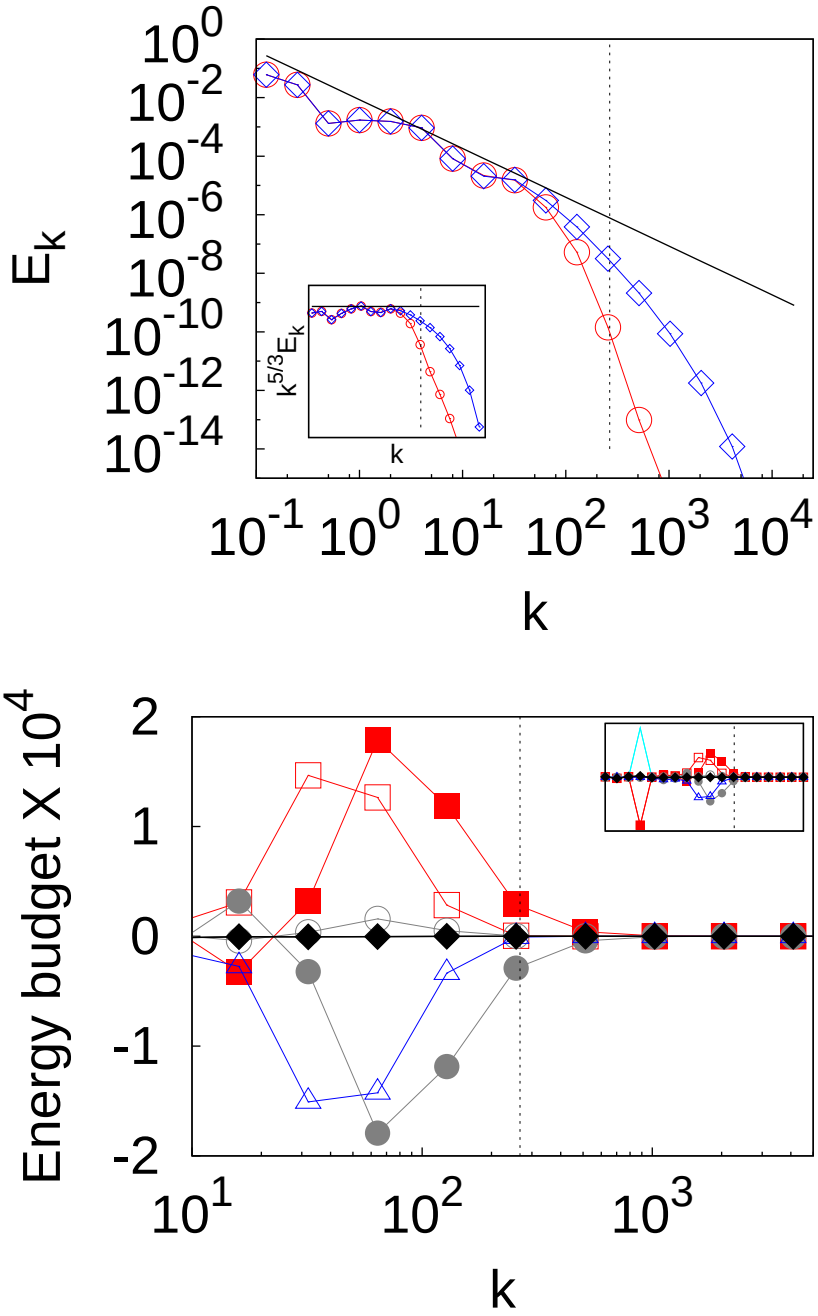

Figure 4.1: Top: Main plot: Superfluid (blue diamond) and normal fluid (red circle) energy spectra E_k (cm^2 s^{-2}) vs wavenumber k (cm^{-1}) at $T = 2.157$ K. Also $k^{-5/3}$ Kolmogorov spectrum (solid line) and intervortex spacing k_ℓ (dotted line). Inset: Compensated spectra. As above, but $k^{5/3}E_k$ vs k. Bottom: Main plot: Scale-by-scale time-averaged energy budget (cm^2 s^{-3}) vs wavenumber k (cm^{-1}) at 2.157K for normal fluid (hollow symbols) and superfluid (solid symbols). Balance in normal fluid between inertial term T_m^n (red squares) and viscous term D_m^n (blue triangles), and in superfluid between inertial term T_m^s (red squares) and mutual friction term M_m^s (grey circles). Also scale-by-scale total energy budget dE_m/dt (black diamonds). Inset: Energy budget over all m, including external forcing $\epsilon_{inj}^{n,s}$ (light blue line), nonzero only at shell $m = 4$. Also k_ℓ (dotted line).

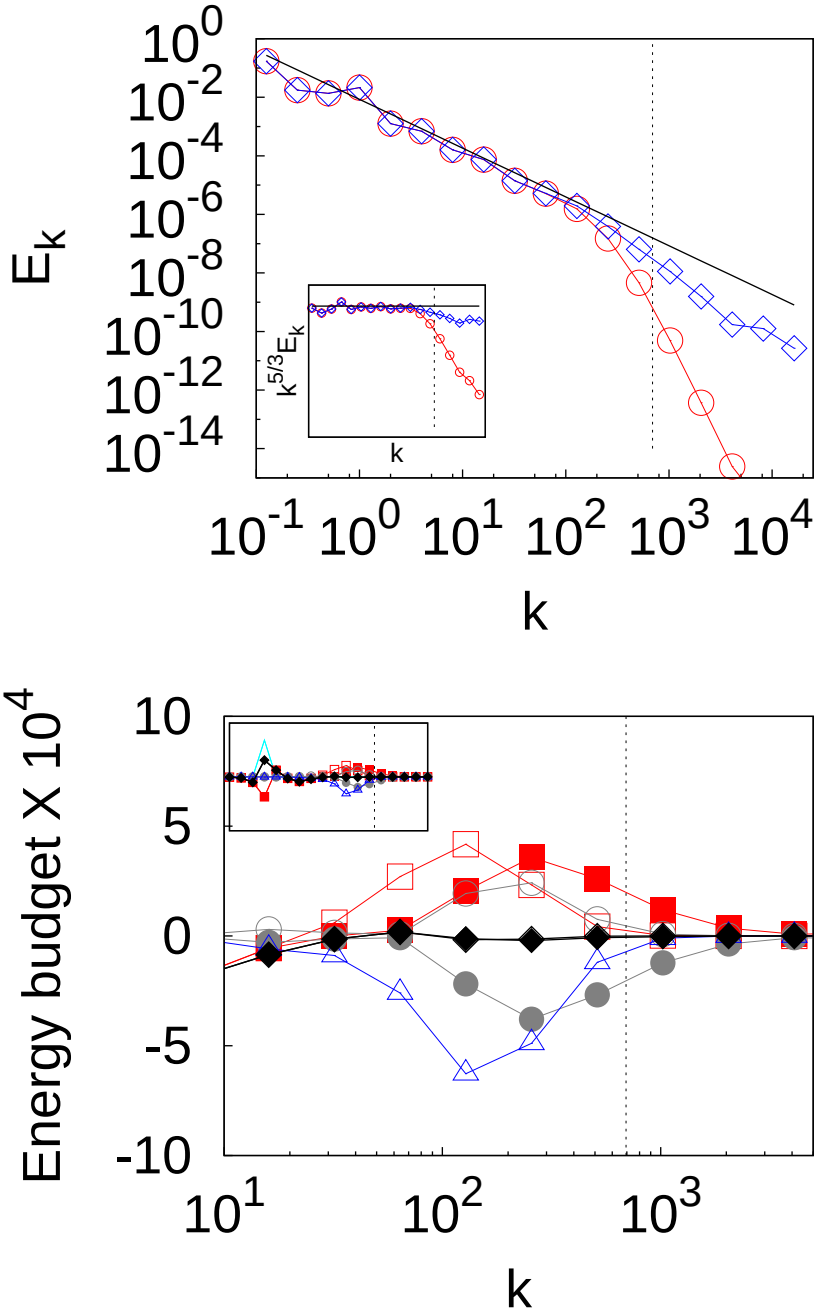

Figure 4.2: Energy spectra (top) and scale-by-scale energy budget (bottom) at $T = 1.96$ K. Details as in Figure 4.1.

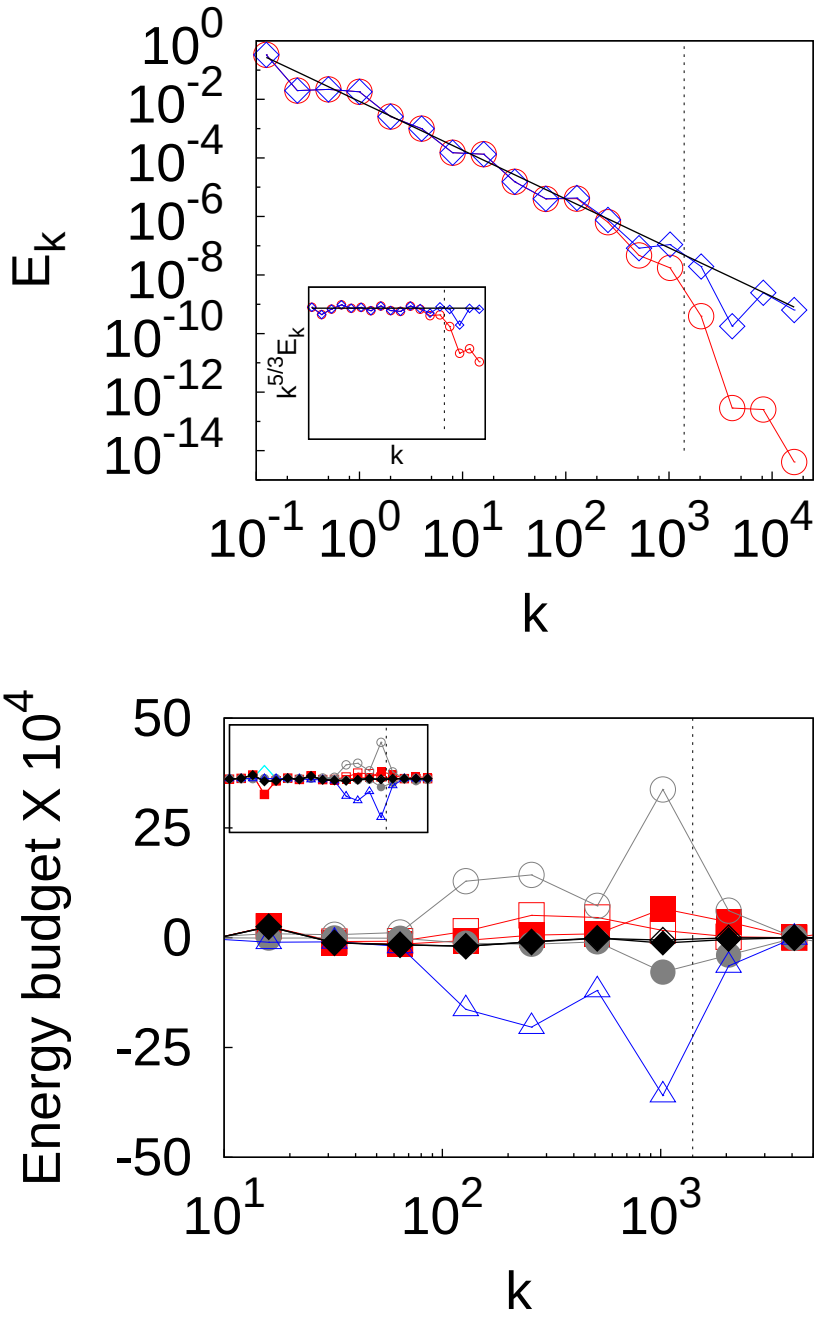

Figure 4.3: Energy spectra (top) and scale-by-scale energy budget (bottom) at $T = 1.44$ K. At this temperature, in the normal fluid the balance is between the mutual friction term M_m^n (grey circles) and the viscous term D_m^n (blue triangles). Details as in Figure 4.1.

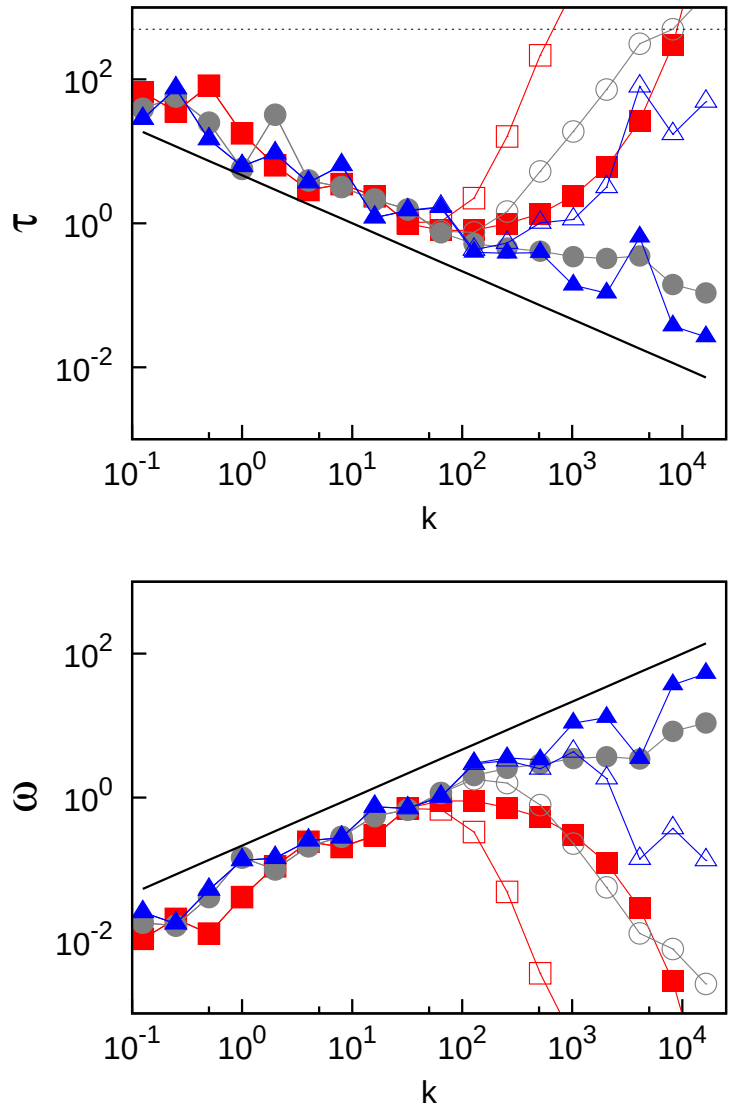

Figure 4.4: Top: Log-log plot of time-averaged turnover time τ (s) vs k (cm^{-1}) for the normal fluid (hollow symbols) and the superfluid (solid symbols), at high (red squares), medium (grey circles) and low (blue triangles) temperatures. The solid black line denotes the $k^{-2/3}$ power law predicted by the K41 theory. The dashed black line denotes the final time, 500 seconds. Bottom: Log-log plot of time-averaged vorticity spectrum ω (s^{-1}) vs k (cm^{-1}) for the normal fluid (hollow symbols) and the superfluid (solid symbols), at high (red squares), medium (grey circles) and low (blue triangles) temperatures. The solid black line denotes the $k^{2/3}$ predicted by the K41 theory.

4.2 Equal energy injection

Up to this stage I have held the forcing constant ($f^s = f^n = (1+i) \times 5 \times 10^{-3}$) for both fluids at all temperatures, even though it is known that the fractional densities of the two fluids vary with temperature. It is important to point out that this is by no means a simple assumption. One can expect that the kinetic energy and hence the velocity imparted by a force onto a liquid volume varies with the density of the liquid. It is therefore crucial in order to compare like-with-like, to vary the forcing with the fluid density.

4.2.1 Forcing coefficient

For two different densities, ρ^i and ρ^j, and a suitable choice for the forcing (per unit volume), F^i, I determine the value of the F^j such that the same kinetic energy is injected at both densities, $E^i = E^j$. Write

$$F^i = \rho^i \frac{du^i}{dt} \approx \rho^i \frac{u^i_{n+1} - u^i_n}{\Delta t}, \tag{4.11}$$

where subscripts n and $n+1$ denote two consecutive timesteps.

Rearranging gives

$$u^i_{n+1} = u^i_n + \frac{F^i \Delta t}{\rho^i}. \tag{4.12}$$

Now given $E^i = 1/2\rho^i (u^i)^2 = 1/2\rho^j (u^j)^2 = E^j$, I obtain

$$u^j = \sqrt{\frac{\rho^i}{\rho^j}}\, u^i \tag{4.13}$$

Therefore

$$\begin{aligned} F^j =& \rho^j \frac{du^j}{dt} \approx \rho^j \frac{u^j_{n+1} - u^j_n}{\Delta t} = \sqrt{\frac{\rho^j}{\rho^i}}\, \rho^i \frac{u^i_{n+1} - u^i_n}{\Delta t} \\ \approx& \sqrt{\frac{\rho^j}{\rho^i}}\, \rho^i \frac{du^i}{dt} = \sqrt{\frac{\rho^j}{\rho^i}}\, F^i \end{aligned}$$

Hence, I conclude that

$$F^j = \sqrt{\frac{\rho^j}{\rho^i}}\, F^i. \tag{4.14}$$

I define $E^t_{inj} = E^n_{inj} + E^s_{inj}$ which, under the above condition for the relationship between the forcing at different temperatures, will remain constant at all temperatures.

4.2.2 Results for equal energy injection

The spectra resulting from equal energy being injected at all temperatures are plotted in Figures 4.5 and 4.6. There is no recognisable difference between these results for equal energy injection and my first set of results, in which constant arbitrary forcing was applied at all temperatures. For example the plots of the energy spectra share the same shape, even the 'knee' visible at high k at low temperature in both the normal fluid and superfluid (cf. Figures 4.3(top) and 4.5(top)).

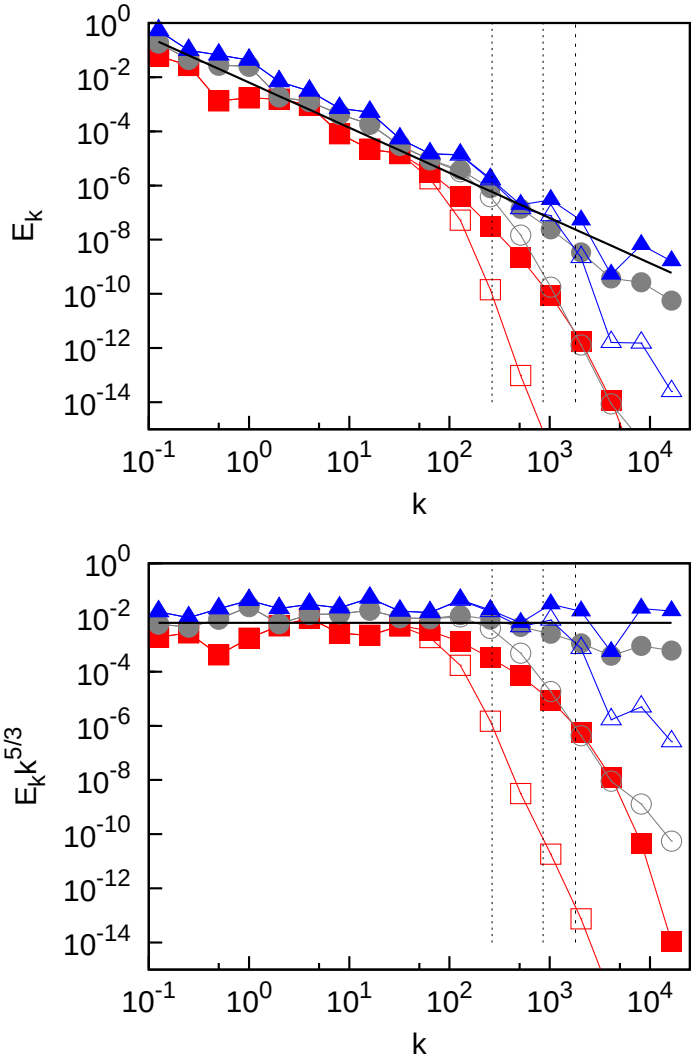

Figure 4.5: Top: Log-log plot of time-averaged energy spectrum E_k ($\mathrm{cm^2 s^{-2}}$) vs k ($\mathrm{cm^{-1}}$) for the normal fluid (hollow symbols) and the superfluid (solid symbols), at high (red squares), medium (grey circles) and low (blue triangles) temperatures. The solid black line denotes the $k^{-5/3}$ power law predicted by the K41 theory. The dashed line denotes the time-averaged wavenumber, k_ℓ, corresponding to the intervortex spacing. Bottom: Log-log plot of time-averaged compensated energy spectrum $E_k k^{5/3}$ vs k for the normal fluid (hollow symbols) and the superfluid (solid symbols), at high (red squares), medium (grey circles) and low (blue triangles) temperatures. The solid black line denotes the compensated $k^{-5/3}$ power law predicted by the K41 theory. The dashed line denotes the time-averaged wavenumber, k_ℓ, corresponding to the intervortex spacing.

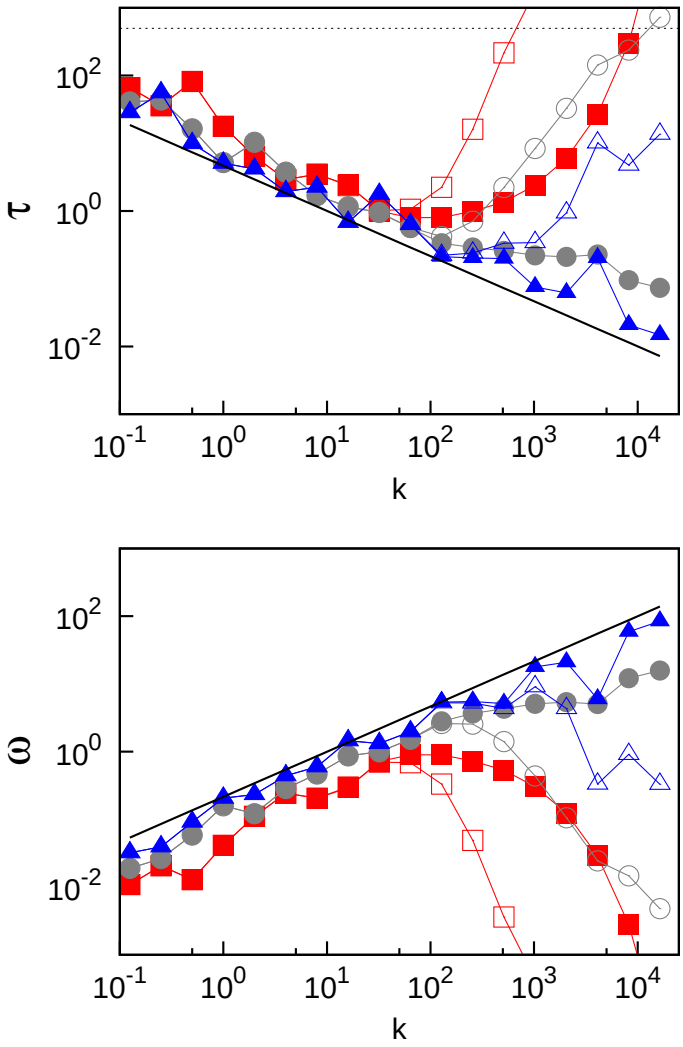

Figure 4.6: Top: Log-log plot of time-averaged turnover time τ (s) vs k (cm^{-1}) for the normal fluid (hollow symbols) and the superfluid (solid symbols), at high (red squares), medium (grey circles) and low (blue triangles) temperatures. The solid black line denotes the $k^{-2/3}$ power law predicted by the K41 theory. The dashed black line denotes the final time, 500 seconds. Bottom: Log-log plot of time-averaged vorticity spectrum ω (s^{-1}) vs k (cm^{-1}) for the normal fluid (hollow symbols) and the superfluid (solid symbols), at high (red squares), medium (grey circles) and low (blue triangles) temperatures. The solid black line denotes the $k^{2/3}$ predicted by the K41 theory.

4.3 Deviations from Kolmogorov $k^{-5/3}$ spectrum

In their pure states ($\rho^s = 0$ and $\rho^n = 0$ respectively) I expect the spectrum of the normal fluid to decay exponentially after k_η (see Equation 4.15), the Kolmogorov microscale at which the inertial term is balanced by the viscous dissipation, and the superfluid to continue to cascade like $k^{-5/3}$; a build-up of energy at high k is thus expected, although the physical interpretation of my model is limited to $k < k_\ell$. I can furthermore expect that as I approach these limiting cases the dominant fluid will cause a deviation in the spectrum of the other fluid. L'vov *et al.* (L'vov *et al.*, 2006) derived approximate expressions for each of these cases.

At low temperatures ($\rho^s \gg \rho^n$), the normal fluid spectrum, instead of decaying exponentially for $k > k_\eta$, deviates slightly from $k^{-5/3}$ due to the force exerted on it by the mutual friction. This continues until the length scale, denoted $k_\star$ (see Equation 4.16), at which the viscous dissipation balances the mutual friction. Beyond this wavenumber the normal fluid spectrum decays with a power-law $k^{-17/3}$; not exponentially as in the case of classical turbulence. This power-law decay is valid at least until k_ℓ, the wavenumber corresponding to the intervortex spacing, at which point the model for the superfluid is no longer valid.

On the other hand, at high temperatures ($\rho^n \gg \rho^s$), the superfluid spectrum beyond k_η is affected by the exponentially decaying normal fluid so that it deviates from its $k^{-5/3}$ power-law to a steeper slope k^{-3}. This continues for as long as the mutual friction dominates over the superfluid inertial term. At some wavenumber, k_+ (see Equation 4.17), this relationship shifts such that the inertial term becomes dominant and the superfluid spectrum regains the $k^{-5/3}$ power-law for as long as the model remains valid ($k < k_\ell$).

Following L'vov (L'vov *et al.*, 2006), I define

$$k_\eta = \epsilon^{1/4}\nu^{-3/4}, \tag{4.15}$$

$$k_\star = \alpha^{1/2}\left(\frac{\rho^s}{\rho^n}\right)^{1/2} Q^{1/4}\nu^{-1/2}, \tag{4.16}$$

$$k_+ = \alpha^{3/2}Q^{3/4}\epsilon^{-1/2}, \tag{4.17}$$

where $\nu = \nu^n$ and $\epsilon \equiv -dE/dt$ is the mean energy dissipation (per unit mass), which, in the inertial subrange, is approximately constant. In the context of shell models I define

$$\epsilon_m = |u_m|^3 k_m. \tag{4.18}$$

I furthermore find, due to the efficient locking of the superfluid and normal fluid velocities in the inertial subrange, that $\epsilon^n \approx \epsilon^s$, which I refer to as ϵ in Equations 4.15 and 4.17.

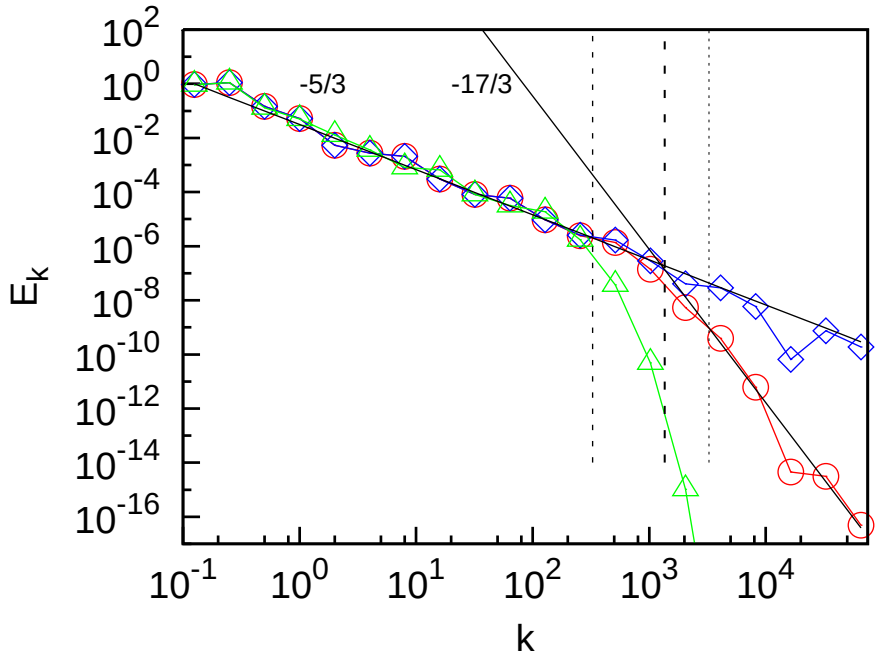

Figure 4.7: Log-log plot showing dissipation of turbulent energy in normal fluid at low temperature. Coupled normal fluid (red circles) is seen to deviate from uncoupled normal fluid (green triangles) as a result of mutual friction with superfluid (blue diamonds). Coupled normal fluid follows $k^{-5/3}$ for $k < k_\eta$, deviates slightly for $k_\eta < k < k_\star$ and follows a $k^{-17/3}$ power-law for $k > k_\star$. The vertical dotted line is k_ℓ and the short- and long-dashed lines are respectively k_η and $k_\star$. For clarity $k_\eta < k_\star < k_\ell$.

Figure 4.7 shows the deviation from the $k^{-5/3}$ scaling at low temperature and the critical wavenumbers at which the spectra change. I calculate these wavenumbers in accordance with the approximations derived by L'vov *et al.* (L'vov *et al.*, 2006). The deviations at high temperature are best realised by considering a system of turbulent superfluid ^{3}He-B (see Section 4.7).

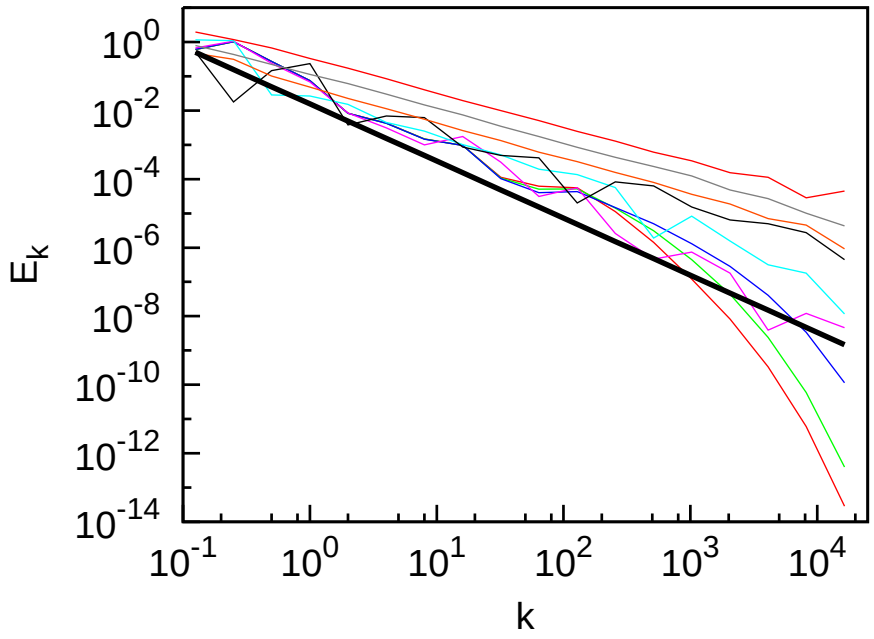

Figure 4.8: Log-log plot of development of build-up of energy in superfluid spectrum. Spectra (bottom to top) at time $t = 0$ (red), 0.025 (green), 0.05 (dark blue), 0.5 (pink), 5 (light blue), 50 (black), 500 (orange), 5000 (grey) and 10000 s (red) after lowering the temperature. k_l (not shown) moves from $k \approx 10^3$ to $k \approx 2 \cdot 10^4$ during this period. The thick black line denotes the $k^{-5/3}$ Kolmogorov spectrum.

4.4 Bottleneck of energy

As mentioned above, I expect that at a sufficiently low temperature the superfluid energy spectrum will build up at high k. This is because the only energy sink for the superfluid is the mutual friction which depends on the presence of the normal fluid to dissipate the superfluid energy. I show the development of the build-up of energy in Figure 4.8. I produced Figure 4.8 by allowing the fluids to attain fully-developed spectra at high temperature. I then reduced the temperature significantly to a finite, fixed temperature well below my previous low T and monitored the changes in the superfluid spectrum over time. In order to maintain numerical stability, I fixed the values of ρ^s, ρ^n and ν^n. Thus the only temperature-dependent variable was α, which alone dictates the magnitude of the mutual friction felt by the superfluid. The spectrum is seen to change as progressively more energy moves to higher k. This phenomenon highlights the necessity for an energy sink at high k such as the Kelvin wave cascade and phonon emission.

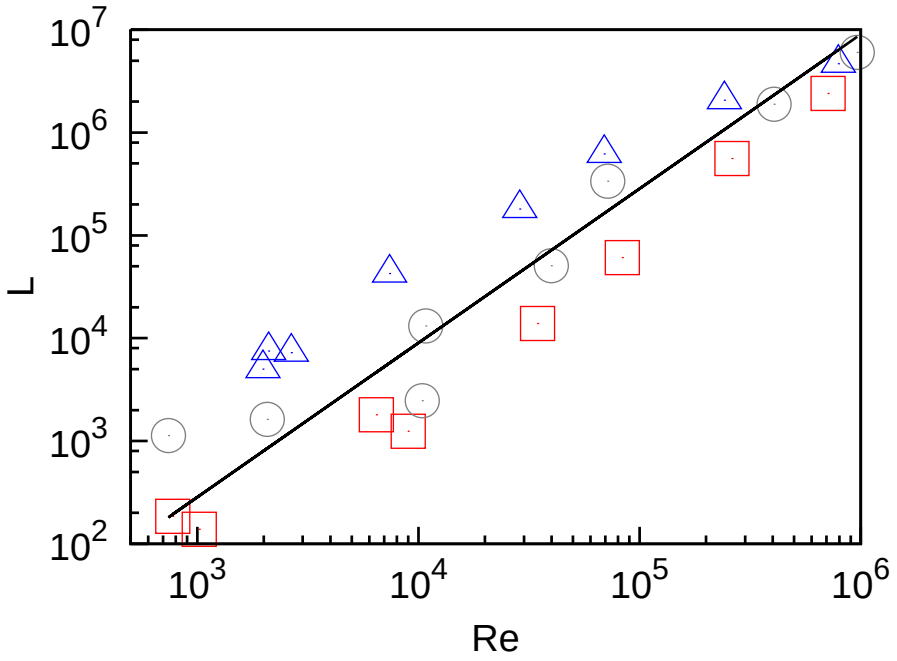

Figure 4.9: Log-log plot of vortex line density, L, vs Reynolds Number, Re, at all three temperatures: high (red squares), medium (grey circles) and low (blue triangles). The points from left to right correspond to increasing forcing, the leftmost point using forcing $f = (1+i)\cdot 5\cdot 10^{-6}$ and the rightmost point $f = (1+i)\cdot 5\cdot 10^{1}$. The Reynolds Number is calculated at the first shell ($m = 1$) giving $D = 2^4$. The solid black line is $L = Re^{3/2}$.

4.5 Quantum Reynolds number

In classical turbulence the Reynolds number, $Re = UD/\nu$, is a measure of the ratio of the inertial and viscous terms, where U and D are the large scale velocity and length scale respectively. The inertial range exists as long as $Re \gg 1$. In the same spirit I may define a quantum Reynolds number as the ratio of the inertial and general dissipative terms, be they due to viscous dissipation or mutual friction. Using this definition I may say that the Reynolds number for the superfluid is temperature-dependent, in agreement with Roche *et al.* (2009): both normal fluid and superfluid spectra extend to higher wavenumbers as the temperature is decreased. I have already shown that the magnitude of the forcing is not responsible for this phenomenon (Section 4.2).

I furthermore show the dependence of the vortex line density, L, on the Reynolds number. According to Kolmogorov, the ratio of the dissipation scale and the scale of the large eddies is $\delta/D \propto Re^{-3/4}$. In superfluid turbulence the smallest scale is $\ell \propto L^{-1/2}$, hence I expect $L \propto Re^{3/2}$. I show that this scaling holds true by considering Re and L and allowing the forcing to vary between $f = (1+i)\cdot 5\cdot 10^{-6}$ and $f = (1+i)\cdot 5\cdot 10^{1}$ in multiples of 10 (see Figure 4.9). This finding agrees with the truncated DNS model of Salort *et al.* (Salort *et al.*, 2011).

4.6 Decaying turbulence

To study the decay of turbulence I set $f = 0$ and start from saturated spectra as an initial condition. I observe that during the decay both the superfluid and normal fluid spectra maintain their initial shape ($k^{-5/3}$ at low to intermediate values of k, followed by a more rapid drop at larger k), as shown in Figure 4.10 (top and bottom). The spectra shown in these figures are the result of ensemble averaging over 10 realisations. I also found that the total turbulent kinetic energy, $E(t)$, where

$$E^j(t) = \sum_m \frac{1}{2}|u_m^j(t)|^2, \ (j = n, s), \tag{4.19}$$

and the vortex line density, $L(t)$, decay as $E(t) \propto t^{-2}$ and $L(t) \propto t^{-3/2}$ as shown in Figures 4.11 and 4.12, which is in agreement with experiments (Stalp *et al.*, 1999; Walmsley *et al.*, 2007, 2008) and theoretical models (Skrbek *et al.*, 2000).

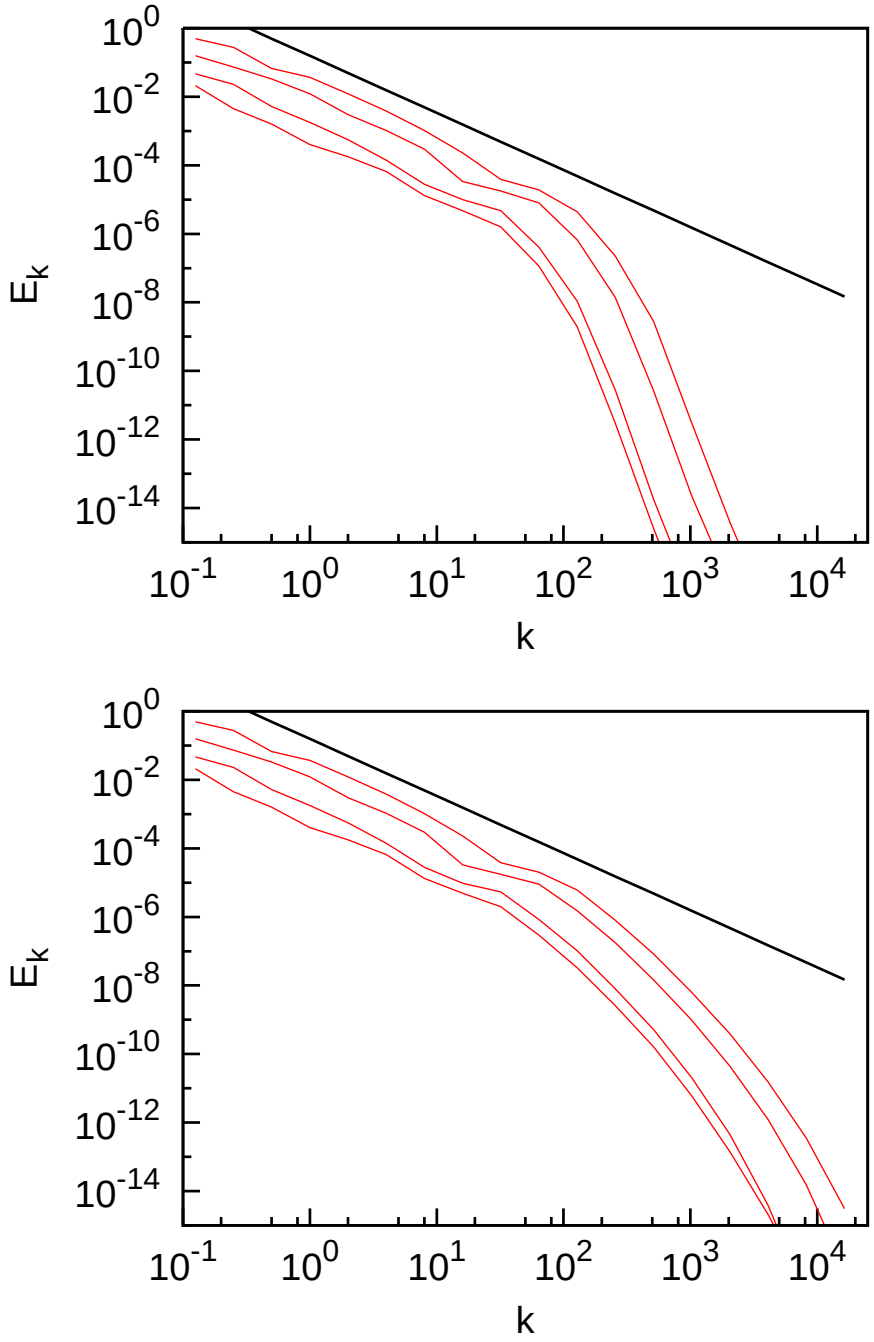

Figure 4.10: Decay of energy spectra for normal fluid (top) and superfluid (bottom) over 10 realisations. Spectra top to bottom: After 500, 1000 , 2500 and 5000 s. Also shown is the $k^{-5/3}$ spectrum (solid black line).

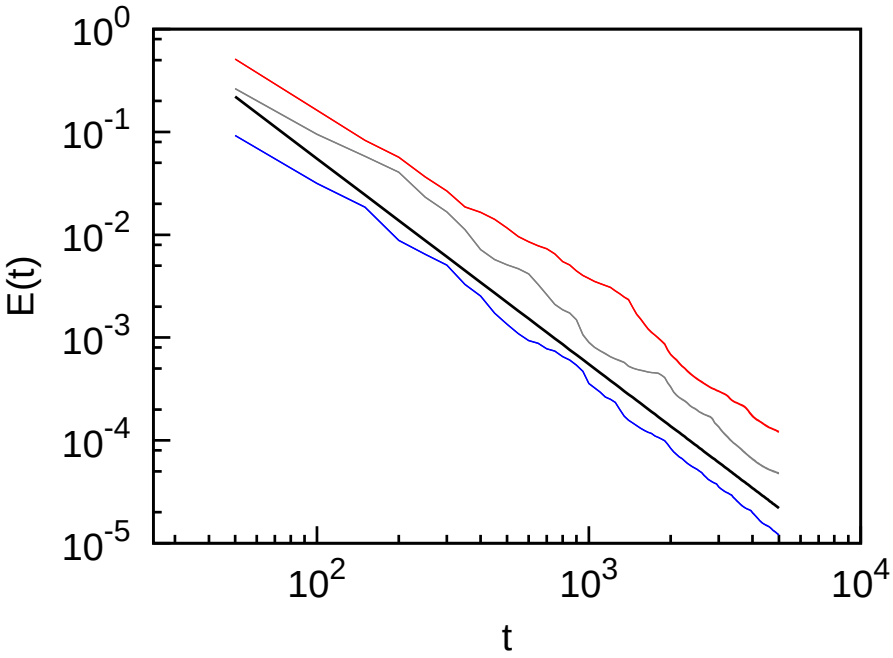

Figure 4.11: Decay of total energy over period of 5000 s ensemble averaged over 10 realisations. Top to bottom: High (red line), medium (grey line) and low (blue line) temperatures. Shifted to show power law. Also shown is the t^{-2} spectrum (solid black line).

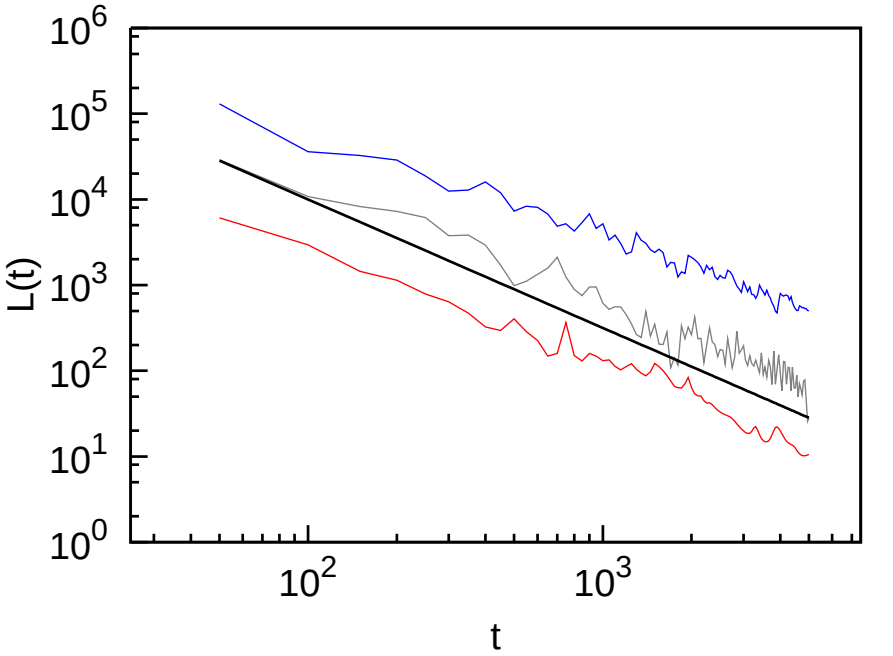

Figure 4.12: Decay of vortex line density over period of 5000 s ensemble averaged over 10 realisations. Top to bottom: Low (blue line), medium (grey line) and high (red line) temperatures. Data is not shifted. Also shown is the $t^{-3/2}$ spectrum (solid black line).

4.7 Forced turbulence in superfluid ^{3}He-B

The other non-radioactive isotope of liquid helium is ^{3}He. ^{3}He atoms are fermions, having only a single neutron in their nuclei, and achieve superfluidity by the Cooper pairing of two atoms. Although T_c for ^{4}He is about 2.17 K, for ^{3}He it is much lower, at about 1 mK. Experimental studies of ^{3}He have focused on the so-called B-phase, known as ^{3}He-B. The most notable physical property of ^{3}He-B is the rapid increase in the normal fluid viscosity below T_c, which is proportional to $1/T^2$ (Landau & Lifshitz, 1987). In fact the viscosity is so great that for all intents and purposes the normal fluid may be considered to be at rest. I may thus consider such a system to be that of a turbulent superfluid in the presence of a stationary normal fluid. This description is equally applicable to that of high temperature ^{4}He in the wavenumber subrange $k \gg k_\eta$. This correspondence has already been noted by L'vov *et al.* (L'vov *et al.*, 2006). A second relevant physical property is the change in its quantum of circulation such that $\kappa = h/2m_3$, or about 2/3 that of ^{4}He, where m_3 denotes the mass of a ^{3}He atom.

In a theoretical paper Vinen (Vinen, 2005) showed that in superfluid ^{3}He-B the positions of the dissipative subrange and the inertial subrange are reversed, such that the dissipation due to the mutual friction occurs at low wavenumbers whereas the inertial subrange obeying the $k^{-5/3}$ power-law is located at high wavenumbers. His prediction for the wavenumber at which this changeover takes place is in agreement with that of L'vov *et al.* (L'vov *et al.*, 2004, 2006). L'vov *et al.* (L'vov *et al.*, 2004) furthermore predicted that the dissipation should follow a k^{-3} power-law, the same power law as that of high temperature ^{4}He in the wavenumber subrange $k \gg k_\eta$ (L'vov *et al.*, 2006).

In order to model turbulence in ^{3}He-B I reduced my two-fluids shell model back to a single-fluid model, replacing viscous dissipation with a dissipation due to mutual friction. The shell model equation then becomes

$$\frac{d}{dt}u_m^s = G_m[u^s] - F_m + f^s\delta_{m,m'}, \tag{4.20}$$

where the mutual friction is now of the form

$$F_m = \alpha\kappa^{^3He}Lu_m^s. \tag{4.21}$$

The temperature dependence of Equation 4.20 is controlled by the parameter α alone. Experience has shown that a mutual friction of this form is extremely efficient at dissipating energy and in order to attain a steady spectrum of the kind described in Vinen (2005) and L'vov *et al.* (2004, 2006) it is necessary both to reduce α to $O(10^{-2})$ (much below T_c and very close to a pure superfluid state) and to increase the forcing to $O(10^2)$ (5 orders of magnitude greater than that used for ^{4}He). The

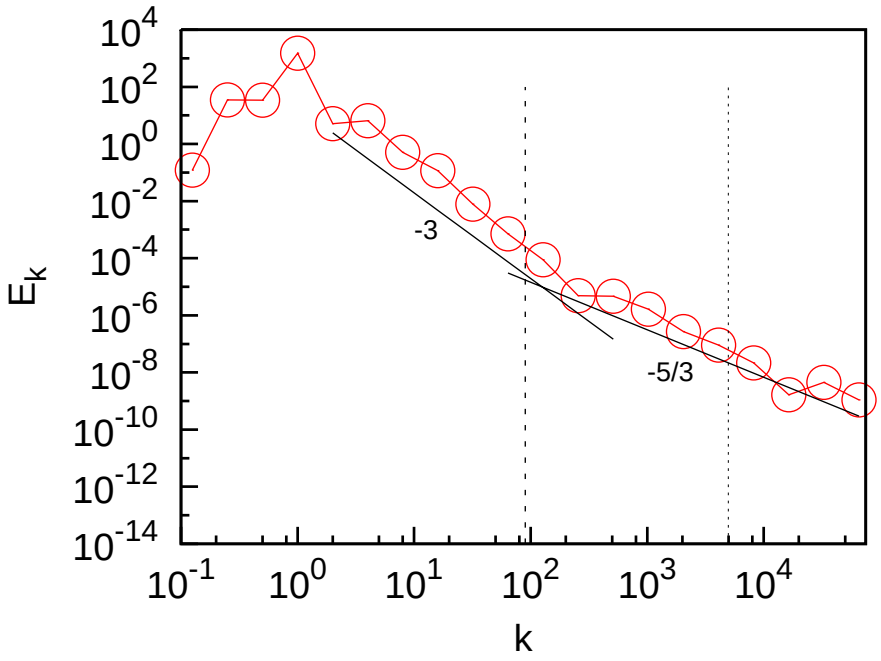

Figure 4.13: Log-log plot of fully developed, steady power spectrum for superfluid (red circles) in the presence of a stationary normal fluid in ^{3}He-B. I show the two power-laws, k^{-3} and $k^{-5/3}$. The dashed line is k_+, the wavenumber at which the inertial term becomes of the same order as the mutual friction term, and the dotted line is k_ℓ, the intervortex spacing.

numerical results show the spectrum initially decreasing like k^{-3} which subsequently changes to $k^{-5/3}$. The changeover wavenumber is in reasonably good agreement with k_+ predicted by L'vov (see Figure 4.13). I used the following parameters $(M, \lambda, m') = (20, 2, 4)$.

Chapter 5

Discussion and further work

I have developed a two-fluids shell model based on the GOY shell model of classical turbulence. I have shown that, in continually excited turbulence, the mutual friction effectively locks together the normal fluid and superfluid over a wide range of wavenumbers, forming a $k^{-5/3}$ Kolmogorov spectrum. By reducing the temperature and hence the normal fluid fraction, I have shown that this range's cut-offs are temperature-dependent for both the normal fluid and superfluid. In other words, lowering the temperature leads to longer inertial subranges. This result for the energy spectrum agrees with the experiment of Tabeling (Maurer & Tabeling, 1998) and the DNS of Roche *et al.* (Roche *et al.*, 2009). The relation which I find between vortex line density and Reynolds number agrees with Salort *et al.* (Salort *et al.*, 2011). I have realised the deviations from the $k^{-5/3}$ spectrum due to the mutual friction predicted by L'vov (L'vov *et al.*, 2006) for ^{4}He at low temperature and by Vinen (Vinen, 2005) and L'vov (L'vov *et al.*, 2004, 2006) for ^{3}He-B. In the zero-temperature limit my model develops a build-up of energy at high wavenumbers, highlighting the necessity for an energy sink at high k, such as the Kelvin wave cascade and phonon emission (Baggaley & Barenghi, 2011*a*). My model shares the common advantage of all shell models: being flexible and computationally inexpensive, it is relatively easy to investigate the decay of turbulence, which would be more difficult with DNS. My results for the decay of turbulence are in agreement with experiments (Stalp *et al.*, 1999; Walmsley *et al.*, 2007, 2008) and theoretical models (Skrbek *et al.*, 2000).

I anticipate that my two-fluids model can be used to study other aspects of quantum turbulence. Logical continuations of the work already included in this thesis could include the decay of turbulence in ^{3}He-B. Does the superfluid energy spectrum of ^{3}He-B decay in the same way as both the normal fluid and superfluid spectra did in ^{4}He, maintaining its shape as the energy decayed, or in some other way? Does ^{3}He-B decay obey the same power laws for $E(t)$ and $L(t)$ as ^{4}He?

I have discussed the deviations from the $k^{-5/3}$ spectrum of the energy spectra of the superfluid and normal fluid. Figure 4.4 seems to show similar deviations for

the spectra of the turnover time τ and the vorticity ω. Do these deviations follow new power-laws and, if so, can they be predicted theoretically as was done for the deviations in the energy spectra?

A further extension of my work would be to study the Kelvin Wave cascade, which is predicted to exist at high wavenumbers and to act as an energy sink for the build-up of energy which I have shown to occur at low temperatures when the normal fluid fraction can no longer dissipate the energy carried by the superfluid fraction. The spectrum of the Kelvin Wave cascade also obeys a power-law, although the exact value of that power-law is currently subject to intense debate (Kivotides *et al.*, 2001; Krstulovic, 2012). I have shown in Appendix C how any power-law can be replicated by the correct choice of the shell coefficient b. The cross-over region between the inertial subrange and the wavenumber range of the Kelvin Wave cascade is subject to a similar debate. It would be informative to examine both of these regions by means of a two-fluids shell model which couples not only the normal fluid and superfluid, but also the two subranges.

Finally, it would be of interest to study 2D two-fluids turbulence. As mentioned in Chapter 2, the only difference between the 2D and 3D GOY shell models is in the choice of b. It should be relatively straightforward to perform the same analysis as was carried out in this thesis for the 2D case. Does mutual friction lock together the two fluids in 2D? In what way? Are there deviations from the classical 2D spectrum for a single fluid? Can they be predicted theoretically? In what way do the energy spectra decay?

Part II

Complex vortex flows: towards anisotropic turbulence

Chapter 6

An introduction to thin-cored vortex rings

6.1 The history of classical vortex rings

Vortex rings have a long and interesting history reaching back over one and a half centuries to Helmholtz's classical paper (Helmholtz, 1858) (translated into English by Tait in 1867 (Tait, 1867)) that laid the foundations for vortex dynamics. Indeed Lord Kelvin (Koenigsberger, 1906) described Helmholtz's theory of vortex rings as 'one of the most beautiful pieces of all beautiful pieces of mathematical work ... in the dynamics of incompressible fluids'. Saffman writes (Saffman, 1981) that vortex rings are a commonly known phenomenon that exemplify the whole range of problems of vortex motion: 'Their formation is a problem of vortex sheet dynamics, the steady state is a problem of existence, their duration is a problem of stability, and if there are several, we have the problem of vortex interactions'. It is precisely the last of these problems (in the context of superfluid turbulence) which is the subject of this Section of my thesis.

Classical vortex rings are easily produced and observed experimentally. The first observation of vortex rings was made by Rogers (Rogers, 1858) in the same year as Helmholtz's paper was published. A much more detailed study was performed by Thomson and Newall in 1885 (Thomson & Newall, 1885) and studies continue into the modern era including such seminal topics as the Crow instability (Crow, 1970), head-on collision of two vortex rings (Lim & Nickels, 1992) and the interaction of a vortex ring with a piston vortex (Allen & Auvity, 2002). Beautiful pictures of vortex ring motion can be found in van Dyke (1982) and online, together with movies, at http://media.efluids.com/galleries/vortex and http://fyfd.tumblr.com. Comprehensive review articles of vortex rings are also available (Shariff & Leonard, 1992; Meleshko, 2010).

It was Dyson (Dyson, 1893) who first developed a simplified model of thin (i.e. the core dynamics can be neglected) interacting coaxial vortex rings with circular

cores of small radius. The opposite extreme, the spherical vortex, was discovered by Hill (Hill, 1894) in the following year. After Dyson, Hicks (Hicks, 1922) employed this model to study the phenomenon of two leapfrogging vortices, or, as he referred to it in the title of his paper, the 'mutual threading' of vortex rings. The result was the Dyson-Hicks Model.

Leapfrogging is not limited to the 3D case of vortex rings, but can be found in a much simpler 2D system consisting of just two vortex-antivortex pairs. Such a system was investigated by Love (Love, 1894) well before Hicks' paper on vortex rings. Love showed that the ratio of the distances between the inner and outer pairs when they are coplanar must be greater than $3 - 2\sqrt{2}$, or approximately 0.172, in order for leapfrogging to occur. If the ratio is less than this critical value, then the smaller pair passes through too quickly for the larger pair to catch up and the pairs move successively further apart. Acheson (Acheson, 2000) took Love's work a step further when he looked at the stability of two dimensional leapfrogging under small disturbances. He discovered that as the ratio increases the vortex-antivortex pairs undergo different regimes of instability, until finally reaching the point where the pairs are insensitive to small perturbations.

6.2 The Dyson-Hicks model for classical thin-cored vortex rings

According to the Dyson-Hicks model, in incompressible, inviscid flow each circular vortex ring moves under its own self-induced axial velocity (which preserves the size of its radius). In addition to this there is a contribution to its velocity due to its interaction with other vortex rings. The rings are modelled as circular vortex filaments of radius R and circular cross-sectional radius a, which remains small compared to R. The rings are aligned coaxially in one plane and translate in the direction normal to that plane. The volume of each ring remains constant over time, $2\pi^2 a^2 R = constant$, such that a change in the radius of the ring must be accompanied by a compensatory change in the cross-sectional radius.

Theoretical studies gave the equation for the self-induced velocity to leading order as

$$v_{si} = \frac{\Gamma}{4\pi R}\left[ln\left(\frac{8R}{a}\right) - C\right] + O\left[\frac{a^2}{R^2}\, ln\left(\frac{8R}{a}\right)\right], \tag{6.1}$$

where C is a constant. Lord Kelvin (Kelvin, 1867) gave, without proof, the value of C as $1/4$. This was later shown to be true by Lamb (Lamb, 1895). Hicks (Hicks, 1885) also confirmed Lord Kelvin's result and furthermore showed that $C = 1/2$ when the vortex core is either hollow or the fluid inside is stagnant.

(a)

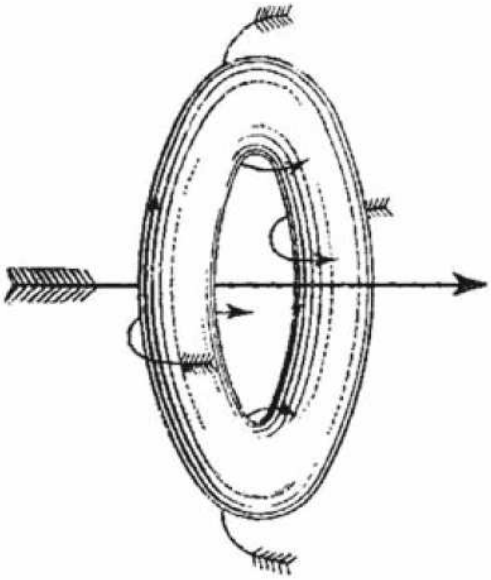

(b)

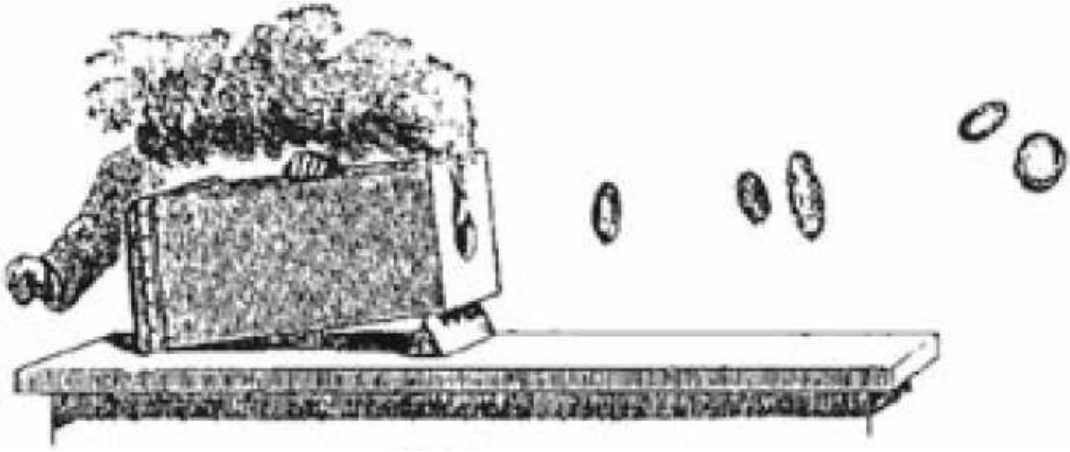

(c)

Figure 6.1: (a) Portrait of Hermann Ludwig Ferdinand Helmholtz (c.1858) (b) Diagram by Tait (Tait, 1876) of vortex moving under self-induced velocity (c) Diagram by Tait (Tait, 1876) of vortex ring box generator.

The self-induced velocity (for a solid core) is then given by

$$v_{si} = \frac{\Gamma}{4\pi R}\left[\, ln\left(\frac{8R}{a}\right) - \frac{1}{4}\right], \tag{6.2}$$

in which case the total kinetic energy E/ρ (per unit density) of the fluid is given by

$$\frac{E}{\rho} = \frac{1}{2}\Gamma^2 R\left[\, ln\left(\frac{8R}{a}\right) - \frac{7}{4}\right]. \tag{6.3}$$

and the impulse P by

$$P = \rho\Gamma\pi R^2 \tag{6.4}$$

where the relation

$$v_{si} = \frac{\partial \rho E}{\partial P} \tag{6.5}$$

holds true for vortex rings of constant volume.

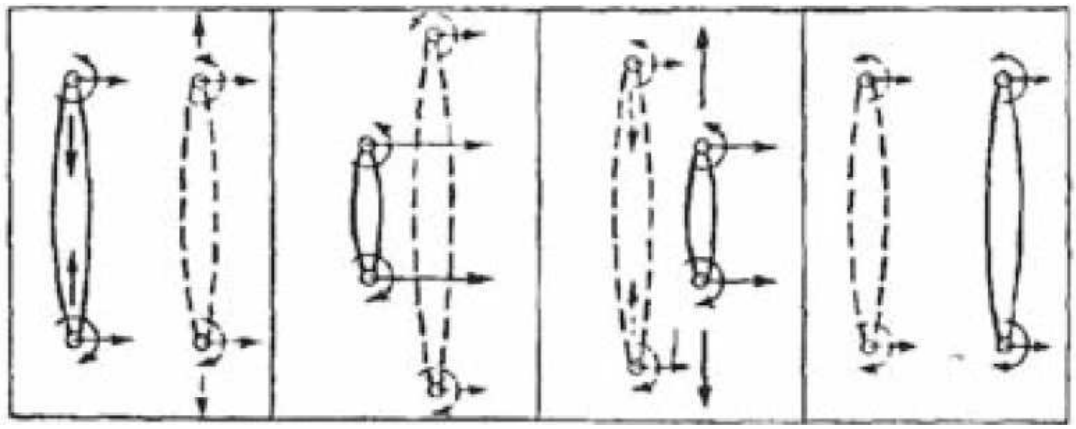

(a)

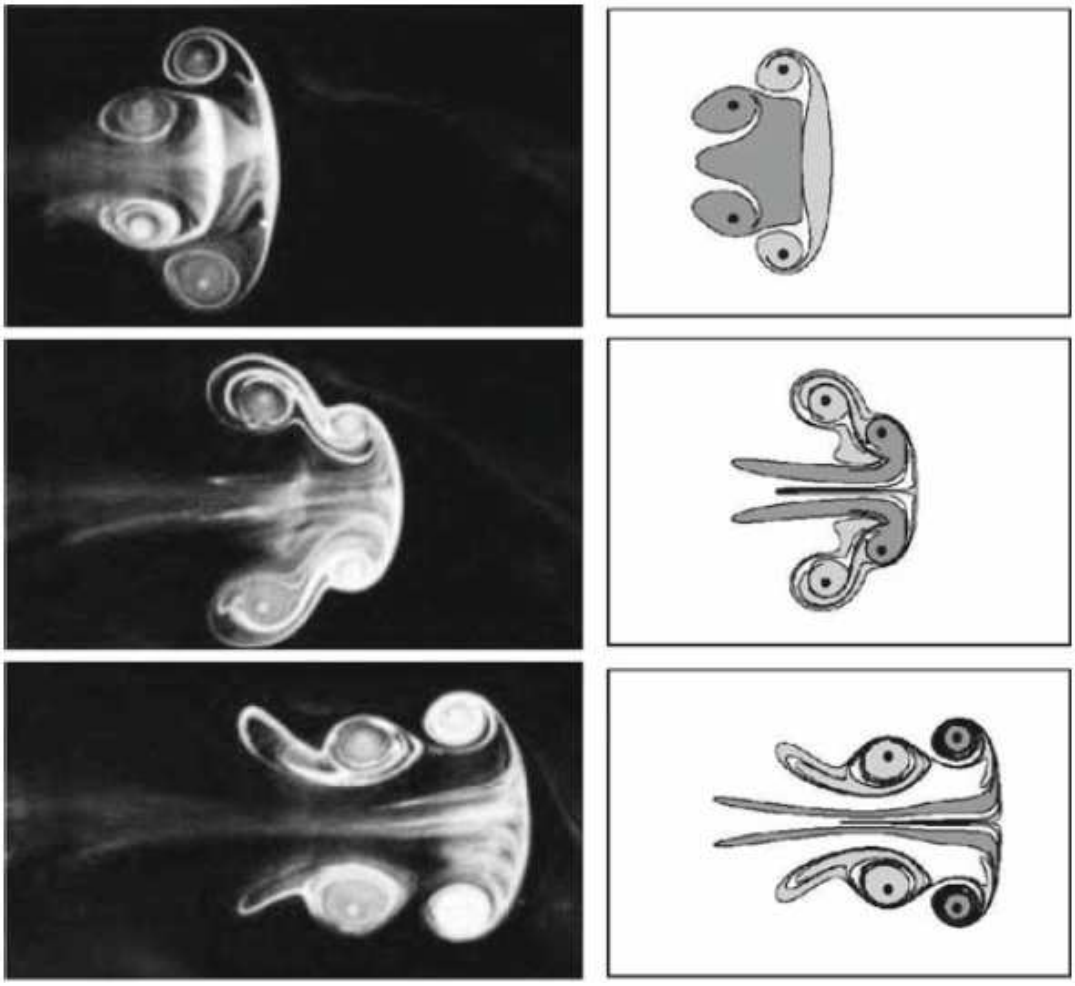

(b)

Figure 6.2: Leapfrogging of two identical vortices (a) Qualitative description (Sommerfeld, 1950) (b) (left) Photographs of two leapfrogging rings (Yamada & Matsui, 1978) and (right) contour tracking of vortex ring 'atmospheres' (fluid entrainment) using the Dyson model.

6.3 Quantised vortex rings

In superfluid ^{4}He, thin-cored vortex rings are not theoretical objects, travelling through an idealised inviscid fluid. Quantised vortex rings are a natural consequence of the quantum nature of superfluid ^{4}He. They are unlike classical vortex rings which are unconstrained in terms of their diameter and the strength of their circulation. In superfluid ^{4}He quantised vortex rings, as with all quantised vortices, have uniform core radius, approximately $a_0 = 1.3 \times 10^{-8}$ cm, and uniform fixed circulation, $\kappa = h/m_4 = 9.97 \times 10^{-4}$ cms^{-2}, where h is Planck's constant and m_4 is the mass of a helium 4 atom. In contrast, the fermionic nature of the superfluid phase ^{3}He-B leads to somewhat different values, $a_0 \approx 10^{-5}$ cm and $k = h/2m_3 \approx 2/3 \times h/m_4$ cms^{-2}.

Quantised vortex rings were detected in superfluid He II over 40 years ago by Rayfield & Reif (1964) and Careri *et al.* (1964). At that time experimentalists were engaged in studying the time-of-flight of ions through a sample of superfluid helium. For an unknown reason the ions travelled much slower than expected. Rayfield and Reif understood that the quickly moving ions exceeded Landau's critical velocity and consequently caused quantised vortex rings to be nucleated. The ions then became trapped on the core of the rings causing the ions to slow down.

Barenghi *et al.* (1983) (Appendix B.2) report the equivalent equations for thin ($R \gg a_0$) solid- (Rayfield & Reif, 1964) and hollow-cored (Roberts & Donnelly, 1970) quantised vortex rings. They give both the energy (per unit density), E/ρ_s, and the self-induced velocity, v_{si}. In the solid-core model

$$\frac{E}{\rho_s} = \frac{1}{2}\kappa^2 R \left[ln\left(\frac{8R}{a_0}\right) - \frac{7}{4}\right], \tag{6.6}$$

and

$$v_{si} = \frac{\kappa}{4\pi\ R}\left[ln\left(\frac{8R}{a_0}\right) - \frac{1}{4}\right]. \tag{6.7}$$

However, this solid-core model is only valid for a core of constant volume, which requires a_0 to decrease or increase as R increases or decreases, something that cannot occur in the context of quantised vortices. The solid-core model also assumes that the core rotates with solid body rotation, for which there is no evidence. For these reasons Roberts *et al.* (Roberts & Donnelly, 1970) proposed the hollow-core model which preserves a_0 as R changes. In this case

$$\frac{E}{\rho_s} = \frac{1}{2}\kappa^2 R \left[ln\left(\frac{8R}{a_0}\right) - \frac{3}{2}\right], \tag{6.8}$$

and

$$v_{si} = \frac{\kappa}{4\pi\ R}\left[ln\left(\frac{8R}{a_0}\right) - \frac{1}{2}\right]. \tag{6.9}$$

I will use the more accurate hollow-core model throughout when comparing theoretical predictions with numerical results.

At finite temperatures the superfluid vortex ring is subject to the mutual friction force as a result of the presence of the normal fluid fraction. This causes the ring to shrink and eventually disappear (i.e. when $R \approx a_0$). Barenghi *et al.* (Barenghi *et al.*, 1983) (Section 3) show that the rate of change of the radius R is given by

$$\dot{R} = \frac{\gamma}{\rho_s \kappa} \, (v_n - v_s - v_{si}), \tag{6.10}$$

where v_n and v_s are imposed axial normal fluid and superfluid velocities and

$$\gamma = \gamma_0 \rho_s^2 \kappa^2 / [\gamma_0^2 + (\rho_s \kappa - \gamma_0')^2], \tag{6.11}$$

where γ, γ_0 and γ_0' are phenomenological parameters which describe the drag force per unit length on the vortex rings. They are related to the friction coefficients B and B' for rotating ^{4}He. Barenghi *et al.* (1983) (Section 3.3) give their values at $T = 2.02$ K (a temperature which I will have recourse to use later) as $\gamma = 1.82 \times 10^{-5}$ gcm^{-1}s^{-1}, $\gamma_0 = 1.69 \times 10^{-5}$ and $\gamma_0' = 4.65 \times 10^{-6}$ ($\rho_s = 0.0601$ gcm^{-3} at that temperature). In the absence of counterflow ($v_n = v_s = 0$) this reduces simply to

$$\dot{R} = -\frac{\gamma}{\rho_s \kappa} \, v_{si}. \tag{6.12}$$

If the slowly-varying part of v_{si} is approximated as a constant

$$\bar{L} = ln \left(\frac{8R}{a_0} \right) - \frac{1}{2}, \tag{6.13}$$

then the lifetime of the ring, τ_{ring}, is given by

$$\tau_{ring} = \frac{2\pi \rho_s (R^2 - a_0^2)}{\gamma \bar{L}} + \frac{(4\pi)^2 \rho_s (v_n - v_s)(R^3 - a_0^3)}{3\gamma\kappa\bar{L}^2}, \tag{6.14}$$

which in the absence of counterflow ($v_n = v_s = 0$) becomes simply

$$\tau_{ring} = \frac{2\pi \rho_s}{\gamma \bar{L}} \, (R^2 - a_0^2). \tag{6.15}$$

The distance travelled in the absence of counterflow in the x direction before the ring disappears is given by

$$\Delta x = \frac{\rho_s \kappa}{\gamma} \, \frac{1 - \gamma\gamma_0/\rho_s^2\kappa^2}{1 - \gamma_0'/\rho_s\kappa} \, (R - a_0). \tag{6.16}$$

(a)

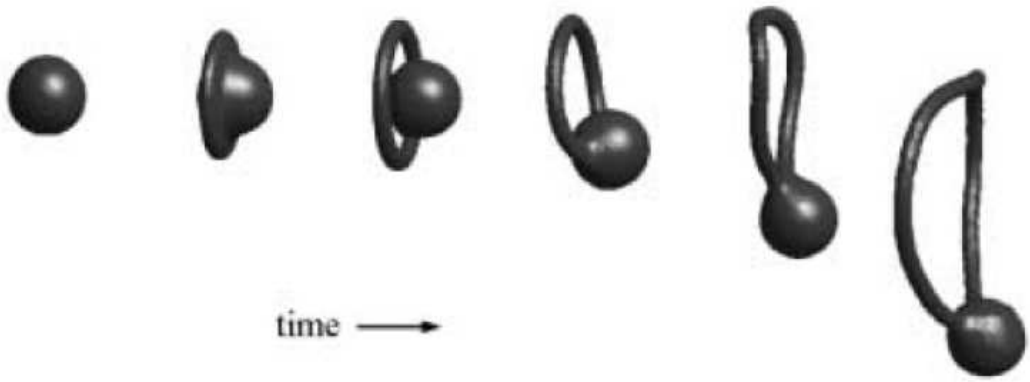

(b)

Figure 6.3: (a) Photographs of superfluid vortex ring taken 1 s apart, as the vortex ring passes through a sheet of illuminating light. The vortex is made visible by a collection of hydrogen particles that are trapped on its core. The width of each photo is 2 mm (Bewley & Sreenivasan, 2009) (b) An ion bubble, moving at speed that exceeds the critical velocity, creates a vortex ring. Calculation performed using the NLSE model (Winiecki & Adams, 2000).

Chapter 7

Superfluid vortex ring experiments

7.1 Piston-induced vortex rings: Experiments by Borner *et al.*

In a series of papers (Borner *et al.*, 1981, 1983; Borner & Schmidt, 1985) Borner *et al.* report the results of experiments to measure the translational velocity and circulation of macroscopic quantised superfluid vortex rings in ^{4}He. The rings were created by means of a single stroke of a piston which forced the superfluid ^{4}He through the circular orifice of a tube. After leaving the tube orifice, the rings travelled downstream along the tube axis. Transmitters and receivers on either side of the ring's path measured the flow-induced running-time differences of first and second sound at a number of points downstream. The results of these experiments proved to be very reproducible. Figure 7.1(a) shows a schematic diagram of the apparatus and Figure 7.1(b) shows a schematic of the principle of circulation measurement described below (Borner *et al.*, 1983).

The inner diameter of the orifice of the piston tube was $P_D = 0.8$ cm. It was oriented so that the axis of the tube lay at 45° relative to the sound waves used to make the measurements. The experiment was performed at temperatures in the range 1.3 K $\leq T \leq$ 2.15 K, at uniform piston velocities 1.0 cms^{-1} $\leq P_U \leq$ 10.0 cms^{-1} and at varying lengths of piston stroke 0.2 cm $\leq P_L \leq$ 1.0 cm. Each measurement was performed 10 times and averaged, giving small error bars. Measurements were taken in the range $1P_D \leq z \leq 7P_D$ downstream of the piston orifice.

7.1.1 Method of circulation measurement

In a fluid which is at rest, first and second sound travel at velocities c_1 and c_2 respectively through superfluid ^{4}He. The passage of the vortex ring across the path taken by the sound waves leads to a delay (Doppler effect), Δt_{F1} and Δt_{F2} for first and second sound respectively, in the time of arrival of the sound waves. This delay is related to the strength of the superfluid and normal fluid circulations, Γ_s and Γ_n

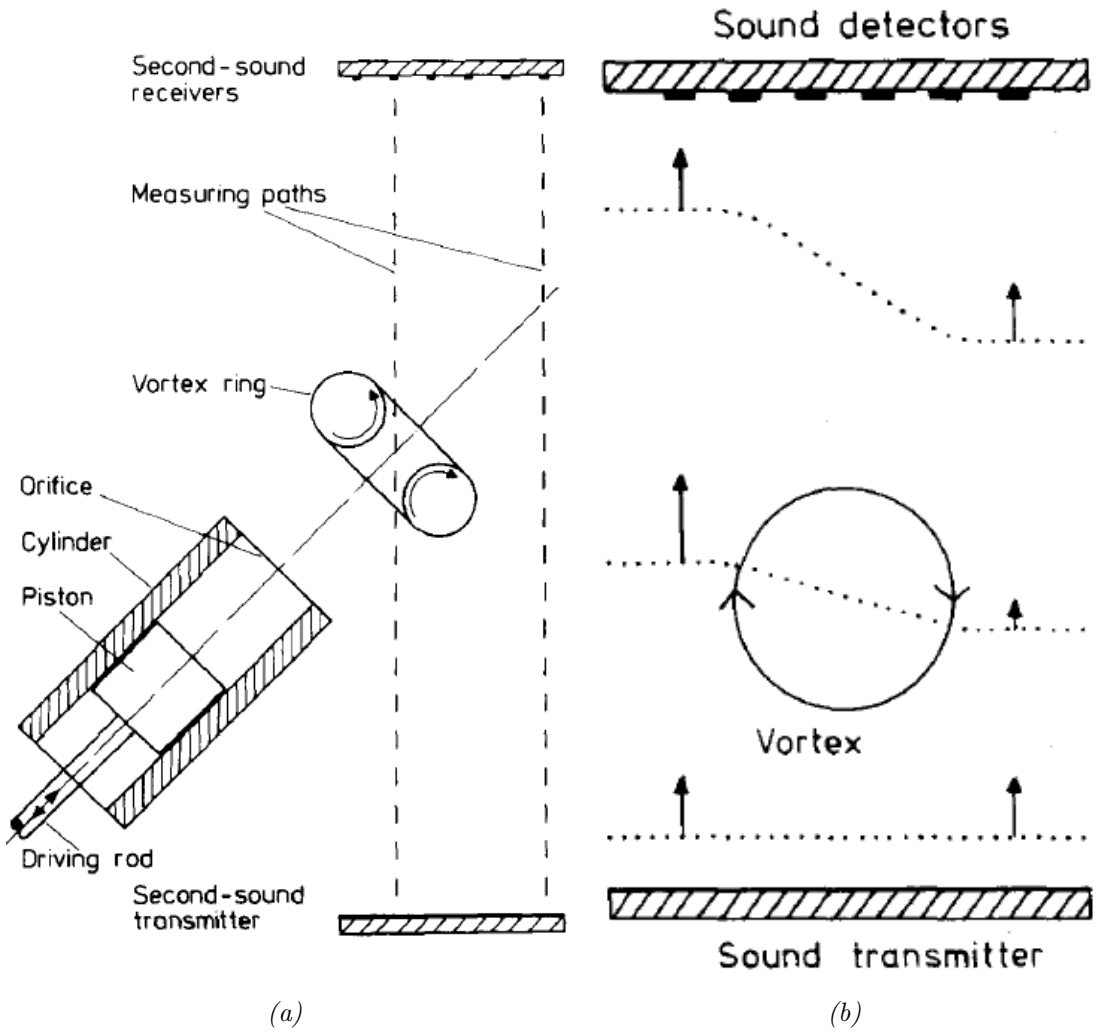

Figure 7.1: (a) Schematic diagram of apparatus used by Borner *et al.* (Borner *et al.*, 1983). Notice that the diagram indicates the presence of second sound detectors only. (b) Schematic diagram of principle of circulation measurement used by Borner *et al.* (Borner *et al.*, 1983). Dotted lines show surface of constant phase (starting with a plane wave at bottom of diagram) and size of arrows show propagation speed.

respectively, contained within the ring.

Below are the equations for the flow-induced running-time differences for first and second sound:

$$\Delta t_{F1} = \frac{1}{c_1^2}\left(\frac{\rho_s}{\rho}\Gamma_s + \frac{\rho_n}{\rho}\Gamma_n\right), \tag{7.1}$$

$$\Delta t_{F2} = \frac{1}{c_2^2}\left[\left(\frac{\rho_n}{\rho} - (1-\sigma)\right)\Gamma_s + \left(\frac{\rho_s}{\rho} - (1-\sigma)\right)\Gamma_n\right], \tag{7.2}$$

where c_1 and c_2 are the speed of first and second sound when the fluid is at rest,

$$\Gamma_i = \oint \mathbf{v}_i \cdot d\mathbf{s} = \iint (\nabla \times \mathbf{v}_i) \cdot \, d\mathbf{a} \quad (i = n, s), \tag{7.3}$$

and

$$\sigma = \frac{\partial\ (ln(\rho_n/\rho))/\partial\ T}{\partial\ (ln\ s)/\partial\ T}, \tag{7.4}$$

where **a** is the control surface enclosed between the measuring paths, ρ_s/ρ is the superfluid fraction, ρ_n/ρ is the normal fluid fraction and s is the specific entropy.

Borner *et al.* (1981, 1983) used flow-induced variations of travelling times of second-sound shock waves only and thus could not calculate the exact values of the circulations of the superfluid and normal fluid. However, combined with knowledge of the superfluid and normal fluid fractions for $T < T_\lambda$ this already gave strong indications of the normal fluid circulation for $T < 1.95K$ and the superfluid circulation for $T > 1.95K$. Borner & Schmidt (1985) used both first and second sound shock waves, which allowed them to calculate exactly the circulation of the superfluid and normal fluid.

7.2 Piston-induced vortex rings: Experiment by Murakami *et al.*

What appears to be an almost identical experiment was performed two years later by Murakami *et al.* (1987). They too utilised a piston with a circular nozzle of 0.8 cm diameter and studied a range of piston stroke velocities, 8.0 cms^{-1} $\leq$ P_U $\leq$ 20.0 cms^{-1}, and stroke lengths, 0.5 cm $\leq$ P_L $\leq$ 1.5 cm. In this case however, the vortex rings were visualised by means of H_2-D_2 tracer particles which became trapped in the vortex cores and were carried along with the flow, allowing Murakami to track the velocity and diameter of the ring.

7.3 Counterflow-induced vortex rings: Experiments by Stamm *et al.*

It is worth noting that another experimental method has been used to produce and study macroscopic vortex rings. Stamm *et al.* produced macroscopic vortex rings by releasing a heat pulse at the bottom of a circular channel with a sharp-edged nozzle. In the first paper (Stamm *et al.*, 1994*a*) they visualised their counterflow-induced vortex rings by means of hollow glass spheres and in the second paper (Stamm *et al.*, 1994*b*) they instead used second sound to measure differences in time-of-flight due to the passage of vortex rings. They make reference to both Borner's and Murakami's papers. Their results show that the maximum range for counterflow-induced vortex rings lies between 5-10 diameters, with the rings following irregular and unstable paths and the diameter of the rings increasing significantly over a short distance. They conclude that counterflow-induced vortex rings are neither as stable nor as reproducible as piston-induced vortex rings.

7.4 Discussion of results of piston experiments

What is most striking about the vortex rings produced by means of a piston is their ability to travel significant distances in an apparently robust and stable formation. The results of both Borner and Murakami testify to this fact.

Borner followed the ring for a distance of approximately 5.6 cm. Assuming that the diameter of the ring was initially similar to that of the piston orifice from which it was fired, $D \approx P_D = 0.8$ cm, or $R \approx 0.4$ cm, this means that the ring travelled about 7 diameters downstream. Borner *et al.* (1983) (see Figure 7.2(a)) shows that, at $T = 2.02$ K, the ring moved faster initially ($1P_D \leq z \leq 2P_D$) and subsequently ($z > 2P_D$) slowed down to a steady velocity (U_T see Table 7.1) for as long as measurements were taken, that is up to $7P_D$. This shows that the ring possessed and retained a coherent, stable structure capable of maintaining a steady velocity over a significant distance.

Borner & Schmidt (1985) concluded (page 139) that: Γ_1 and Γ_2 (circulation as measured by first and second sound respectively) are independent of T to experimental accuracy and are equal to each other. It follows from the above equations that the total normal fluid circulation and the total superfluid circulation are identical for all T ($1.3\ K \leq T \leq 2.15\ K$) such that $\Gamma_{n0} = \Gamma_{s0} = \Gamma_{10} = \Gamma_{20}$, where the subscript '0' indicates the maximum value. This is true for all piston strokes P_L and all piston velocities P_U under investigation.

The natural explanation for this phenomenon is that it is due to the mutual friction. Borner & Schmidt (1985) (page 142) relate the following with regard to timescales: (1) the time necessary to create the rings is only a few milliseconds, (2) the typical duration of an ejection is 100 milliseconds, and (3) the characteristic time for equalisation of normal and rotational superfluid flow is at least one order of magnitude less than the duration of ejection (Fiszdon *et al.*, 1985). So the mutual friction will have caused the normal fluid and superfluid velocity fields to become equal whilst still inside the tube, hence there should be no observable relative velocity outside the tube hence the same circulation was observed outside the tube.

On the other hand, Borner *et al.* (1983) showed that temperature is a significant factor. See Figure 7.2(b) in which the same piston stroke parameters (P_U, P_L and P_D) lead to both vastly different initial circulations and vastly different subsequent behaviour depending on the temperature. In addition to this are Murakami's results, in which the rings are clearly seen to slow down (see Figure 7.2(c)). Having said this, Murakami also claims that his experiment is evidence of the stability of the macroscopic vortex rings since they too translated a significant distance, approximately 13 diameters (even more than Borner reported), with no evidence of a transition to turbulence, which would be evident, for example, from a considerable increase in D (see Figure 7.2(d)).

Under these circumstances it is impossible to decide in favour of one experiment

over another. It remains to pursue a broad numerical investigation, in which it is hoped that evidence will emerge to support the basic tenet of stability in macroscopic vortex rings.

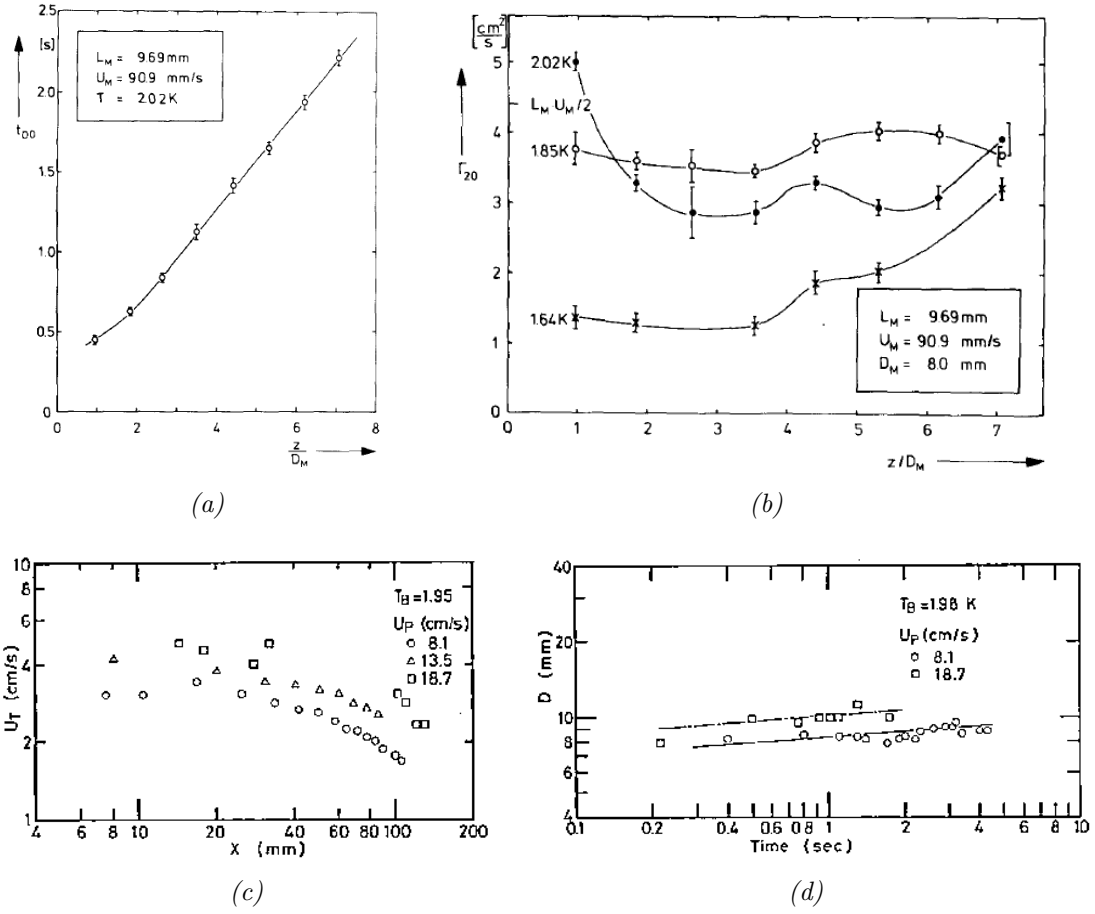

Figure 7.2: Results of piston-induced macroscopic vortex ring experiments. (a) Time displacement curve of a vortex ring at $T = 2.02$ K. The line is drawn to guide the eye. The ring is seen to travel at constant velocity between 2 and 7 ring diameters downstream of the piston nozzle (Borner *et al.* (1983) Figure 4). (b) Variation of the total circulation as measured by second sound Γ_{20} of a vortex ring travelling along its axis of propagation for three different temperatures, $T = 2.02$, 1.85 and 1.64 K. The lines are drawn to guide the eye. Changes in circulation should indicate changes in translational velocity (Borner *et al.* (1983) Figure 7). (c) Variations in translational velocity U_T with distance, x (mm), from nozzle for several different piston velocities at fixed temperature $T = 1.95$ K. If ring size is initially same as nozzle size, then this corresponds to range $1 \leq x/D \leq 13$. Translational velocity is seen to decrease after about 2 diameters in all cases (Murakami *et al.* (1987) Figure 4). (d) Variations in ring diameter D (mm) with time t (s) for two piston velocities at fixed temperature $T = 1.95$ K. Ring diameter increases in both cases (Murakami *et al.* (1987) Figure 5).

7.5 Table of results from Borner & Schmidt (1985)

The most detailed results are to be found in Borner & Schmidt (1985). In Table 7.1 I record the results of their experiments for six different scenarios of temperature,

piston stroke length and velocity. Borner measured the circulation at two different points $z_1 = 2.26D = 1.81$ cm and $z_2 = 5.80D = 4.65$ cm downstream of the piston. A brief discussion of these results will provide a starting point for numerical analysis.

T (K)	P_L (cm)	P_U (cm/s)	$\Gamma_0(z_1)$ (cm^2/s)	$\Gamma_0(z_2)$ (cm^2/s)	$D(z_1)$ (cm)	$D(z_2)$ (cm)	$D/d(z_1)$	$D/d(z_2)$	U_T (cm/s)
1.30	0.902	9.00	4.81	4.52	0.90	0.96	3.64	3.88	2.67
2.15	0.902	9.00	4.85	4.57	0.90	0.94	3.65	3.65	2.69
1.30	0.969	4.50	2.36	2.35	0.88	0.95	3.96	3.82	1.39
2.15	0.969	4.50	2.33	2.32	0.89	0.94	4.02	3.77	1.36
1.30	0.503	9.00	2.55	2.38	0.80	0.84	4.18	3.91	1.73
2.15	0.503	9.00	3.24	3.04	0.77	0.86	3.81	3.90	2.18

Table 7.1: Results of Borner's experiment (Borner & Schmidt, 1985). P_L is the length of piston stroke, P_U the velocity of the piston stroke, Γ_0 is the maximum measured circulation, D/d is the ratio of the ring to core diameters (equivalent to R/a) and U_T is its translational velocity.

Borner reports that the superfluid and normal fluid circulations are identical in all cases. I may therefore take the value of Γ_0 to be the value of circulation for both fluids: $\Gamma_s = \Gamma_n = \Gamma_0$. Taking the quantum of circulation to be 9.97×10^{-4} cm^2/s, I can calculate the number of superfluid vortex rings N present in the macroscopic ring. These values are reported in Table 7.2 to emphasise the multitude of individual vortex rings which constitute a single macroscopic vortex ring. Knowing N and the value of $a = d/2$, I can calculate the vortex line density, L, in a cross-section of the macroscopic vortex ring since $L = N/\pi a^2$ cm^{-2}. This in turn leads to the value of the inter-vortex spacing $\ell = L^{-1/2}$ cm. I record these figures in Table 7.2, denoting the 6 above-mentioned scenarios a-f.

I will refer to these values when deciding which parameters to investigate in my numerical simulation. Considering the information Tables 7.1 and 7.2, I notice that D (and hence R), d (and hence a) and ℓ increase over time (with L decreasing), but D/d (and hence R/a) increases in some cases and decreases in others, although the average value $\langle D/d \rangle$ (or $\langle R/a \rangle$) decreases with time (see Table 7.3) meaning that the average increase in a is greater than the average increase in R. The increase in D over time agrees with Murakami's results (Murakami *et al.*, 1987) (see Figure 7.2(d)). Also, the values for $\ell = O(10^{-3})$ cm lie comfortably within the typical range for inter-vortex spacing: $10^{-4} \leq \ell \leq 10^{-2}$ cm.

Case	$N(z_1)$	$L(z_1)$ (cm^{-2})	$\ell(z_1)$ (cm)	$N(z_1)$	$L(z_2)$ (cm^{-2})	$\ell(z_2)$ (cm)
a	4824	100178	0.0032	4534	94009	0.0033
b	4865	101567	0.0031	4584	87732	0.0034
c	2367	60848	0.0041	2357	48379	0.0045
d	2337	60525	0.0041	2327	47514	0.0046
e	2558	88639	0.0034	2387	65657	0.0039
f	3250	101001	0.0031	3049	79601	0.0035

Table 7.2: Number of individual vortex rings, values of vortex line density and inter-vortex spacing deduced from the results of Borner's experiment Borner & Schmidt (1985). *a*-*f* refer to six rows in Borner's table of results (Table 7.1). I list here the vortex line density and inter-vortex spacing at the two measurement positions, $z_1 = 2.26D = 1.81$ cm and $z_2 = 5.80D = 4.65$ cm downstream of the piston.

7.6 An alternative interpretation of the experimental results

There remains one point with regard to the experimental results which requires further clarification. I have assumed in the discussion up till now that when Borner and Murakami refer to D and d or R and a, that $D = 2R$, such that the diameter of the ring from edge to edge would be given by $D + 2a = D + d$. It may be however that both Borner and Murakami define $D = 2R + 2a$ (see Figure 7.3). The reason to suspect this is twofold. Firstly, Borner (Borner & Schmidt (1985) page 139) writes that, knowing the translational velocity U_T, the ring diameter can be deduced from the measurements of the circulation, because it is then possible to calculate the spatial extent within which the circulation is non-zero. This implies that D is taken to be the entirety of this spatial extent. Secondly, it is likely that Murakami took his values for D directly from the photographs of the vortex rings. Neither author defines the meaning of D.

It must be emphasised that changing the definition of D in no way affects the vortex line density or the inter-vortex spacing, as these parameters are controlled by the value of a (or d). What is affected, is the ratio R/a. According to my initial assumption, $R/a = D/d$, whereas according to this new suggestion $R/a = (D-d)/d$.

It is clear that for either choice of the definition of D, the value of R/a decreases over time (see Table 7.3). Assuming a linear change in the sizes of R and a and extrapolating back to the mouth of the nozzle: $\langle R/a(z=0)\rangle = 3.91$ ($D = 2R$) and 2.91 ($D = 2R + 2a$). The relatively small difference between these values of R/a lead to a big difference in the stability of the macroscopic vortex rings. According to Acheson (Acheson, 2000) the smaller the value of R/a, the more unstable the ensuing leapfrogging, such that there exists a critical value of R/a below which

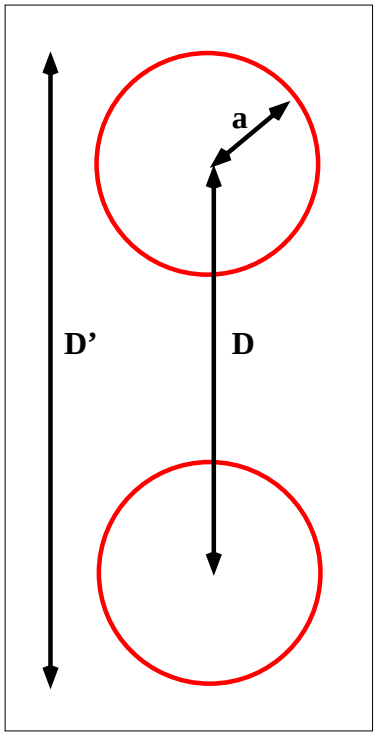

Figure 7.3: Two possible definitions for the parameter D.

	$D = 2R$		$D = 2R + 2a$	
Case	$R/a(z_1)$	$R/a(z_2)$	$R/a(z_1)$	$R/a(z_2)$
a	3.64	3.88	2.64	2.88
b	3.65	3.65	2.65	2.65
c	3.96	3.82	2.96	2.82
d	4.02	3.77	3.02	2.77
e	4.18	3.91	3.18	2.91
f	3.81	3.90	2.81	2.90
$\langle R/a \rangle$	3.88	3.82	2.88	2.82

Table 7.3: Table of values of R/a at z_1 and z_2 due to 2 different definitions for the variable D.

leapfrogging does not take place at all. This issue will be discussed in more detail later (Section 10.8).

7.7 Orifice and nozzle geometry

One issue which deserves mention and further investigation is the geometry of the orifice and nozzle of the piston out of which the vortex ring emerges and its effect on the formation and stability of macroscopic vortex rings in superfluid ^{4}He. This

issue has been addressed experimentally (Didden, 1979; Allen & Auvity, 2002) and numerically (Nitshce & Krasny, 1994) in the context of piston-induced classical vortex rings. See also Section 2 from review paper by Shariff & Leonard (1992). A cursory glance (see for example Figure 7.4) at the literature on this subject is enough to show that vortex rings emerging from a piston immediately develop to be somewhat larger than the opening out of which they emerged. This would imply that a numerical model of a vortex ring emerging from a piston with an opening of width 0.8 cm must possess a diameter greater than 0.8 cm in order to take into account the immediate 'growth' of the vortex ring.

If I once again assume a linear change in the sizes of R and a and extrapolate back to the mouth of the nozzle, then $\langle D(z=0)\rangle = 0.82$ cm. If D measures the total diameter $(2R+2a)$ of the vortex ring, then there does not appear to have been much growth in the vortex on emerging from the orifice. If however $D = 2R$, then there is an additional a cm on either size of D which can be considered to correspond to the immediate growth.

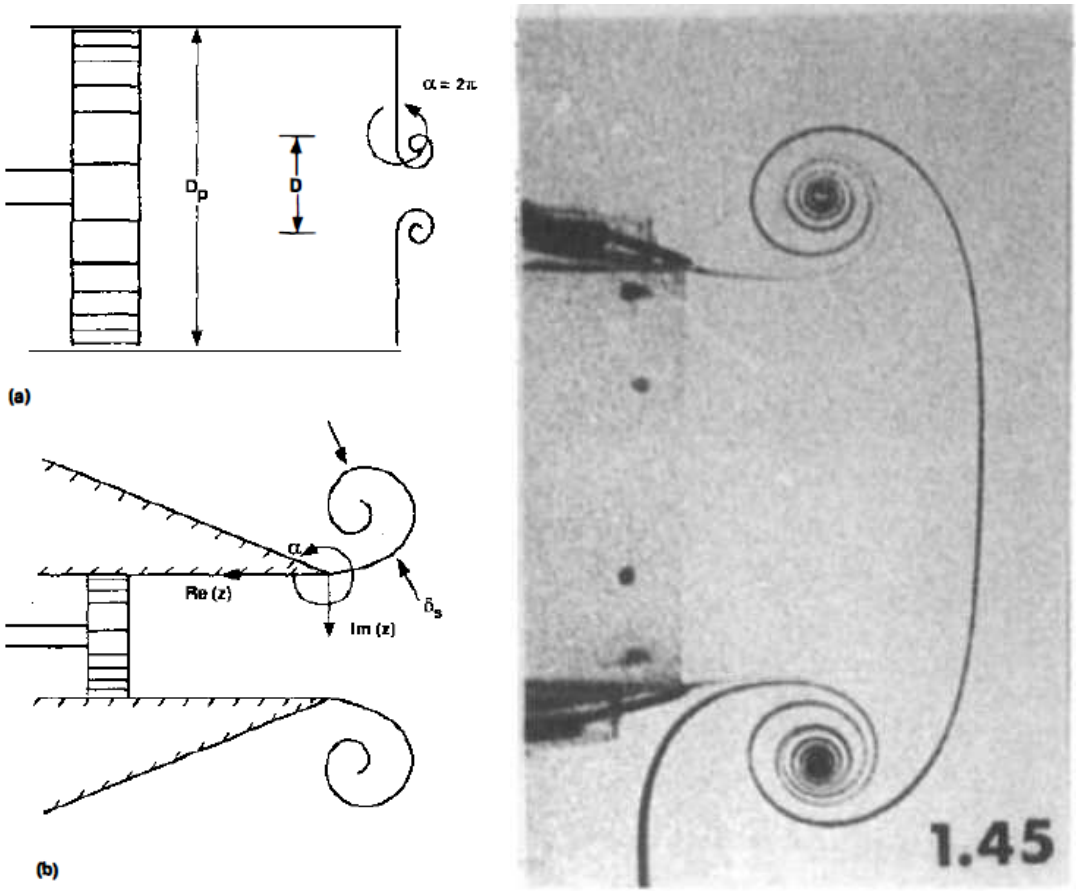

(a) *(b)*

Figure 7.4: Vortex ring generators: (a) Schematic of (left top) orifice geometry (left bottom) nozzle geometry from Shariff & Leonard (1992) (b) (right) Photograph from Didden (1979). Notice vortex rings are always (depicted as) wider than width of orifice/nozzle.

7.8 Summary

In this Chapter I have reviewed the small number of experiments that have been carried out to study vortex rings in superfluid helium II. The experiments were made particularly interesting due to the fact that the circulation they reported corresponds to the presence of a large number of vortex rings $N = O(10^3)$ and that this system of vortex rings, known as a macroscopic or large-scale vortex ring, was shown to have travelled a considerable distance, some 10 times the original diameter of the macroscopic ring without having undergone a turbulent transformation. I have analysed the data from the experiments as much as possible and have discussed how the parameters R, a, R/a, N, L and ℓ change as the system evolves. I have highlighted several features that remain unclear, such as the effect of the orifice and nozzle geometry on the shape and size of the vortex rings and whether the correct ratio of ring to core radii, R/a, is approximately 3 or 4.

Chapter 8

The vortex filament model

8.1 Schwarz's vortex filament model

Following Schwarz (Schwarz, 1985, 1988) who pioneered the vortex filament model, I model the quantised vortices as space curves of infinitesimal thickness. Schwarz argued that this approximation is valid since the radius of the core of a quantised vortex is approximately $a_0 = 10^{-8}$ cm, many orders of magnitude less than all other length scales of interest, such as the inter-vortex spacing, which typically lies between 10^{-2} and 10^{-4} cm.

Let $\mathbf{s} = \mathbf{s}(\xi, t)$ be the position of a point on the vortex filament, where ξ is the arc length and t is the time. Write the first derivative of $\mathbf{s}$ with respect to arc length ξ as $\mathbf{s}'$ and the second as $\mathbf{s}''$. Now define three unit vectors at the point $\mathbf{s}$: the tangent, normal and binormal. The tangent is given by $\mathbf{s}'$, the normal by $\mathbf{s}''/|\mathbf{s}''| = \mathbf{s}''/c$, where $c = |\mathbf{s}''|$ is the local curvature at $\mathbf{s}$ ($1/c$ is the local radius of curvature) and the binormal as $\mathbf{s}' \times \mathbf{s}''$. Figure 8.1 shows the directions of each of these tangents.

Each space curve is discretised by a large number of points. The exact number varies as the line length shrinks and grows. An algorithm ensures that the actual distance between any two points along the curve, δ, remains between 50 and 100 % of the discretisation size $\Delta\xi$ i.e. $\Delta\xi/2 \leq \delta \leq \Delta\xi$. If δ falls below $\Delta\xi/2$, one or more points are removed from the system. If δ exceeds $\Delta\xi$ one or more points are added to the system.

The full motion of a vortex filament is determined by taking into account both the effect of the normal fluid velocity field, felt by the superfluid vortex filaments because of the mutual friction, and the self-induced velocity due to the presence of superfluid vortices, whether the force exerted on a vortex by itself or due to independent vortices. The governing equation of motion of the superfluid vortex lines, at point $\mathbf{s}$ is given by the Schwarz equation

$$\frac{d\mathbf{s}}{dt} = \mathbf{v}_s + \alpha\mathbf{s}' \times (\mathbf{v}_n - \mathbf{v}_s) - \alpha'\mathbf{s}' \times [\mathbf{s}' \times (\mathbf{v}_n - \mathbf{v}_s)], \tag{8.1}$$

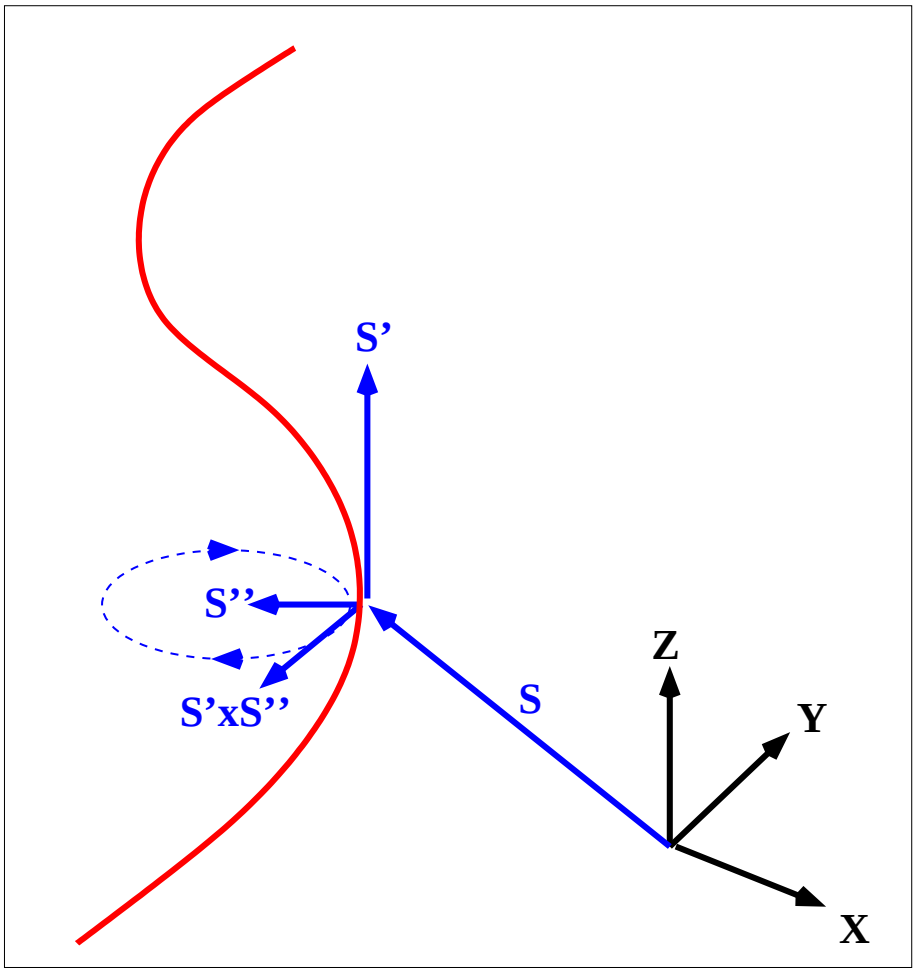

Figure 8.1: Schematic diagram of direction of tangent ($\mathbf{s}'$), normal ($\mathbf{s}''$) and binormal ($\mathbf{s}' \times \mathbf{s}''$) unit vectors (blue) at a point $\mathbf{s}$ on a curved vortex filament (red).

where α and α' are temperature dependent friction coefficients, $\mathbf{v}_n$ is the normal fluids velocity, and $\mathbf{v}_s$ is the superfluid velocity field, which consists of the imposed velocity $\mathbf{v}_s^{ext}$ and the self-induced velocity $\mathbf{v}_{si}$: $\mathbf{v}_s = \mathbf{v}_s^{ext} + \mathbf{v}_{si}$.

Treated rigorously, Schwarz's equation for the superfluid velocity field should be coupled with a suitably adapted viscous Navier-Stokes equation for the normal fluid velocity field which includes a term describing the back reaction of the superfluid on the normal fluid component. However, the complexity and computational cost of treating the two velocity fields self-consistently is beyond the scope of this thesis and, where a normal fluid velocity field (or more to the point a normal fluid vortex ring) is required, it will simply be prescribed. I will consider only the effect of the normal fluid velocity field on the superfluid velocity field and not the other way round.

In the initial condition I prescribe a system of quantised vortices which define the vorticity field. The self-induced velocity field $\mathbf{v}_{si}$ at $\mathbf{r}$ is recovered numerically by solving the Biot-Savart (BS) Law,

$$\mathbf{v}_{si}(\mathbf{r}) = -\frac{\kappa}{4\pi}\oint_L \frac{(\mathbf{s}-\mathbf{r})}{|\mathbf{s}-\mathbf{r}|^3}\times d\mathbf{r}. \tag{8.2}$$

The BS integral diverges as $\mathbf{s}\to\mathbf{r}$. In Schwarz (1985, 1988) Schwarz describes the technique to de-singularise the integral by taking into account the small, but non-zero vortex core radius. To leading order, the BS Law can be approximated by the so-called Local Induction Approximation (LIA)

$$\mathbf{v}_{si}(\mathbf{r}) \approx \frac{\kappa}{4\pi} ln\left(\frac{1}{ca_{eff}}\right)\mathbf{s}'\times\mathbf{s}'', \tag{8.3}$$

where c is the local curvature and a_{eff} is an effective core radius. Schwarz proposed the LIA as a computationally inexpensive alternative to the BS Law. According to the LIA, a vortex filament will only travel along in its binormal direction. This means that the LIA is incapable of modelling the leapfrogging motion of two vortex rings, since leapfrogging requires the rings to move simultaneously in more than one direction: shrinking and moving forward at the same time. On the other hand the BS Law can model leapfrogging and is possessed of a high degree of accuracy. For this reason it is preferable to use the BS Law as much as possible even though the computational cost is relatively high. According to BS each point is moved by all of the other points, so the computational cost of using the BS Law scales like N_p^2, where N_p is the number of discretisation points in the system.

I will return to discussing numerical approaches after describing in some detail the design of the initial configuration and the choice of parameters which will best reproduce the experimental setup of Borner and Murakami.

This level of computational cost quickly becomes unrealistic. As an illustration of this consider Borner's experiment. Borner measured a circulation of $O(1)$ cm^{2}s^{-1} in his experiment, indicating the presence of $O(10^3)$ quantised vortex rings (the quantum of circulation being approximately 10^{-3} cm^{2}s^{-1}). If I let the inter-vortex spacing be $\ell = 0.003$ cm (see Table 7.2) and insist, for the sake of numerical stability, that $\ell/\Delta\xi \geq 10$, then $\Delta\xi \leq 0.0003$ cm. Using the centred hexagonal formation described below, there would need to be 19 layers, making a total of 1027 vortex rings. This in turn would mean that $a = (19-1)\ell = 0.054$ cm and, assuming $R/a = 4$ (see Table 7.1), then $R = 0.216$ cm. The number of discretisation points per ring would then be given by

$$N_p = \frac{2\pi R}{\Delta\xi}\frac{4}{3} \approx 6000,$$

the factor of 4/3 allows the average distance between points to be set at the optimal value, halfway between the upper and lower limit (i.e. at 3/4 $\Delta\xi$). In total, for 1027 rings this would mean more than 6×10^6 points or 36×10^{12} operations per time step, which is well beyond current computational capabilities.

There exists an alternative approach to the full BS Law which is less computer intensive. The Tree Algorithm has been used extensively in astrophysics to study N-body simulations with relatively small loss of accuracy since being pioneered originally by Barnes & Hut (1986). The Tree Algorithm has the capability to reduce the number of operations per time step from N_p^2 to $N_p \log(N_p)$. It has recently been applied to quantised vortex simulations by Baggaley *et al.* (Baggaley & Barenghi, 2011*b*; Baggaley, 2012). For the moment suffice it to say that the enhanced speed of the tree method is apparent when calculating the induced velocity at each vortex point $\mathbf{s}_i$. According to the BS Law the full contribution of all points whether near to or far from $\mathbf{s}_i$ are taken into account. Whereas the Tree Algorithm only considers the full contribution of points near to the vortex point in question. The induced velocity from far vortex points is an average contribution, hence the number of evaluations required per point is significantly smaller than $N1$. A full discussion of its application to quantised vortices dynamics can be found in Baggaley & Barenghi (2012).

Ideally, one would like to use the BS Law in all instances. The limitations of computing facilities and time however place a limit on this usage. I have been able to use the BS Law when considering systems containing 19 or fewer vortex rings. For those with a greater number of rings, I have resorted to the use of the Tree Algorithm. Although Baggaley & Barenghi (2012) discuss the general application of the Tree Algorithm to quantised vortex dynamics, I have performed a series of comparisons between the full BS Law and the Tree Algorithm which validate its use in vortex ring systems. Even with the speed-up gained by use of the Tree Algorithm, the largest system of vortex rings that I have been able to simulate for some length of time is one containing 91 rings, approximately one order of magnitude less than the number of rings expected to have been induced in the piston experiments (see Chapter 14).

8.2 Numerics

Numerical simulations, both those using the full BS Law and those using the Tree Algorithm, were performed using the Qvort Fortran 2003 code written by A.W. Baggaley (http://www.staff.ncl.ac.uk/a.w.baggaley/doxy/html/index.html). Simulations were performed in a computational box of side 10.0 cm ($5.0 \leq x, y, z \leq 5.0$) with open boundaries throughout. The macroscopic vortex is initially positioned at the left hand side of the box and moves to the right. Unless otherwise stated, the ratio of the inter-vortex spacing to the spatial resolution is initially at $\ell/\Delta\xi = 10$, so ℓ is in fact 20 times the smallest length scale ($\Delta\xi/2$).

Some of the relevant parameters entered in the `run.in` file are as follows (notice that they are dimensional):

- number of time steps
- frequency of snapshots
- size of time step Δt (seconds)
- spatial resolution along rings $\Delta\xi$ (cm)
- radius of macroscopic vortex ring R (cm)
- radius of 'core' a (cm)
- number of centred hexagonal layers n
- temperature dependent friction coefficients α and α'
- θ, a measure of the averaging used in Tree Algorithm

Some of the following relevant flags were also used:

- use of full BS Law or Tree Algorithm
- type of normal fluid flow field, which can also be zero
- serial or parallel (`openmp`) run

When necessary additional parameters such as those defining 3D or 2D meshes can also be input. The intervortex spacing ℓ does not feature explicitly amongst the parameters, but is generally a product of the choice of n and a (see Section 8.3).

A vital feature lacking in the BS Law (but present in the Gross-Pitaevskii Equation) is the ability for vortex lines to reconnect. Reconnection between vortex lines or self-reconnections must be handled algorithmically. Most reconnection algorithms use the maximum spatial resolution to define the critical reconnection distance such that a reconnection takes place if two points $\mathbf{s}_i$ and $\mathbf{s}_j$ come within a distance $\Delta\xi/2$ of each other. This is subject to the condition that the vortex lines to which the points belong are anti-parallel. This is checked prior to a reconnection by taking the inner product of the two local tangent vectors $\mathbf{s}'_i = d\mathbf{s}_i/d\xi$ and $\mathbf{s}'_j = d\mathbf{s}_j/d\xi$ (see Baggaley (2012)). It is important to point out that physically reconnections are accompanied by energy emission in the form of phonons, such that energy is not conserved through a reconnection event. In an attempt to build this loss of energy into the reconnection algorithm the total line length (a proxy for the vortex line energy) is reduced through a reconnection event. That is to say that, when lines A-B and C-D reconnect to form A-C and D-B, the total line length after is less than before. The exact change in line length depends on the choice of algorithm.

The position and translational velocity of the macroscopic ring is tracked by calculating at each time step the position of the centre of vorticity, that is the 'centre of mass' of all discretisation points which constitute the vortex rings. The

translational velocity then follows by considering the change in the centre of vorticity over any two consecutive time steps.

8.3 Initial configuration

The initial condition arranges all of the vortex rings coaxially, lying in the y-z plane, oriented so that they will travel in the positive x direction as a result of their own self-induced velocity. For $N \geq 7$ I base myself on a centred hexagonal layout for the cross-section of the core of the macroscopic ring such that each successive hexagonal layer is positioned at a distance ℓ, the inter-vortex spacing, further out from the centre than the previous layer. The reason for choosing an hexagonal layout is because it is the most energetically favourable formation, as discussed in Donnelly (1991) Chapter 5. The number of vortices in this hexagonal layout is given by centred hexagonal numbers, such that $N = 3n(n-1)+1$ for $n \geq 1$.

$N = 2$ and $N = 3$ are special cases. They are investigated as relatively simple, computationally inexpensive cases which exhibit some of the interesting features of the more complicated cases. For $N = 2$ the initial condition is both co-axial and concentric such that both rings lie in the same $y - z$ plane at a distance equal to ℓ. This means that $a = \ell/2$ (see Figure 8.2). For $N = 3$ the initial condition has a cross-section in the shape of an equilateral triangle, which is also the basic unit of the hexagonal layout, of side ℓ. This means that $a = \ell/\sqrt{3}$ (see Figure 8.3). In general, for a centred hexagonal layout with $N = 3n(n-1)+1$ vortex rings where $n \geq 2$, $a = (n-1)\ell$. For example, when $n = 2$ then $a = \ell$ and when $n = 3$ then $a = 2\ell$ (see Figures 8.4 and 8.5).

Below are figures showing a cross-section of the core of several macroscopic vortex rings: $N = 2$, 3, 7 and 19 rings. Each figure shows R and a, the position of the vortices (blue dots, solid and hollow) and the rotational direction of each core (red arrows).

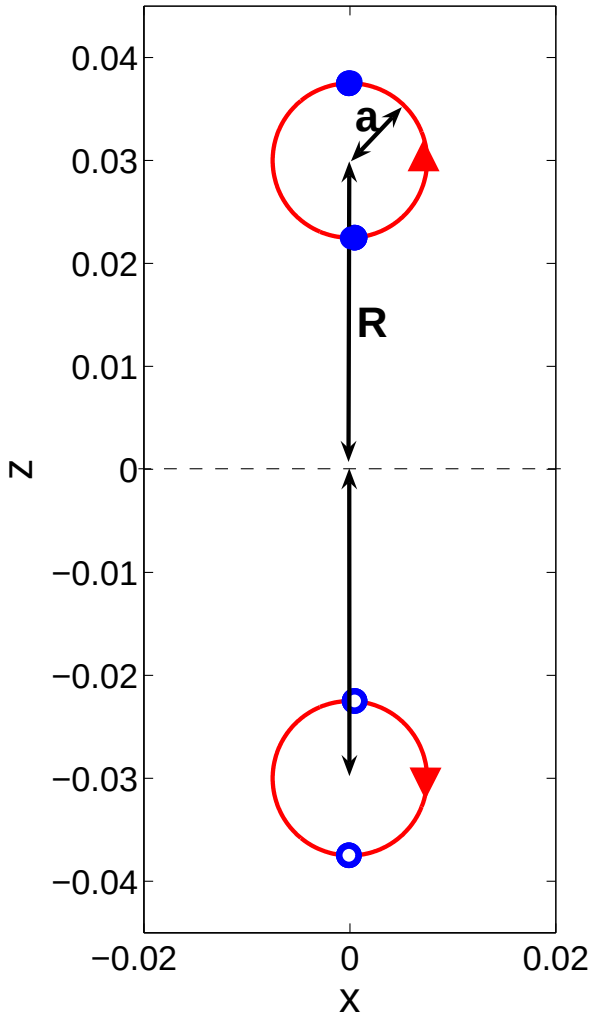

Figure 8.2: Initial configuration in x-z plane for 2 co-axial and concentric vortex rings. $R = 0.03$ cm and $a = \ell/2 = 0.0075$ cm, consistent with $R/a = 4$. Solid and hollow blue dots show where vortex rings cut x-z plane with positive (anticlockwise) and negative (clockwise) circulation respectively, as indicated by the red arrows. The red circles are for visualisation purposes and are centred on $z = \pm 0.03$ cm and have radius $a = 0.0075$ cm.

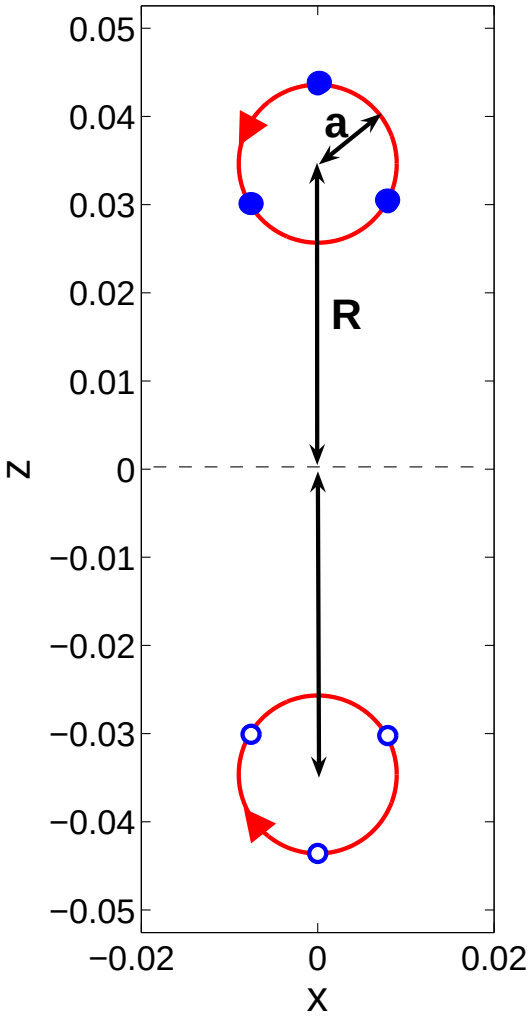

Figure 8.3: Initial configuration for 3 co-axial vortex rings. Solid and hollow blue dots show where vortex rings cut x-z plane with positive (anticlockwise) and negative (clockwise) circulation respectively, as indicated by the red arrows. The vortex rings are positioned so that they cut the x-z plane at the vertices of equilateral triangles, centred at $z = \pm 0.0346$ cm and of side $\ell = 0.015$ cm, such that $a = \ell/\sqrt{3} = 0.00866$ cm (which is also the radius of the red circles) and $R/a = 4$. The red circles are for visualisation purposes only.

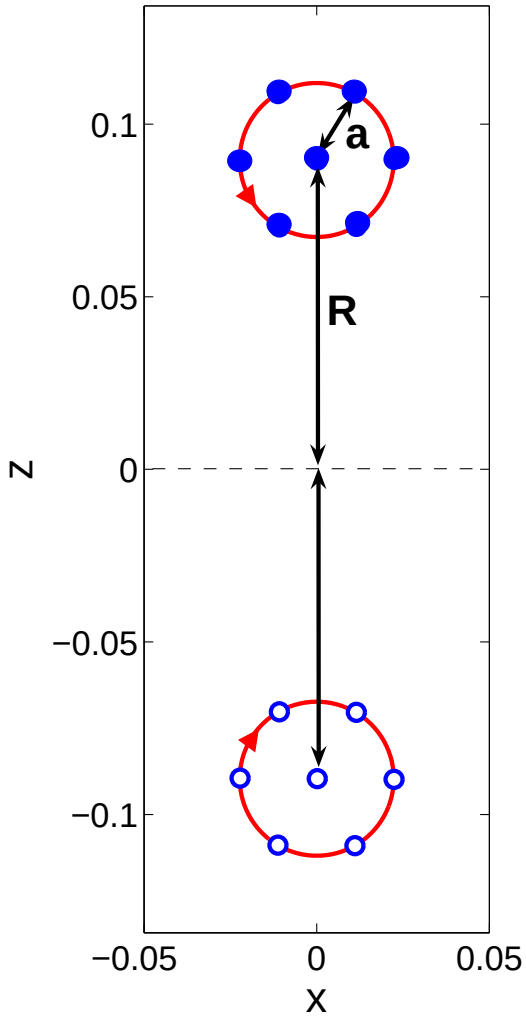

Figure 8.4: Initial configuration for 7 co-axial vortex rings. Solid and hollow blue dots show where vortex rings cut x-z plane with positive (anticlockwise) and negative (clockwise) circulation respectively, as indicated by the red arrows. The vortex rings are positioned so that they cut the x-z plane in hexagonal formation, centred at $R = 0.0896$ cm. $a = 0.0223$ cm and $R/a = 4$. The red circles are for visualisation purposes only.

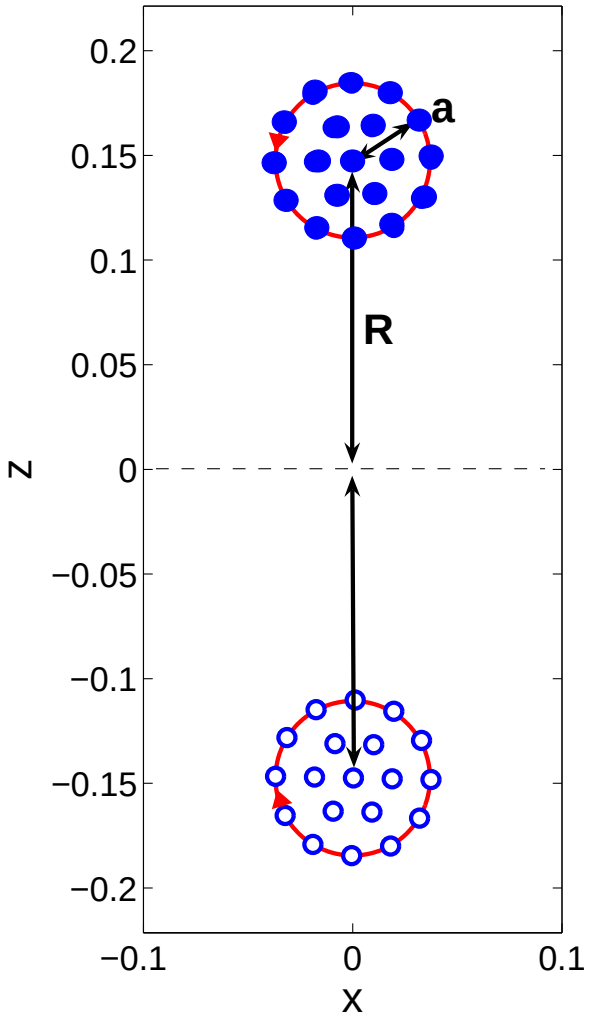

Figure 8.5: Initial configuration for 19 co-axial vortex rings. Solid and hollow blue dots show where vortex rings cut x-z plane with positive (anticlockwise) and negative (clockwise) circulation respectively, as indicated by the red arrows. The vortex rings are positioned so that they cut the x-z plane in hexagonal formation, centred at $R = 0.1476$ cm. $a = 0.0369$ cm and $R/a = 4$. The red circles are for visualisation purposes only.

8.4 Imposed normal fluid velocity field

As mentioned previously, in an ideal world I would be able to model self-consistently both the superfluid and normal fluid dynamics. This would entail evolving simultaneously the Biot-Savart law, which describes the motion of the superfluid vortex filaments, and the Navier-Stokes equations including a term for the mutual friction, which describes the normal fluid velocity field. The complexities of the interaction between vortex filaments, which are discretised along space-curves, and the normal fluid velocity field, which is discretised on a 3D mesh, are beyond the scope of this thesis. An attempt to model this interaction has been made by Kivotides *et al.* (2000).

On the other hand, experiments are conducted at finite temperatures, not at the ideal, zero temperature limit. In particular, Borner reports results for temperatures ranging from 1.3 to 2.15 K, and it must be anticipated that this has a not insignificant effect on the evolution and stability of the superfluid vortex rings.

There are two extra effects which must be taken into account when considering the evolution of the rings at non-zero temperatures. The most obvious is the dissipative effect of the mutual friction. In the absence of some restorative force, such as an electric field (Barenghi *et al.*, 1983), the rings must decay within a finite time. However, one must bear in mind that the piston stroke nucleated not only a bundle of quantised superfluid vortex rings, but also a classical, normal fluid ring, possessing its own circulation and velocity field (Borner *et al.* (1983); Borner & Schmidt (1985) measured the strength of the circulation of the normal fluid). The effect of the presence of this normal fluid ring is beneficial to the superfluid ring, not detrimental.

Both of these effects are apparent when considering the equation for the decay of the radius of a superfluid vortex ring at finite temperature. This equation is given by

$$\dot{R} = \frac{\gamma}{\rho_s \kappa} \left(v_n - v_s^{ext} - v_{si} \right), \tag{8.4}$$

where v_{si} is the self-induced velocity of the superfluid vortex rings, v_s^{ext} is the superfluid velocity induced by external sources, such as a heat source, and v_n is the total normal fluid velocity field, that is the sum of the normal fluid ring's self-induced velocity and velocity due to external sources. In the absence of counterflow velocities, this equation reduces to

$$\dot{R} = \frac{-\gamma v_{si}}{\rho_s \kappa}, \tag{8.5}$$

which has a purely dissipative effect on the superfluid vortex rings. By introducing a non-zero v_n, this dissipative effect is to some extent mitigated. The greater the similarity between v_n and v_{si}, the more the effect is mitigated.

Borner (Borner & Schmidt, 1985) reports that the time taken for the rings to form is a few milliseconds, the time taken for the velocity fields to equalise as a

result of the effect of mutual friction is of the order of tens of milliseconds and the time taken for the rings to emerge from the piston is of the order of 100 milliseconds. With this he explains why there is no observable relative velocity outside the piston tube and hence no difference in the circulation measured. This means that the centre of vorticity of the normal fluid ring will translate with the same velocity as the centre of vorticity of the superfluid rings. I take this as one component of the normal fluid velocity field: that is a uniform velocity field whose components are the x, y and z components of the velocity of the centre of vorticity.

The other component of the normal fluid velocity is that which is self-induced by the normal fluid vortex ring. This cannot be calculated without a detailed knowledge of the size, shape and structure of the ring and the cross-sectional composition of its core. However, given that the mutual friction is extremely efficient at matching the velocity and circulation of the two fluids, as reported by Borner, it may be expected that the composition of the velocity field of the normal fluid vortex ring will to a large extent match that induced by the superfluid vortex ring formation.

Figures 8.6-8.9 show the velocity field induced by a superfluid vortex ring formation of 19 rings at zero temperature. $R = 0.0896$ cm and $a = \ell = 0.0223$ cm (such that $R/a = 4$). Figures 8.6 is produced in a computational box of unit size and discretised by a 128^3 mesh, which is sufficient to distinguish the main features of the flow pattern. It shows the magnitude of the velocity in the x-y plane. Since the vortex rings are axisymmetric, a similar figure of the x-z plane is identical. This plane cuts through the vortex rings along their axis of propagation, giving a cross-sectional view of the 'core' of the macroscopic ring (the 'core' of the macroscopic ring should not be confused with the 'core' of an individual vortex). The circular 'core' region containing the vortices is clearly identifiable. I include a second figure (Figure 8.7) of the same rings which was produced in the same unit box, but using a 512^2 2D discretisation of the x-y plane. In Figure 8.7 the velocity 'hot-spots' due to the $1/r$ superfluid vortex velocity field are even more clearly visible. In Figure 8.6 I show the entire flow pattern and in Figure 8.7 I zoom in to focus on the pattern inside the 'core'.

Figure 8.8 shows, by means of arrows, the strength and direction of the flow of the 3D velocity field in the x-y plane. Hence, it is apparent that the circulation around the upper cross-section (shown) is anticlockwise (positive or 'out-of-the-page') and around the lower one (not shown) it is clockwise (negative or 'into-the-page'). It is also clear that the arrows are larger (i.e. the velocity has a higher magnitude) at the edge of the 'core' than at its centre. This is because the velocity induced at the centre by each vortex is almost cancelled out by an equal and opposite effect of the vortex opposite it in the vortex array. So, although a single vortex has a $1/r$ velocity field, an hexagonal array of identical vortices has a velocity field $\propto r$ for $r < a$. Outside this range (i.e. $r > a$) the velocity field soon tends to zero.

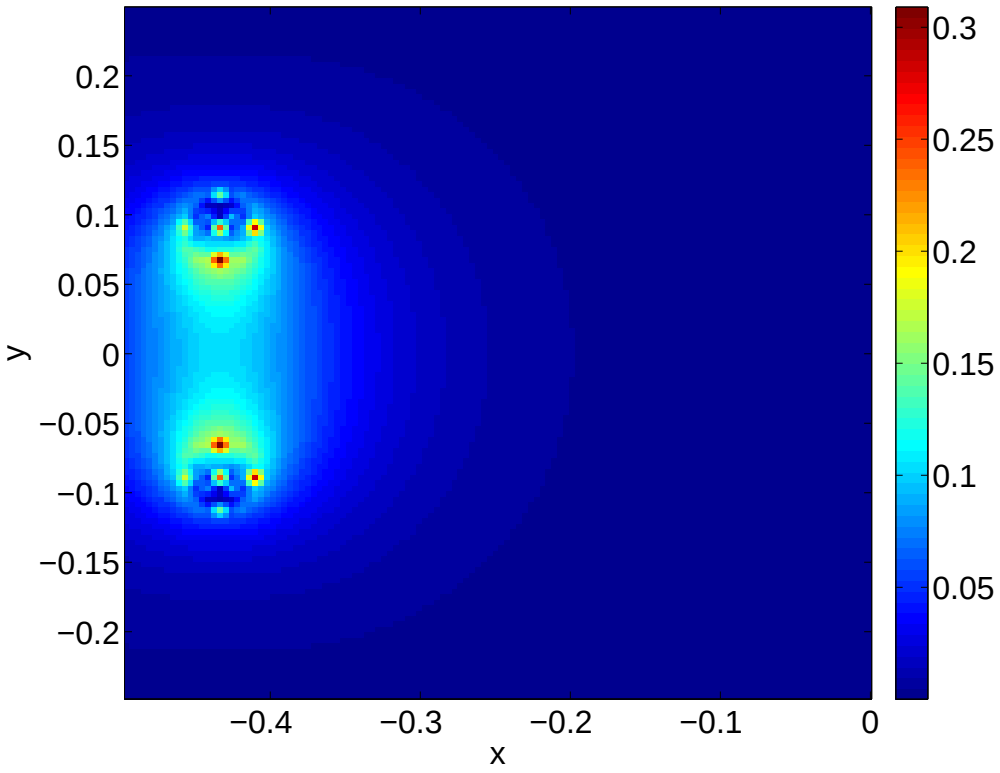

Figure 8.6: Magnitude of superfluid velocity field of 19 rings in the x-y plane on a 128^3 3D mesh. Figure shows the larger flow field. $R = 0.0896$ cm and $a = \ell = 0.0223$ cm (such that $R/a = 4$).

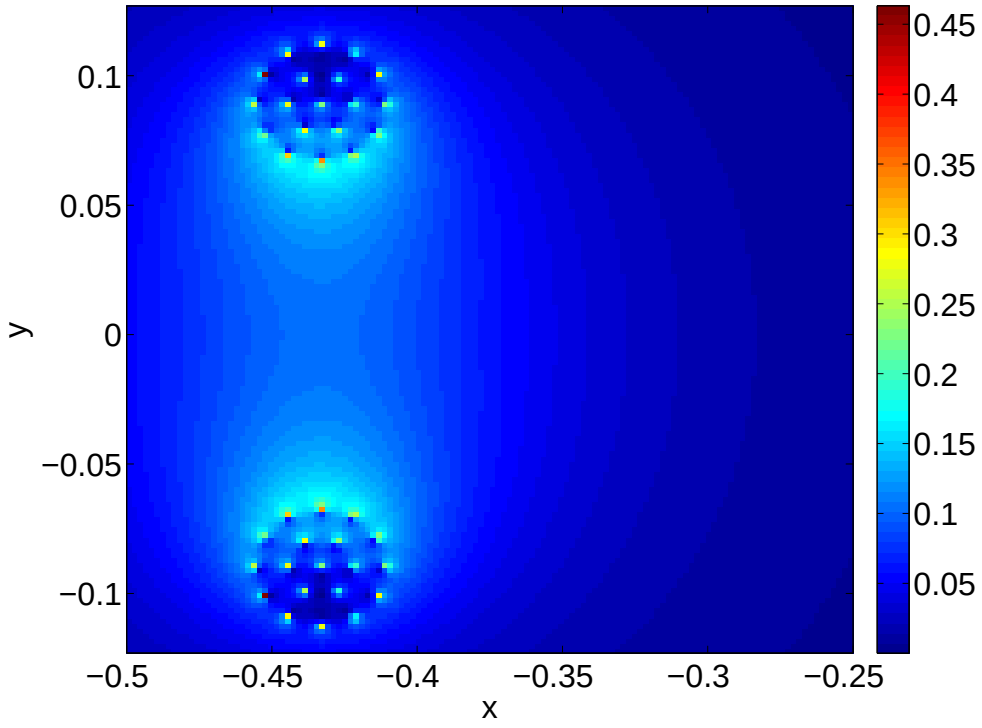

Figure 8.7: Magnitude of superfluid velocity field of 19 rings in the x-y plane on a 512^2 2D mesh. Figure focuses on structure inside 'core'. $R = 0.0896$ cm and $a = \ell = 0.0223$ cm (such that $R/a = 4$).

This effect is consistent with our understanding of vortices in a rotating cylinder (Donnelly, 1991).

In order to emphasise visually the effect of the velocity field inside the core, I include a fourth figure (Figure 8.9). The initial configuration of a bundle of 19 vortex rings is made up of 3 layers: a single ring in the centre, 6 rings arranged periodically around it in the second layer and 12 rings in the third layer. The location of the outer 2 layers is marked by red circles for illustrative purposes, with the radius of the outer circle twice that of the inner one. This figure shows the trajectories in the x-z plane, following the reference frame of the centre of vorticity, of one ring from each layer. The starting point of each ring is on the right hand side of the plot. I plot every 10th of the first 100 snapshots of the trajectories. The trajectories move anticlockwise around the centre of the core because that is the sense of the circulation of this core. The outermost ring clearly moves the greatest distance whilst describing a circular trajectory. The middle ring moves approximately the same angle around the centre as the outer ring, but with a correspondingly shorter trajectory. The inner ring barely moves at all. All this is in keeping with solid body rotation. The erraticity of its motion, and that of the other rings, is partially due to irregularities in the translational motion of the centre of vorticity. This data was produced using the Biot-Savart law with the following parameters: 19 rings,

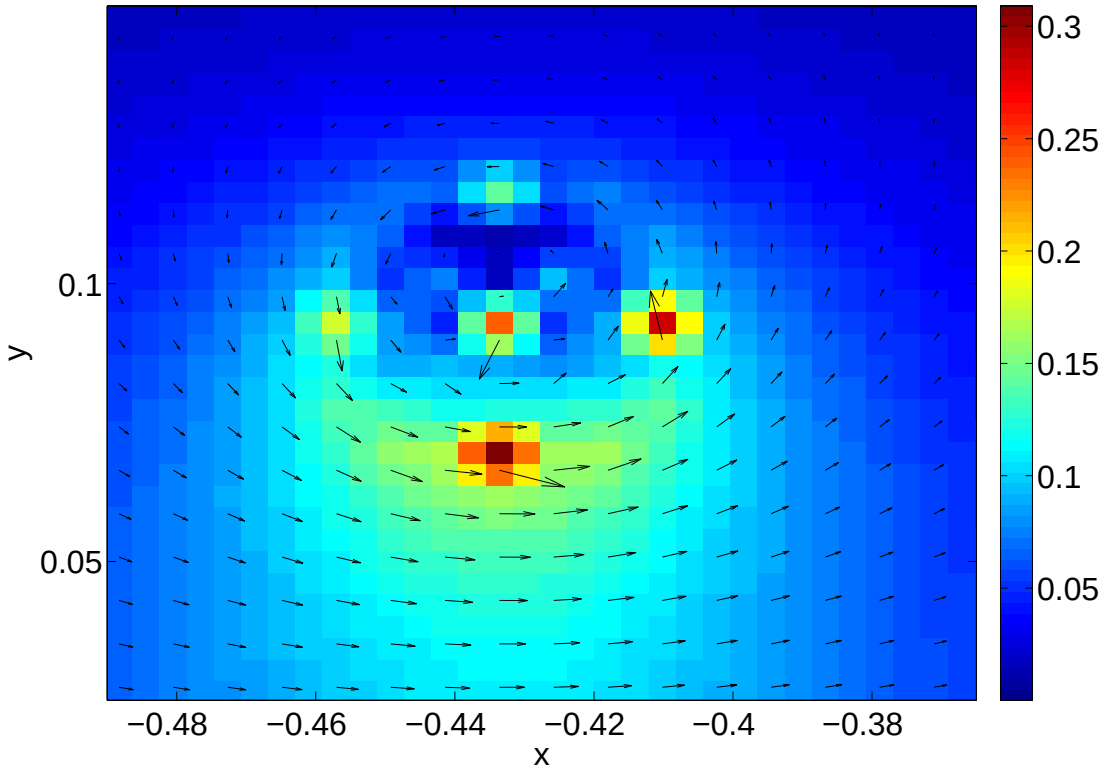

Figure 8.8: Magnitude of superfluid velocity field of 19 rings in the x-y plane on a 128^3 3D mesh. Figure focuses on structure inside one of the 'core's (the upper one). Arrows depict direction and magnitude of flow. $R = 0.0896$ cm and $a = \ell = 0.0223$ cm (such that $R/a = 4$).

$R = 0.04$ cm, $a = 0.005$ cm ($R/a = 8$) and $\ell = 0.0025$ cm. It is worth mentioning in passing that I will show that it is in the nature of 'small' intervortex spacings to produce such circular trajectories, whilst larger ones tend to produce more elliptical ones (see Chapter 11).

At this point it is worth stressing that, although there exist analytical descriptions for the velocity field inside and outside a classical vortex ring of finite cross-section (Yoon & Heister, 2004; Morton, 2004), it would be superfluous to go to the lengths of introducing them as a description of the normal fluid ring in this system, since neither the exact shape of the ring nor the vorticity distribution of its core are known. These may or may not agree with the analytical description, especially as they are bound to respond to the force exerted on the normal fluid ring by the superfluid ring. Furthermore, the purpose of introducing a normal fluid velocity field is only to mitigate somewhat the dissipative effects of the mutual friction felt by the superfluid vortices in order to examine whether Borner's results are better replicated by taking into account the presence of the normal fluid ring.

Therefore, bearing in mind the numerically-observed properties of the superfluid velocity field and in the interest of simplicity, I suggest the use of the Rankine model

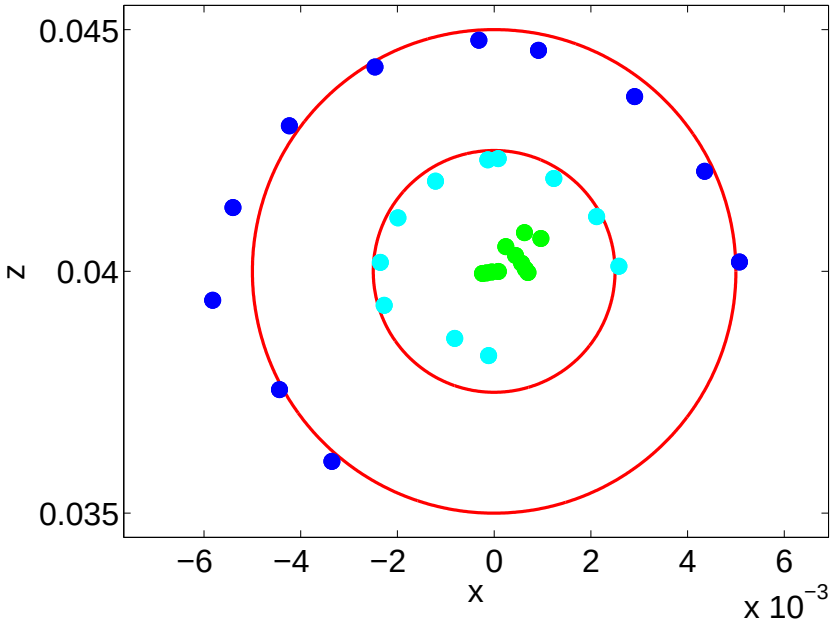

Figure 8.9: Every 10th one of the first 100 snapshots of trajectories of 3 vortex rings out of 19 ring ensemble starting at right hand side of plot and moving anticlockwise. Red circles are for visualisation purposes only. The outermost ring (blue dots) is seen to move the greatest distance, the middle ring (cyan dots) less and the innermost ring (green dots) almost not at all: signs of solid body rotation. 19 rings, $R = 0.04$ cm, $a = 0.005$ cm ($R/a = 8$) and $\ell = 0.0025$ cm.

for the normal fluid velocity field, in which $v(r) \propto r$ $(r < a)$ (solid body rotation) and $v(r) \propto 1/r$ $(r > a)$. Although the Rankine model is a 2D model, I will apply it to my 3D system by constructing the relevant plane for each vortex point. This plane will contain the centre of vorticity ($\mathbf{x}$), the vortex point ($\mathbf{x}_i$) and will be parallel to the x-axis.

In order to allow a margin for changes in the cross-sectional shape of the core of the macroscopic vortex ring and also to account somewhat for the dissipative nature of the Navier-Stokes equations, which describe the normal fluid velocity field, I make the switch over from the $\propto r$ regime to the $\propto 1/r$ regime at $r = 2a$, rather than at $r = a$. Figure 8.11 is a schematic diagram for the cross-section of the normal fluid vortex cores. The region A rotates anticlockwise (positive circulation) and the region B rotates clockwise (negative circulation).

The magnitude of the superfluid, and hence normal fluid, circulation is $N\kappa$, the number of vortex rings times the quantum of circulation. Hence, in plane polar coordinates the azimuthal velocity at a point $\mathbf{r}_i$ due to region A is given by

$$u_\theta^A(\mathbf{r}_i) = +\frac{N\kappa}{4\pi a}\begin{cases} \frac{r_A}{2a} & \text{if } 0 \le r_A \le 2a \\ \frac{2a}{r_A} & \text{if } r_A > 2a \end{cases}$$

and due to region B is

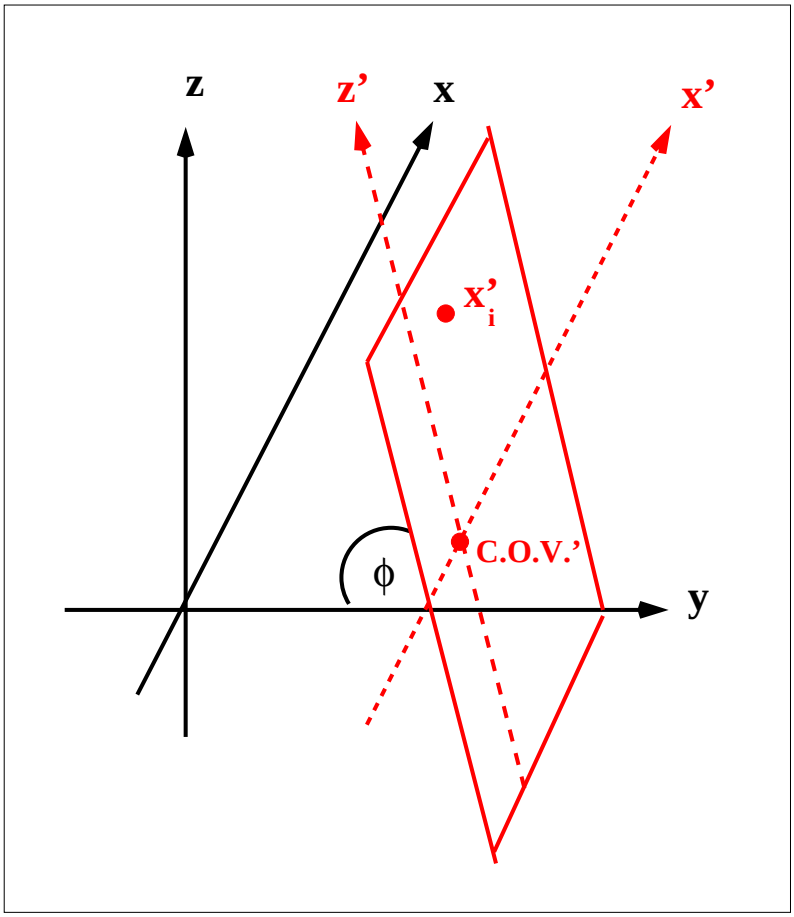

Figure 8.10: Schematic diagram showing the construction of the x'-z' plane (red) containing the centre of vorticity, a vortex point ($\mathbf{x}_i'$) and which is parallel to the x-axis. This plane is at angle ϕ to the original reference frame (black). C.O.V. is the centre of vorticity in the x'-z' plane.

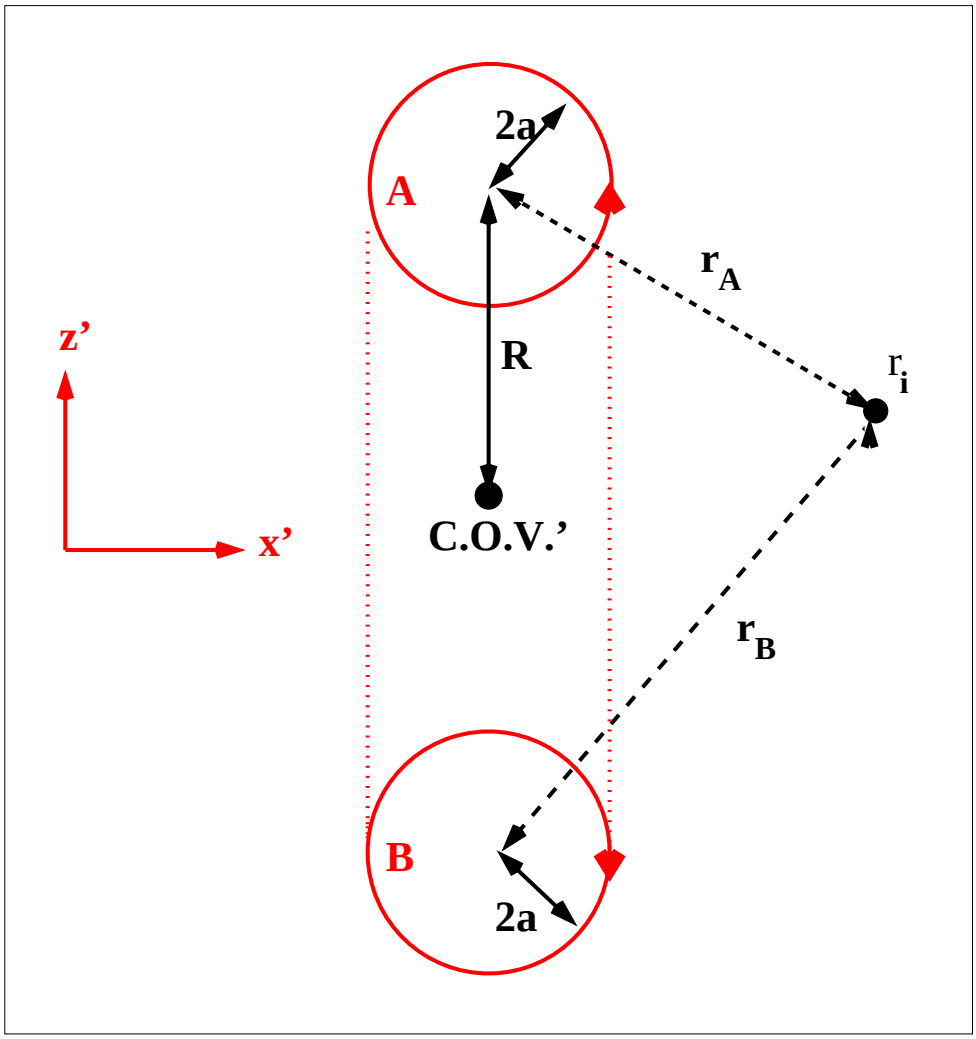

Figure 8.11: Schematic diagram showing the construction of the 2D normal fluid velocity field within the x'-z' plane. The element of velocity due to region A is proportional to r (solid body rotation) within that region and proportional to $1/r$ elsewhere and similarly for the element of velocity due to region B. The point $\mathbf{r}_i$ can reside anywhere in the plane. C.O.V.' is the centre of vorticity in the x'-z' plane.

$$u_\theta^B(\mathbf{r}_i) = -\frac{N\kappa}{4\pi a}\begin{cases}\frac{r_B}{2a} & \text{if } 0 \le r_B \le 2a \\ \frac{2a}{r_B} & \text{if } r_B > 2a\end{cases}$$

Thus the total velocity at any point $\mathbf{r}_i$ in the x'-z' plane is given by

$$\begin{aligned} u_\theta(\mathbf{r}_i) &= u_\theta^A(\mathbf{r}_i) + u_\theta^B(\mathbf{r}_i) \\ &= \frac{N\kappa}{4\pi a}\begin{cases}\frac{r_A}{2a} - \frac{2a}{r_B} & \text{if } \mathbf{r}_i\text{is an element of } A \\ \frac{2a}{r_A} - \frac{r_B}{2a} & \text{if } \mathbf{r}_i\text{is an element of } B \\ \frac{2a}{r_A} - \frac{2a}{r_B} & \text{if } \mathbf{r}_i\text{is not an element of } A, B\end{cases} \end{aligned}$$

The next step is to convert the plane polar azimuthal velocity $u_\theta(\mathbf{r}_i)$ into Cartesian coordinate velocity components, $v_{x'}$ and $v_{z'}$, for which it is necessary to know the angles θ_A and θ_B, between the point $\mathbf{r}_i$ and the centres of A and B. Then I use the angle ϕ to convert these 2D velocity components into 3D components: $v_x = v_{x'}$, $v_y = v_{z'}\cos\phi$ and $v_z = v_{z'}\sin\phi$. These are the velocity components induced by the presence of the normal fluid ring itself. Finally the velocity of the centre of vorticity is added to this velocity to give the total velocity field of the normal fluid flow. The algorithm performs all of these steps for each discretisation point on the superfluid vortex rings. This then is the value of v_n from Equation 6.10 which will reduce the dissipative effects of the mutual friction.

So as not to distort the natural flow pattern of this pseudo-Rankine model, the velocity of the centre of vorticity has been omitted in calculating the normal fluid velocity field in the following figures. Figure 8.12 shows the magnitude of the velocity. Notice the low value regions at the centres of the regions A and B and along a line running in between the two regions. Figure 8.13 is a close up image of the (upper) region A. The arrows show the magnitude and direction of the flow. On comparison with the superfluid velocity field, it is evident that the flow patterns are not dissimilar and this rough model of the normal fluid velocity field will serve as an adequate model to test the hypothesis that the introduction of a normal fluid ring will benefit the stability of the macroscopic superfluid ring.

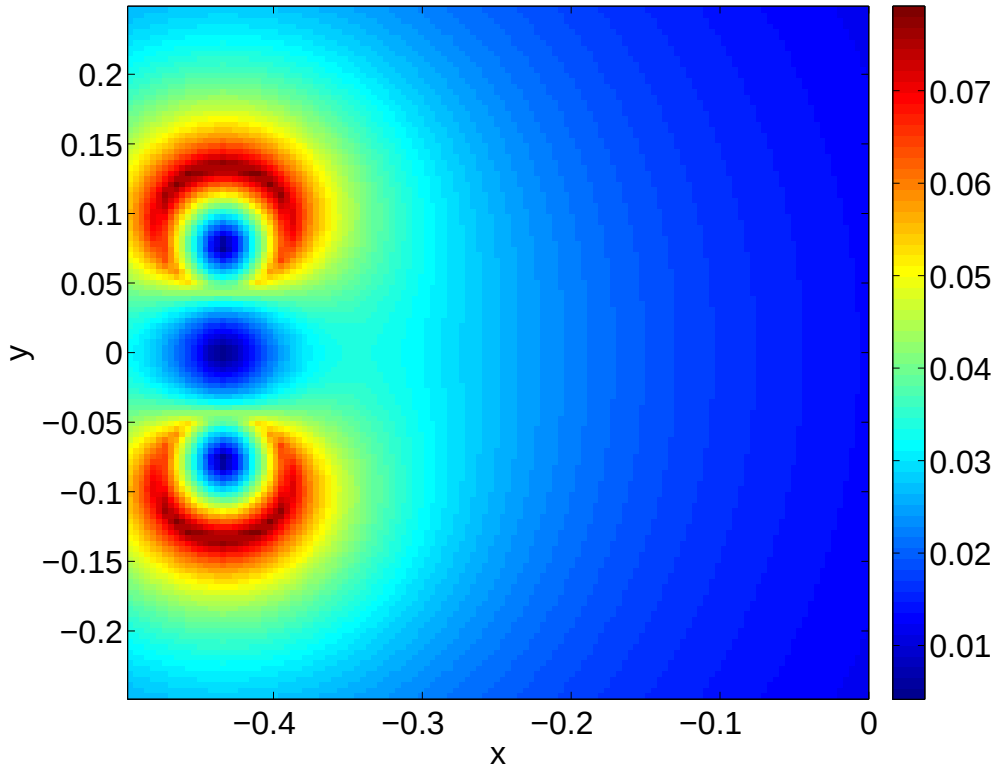

Figure 8.12: Magnitude of normal fluid velocity field of 19 rings in the x-y plane on a 128^3 3D mesh. Figure shows the larger flow field due only to the normal fluid rings themselves, ignoring any contribution from the motion of the centre of vorticity. $R = 0.0896$ cm and $a = \ell = 0.0223$ cm (such that $R/a = 4$).

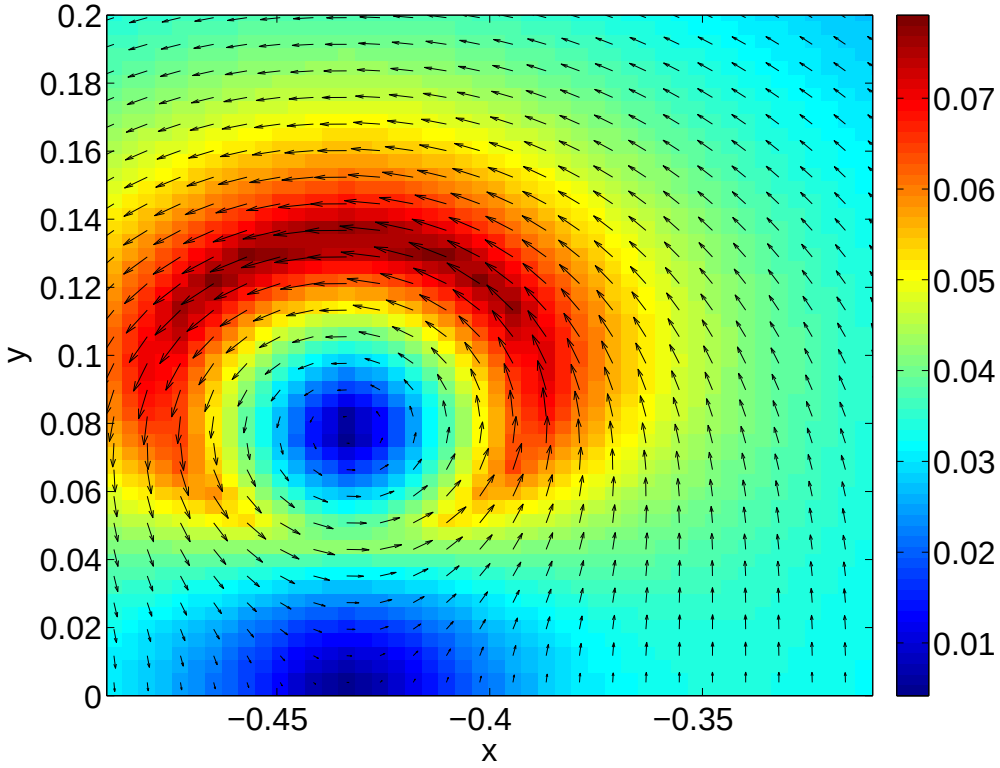

Figure 8.13: Magnitude of normal fluid velocity field of 19 rings in the x-y plane on a 128^3 3D mesh. Figure focuses on structure inside one of the 'core's (the upper one) due only to the normal fluid rings themselves, ignoring any contribution from the motion of the centre of vorticity. Arrows depict direction and magnitude of flow. $R = 0.0896$ cm and $a = \ell = 0.0223$ cm (such that $R/a = 4$).

8.5 Aims for vortex filament approach

I list here the topics that I will study by applying the vortex filament approach to the problem of macroscopic vortex rings.

- I aim to reproduce the results of the piston-induced macroscopic vortex rings, keeping as close as possible, if not quantitatively, then at least qualitatively, to the experimental conditions. In terms of orders of magnitude, Borner's experiment involved a number of quantised vortex rings which was of the order $O(10^3)$ and which travelled a distance of order $O(10)$ times the initial diameter, D, of the ring without dispersing (perhaps as a result of a turbulent transition). I will reproduce the same translation numerically for $O(10)$ rings using the fulls BS Law and for $O(10^2)$ rings using the Tree Algorithm. I will show that the numerical rings, although developing a degree of instability, is robust and retains its toroidal shape.

- I will investigate the phenomenon of generalised leapfrogging of more than 2 vortex rings which the macroscopic vortex ring exhibits during the stable phase of its translational motion.

- I will discuss the subsequent development of instabilities and turbulence, considering each stage of its development as it builds up towards reconnection events and beyond until a turbulent vortex bundle develops.

- I will suggest an approximate form for the equation of self-induced velocity and vortex energy for multiple vortex rings. I will evaluate the agreement between these equations, numerical results and experimental results.

- I will consider finite temperature effects, with and without a prescribed normal fluid velocity field due to the presence of a normal fluid vortex ring.

8.6 Numerical tests and considerations

8.6.1 A single ring

Having designed the systems of vortex rings, I test some basic features of vortex rings. The simplest system is that of a single vortex ring at zero temperature. The expectation is that this ring will translate along its axis of rotation under its self-imposed velocity, v_{si}, and that the value of this velocity should equal that given by Equation 6.9, the equation for the velocity of a single (hollow-cored) ring at zero temperature. Similarly the vortex ring's kinetic energy, E, should agree with that given by Equation 6.8. The kinetic energy (per unit density) of a quantised vortex ring is given by

$$E = \frac{1}{2}\int_V \mathbf{u}^2 dV == \kappa \oint_{\mathcal{L}} \mathbf{u}\cdot\mathbf{s}\times\mathbf{s}' d\xi, \tag{8.6}$$

which can be evaluated numerically by means of the trapezium rule. Furthermore at zero temperature the kinetic energy should be conserved and I confirm that it is indeed conserved to within about 10^{-12} %. Further details will follow in Section 10.6. It must be stressed that this will only be true before the onset of reconnections. After the onset of reconnections, however, energy will not be conserved, since, as mentioned above (Section 8.2) the reconnection algorithm is designed to 'leak' energy corresponding to the phonon emission of a physical reconnection.

I can also calculate, at finite temperature, the momentary rate at which the radius of the ring decreases ($\dot{R}$), its lifetime (τ) and the distance it travels before disappearing (Δx). I record the theoretical predictions and numerical results for a ring of initial radius $R = 0.0896$cm at $T = 0$ K and for a similar ring at $T = 2.02$ K. I also show the percentage error of the absolute value of the difference between the two results. In order to calculate the theoretical values for finite temperature I used Table II from Barenghi *et al.* (1983) for the values of the drag coefficients $\gamma = 1.82 \times 10^{-5}$ gcm^{-1}s^{-1}, $\gamma_0 = 1.69 \times 10^{-5}$ and $\gamma_0' = 4.65 \times 10^{-6}$ ($\rho_s = 0.0601$ gcm^{-3} at that temperature).

	Theory	Numerical	Error (%)
$T = 0$ K			
v_{si}	0.01534	0.01573	2.54
$\rho_s E$	1.06×10^{-7}	1.15×10^{-7}	8.49
$T = 2.02$ K			
$\dot{R}$	-0.00466	-0.00475	1.93
τ	9.621	9.712	0.95
Δx	0.2926	0.2910	0.55

Table 8.1: Table comparing theoretical and numerical results for a single vortex ring.

8.6.2 Stable translatory motion of 2 vortex rings; leapfrogging motion; independence of results on level of resolution

It is expected that two coaxial vortex rings will translate along their rotational axis whilst performing the leapfrogging manoeuvre observed in classical vortex rings and that the rings will retain their stability throughout this motion. It is also expected that this motion will not depend on the choice of spatial resolution along the rings.

I compare 3 different values of $\Delta\xi$ and show that, during the stable period of the translation, the results are identical and do not depend on my choice of $\Delta\xi$.

Throughout my work I have used $\Delta\xi \approx 0.0015$. I now compare the results for this value of $\Delta\xi$ with those of $\Delta\xi = 0.001$ and $\Delta\xi = 0.0005$ in the case of 2 vortex rings at zero temperature using the Biot-Savart filament method. Due to the interdependence of $\Delta\xi$ and Δt (Δt has to be small enough to resolve motion on smallest length scale $\Delta\xi/2$), these choices of $\Delta\xi$ impose maximum values on Δt such that $\Delta t = 5.0 \cdot 10^{-5}$ (the standard value of Δt used throughout this work), $2.5 \cdot 10^{-5}$ and $0.625 \cdot 10^{-5}$ seconds respectively. In Figure 8.14 I show (top pane) how the distance measured along the x-axis between the two rings varies over time. At $t = 0$ the rings are aligned coaxially in the same y-z plane. The maximum value for the distance, δx, between the rings is reached when they are not only coaxial, but also possess the same radius R. The top pane shows a series of 4 leapfrogs taking place over a period of approximately 40 seconds before the system becomes unstable. I also show (Figure 8.14 lower pane) the progression of the centre of vorticity over the same period, during which the rings travel approximately 20 times their original diameter. Further details pertaining to the leapfrogging of 2 vortex rings are left for the more detailed discussion of leapfrogging (Section 10.7). Finally, in Figure 8.15, I show how well the vortex energy is conserved for each of the values of $\Delta\xi$, before the onset of instabilities and turbulence. All 3 values of $\Delta\xi$ conserve energy to within about 0.5% of their value at the initial time, E_0. Further details will follow in Section 10.6.

8.7 Summary

In this Chapter I have introduced Schwarz's filament method, due to the lack of suitable governing equations (as described in Chapter 1), as a means of following the evolution of the macroscopic ring. I designed an initial configuration which followed a centred hexagonal pattern and, most importantly, a prescribed normal fluid velocity field. The importance of the normal fluid velocity field cannot be understated. It is literally the 'life' of the macroscopic superfluid vortex ring, as I showed that, in its absence, the macroscopic superfluid vortex ring quickly decayed due to the mutual friction (see, for example, Table 8.1). I tested my code and the initial configuration for $N = 1$ and $N = 2$ rings and found them to behave as expected (e.g. 2 rings perform leapfrogs) and to be independent of the choice of time and spatial discretisation. I also detailed the overall aims of this Part of my thesis (Section 8.5).

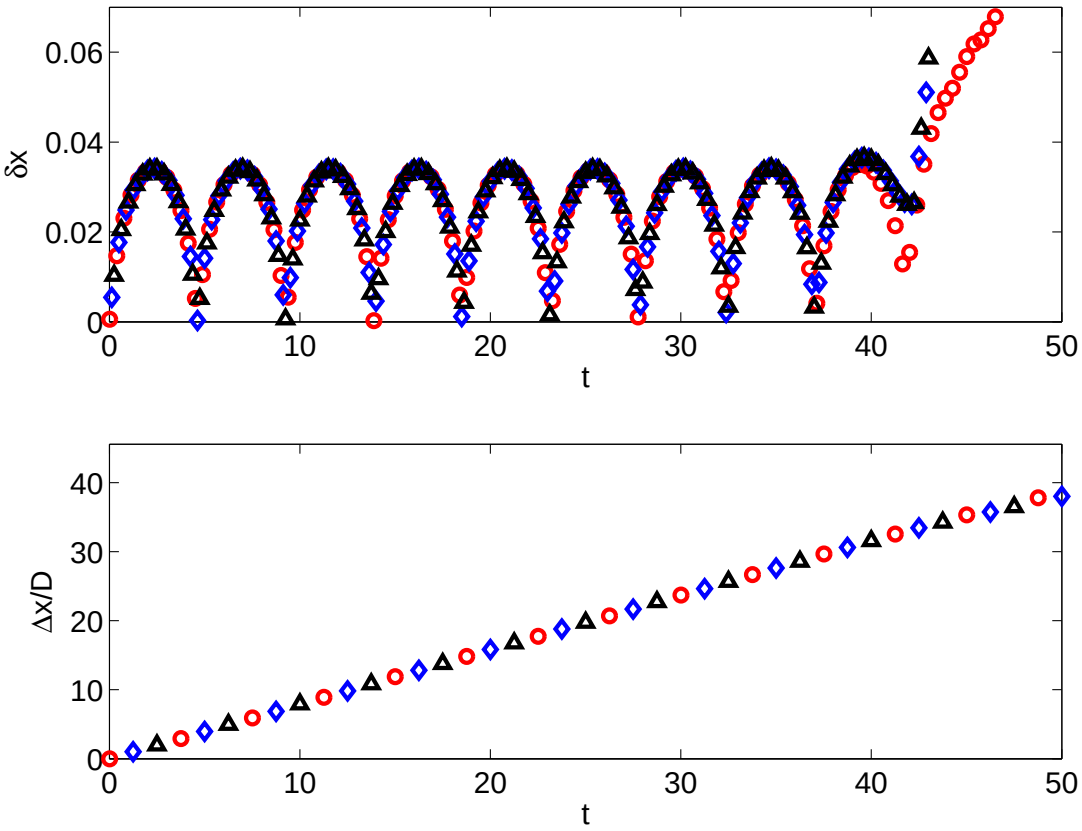

Figure 8.14: Comparison of 3 values of spatial resolution $\Delta\xi$ for $N = 2$. Shown here are (top) δx (cm) vs time t (s) where δx is the distance in the x direction between the front ring and the back ring (so at every other minimum the rings have returned to their original configuration, having performed one complete leapfrog) and (bottom) the number of initial diameters D travelled vs time t (s), in which I compare the values for $\Delta\xi = 0.00149$ (red circles), $\Delta\xi = 0.001$ (blue diamonds), $\Delta\xi = 0.0005$ (black triangles). Parameters in common for all 3 values of $\Delta\xi$: $R = 0.03$ cm and $a = 0.0075$ cm ($R/a = 4$).

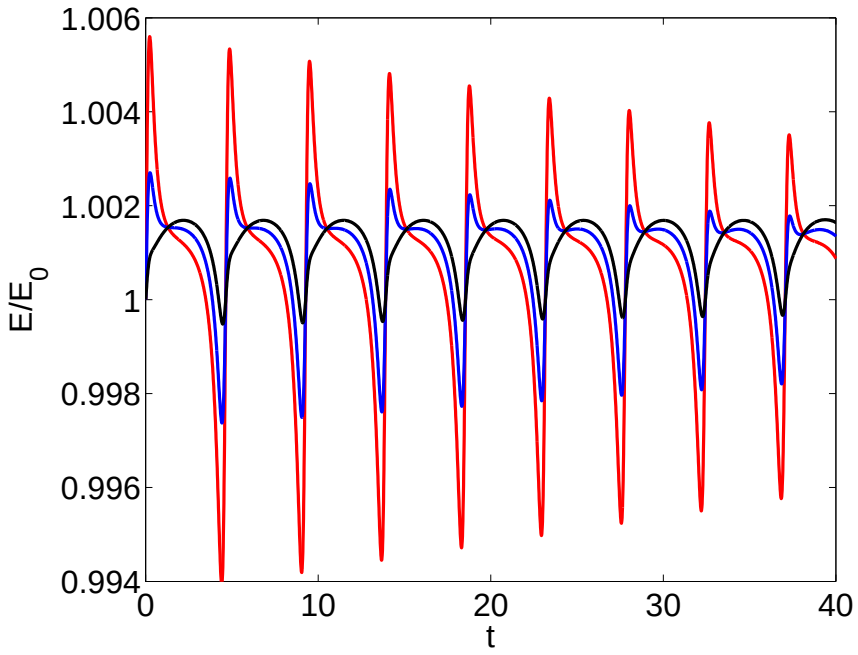

Figure 8.15: Comparison of conservation of vortex energy for 3 values of spatial resolution $\Delta\xi$ for $N = 2$. Vortex energy, E, normalised by its initial value, E_0, for $\Delta\xi = 0.00149$ (red), $\Delta\xi = 0.001$ (blue), $\Delta\xi = 0.0005$ (black). Parameters in common for all 3 values of $\Delta\xi$: $R = 0.03$ cm and $a = 0.0075$ cm ($R/a = 4$).

Chapter 9

A quantitative comparison between mathematical model, numerical model and experimental results for self-induced velocity and vortex energy

I would like to compare Borner's experimental results, my numerical model and results of the equations for self-induced velocity and vortex energy for a single ring, suitably adapted to model a bundle of many vortex rings. In Borner & Schmidt (1985) Borner gives details of translational velocities and circulations for 6 experiments measured at 2 different locations downstream of the piston orifice (see Table 7.1). As noted previously these results imply the presence of $O(10^3)$ quantised vortex rings, the development of which cannot be simulated numerically due to limitations on time and computer resources. Neither is there yet any equation which describes the self-induced translational velocity or vortex energy of a macroscopic vortex ring consisting of multiple quantised vortex rings. In this chapter I will suggest an approximate mathematical model for the self-induced velocity and vortex energy of a macroscopic vortex ring. I will also develop a method for obtaining numerical results which are directly comparable with the experimental results.

9.1 Mathematical model

Recall Equations 6.8 and 6.9 for a single hollow-cored quantised vortex ring

$$E = \frac{1}{2}\kappa^2 R\left[ln\left(\frac{8R}{a}\right) - \frac{3}{2}\right],$$

and

$$v_{si} = \frac{\kappa}{4\pi\ R}\left[ln\left(\frac{8R}{a}\right) - \frac{1}{2}\right],$$

where κ is the quantum of circulation, R is the radius of the ring and $a = a_0$ is the radius of the vortex core. As a first approximation I can replace κ by $N\kappa$ throughout, where N is the number of individual vortex rings in the macroscopic vortex ring, and use R and a as defined in my discussion of the initial configuration. In other words I model the macroscopic vortex ring, whose vorticity is discrete, as a single thick-cored vortex ring of circulation $\Gamma = N\kappa$, radius R and core radius a. The model equations then become

$$E' = \frac{1}{2}N^2\kappa^2 R\left[ln\left(\frac{8R}{a}\right) - \frac{3}{2}\right], \tag{9.1}$$

and

$$v'_{si} = \frac{N\kappa}{4\pi\ R}\left[ln\left(\frac{8R}{a}\right) - \frac{1}{2}\right]. \tag{9.2}$$

The validity of this model still depends on the condition $R \gg a$.

9.2 Optimisation of numerical model

In order to obtain values for v_{si} and E using a numerical method it is sufficient to time step the initial configuration only twice. Even if a full study of the stability of the system is beyond the reach of present computational capabilities, two time steps will most probably not be. The most accurate vortex filament method is the Biot-Savart law. Numerical simulations of N_p vortex points using the BS Law require N_p^2 operations at each time step. It is therefore of interest to reduce N_p as much as possible whilst retaining all important features of the rings, such as the self-induced velocity and vortex energy.

I show in Table 9.1 to what extent the velocity of the centre of vorticity and the vortex energy of smooth rings (i.e. rings without small scale motion) depend on the number of discretisation points per ring. It is clear that there is little or no difference between 1000 points per ring and 100 points per ring.

Hence, in order to maintain an ideal level of discretisation ($\Delta\xi = \ell/10$) for a ring of radius $R = 0.4$ cm such as Borner produced in his experiment, I should use $\frac{N_p}{N} = \frac{2\pi R}{\Delta\xi}\frac{4}{3}$ points per ring. However, in Borner's experiment $\ell \approx 0.003$ cm (see Table 7.2), which would mean that $\Delta\xi = 0.0003$ cm, which in turn would mean $N_p/N \approx 11170$ points per ring, which quickly becomes impossible to simulate numerically even for only very few rings and a very few time steps.

One answer then is to reduce the number of discretisation points per ring to a more manageable number, such as 100. This would allow large numbers of rings, of the order $O(10^3)$ such as in Borner's experiment to be simulated over a short period

	R (cm)	a (cm)	N_p/ring	$\Delta\xi$ (cm) (6dp)	v_x (cm/s) (4sf)	E (cm^2/s^2) (2dp)
$N=1$	0.04	-	1000	0.00335	0.03363	3.37×10^{-7}
	0.04	-	500	0.00670	0.03363	3.37×10^{-7}
	0.04	-	100	0.03351	0.03362	3.37×10^{-7}
	0.04	-	50	0.06702	0.03357	3.36×10^{-7}
	0.04	-	10	0.33510	0.03215	3.01×10^{-7}
$N=7$	0.04	0.01	1000	0.00335	0.06673	3.42×10^{-6}
	0.04	0.01	500	0.00670	0.06673	3.42×10^{-6}
	0.04	0.01	100	0.03351	0.06672	3.41×10^{-6}
	0.04	0.01	50	0.06702	0.06668	3.40×10^{-6}
	0.04	0.01	10	0.33510	0.06638	3.17×10^{-6}
$N=19$	0.04	0.01	1000	0.00335	0.1392	1.64×10^{-5}
	0.04	0.01	500	0.00670	0.1392	1.64×10^{-5}
	0.04	0.01	100	0.03351	0.1392	1.64×10^{-5}
	0.04	0.01	50	0.06702	0.1392	1.64×10^{-5}
	0.04	0.01	10	0.33510	0.1463	1.66×10^{-5}

Table 9.1: Numerical results showing to what extent velocity of the centre of vorticity and vortex energy of smooth rings (i.e. rings without small scale motion) depend on the number of discretisation points per ring. I record the velocity and energy data at the first possible time step. I use Biot-Savart law with $\Delta t = 10^{-10}$ seconds. I conclude that for $N_p \geq 100$ per ring there is no significant change in the velocity and energy for smooth rings.

of time. In practical terms I used $\Delta\xi = \frac{2\pi R}{100}\frac{4}{3} \approx 0.0335$ cm.

It must be stressed that this approach is only valid when one uses it for a few time steps, since the numerical resolution is now such that $\Delta\xi \approx 10\ell$ or 100 times what is normally acceptable and hence it is unable to resolve any small scale motion. I also check that during the first few time steps there is no chance of the rings reconnecting. The maximum self-induced velocity is of order $O(1)$ cms^{-1} (for example in the case of 1027 rings). The inter-vortex spacing is $\ell = 0.003$ cm. The maximum distance moved towards each other by two vortex lines in close proximity is $2\Delta t v_{max}$. As long as this distance is much less than ℓ, there is no chance of reconnections taking place. If I let $\Delta t = 10^{-6}$ seconds, then the maximum distance moved will be no greater than 10^{-5} cm or two orders of magnitude smaller than the inter-vortex spacing.

A further point which must be clarified is whether the velocities recorded in the numerical simulations are transient or (approximately) steady. Transient velocities can be observed as the initial hexagonally centred vortex configuration relaxes to a

D-shaped configuration, similar to that observed in the classical analogue (van Dyke, 1982; Southerland *et al.*, 1991). Such a change in formation leads to a change in the velocity of the centre of vorticity and it must be asked whether this will occur when using the above parameters. I have considered (see Chapter 11) several possible values of inter-vortex spacing, $\ell = 0.0223$, 0.010 and 0.005 cm, and their effects on the evolution of the system. One phenomenon clearly visible from considering the trajectories of the individual vortices over time whilst following the centre of vorticity is that they change from somewhat elliptical (or D-shaped) orbits when $\ell = 0.0223$ cm to almost circular ones when $\ell = 0.010$ cm. This will be all the more true for $\ell = 0.003$ cm and I am justified in taking the initial velocity as representative of a long-term, steady velocity.

The experiment was conducted at finite temperature; the tabulated results (Table 7.1) being for two different temperatures $T = 1.30$ K and $T = 2.15$ K. The numerical simulations should also be carried out using parameters particular to these temperatures, such as the coefficients of mutual friction, α and α', and the superfluid density, ρ_s. However, in practice there does not appear to be any need for this as it makes little difference initially (i.e. in the first few time steps) which temperature is used or whether a normal fluid ring is introduced to counteract the dissipative effects of the mutual friction. More specifically, I carried out tests at $T = 2.02$ K with and without a normal fluid ring and found that both the self-induced velocity and the vortex energy per unit density are approximately the same as at $T = 0$ K (for the first few time steps).

9.3 Results of quantitative comparison

I performed numerical runs for all hexagonally centred numbers up to and including $N = 1027$, this being the first $O(10^3)$ hexagonally centred number (and thus of the same order as the number of rings measured experimentally - see Table 7.2). Numerically this means evolving a system of $N_p = 102700$ points over a few time steps (using the full BS law). I present the results in Figures 9.1 and 9.2 for the self-induced velocity and vortex energy respectively. Experimental data is available for velocity, but not for vortex energy. I then present a comparison of the data for the numerical simulation and the mathematical model in Table 9.2 for the self-induced velocity and Table 9.3 for the energy. Lastly I present a comparison of the experimental data with the mathematical predictions for the velocity and, in light of this comparison, discuss the accuracy of the two different interpretations of Borner's parameter D, as described in Section 7.6.

It is clear from the comparisons of both the self-induced velocity and the vortex energy that there is reasonably good agreement between the numerical results, the predictions of the mathematical model and the experimental results, especially when taking into account the approximations involved in constructing the mathematical model and the inaccuracies involved in taking experimental measurements.

The caveat upon which the equations for self-induced velocity and vortex energy depend is that $R \gg a$. This follows naturally in the case of a single vortex ring where $a = a_0 \approx 10^{-8}$ cm, which is much smaller than any other length scale in the system. One would therefore expect that there should be better agreement between the mathematical model and the numerical and experimental results for large values of R/a than for smaller values. A look at the tables below (Tables 9.2 and 9.3) however shows the opposite to be true: with the exception of $N = 1$ the agreement is better for smaller values of R/a than for larger values. Also note that although v'_x consistently underestimates the value of v_x, E' underestimates E until $N = 61$ and thereafter increasingly overestimates its value. This is clearly visible when comparing plots (b) and (d) of the velocity with plots (a) and (c) of the vortex energy. The reason is due to an interesting property of vortex rings in which they differ from many other systems: their energy decreases as their velocity increases. This is because the self-induced velocity scales like $1/R$ and the vortex energy scales like R. Therefore, if one imagines that the vortex bundle has some effective radius R_{eff} which induces a velocity greater than v', implying that $R_{eff} < R$, then it follows that the vortex bundle's energy will be less than E'. The inconsistency with this approach is in the range $N < 91$. In this range both v_x and E are greater than the corresponding v'_x and E'. This indicates that there is a need for some nonlinear correction to the equations.

9.3.1 Figures comparing numerical, mathematical and experimental results for v_{si} and E

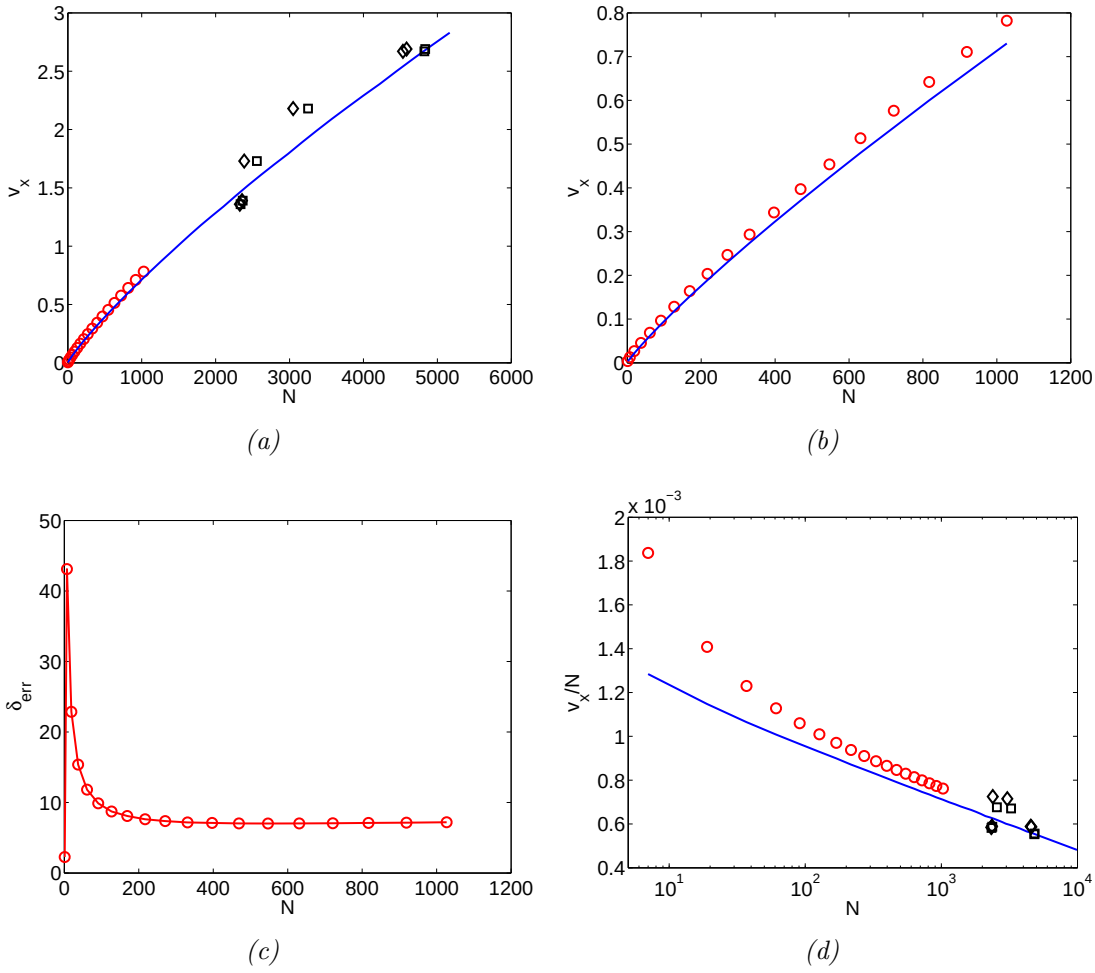

Figure 9.1: Comparison of mathematical model, numerical results and experimental results for v_{si}: (a) numerical results for $N \leq 1027$ (red circles), mathematical model (blue line) and Borner's experimental results at z_1 (black squares) and z_2 (black diamonds), (b) zooms in to range $N \leq 1027$ to highlight agreement between numerical results (red circles) and mathematical model (blue line), (c) percentage error δ_{err} between numerical results and mathematical model, where $\delta_{err} = 100 \times \frac{|v_x - v'_x|}{v'_x}$, and (d) log-lin plot of v_x/N (contribution per ring to the self-induced velocity) using the same symbols as (a). Parameters reflect the actual parameters of Borner's experiment: $R = 0.4$ cm, $\ell = 0.003$ cm, $a = (n-1)\ell$ cm where n is the number of hexagonal layers in the initial condition. Numerical parameters $\Delta t = 10^{-6}$ seconds and $\Delta\xi \approx 0.0335$ cm (100 discretisation points per ring).

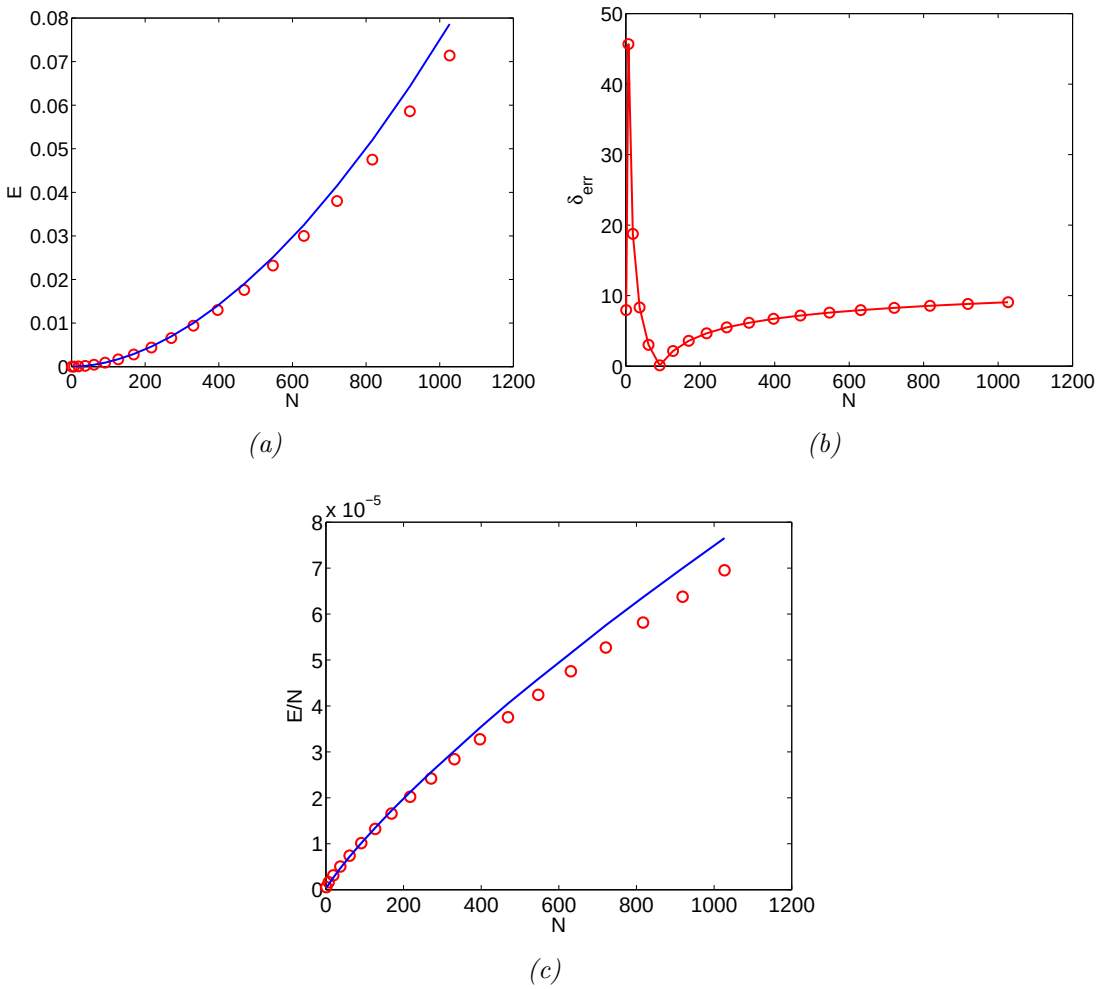

Figure 9.2: Comparison of mathematical model and numerical results for E: (a) numerical results for $N \leq 1027$ (red circles) and mathematical model (blue line), (b) percentage error δ_{err} between numerical results and mathematical model, where $\delta_{err} = 100 \times \frac{|E-E'|}{E'}$, and (c) E/N (contribution per ring to vortex energy) using the same symbols as (a). Parameters reflect the actual parameters of Borner's experiment: $R = 0.4$ cm, $\ell = 0.003$ cm, $a = (n-1)\ell$ cm where n is the number of hexagonal layers in the initial condition. Numerical parameters $\Delta t = 10^{-6}$ seconds and $\Delta\xi \approx 0.0335$ cm (100 discretisation points per ring).

9.3.2 Tables comparing numerical results and mathematical model for v_{si} and E

N	a (cm)	R/a	v_x (cm/s)	v'_x (cm/s)	δ_{err} (%)
1	1.3×10^{-8}	3.08×10^{7}	0.0038	0.0037	2.27
7	0.003	133.33	0.0129	0.0090	43.11
19	0.006	66.67	0.0268	0.0218	22.87
37	0.009	44.44	0.0455	0.0394	15.38
61	0.012	33.33	0.0688	0.0615	11.82
91	0.015	26.67	0.0964	0.0878	9.89
127	0.018	22.22	0.1282	0.1179	8.73
169	0.021	19.05	0.1640	0.1517	8.09
217	0.024	16.67	0.2035	0.1891	7.63
271	0.027	14.81	0.2467	0.2298	7.36
331	0.030	13.33	0.2934	0.2738	7.18
397	0.033	12.12	0.3436	0.3208	7.10
469	0.036	11.11	0.3970	0.3709	7.03
547	0.039	10.26	0.4537	0.4239	7.02
631	0.042	9.52	0.5135	0.4798	7.03
721	0.045	8.89	0.5763	0.5383	7.06
817	0.048	8.33	0.6421	0.5995	7.10
919	0.051	7.84	0.7107	0.6633	7.14
1027	0.054	7.41	0.7822	0.7296	7.20

Table 9.2: Table comparing numerical results with predictions of mathematical model for self-induced velocity for a series of bundles of hexagonally centred vortex rings which possess similar parameters to Borner's experiment, namely: $R = 0.4$ cm and $\ell = 0.003$ cm. I recorded the numerical data after the first time step: $\Delta t = 10^{-6}$ seconds. Each ring was discretised so as to consist of 100 points, as described in the text.

N	a (cm)	R/a	$\rho_s E$ ($\mathrm{cm}^2/\mathrm{s}^2$)	$\rho_s E'$ ($\mathrm{cm}^2/\mathrm{s}^2$)	δ_{err} (%)
1	1.3×10^{-8}	3.08×10^{7}	5.55×10^{-7}	5.14×10^{-7}	7.94
7	0.003	133.33	1.13×10^{-5}	7.74×10^{-6}	45.68
19	0.006	66.67	5.91×10^{-5}	4.98×10^{-5}	18.76
37	0.009	44.44	1.87×10^{-4}	1.73×10^{-4}	8.32
61	0.012	33.33	4.52×10^{-4}	4.39×10^{-4}	3.02
91	0.015	26.67	9.22×10^{-4}	9.23×10^{-4}	0.11
127	0.018	22.22	1.68×10^{-3}	1.71×10^{-3}	2.15
169	0.021	19.05	2.80×10^{-3}	2.91×10^{-3}	3.59
217	0.024	16.67	4.39×10^{-3}	4.61×10^{-3}	4.66
271	0.027	14.81	6.56×10^{-3}	6.94×10^{-3}	5.49
331	0.030	13.33	9.40×10^{-3}	1.00×10^{-2}	6.15
397	0.033	12.12	1.30×10^{-2}	1.40×10^{-2}	6.71
469	0.036	11.11	1.76×10^{-2}	1.90×10^{-2}	7.18
547	0.039	10.26	2.32×10^{-2}	2.51×10^{-2}	7.59
631	0.042	9.52	3.00×10^{-2}	3.25×10^{-2}	7.95
721	0.045	8.89	3.80×10^{-2}	4.15×10^{-2}	8.27
817	0.048	8.33	4.75×10^{-2}	5.20×10^{-2}	8.56
919	0.051	7.84	5.86×10^{-2}	6.43×10^{-2}	8.82
1027	0.054	7.41	7.14×10^{-2}	7.86×10^{-2}	9.07

Table 9.3: Table comparing numerical results with predictions of mathematical model for vortex energy for a series of bundles of hexagonally centred vortex rings which possess similar parameters to Borner's experiment, namely: $R = 0.4$ cm and $\ell = 0.003$ cm. I recorded the numerical data after the first time step: $\Delta t = 10^{-6}$ seconds. Each ring was discretised so as to consist of 100 points, as described in the text.

9.3.3 Tables comparing experimental results and mathematical model for v_{si}

In light of the discussion in Section 7.6, I now present two further tables comparing Borner's experimental results with the predictions of the mathematical model for those cases. I present only the results assuming that U_T is the average velocity during the motion from z_1 to z_2, that is assuming that the instantaneous velocity changed in accordance with the decrease in Γ and the increase in R. The first table (Table 9.4) assumes that Borner's variable D is the same as the one used throughout this thesis and is defined as $D = 2R$. However, as I have discussed in Section 7.6, there are indications that the parameter D is in fact given by $D = 2R + 2a$. The seconds table (Table 9.5) assumes this value for D, which results in smaller values of R and hence faster velocities predicted by the mathematical model. It is clear from the percentage errors that agreement between experiment and mathematical model is far better in the second table, indicating that the second approach is the correct one.

Case	$N(z_1)$	$N(z_2)$	U_T (cm/s)	$v'_x(z_1)$ (cm/s)	$v'_x(z_2)$ (cm/s)	$< v'_x >$ (cm/s)	δ_{err} (%)
a	4824	4534	2.67	2.44	2.20	2.32	15.04
b	4865	4584	2.69	2.47	2.22	2.34	14.74
c	2367	2357	1.39	1.26	1.15	1.21	15.30
d	2337	2327	1.36	1.24	1.14	1.19	14.31
e	2558	2387	1.73	1.53	1.33	1.43	21.23
f	3250	3049	2.18	1.95	1.65	1.80	20.85

Table 9.4: Columns $1-4$ experimental results from Borner & Schmidt (1985). Columns $5-8$ results of mathematical model, v'_x calculated assuming that $D = 2R$.

Case	$N(z_1)$	$N(z_2)$	U_T (cm/s)	$v'_x(z_1)$ (cm/s)	$v'_x(z_2)$ (cm/s)	$< v'_x >$ (cm/s)	δ_{err} (%)
a	4824	4534	2.67	2.99	2.66	2.83	5.54
b	4865	4584	2.69	3.02	2.72	2.87	6.26
c	2367	2357	1.39	1.52	1.40	1.46	4.69
d	2337	2327	1.36	1.49	1.39	1.44	5.49
e	2558	2387	1.73	1.82	1.60	1.71	0.91
f	3250	3049	2.18	2.37	2.00	2.19	0.29

Table 9.5: Columns $1-4$ experimental results from Borner & Schmidt (1985). Columns $5-8$ results of mathematical model, v'_x calculated assuming that $D = 2R + 2a$.

9.4 Summary

In this Chapter I have suggested forms for the expressions governing the self-induced velocity and vortex energy of a macroscopic vortex ring. I then optimised the form of the numerical macroscopic ring in such a way that I was able to calculate the self-induced velocity and vortex energy for a ring of $N = 1027$, of the same order of magnitude as the experimental data. I compared the predictions of the mathematical model with those of an optimised form of the numerical macroscopic ring and with the experimental measurements. The results compared favourably with each other, with relatively small percentage errors considering the crude nature of the mathematical model and experimental errors. I also showed that the mathematical model agrees much better with the experimental data when Borner's parameter D is identified as $2R + 2a$ rather than just $2R$ (see Section 7.6).

Chapter 10

The translation of coherent macroscopic vortex rings

10.1 Introduction

I will now proceed to investigate the motion of the macroscopic vortex rings. Unlike the previous Chapter (Chapter 9) in which I was able to quantitatively compare numerical and experimental results, in this Chapter I will look at a more qualitative comparison. One of the main results of the piston experiments was to produce a robust vortex ring structure which was capable of travelling a considerable distance without undergoing a turbulent transformation into a random vortex tangle. Whilst Borner's ring contained $O(10^3)$ vortex rings, I will discuss somewhat more humble systems of 1, 2, 3, 7 and 19 rings. Vortex ring systems of these sizes can be simulated by the full BS Law at computational costs that are not too prohibitive. I will study the stability of these systems and how far they are capable of travelling in a coherent manner. A fuller study of the unstable stage of their development will follow in Chapter 13. I will investigate the effect of varying the values of the intervortex spacing, ℓ, and the ratio of macroscopic vortex radius to core radius, R/a, in Chapter 11.

An important issue for which there is no evidence one way or the other from the experiments is generalised leapfrogging. Leapfrogging of two vortex rings is a well known phenomenon in classical fluid mechanics. Much less is known about more generalised leapfrogging when $N > 2$. A topic related to that of leapfrogging is that of the trajectories described by the individual vortices in the frame of reference moving with the centre of vorticity. That is the path taken by the vortices as they undergo the leapfrog manoeuvre. I will discuss the dependence of the shape of this path on ℓ and R/a. Another point of interest is whether these trajectories are synonymous with the streamlines inside and around the cross-sectional vortex cores.

My purpose in this Chapter is three-fold: Firstly, to show that macroscopic vortex rings can and do travel significant distances at zero temperature. Secondly,

to show that in the presence of the normal fluid fraction the rings are quickly killed due to mutual friction and hence show the need for a normal fluid velocity field. Thirdly, to show that with the addition of a suitable normal fluid velocity field the rings are once again able to travel significant distances. For the sake of brevity, I will refer to the macroscopic vortex rings at zero temperature as T0 rings, at finite temperature with no normal fluid velocity field as T1 rings and with a normal fluid velocity field as T2 rings. I begin with the second point first.

10.2 Finite temperature effects

In Section 6.3 I noted that for a single vortex ring in the absence of counterflow the vortex rings shrinks at a rate $\dot{R} = -\gamma v_{si}/\rho_s\kappa$ (Equation 6.12), whereas in the presence of counterflow $\dot{R} = (\gamma/\rho_s\kappa)(v_n - v_s - v_{si})$ (Equation 6.10). Clearly, for positive v_n, the ring will shrink faster in the absence of a counterflow than in the presence of a counterflow. In Section 8.4 I developed a simple normal fluid velocity field based on Borner & Schmidt (1985) that mutual friction quickly and efficiently equalises the superfluid and normal fluid vorticity fields. It must be emphasised that this is a very simplistic model of the normal fluid velocity field, which simply puts together the normal fluid ring's translational velocity, which is assumed to be the same as the superfluid ring's translational velocity, and an arbitrary pseudo-Rankine model (approximately solid body rotation) for the velocity field of the normal fluid ring itself. Were it not for the fact that the piston experiments were conducted at finite temperatures which quickly kill vortex rings, it would be sufficient to investigate the behaviour of the rings at zero temperature.

It is important to point out that in the reference case of a single vortex ring the superfluid ring at finite temperatures is 'kept alive' by the translational velocity only. This is because by construction the ring coincides with the centre of the solid body rotation so that the contribution of the solid body rotation to the normal fluid velocity field is zero.

Figures 10.1 to 10.5 were produced using the KnotPlot software (http://www.KnotPlot.com/). The top row on each page shows a series of images at zero temperature, the middle row at finite temperature with no normal fluid velocity field and the bottom row at finite temperature with the prescribed normal fluid velocity field. Each image is an accurate representation of the vortex rings at the time indicated below the image, not a schematic diagram or cartoon. The radius of the cylinders, the size of the visualisation box and the orientation of each image is chosen to best exhibit the image's features. All of these macroscopic vortex rings were evolved using the full BS Law. I take this opportunity to stress a point which will become apparent from all of the 3D figures that follow, namely that in all of the calculations presented here the rings retain their initial axisymmetry: this is very

much non-trivial.

There is a clear distinction between the 3 cases. At zero temperature (top rows) there is little change between one frame and another. The total line length, Λ, is preserved and a portion of the leapfrogging phenomenon can be observed. At finite temperature (middle rows) the rings are seen, both visibly and from the values of Λ, to be rapidly disappearing. Adding the normal fluid velocity field (bottom rows) has a significant effect on increasing the lifetime of the rings. Although the total line length still drops to some extent and the configuration of the rings is somewhat different, these rings bear a much greater resemblance to the zero temperature case than to the finite temperature case.

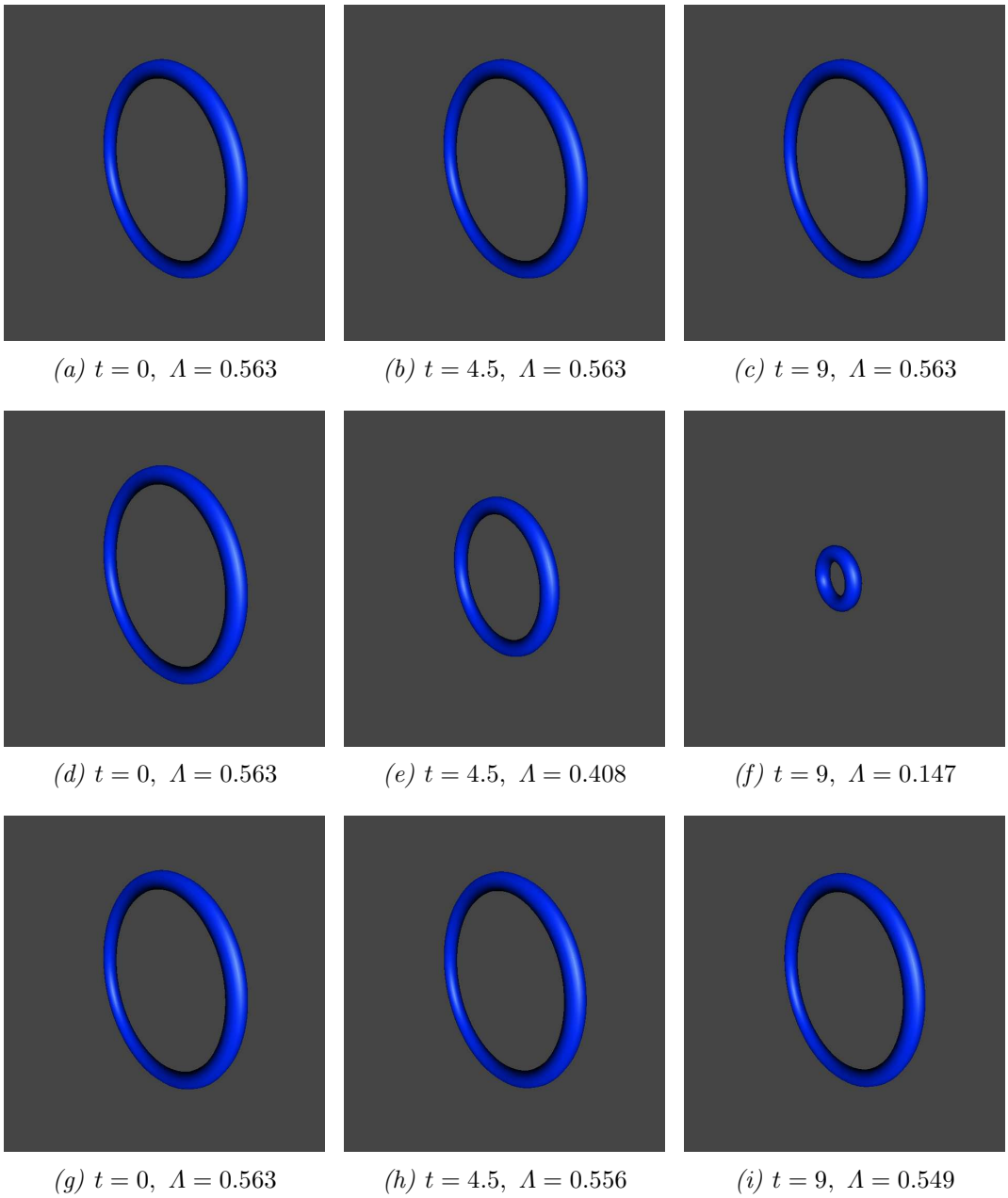

(a) $t = 0,\ \Lambda = 0.563$ *(b)* $t = 4.5,\ \Lambda = 0.563$ *(c)* $t = 9,\ \Lambda = 0.563$

(d) $t = 0,\ \Lambda = 0.563$ *(e)* $t = 4.5,\ \Lambda = 0.408$ *(f)* $t = 9,\ \Lambda = 0.147$

(g) $t = 0,\ \Lambda = 0.563$ *(h)* $t = 4.5,\ \Lambda = 0.556$ *(i)* $t = 9,\ \Lambda = 0.549$

Figure 10.1: Effect of temperature on a single vortex ring. (a-c) $T = 0$, (d-f) $T > 0$ and (g-i) $T > 0$, but with a normal fluid vortex ring, at (left) $t = 0$, (middle) $t = 4.5$ and (right) $t = 9$ seconds. Λ (cm) is total vortex line length. In each plot the centre of vorticity is placed at the origin. Parameters: BS Law, $R = 0.0896$ cm and cylinder radius 0.1 (arbitrary units).

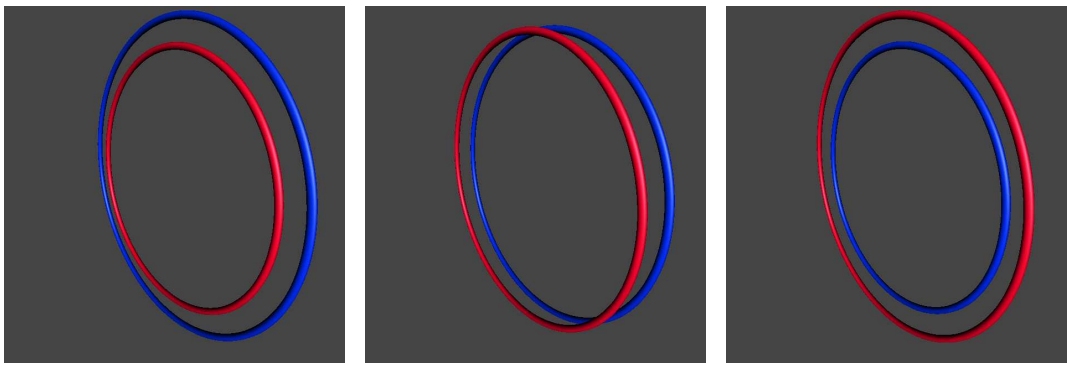

(a) $t = 0,\ \Lambda = 1.126$ (b) $t = 3.6,\ \Lambda = 1.130$ (c) $t = 7.2,\ \Lambda = 1.127$

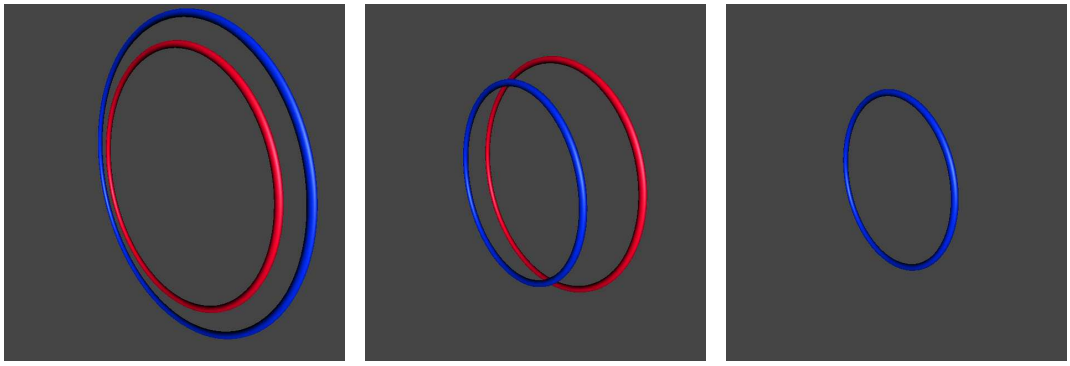

(d) $t = 0,\ \Lambda = 1.125$ (e) $t = 3.6,\ \Lambda = 0.854$ (f) $t = 7.2,\ \Lambda = 0.351$

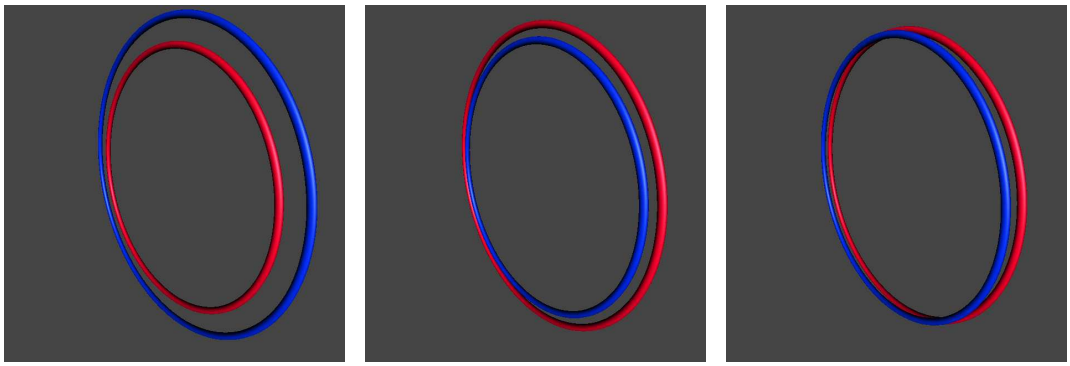

(g) $t = 0,\ \Lambda = 1.126$ (h) $t = 3.6,\ \Lambda = 1.110$ (i) $t = 7.2,\ \Lambda = 1.111$

Figure 10.2: Effect of temperature on 2 vortex rings. (a-c) $T = 0$, (d-f) $T > 0$ and (g-i) $T > 0$, but with a normal fluid vortex ring, at (left) $t = 0$, (middle) $t = 3.6$ and (right) $t = 4.5$ seconds. Λ (cm) is total vortex line length. In each plot the centre of vorticity is placed at the origin. The plots are oriented to best exhibit the rings. Parameters: BS Law, $R = 0.0896$ cm, $a = 0.0075$ cm, $\ell = 0.015$ cm, $R/a \approx 12$ and cylinder radius 0.02 (arbitrary units).

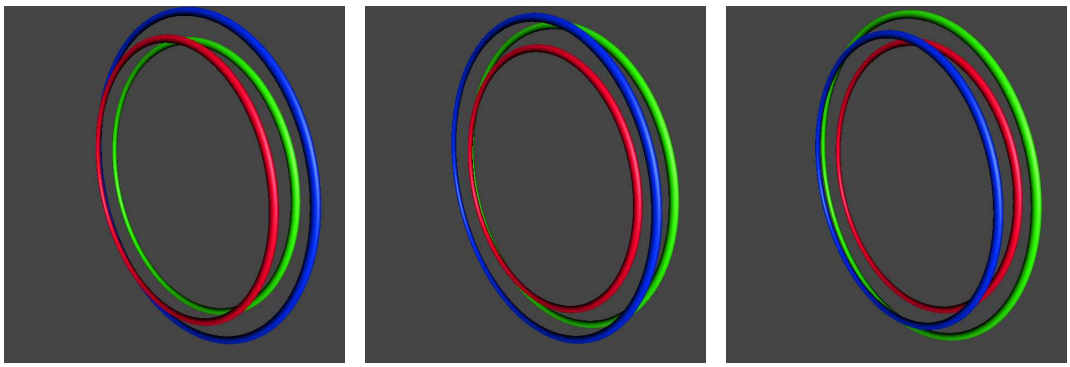

(a) $t = 0,\ \Lambda = 1.689$ (b) $t = 3.6,\ \Lambda = 1.689$ (c) $t = 7.2,\ \Lambda = 1.690$

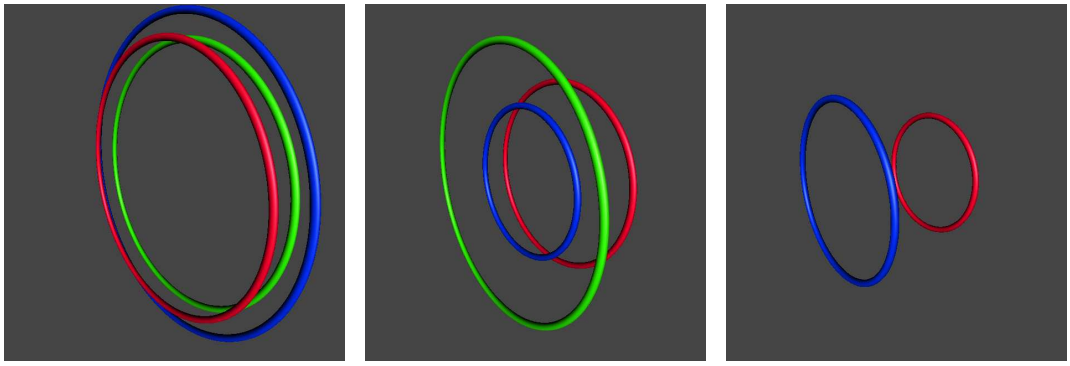

(d) $t = 0,\ \Lambda = 1.688$ (e) $t = 3.6,\ \Lambda = 1.211$ (f) $t = 7.2,\ \Lambda = 0.588$

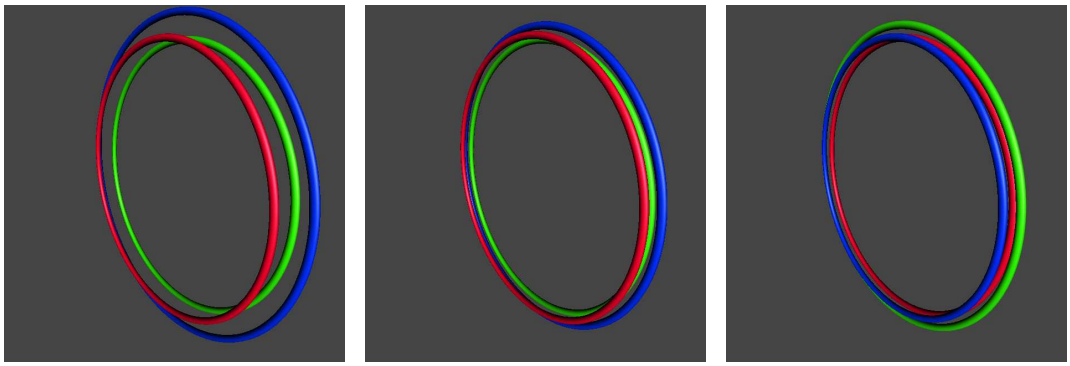

(g) $t = 0,\ \Lambda = 1.688$ (h) $t = 3.6,\ \Lambda = 1.655$ (i) $t = 7.2,\ \Lambda = 1.655$

Figure 10.3: Effect of temperature on 3 vortex rings. (a-c) $T = 0$, (d-f) $T > 0$ and (g-i) $T > 0$, but with a normal fluid vortex ring, at (left) $t = 0$, (middle) $t = 3.6$ and (right) $t = 7.2$ seconds. Λ (cm) is total vortex line length. In each plot the centre of vorticity is placed at the origin. Parameters: BS Law, $R = 0.0896$ cm, $a = \ell/\sqrt{3}$ cm, $\ell = 0.015$ cm, $R/a \approx 10$ and cylinder radius 0.02 (arbitrary units).

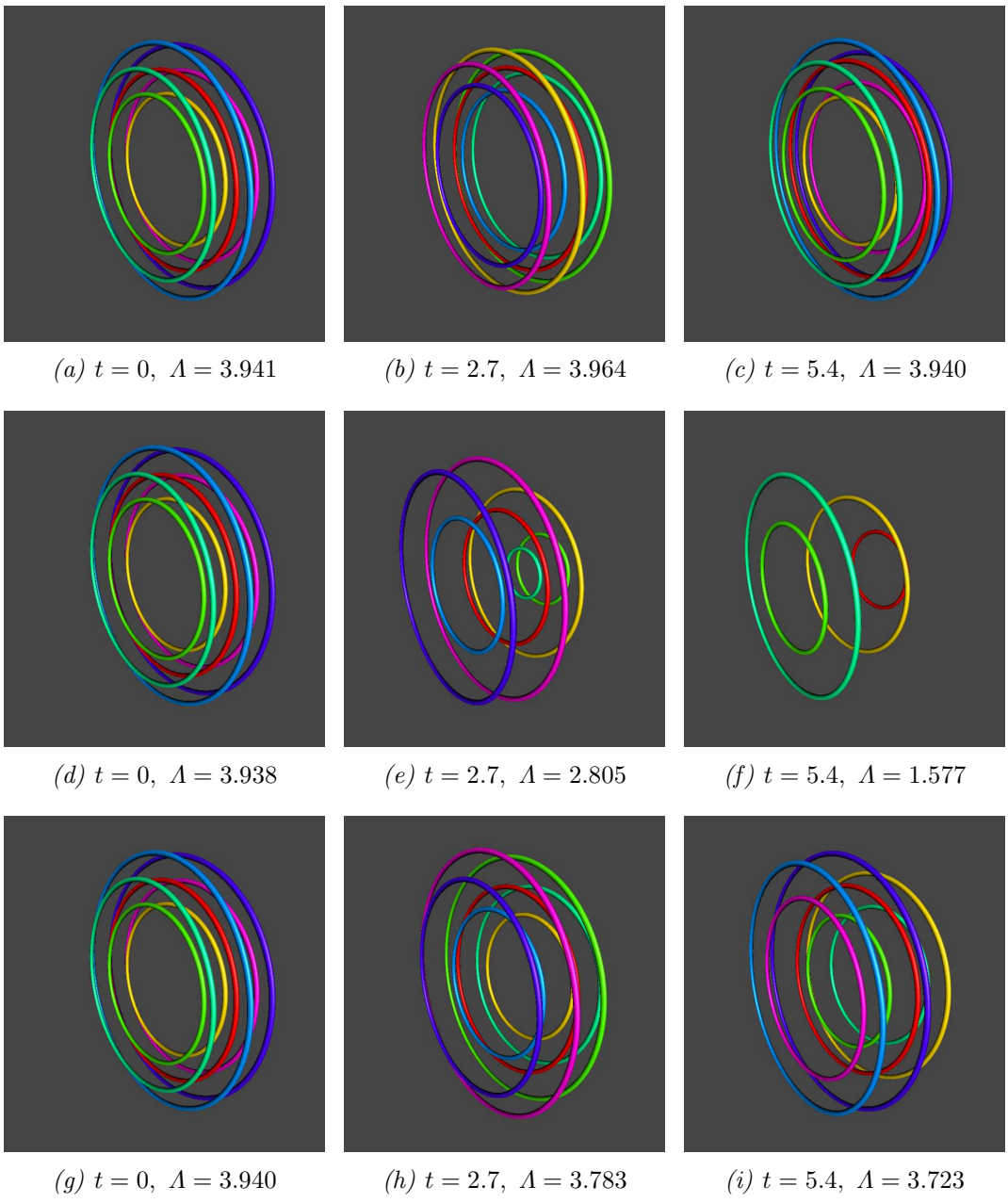

(a) $t = 0,\ \Lambda = 3.941$ *(b)* $t = 2.7,\ \Lambda = 3.964$ *(c)* $t = 5.4,\ \Lambda = 3.940$

(d) $t = 0,\ \Lambda = 3.938$ *(e)* $t = 2.7,\ \Lambda = 2.805$ *(f)* $t = 5.4,\ \Lambda = 1.577$

(g) $t = 0,\ \Lambda = 3.940$ *(h)* $t = 2.7,\ \Lambda = 3.783$ *(i)* $t = 5.4,\ \Lambda = 3.723$

Figure 10.4: Effect of temperature on 7 vortex rings. (a-c) $T = 0$, (d-f) $T > 0$ and (g-i) $T > 0$, but with a normal fluid vortex ring, at (left) $t = 0$, (middle) $t = 2.7$ and (right) $t = 5.4$ seconds. Λ (cm) is total vortex line length. In each plot the centre of vorticity is placed at the origin. Parameters: BS Law, $R = 0.0896$ cm, $a = 0.0223$ cm, $\ell = 0.0223$ cm, $R/a \approx 4$ and cylinder radius 0.02 (arbitrary units).

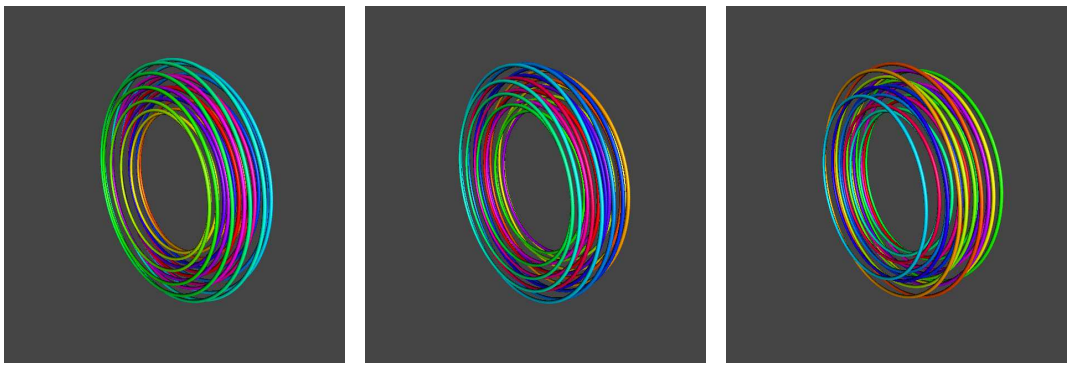

(a) $t = 0,\ \Lambda = 14.326$ (b) $t = 3.6,\ \Lambda = 14.363$ (c) $t = 7.2,\ \Lambda = 14.363$

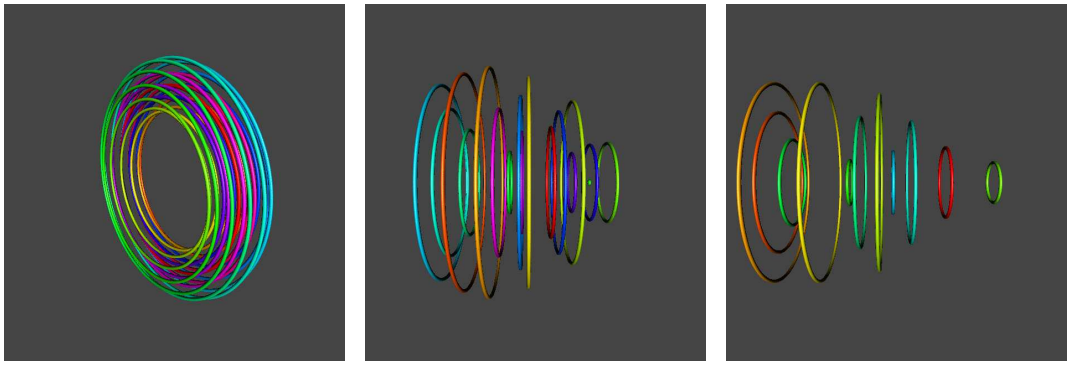

(d) $t = 0,\ \Lambda = 14.309$ (e) $t = 3.6,\ \Lambda = 8.680$ (f) $t = 7.2,\ \Lambda = 4.990$

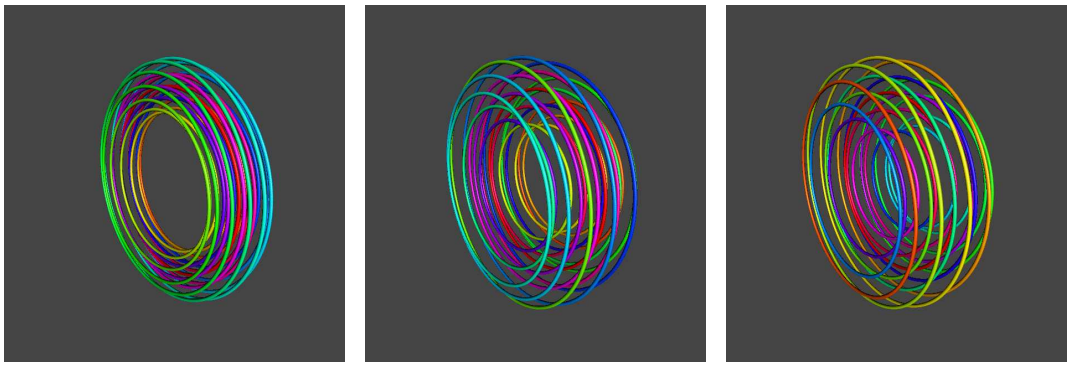

(g) $t = 0,\ \Lambda = 14.321$ (h) $t = 3.6,\ \Lambda = 13.394$ (i) $t = 7.2,\ \Lambda = 12.897$

Figure 10.5: Effect of temperature on 19 vortex rings. (a-c) $T = 0$, (d-f) $T > 0$ and (g-i) $T > 0$, but with a normal fluid vortex ring, at (left) $t = 0$, (middle) $t = 3.6$ and (right) $t = 7.2$ seconds. Λ (cm) is total vortex line length. In each plot the centre of vorticity is placed at the origin. The plots are oriented to best exhibit the rings. Parameters: BS Law, $R = 0.12$ cm, $a = 0.03$ cm, $\ell = 0.015$ cm, $R/a = 4$ and cylinder radius 0.02 (arbitrary units).

10.3 Translation of robust macroscopic vortex rings at zero and finite temperatures

I now move on to consider the total distance travelled a number of rings possessing similar initial parameters and also to consider in which ways they changed during their period of translation. I will firstly describe the parameters used to produce the rings. The self-induced velocity was calculated using the full BS Law. The rings were constructed assuming an intervortex spacing $\ell = 0.015$ cm (recall that typical values of ℓ lie between 10^{-2} and 10^{-4} cm). $N = 7$ rings is the first non-trivial centred hexagonal configuration. I set the ring radius to core radius ratio at $R/a = 4$, such that $R = 0.06$ cm, since $a = \ell$ for $N = 7$. In order to compare like with like in the cases of $N = 1$, 2, 3 and 7, I used this value of the ring radius throughout, since in all cases $R/a \geq 4$. With regard to $N = 19$, in which case $a = 2\ell$, using $R = 0.06$ cm would have meant that $a = 0.03$ cm and hence $R/a = 2$. This value of R/a may not have remained stable (Acheson, 2000). I instead insisted that $R/a = 4$, such that $R = 0.12$ cm. For ease of reference I record these values in Table 10.1.

N	ℓ (cm)	R (cm)	a (cm)	R/a
1	-	0.06	-	-
2	0.015	0.06	0.0075	8
3	0.015	0.06	0.00866	6.92
7	0.015	0.06	0.015	4
19	0.015	0.12	0.03	4

Table 10.1: Values of parameters used in Figure 10.6.

The distance travelled by each configuration and at each temperature (T0, T1 and T2) is shown in Figure 10.6.There are several features which are striking about Figure 10.6. Note that the gradient of the curves give the instantaneous velocity of the centre of vorticity. The T1 rings (thick black lines) are much shorter-lived than the T0 (red lines) and T2 (blue lines) rings. The 'death' of each of the T1 rings is preceded by a rapid burst of speed. This follows naturally from the definition of self-induced velocity for the vortex rings, which scales like $1/R$. Thus the more the configuration of rings shrinks, the more it speeds up. The T0 and T2 rings both succeed in translating significant distances: in the region of $10D$ from their starting points. The velocity of the T2 rings is greater than the T0 rings for $N = 1$, 2 and 3 and vice versa for $N = 7$ and 19. As mentioned $N = 1$, 2, 3 and 7 all share the same value for $R = 0.06$ cm. Comparing the plots for these numbers of rings, one can see that they reach a distance of $10D = 1.2$ cm at progressively shorter times, after approximately 50, 40, 35 and 25 seconds respectively ($N = 19$ cannot be compared

easily, since it has a different value for R). This is in agreement with Equation 6.9, in which for constant value of R, the velocity should increase with an increasing number of rings. The changes in the gradient are due to the onset of instabilities, a feature which will be discussed later (Chapter 13). Recall also that Murakami *et al.* (1987) measured the translational velocity of his piston-induced vortex rings. His measurements indicate that the rings gradually slow down over time. His results can be seen in Figure 7.2(c).

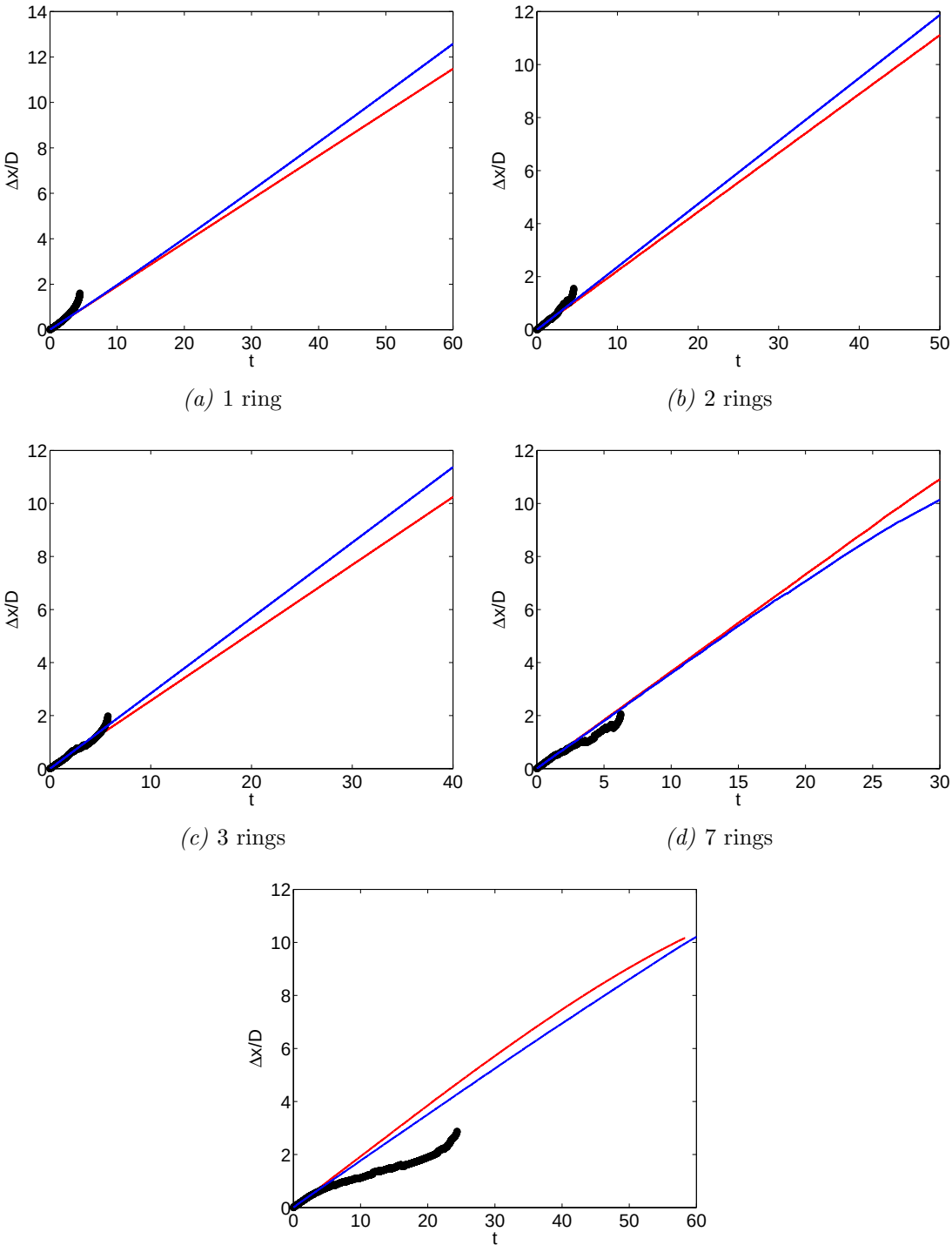

(a) 1 ring

(b) 2 rings

(c) 3 rings

(d) 7 rings

(e) 19 rings

Figure 10.6: Distance travelled by centre of vorticity $\Delta x/D$ vs t (s) for $N = 1$, 2, 3, 7 and 19 at T0 (red line), T1 (thick black lines) and T2 (blue line). A thick line is used for the T1 case to draw attention to its behaviour.

10.4 Tables of results for translation of robust macroscopic vortex rings at zero and finite temperatures

I now record the main results for each macroscopic vortex ring detailed in Table 10.1 and Figures 10.6(a-e). The results for each ($N = 1$, 2, 3, 7 and 19) are recorded in their own table (Tables 10.2 to 10.6). I once again refer to the zero temperature case as 'T0', the finite temperature case as 'T1' and the finite temperature case with the imposed normal fluid velocity field as 'T2'. The following features are highlighted in each case where relevant:

- start - gives data at $t = 0$ (or, to be more precise, at the first snapshot which depends on $\Delta\, t$ and the snapshot frequency).
- finish - gives data at final time in the event that the vortex rings complete the run.
- first - first ring escapes from the macroscopic ring formation and is killed by mutual friction. Data is for the snapshot after the ring dies.
- last - last ring is killed by mutual friction. Data is for the snapshot before the ring dies.
- remove - first point(s) removed from system. In T1 this is a sign of the rings dying and means that the system is shrinking. In T0 and T2 it is a sign of the discretisation points reorganising themselves. It may be a precursor to the onset of instabilities.
- recon - first (visible) reconnection. One must distinguish here between reconnections which are 'visible' (i.e. are self-evident from a 3D plot of the macroscopic ring) and 'algorithmic' (i.e. they are a feature of the reconnection algorithm which may register a reconnection although no visible change occurs). Algorithmic reconnections are prevalent at T2. Use of the Kondaurova reconnection algorithm, which only registers a reconnection when two vortex filaments actually cross each other, greatly inhibits these spurious reconnections.

For each event, the following data is given: time, total line length, average curvature, number of initial diameters travelled and velocity of centre of vorticity.

Case	Event	t (s) (2dp)	Λ (cm) (3dp)	$\bar{c}$ (cm/s^2) (2dp)	$\Delta x/D$ (2dp)	v_x (cm/s) (4dp)
T0	start	0	0.377	16.77	0	0.0230
	finish	60	0.377	16.77	11.48	0.0230
T1	start	0	0.377	16.23	0	0.0230
	remove	2.44	0.250	24.66	0.56	0.0337
	last	4.46	0.010	581.92	1.61	0.6182
T2	start	0	0.377	16.74	0	0.0230
	finish	60	0.329	19.29	12.58	0.0261

Table 10.2: Results for $N = 1$ and $R = 0.06$ cm at $T = 0$ K (T0), $T = 2.02$ K with no normal fluid velocity field (T1) and $T = 2.02$ K with a normal fluid velocity field (T2).

Case	Event	t (s) (2dp)	Λ (cm) (3dp)	$\bar{c}$ (cm/s^2) (2dp)	$\Delta x/D$ (2dp)	v_x (cm/s) (4dp)
T0	start	0	0.754	17.19	0	0.0279
	finish	50	0.760	16.65	11.11	0.0258
T1	start	0	0.753	16.43	0	0.0279
	remove	1.75	0.566	20.84	0.39	0.0310
	first	3.95	0.137	40.03	1	0.0594
	last	4.58	0.011	561.49	1.56	0.6065
T2	start	0	0.754	17.09	0	0.0279
	finish	50	0.731	17.35	11.87	0.0277

Table 10.3: Results for $N = 2$, $R = 0.06$ cm and $a = 0.0075$ cm at $T = 0$ K (T0), $T = 2.02$ K with no normal fluid velocity field (T1) and $T = 2.02$ K with a normal fluid velocity field (T2).

Case	Event	t (s) (2dp)	Λ (cm) (3dp)	$\bar{c}$ (cm/s^2) (2dp)	$\Delta x/D$ (2dp)	v_x (cm/s) (4dp)
T0	start	0	1.131	17.11	0	0.0310
	finish	40	1.131	17.21	10.24	0.0311
T1	start	0	1.130	16.30	0	0.0309
	remove	0.76	0.992	18.05	0.19	0.0299
	first	2.84	0.442	27.95	0.78	0.0533
	last	5.75	0.007	797.60	1.98	0.7812
T2	start	0	1.130	16.76	0	0.0310
	finish	40	1.083	17.96	11.37	0.0341

Table 10.4: Results for $N = 3$, $R = 0.06$ cm and $a = 0.00866$ cm at $T = 0$ K (T0), $T = 2.02$ K with no normal fluid velocity field (T1) and $T = 2.02$ K with a normal fluid velocity field (T2).

Case	Event	t (s) (2dp)	Λ (cm) (3dp)	$\bar{c}$ (cm/s^2) (2dp)	$\Delta x/D$ (2dp)	v_x (cm/s) (4dp)
T0	start	0	2.639	18.08	0	0.0450
	remove	18.91	2.640	17.04	6.93	0.0407
	recon	26.98	2.712	21.02	9.86	0.0395
	finish	30	2.841	69.05	10.91	0.0378
T1	start	0	2.637	16.78	0	0.0450
	remove	0.20	2.521	17.27	0.08	0.0425
	first	1.49	1.646	22.89	0.53	0.0409
	last	6.24	0.005	1172.86	2.07	1.0000
T2	start	0	2.639	17.72	0	0.0450
	remove	0.97	2.551	18.73	0.36	0.0423
	first	18.66	1.917	20.47	6.60	0.0401
	recon	24.06	1.912	22.99	8.42	0.0352
	finish	30	1.521	20.85	10.13	0.0311

Table 10.5: Results for $N = 7$, $R = 0.06$ cm and $a = 0.015$ cm at $T = 0$ K (T0), $T = 2.02$ K with no normal fluid velocity field (T1) and $T = 2.02$ K with a normal fluid velocity field (T2).

Case	Event	t (s) (2dp)	Λ (cm) (3dp)	$\bar{c}$ (cm/s^2) (2dp)	$\Delta x/D$ (2dp)	v_x (cm/s) (4dp)
T0	start	0	14.326	10.87	0	0.0471
	remove	8.06	14.324	10.19	1.55	0.0447
	recon	19.89	14.482	11.91	3.83	0.0459
	finish	60	22.451	199.54	10.38	0.0277
T1	start	0	14.309	9.88	0	0.0471
	remove	0.29	13.842	9.90	0.05	0.0446
	first	2.99	9.579	11.95	0.50	0.0347
	last	24.37	0.014	441.48	2.88	0.4909
T2	start	0	14.321	10.53	0	0.0471
	remove	0.88	14.008	10.44	0.17	0.0432
	first	38.79	11.798	10.57	6.74	0.0356
	recon	45.76	11.929	11.40	7.90	0.0348
	finish	60	11.421	11.31	10.21	0.0301

Table 10.6: Results for $N = 19$, $R = 0.12$ cm and $a = 0.030$ cm at $T = 0$ K (T0), $T = 2.02$ K with no normal fluid velocity field (T1) and $T = 2.02$ K with a normal fluid velocity field (T2).

10.5 Discussion of results

I will comment briefly on the results contained in Tables 10.2 to 10.6. Tables 10.2, 10.3 and 10.4 for $N = 1$, 2 and 3 rings merely serve to emphasise the results plotted in Figures 10.6(a-c). T0 rings translate at least a distance $10D$ with very little, if any, change to line length, average curvature and translational velocity. T1 rings die well before having translated $10D$ and last a fraction of the time of T0 rings. T2 rings, while undergoing some variation in Λ, $\bar{c}$ and v_x, also manage to travel at least $10D$. However Tables 10.5 and 10.6 reveal a more complicated picture both for T0 rings and T2 rings. The tables show the onset of turbulence: points removed (and added) and the occurrence of reconnections. Although in all cases ($N = 7$ and 19 at both $T0$ and $T2$) the macroscopic rings travel the requisite $10D$ distance (and further), it is clear than whilst doing so instabilities have developed that have inhibited its motion. It is furthermore noteworthy that although the average curvature increases both for T0 rings and T2 rings, the increase for T0 rings is many times greater than the increase for T2 rings. Another difference between T0 and T2 rings is that the total line length for T0 rings increases, whereas for T2 rings it deceases. The implications of these results are that the T0 rings are subject to small scale turbulence, which is characterised by high curvature and increased line length, whilst T2 rings are not due to the mutual friction smoothing out small scale instabilities. A fuller discussion of these instabilities is contained in Chapter 13.

10.6 Conservation of vortex energy for $N > 2$

In Section 8.6.1 I discussed briefly the conservation of vortex energy for a single vortex ring in the zero temperature limit and showed that my numerical model conserves this energy to within 10^{-12} %. In Section 8.6.2 I showed that for two rings energy is conserved to within 0.5 %. I now show results for the conservation of energy in more complicated systems consisting of more than two vortex rings. In principle, in the zero temperature limit, in the absence of mutual friction, the total kinetic energy contained in the vortex rings should be conserved just as well for multiple rings as for a single ring. As previously noted (Section 8.2) this will only hold true until a reconnection event takes place.

The kinetic energy per unit density in a fluid volume V of constant density can be written as

$$E = \frac{1}{2}\int_V \mathbf{u}^2 dV, \tag{10.1}$$

where $\mathbf{u}$ is the velocity of the superfluid. For a quantised vortex filament of circulation κ Equation 10.1 becomes

$$E = \kappa \oint_{\mathcal{L}} \mathbf{u}\cdot\mathbf{s}\times\mathbf{s}' d\xi, \tag{10.2}$$

where $\mathbf{u}$ is the velocity of the vortex filament at location $\mathbf{s}$ and $\mathbf{s}'$ is its tangent vector (as noted in Equation 8.6). In the following cases I use the trapezium rule to evaluate numerically the kinetic energy of the vortex filaments at $T = 0$ K for 1, 2, 3, 7 and 19 rings using the Biot-Savart law. I do this both in the case where I fix $R = 0.0896$ cm, allowing R/a to vary (Figure 10.7), and the converse case where I fix $R/a = 4$ allowing R to vary (Figure 10.8). I will not plot the results for a single ring. Its vortex energy varies by about 10^{-12} % throughout. For the other cases I plot the absolute percentage change from the initial vortex energy, E_0. This quantity can be written as

$$\delta_{err} = 100 \times |\Delta E| / E_0, \tag{10.3}$$

where $\Delta E = E(t) - E_0$. Energy is not conserved during a reconnection event. One or more reconnections occur in the cases $N = 7$ and $N = 19$. In these cases I do not show the data after the first reconnection event. Otherwise I plot the data until the rings have travelled at least $10D$. It is useful to consider how the energy is conserved both over time and over distance travelled by the centre of vorticity. I measure this distance, once again, in units of the original diameter of the vortex ring formation, D. As is evident from these plots the percentage change for 2, 3, 7 and 19 rings is well below 1 %. This is not the case for 7 or 19 rings after the onset of reconnections. In which case the change in energy reaches several percent.

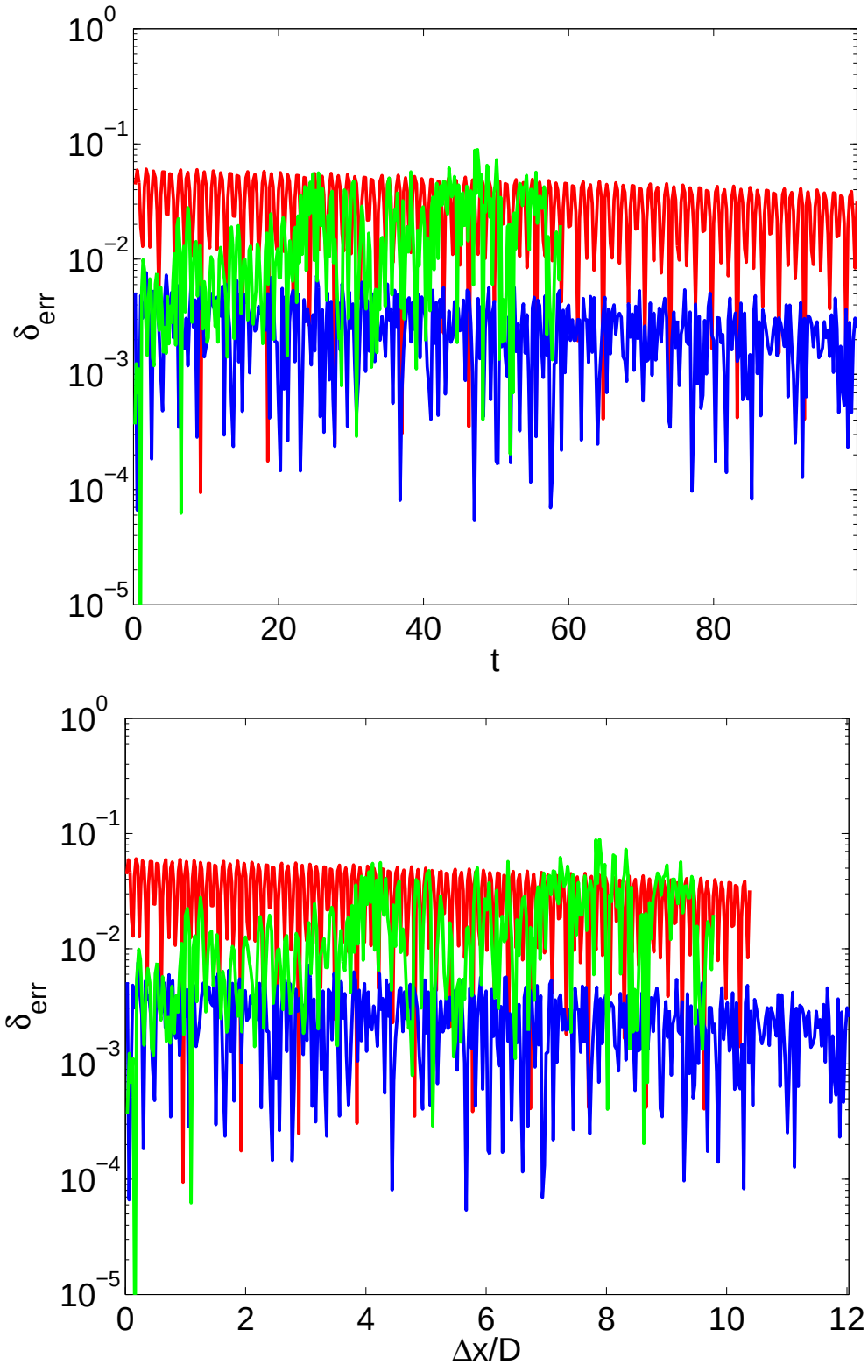

Figure 10.7: Normalised percentage change in vortex energy δ_{err} vs (upper plot) t (s) and (lower plot) distance travelled by the centre of vorticity $\Delta x/D$ at $T = 0$ using the BS law for $N = 2$ (red line), $N = 3$ (blue line) and $N = 7$ (green line). There are no reconnections during the period of this data for $N = 2$ or $N = 3$. For $N = 7$ the first reconnection occurs after about 59 seconds. I do not plot the data beyond this time. In this plot I use the same value for $R = 0.0896$ cm in all cases, but allow R/a to vary.

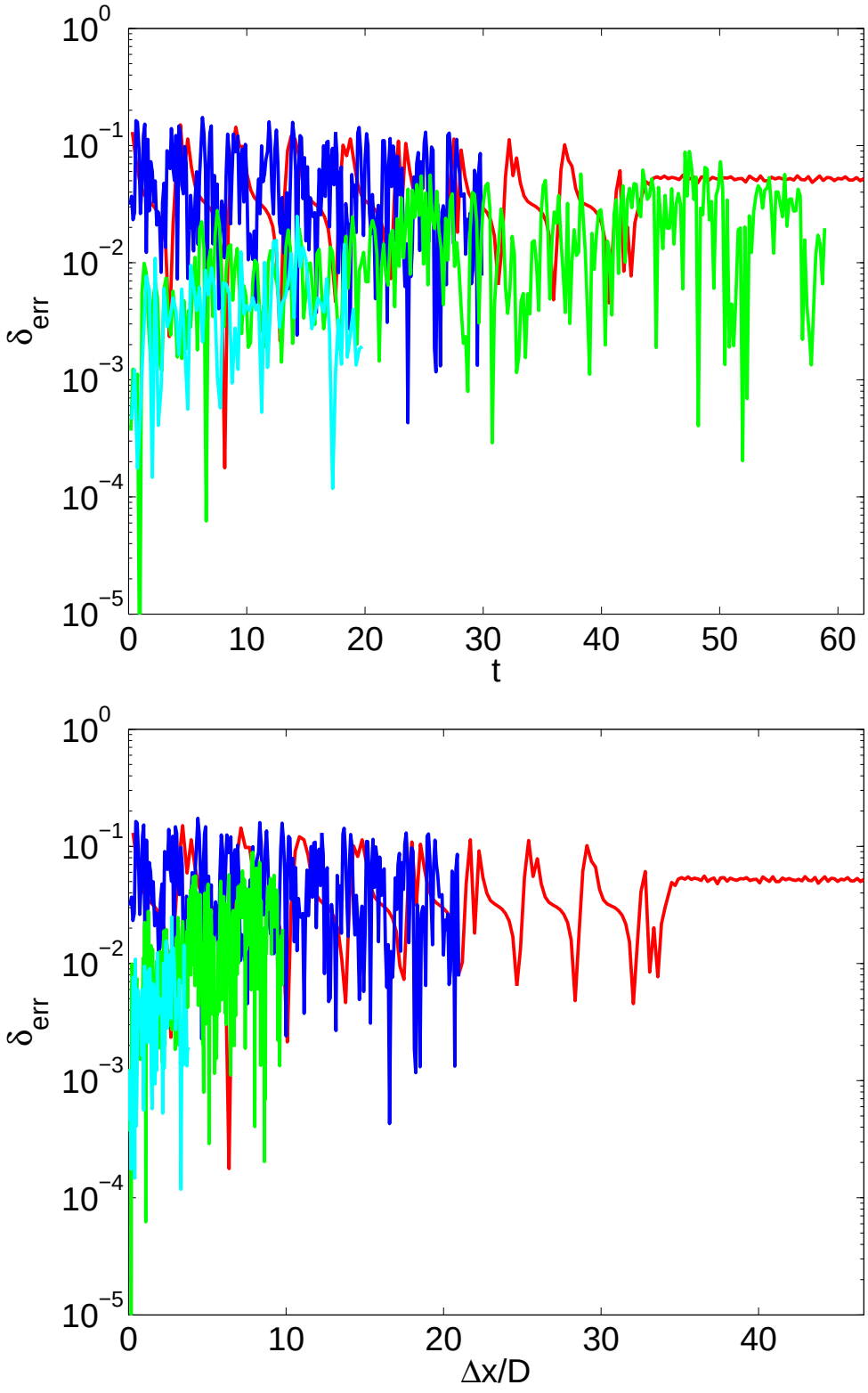

Figure 10.8: Normalised percentage change in vortex energy δ_{err} vs (upper plot) t (s) and (lower plot) distance travelled by the centre of vorticity $\Delta x/D$ at $T = 0$ using the BS law for $N = 2$ (red line), $N = 3$ (blue line), $N = 7$ (green line) and $N = 19$ (cyan line). There are no reconnections during the period of this data for $N = 2$ or $N = 3$. For $N = 7$ and $N = 19$ the first reconnection occurs after about 59 and 19 seconds respectively. I do not plot the data beyond this time.In this plot I use the same value for $R/a = 4$ in all cases, but allow R to vary.

10.7 Generalised leapfrogging

The stable motion which T0 and T2 rings perform is accompanied by a generalised leapfrogging process. The entire formation translates along its rotational axis whilst all the while the individual rings at the back of the macroscopic ring shrink and slip through the middle of the macroscopic ring only to then grow, slow down and move round the outside of the macroscopic ring. Of interest in this motion are the period, τ_{LF}, of an single leapfrog (i.e. the time taken for an individual ring to return to its original position in the macroscopic ring formation), the shape of the trajectory following the reference frame of the centre of vorticity (e.g. circular, elliptical or D-shaped) and its dependence on the values of ℓ and R/a. As I mentioned earlier there is no evidence from the experimental data that the observed translatory motion was accompanied by any form of leapfrogging process. The evidence for this is based on the numerical simulations which I have performed.

In the following series of figures (Figures 10.9 to 10.15) I include 2 types of images. One (Figures 10.9, 10.11 and 10.13) is a series of cross-sectional slices of the core of the macroscopic vortex rings. In these images I follow one of the individual rings as it performs its first leapfrogging motion. The ring being followed is identified by red circles, whilst the other rings are identified by blue circles. There are 2 red circles for each ring where the ring enters the plane, the solid one corresponding to positive (anticlockwise) rotation and the hollow one corresponding to negative (clockwise) rotation. The size of the circles is arbitrary. The other type of image (Figures 10.10, 10.12 and 10.14) is a series of 3D images of the macroscopic ring produced using the KnotPlot software. KnotPlot does not allow arbitrary colouring of each ring, but I have arranged that the red ring in the KnotPlot images corresponds to the ring identified by the red circles in the cross-sectional slices. Once again the radius of the cylinders, the size of the visualisation box and the orientation of each image is chosen to best exhibit the image's features. It becomes increasingly difficult to pick out the motion of individual rings in a 3D plot as N increases. For this reason I do not attempt to show 3D images of $N = 19$. I suffice with an image of one cross-section of the macroscopic vortex core (Figure 10.15).

For $N > 2$ it is evident that the shape of the cross-section of the core of the macroscopic vortex ring quickly deforms from its initial circular shape to a more elliptical shape whose major axis is aligned at an angle to the direction of motion. This mean that the trajectories of individual vortex rings will follow an elliptical path. In fact in all cases, even $N = 2$, the maximum horizontal separation is clearly far greater than the maximum vertical separation. Hence even for $N = 2$ the trajectories are elliptical. This will be discussed further in Chapter 11.

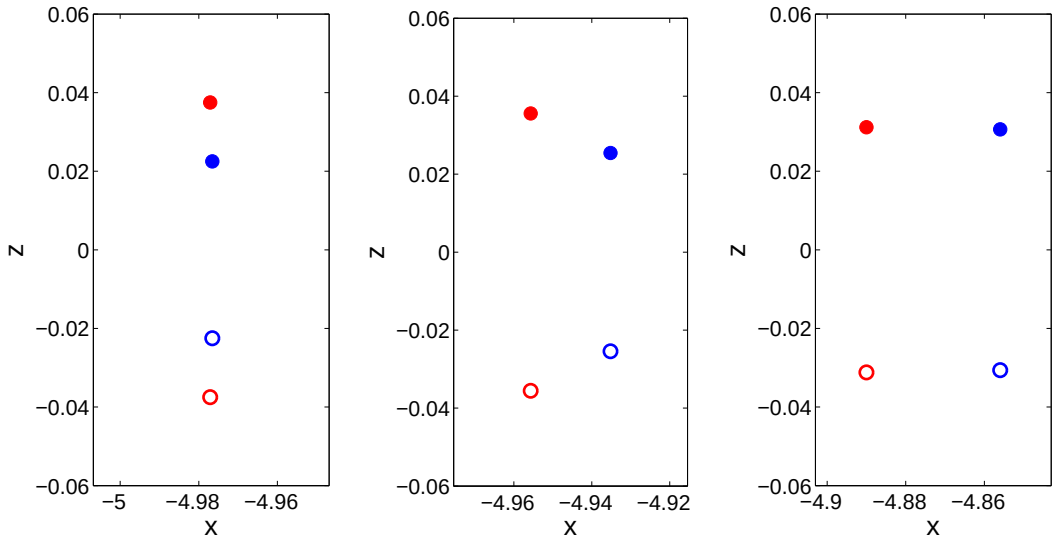

(a) $t = 0.0125$

(b) $t = 0.625$

(c) $t = 2.2$

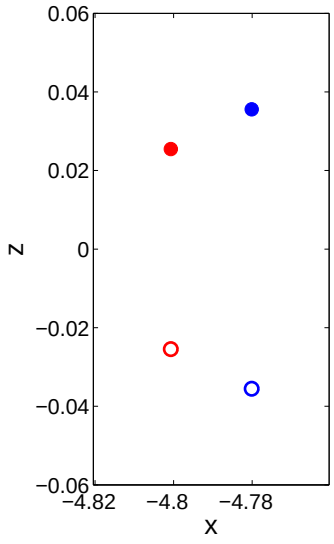

(d) $t = 4$

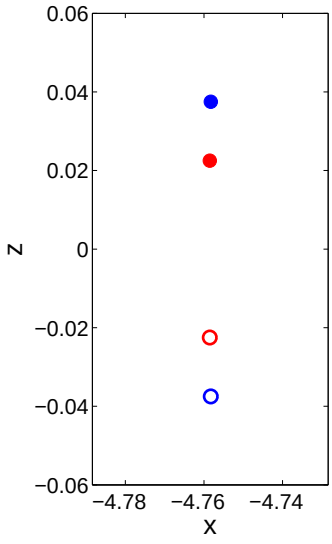

(e) $t = 4.625$

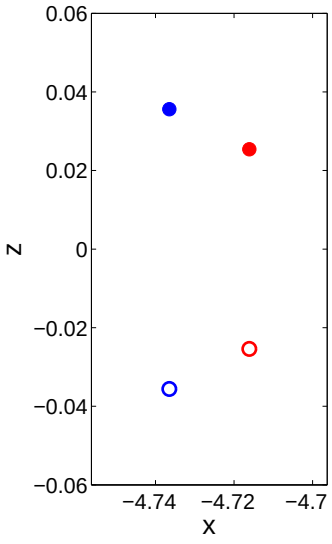

(f) $t = 5.25$

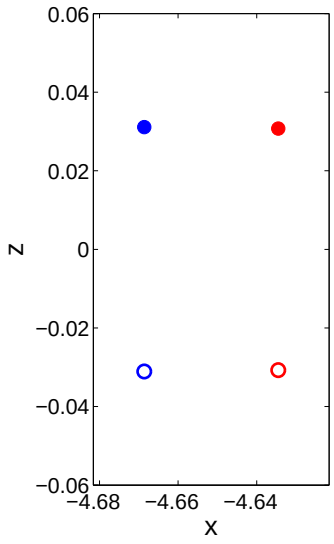

(g) $t = 6.875$

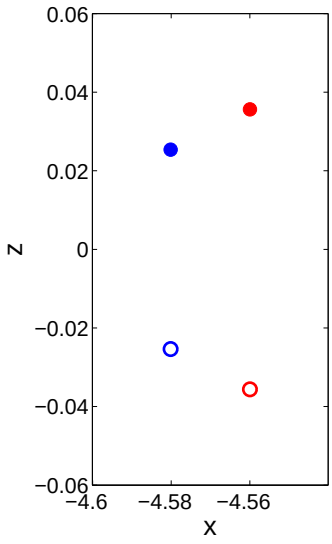

(h) $t = 8.65$

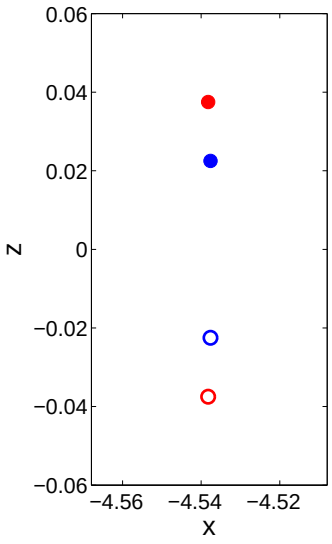

(i) $t = 9.275$

Figure 10.9: Cross-sectional slices of leapfrogging for $N = 2$. Details on next page.

Figure 10.9 shows 9 images of the cross-section of 2 leapfrogging vortex rings undergoing their first complete leapfrog - in the reference frame moving with the rings each ring moves through 360 degrees. The marker size is arbitrary and does not represent the core size of the individual rings. Solid symbols represent positive circulation (anticlockwise) and hollow symbols negative circulation (clockwise). It is evident from the maximum vertical and horizontal separations that the trajectory is elliptical.

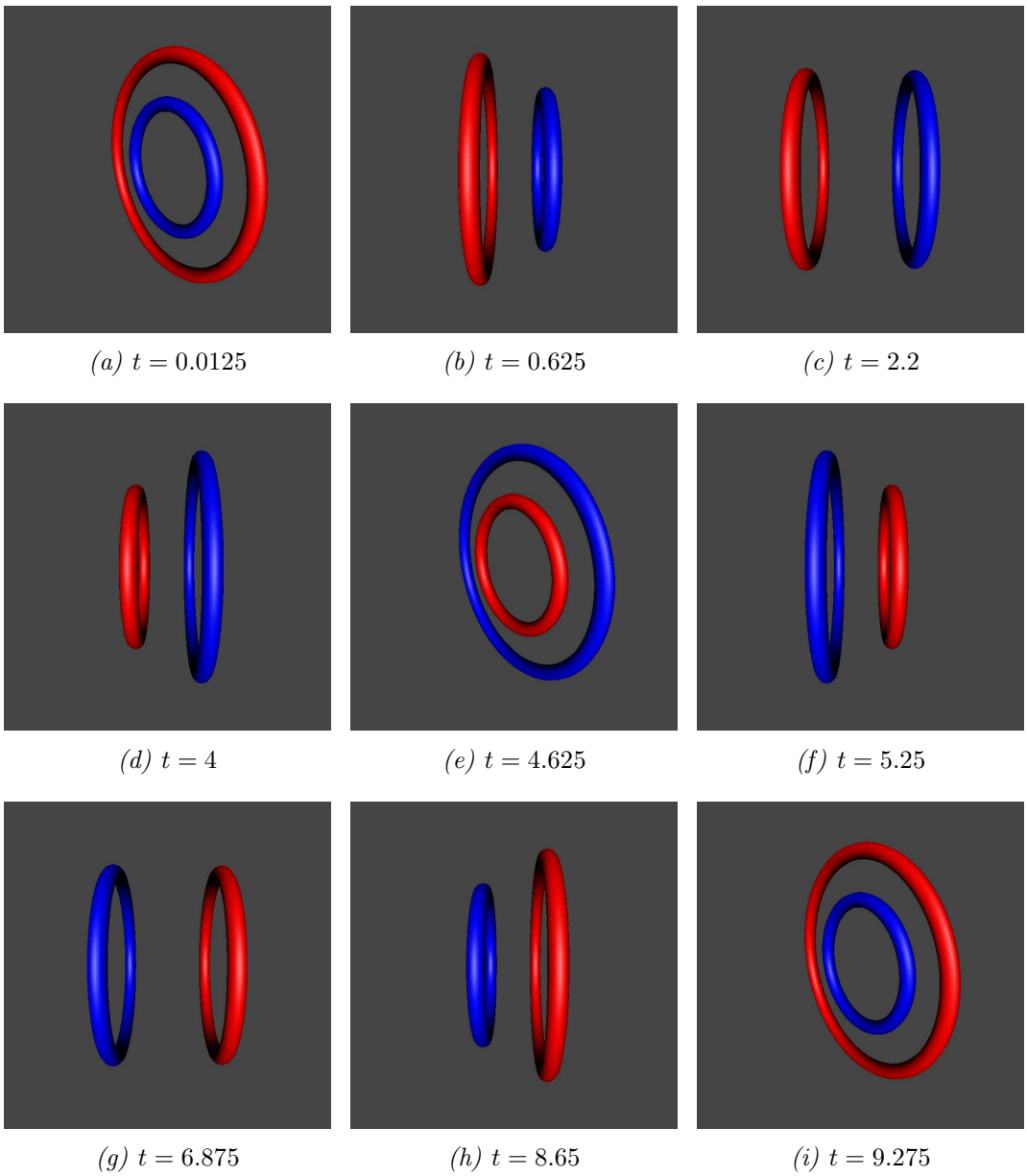

(a) $t = 0.0125$ (b) $t = 0.625$ (c) $t = 2.2$

(d) $t = 4$ (e) $t = 4.625$ (f) $t = 5.25$

(g) $t = 6.875$ (h) $t = 8.65$ (i) $t = 9.275$

Figure 10.10: 3D Knotplot images of leapfrogging for $N = 2$, corresponding to cross-sectional images in Figure 10.9. The radius of the cylinders, the size of the visualisation box and the orientation of each image is chosen to best exhibit the image's features. Parameters: full BS law, $R = 0.03$ cm, $a = 0.0075$ cm, $\ell = 0.015$ cm and $R/a = 4$.

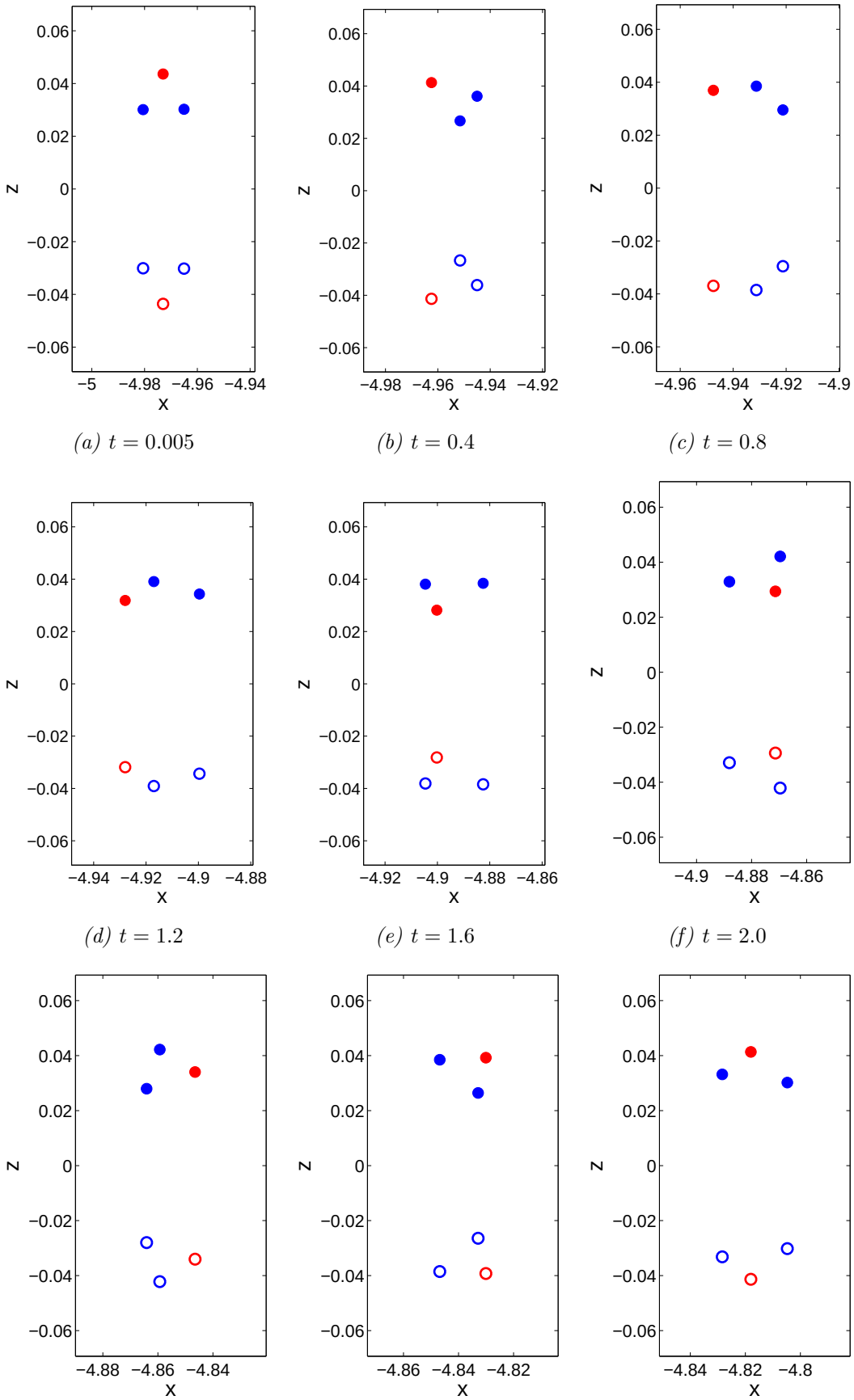

(a) $t = 0.005$ *(b)* $t = 0.4$ *(c)* $t = 0.8$

(d) $t = 1.2$ *(e)* $t = 1.6$ *(f)* $t = 2.0$

(g) $t = 2.4$ *(h)* $t = 2.8$ *(i)* $t = 3.2$

Figure 10.11: Cross-sectional slices of leapfrogging for $N = 3$. Details on next page.

Figure 10.11 shows 9 images of the cross-section of 3 leapfrogging vortex rings undergoing their first complete leapfrog - in the reference frame moving with the rings each ring moves through 360 degrees. I use one pair of red markers to exhibit this feature. The marker size is arbitrary and does not represent the core size of the individual rings. Solid symbols represent positive circulation (anticlockwise) and hollow symbols negative circulation (clockwise). It is evident from the maximum vertical and horizontal separations that the trajectory is elliptical.

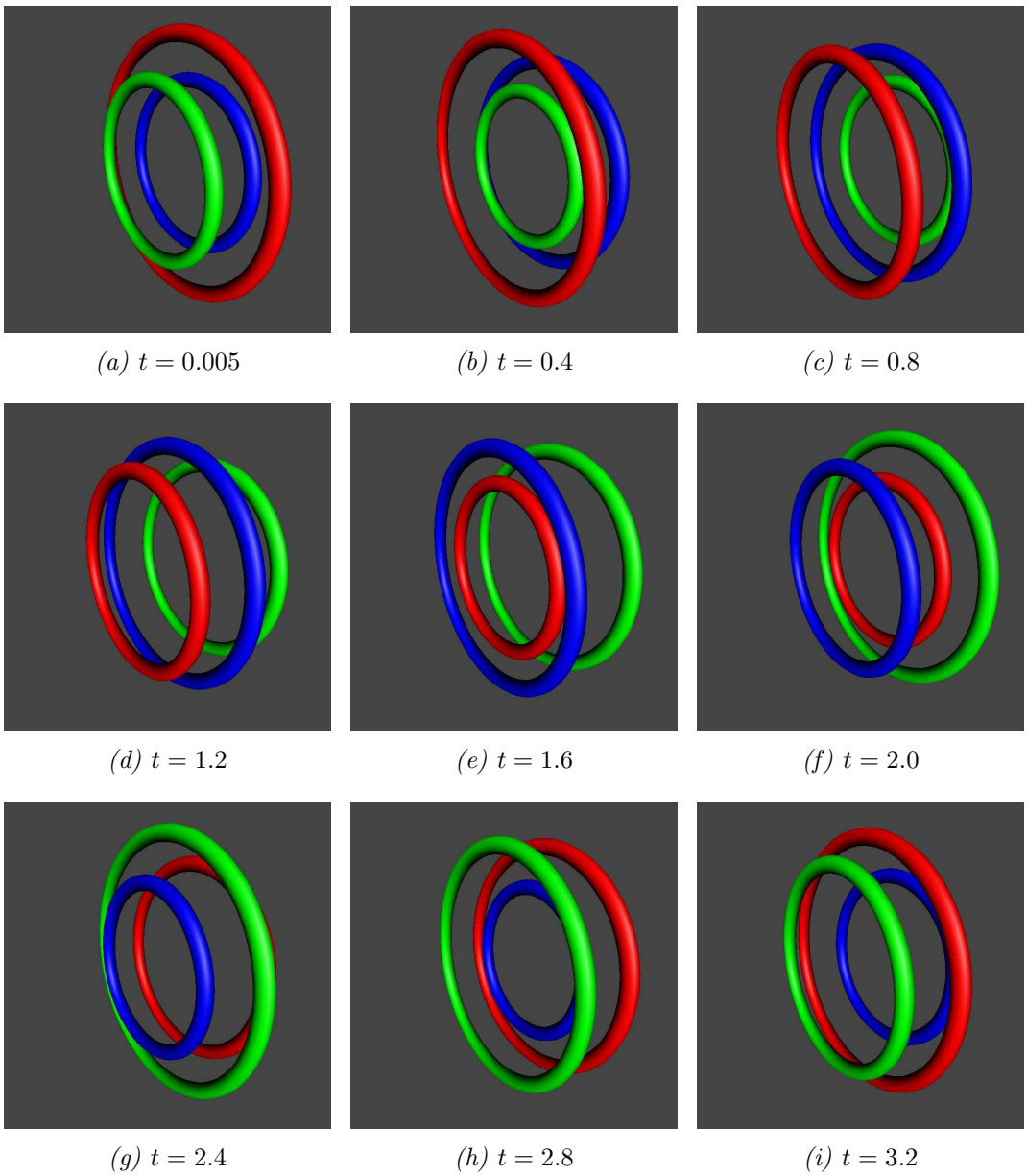

(a) $t = 0.005$ (b) $t = 0.4$ (c) $t = 0.8$

(d) $t = 1.2$ (e) $t = 1.6$ (f) $t = 2.0$

(g) $t = 2.4$ (h) $t = 2.8$ (i) $t = 3.2$

Figure 10.12: 3D Knotplot images of leapfrogging for $N = 3$, corresponding to cross-sectional images in Figure 10.11. The radius of the cylinders, the size of the visualisation box and the orientation of each image is chosen to best exhibit the image's features. Parameters: full BS law, $R = 0.0346$ cm, $a = 0.00866$ cm, $\ell = 0.015$ cm and $R/a = 4$.

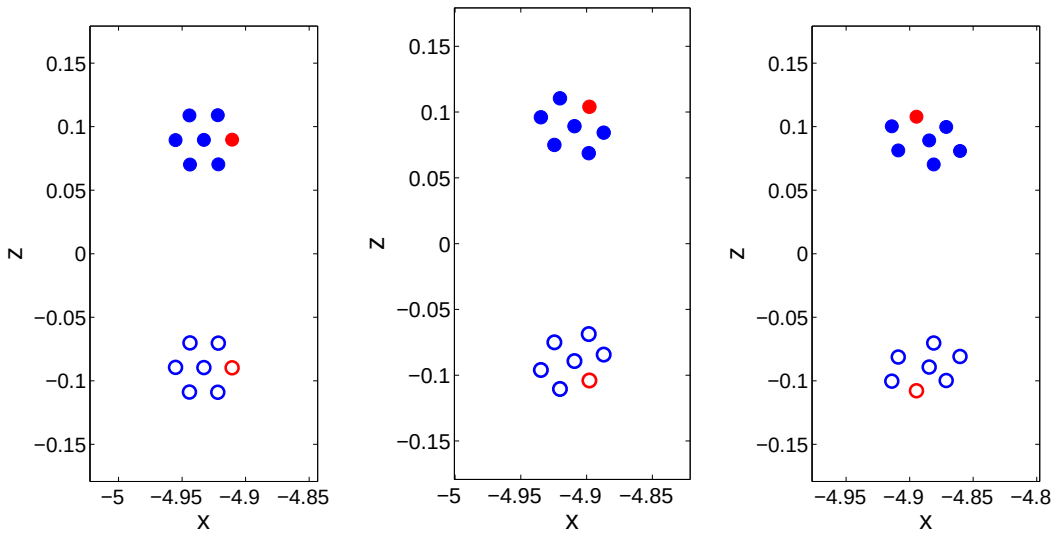

(a) $t = 0.0075$

(b) $t = 0.75$

(c) $t = 1.5$

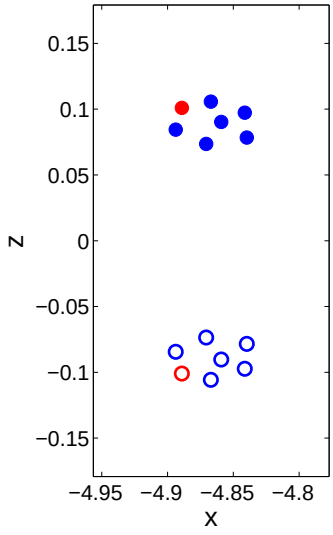

(d) $t = 2.25$

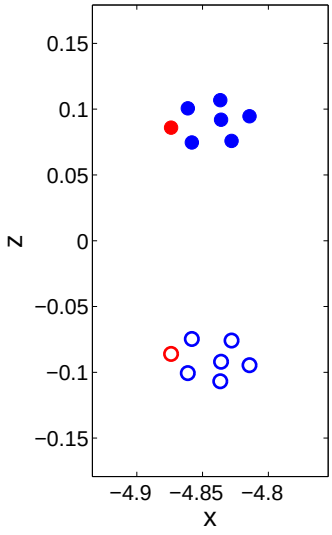

(e) $t = 3$

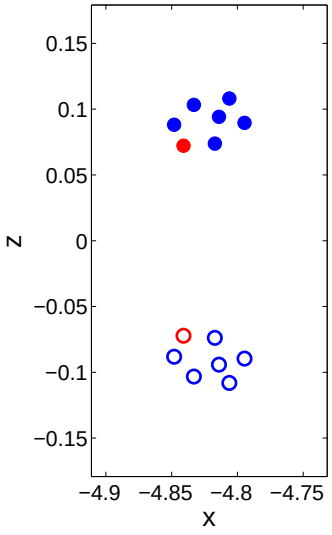

(f) $t = 3.75$

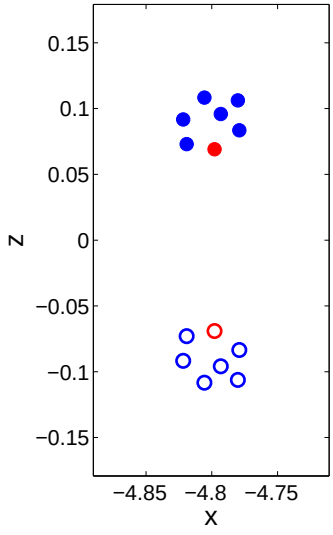

(g) $t = 4.5$

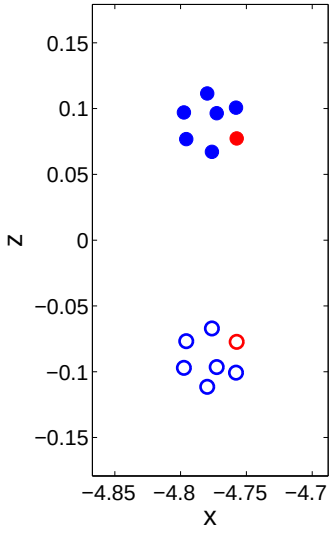

(h) $t = 5.25$

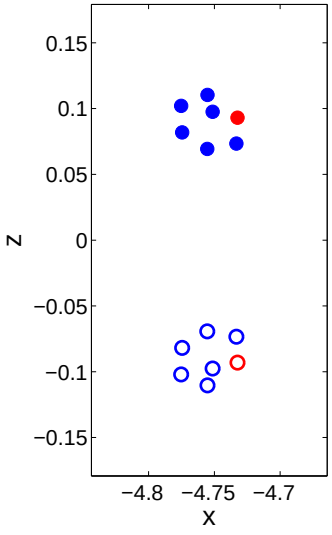

(i) $t = 6$

Figure 10.13: Cross-sectional slices of leapfrogging for $N = 7$. Details on next page.

Figure 10.13 shows 9 images of the cross-section of 7 leapfrogging vortex rings undergoing their first complete leapfrog - in the reference frame moving with the rings each ring moves through 360 degrees. I use one pair of red markers to exhibit this feature. The marker size is arbitrary and does not represent the core size of the individual rings. Solid symbols represent positive circulation (anticlockwise) and hollow symbols negative circulation (clockwise). It is evident from the maximum vertical and horizontal separations that the trajectory is elliptical.

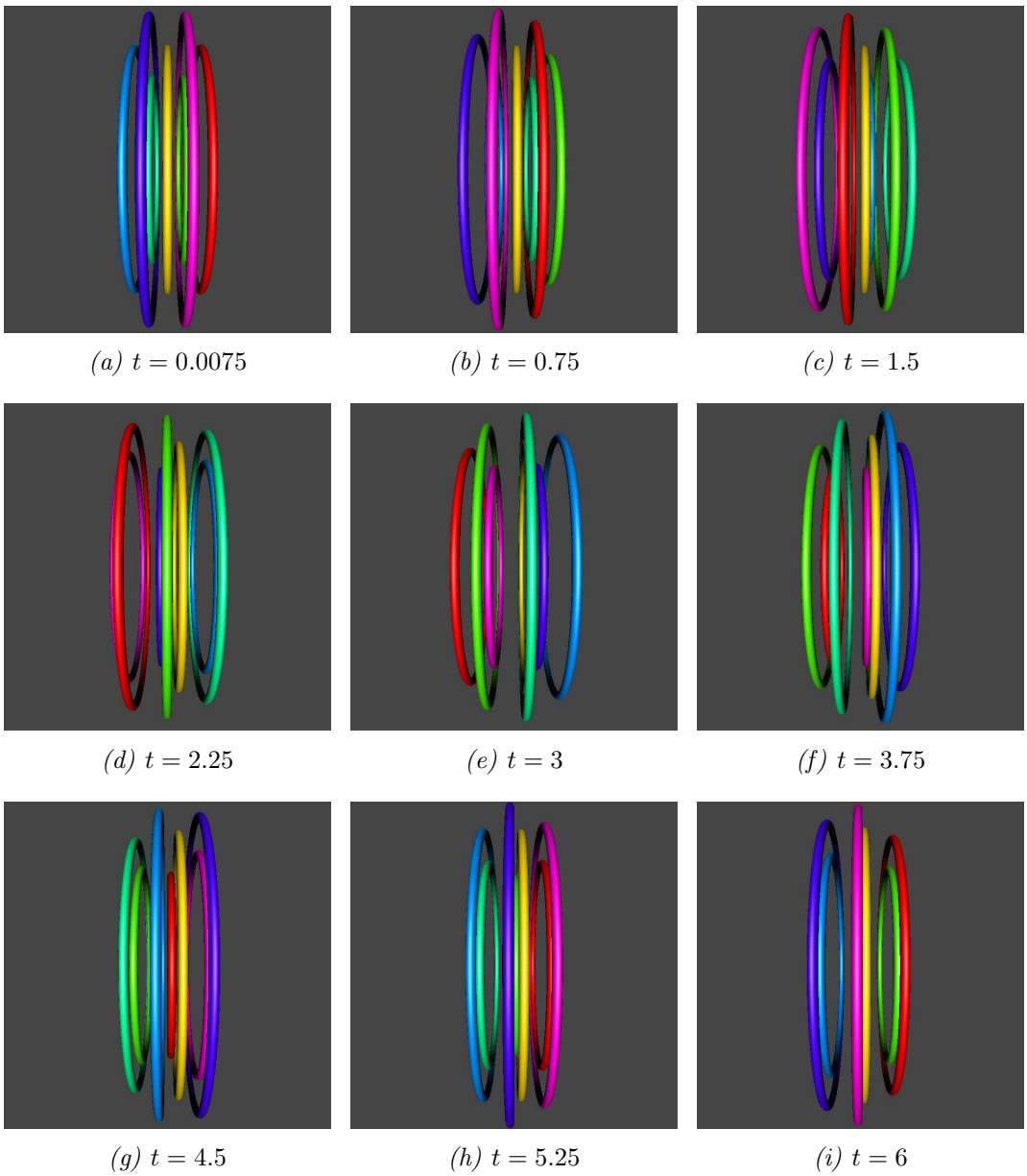

(a) $t = 0.0075$ (b) $t = 0.75$ (c) $t = 1.5$

(d) $t = 2.25$ (e) $t = 3$ (f) $t = 3.75$

(g) $t = 4.5$ (h) $t = 5.25$ (i) $t = 6$

Figure 10.14: 3D Knotplot images of leapfrogging for $N = 7$, corresponding to cross-sectional images in Figure 10.13. The radius of the cylinders, the size of the visualisation box and the orientation of each image is chosen to best exhibit the image's features. Parameters: full BS law, $R = 0.0896$ cm, $a = 0.0223$ cm, $\ell = 0.0223$ cm and $R/a = 4$.

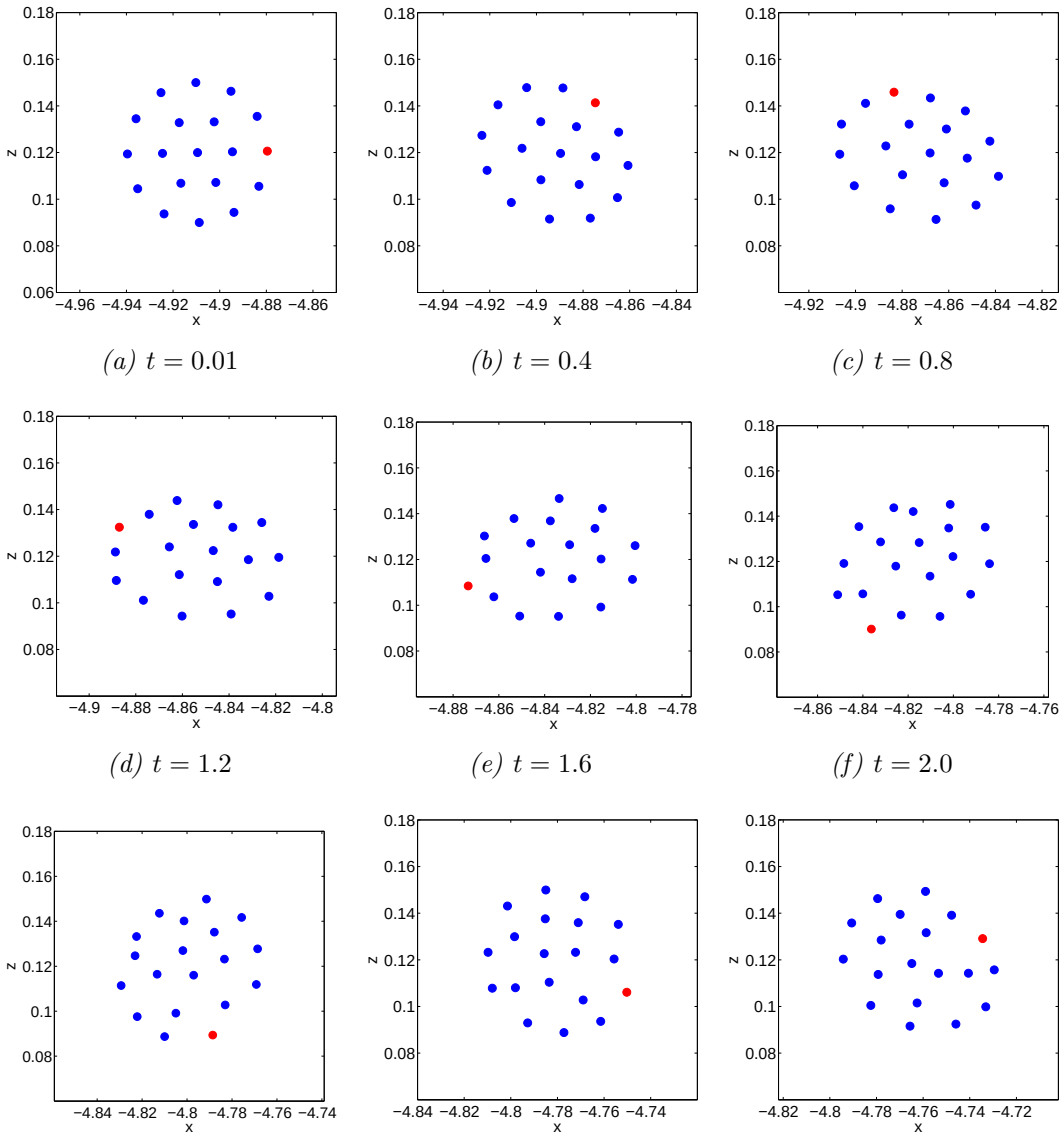

Figure 10.15: Cross-sectional slices of leapfrogging for $N = 19$. 9 images of the cross-section of 19 leapfrogging vortex rings undergoing their first complete leapfrog - in the reference frame moving with the rings each ring moves through 360 degrees. I use a red marker to exhibit this feature. The marker size is arbitrary and does not represent the core size of the individual rings. I show only the 'upper' cross-section in which the circulation is positive (anticlockwise). It is evident from the maximum vertical and horizontal separations that the trajectory is elliptical. Parameters: full BS law, $R = 0.12$ cm, $a = 0.03$ cm, $\ell = 0.015$ cm and $R/a = 4$.

10.8 Existence of critical value for leapfrog parameter

Over 100 years ago A.E.H. Love (Love, 1894) showed analytically that two vortex-antivortex pairs (see Figure 10.16), the 2D analogue of two vortex rings, will only

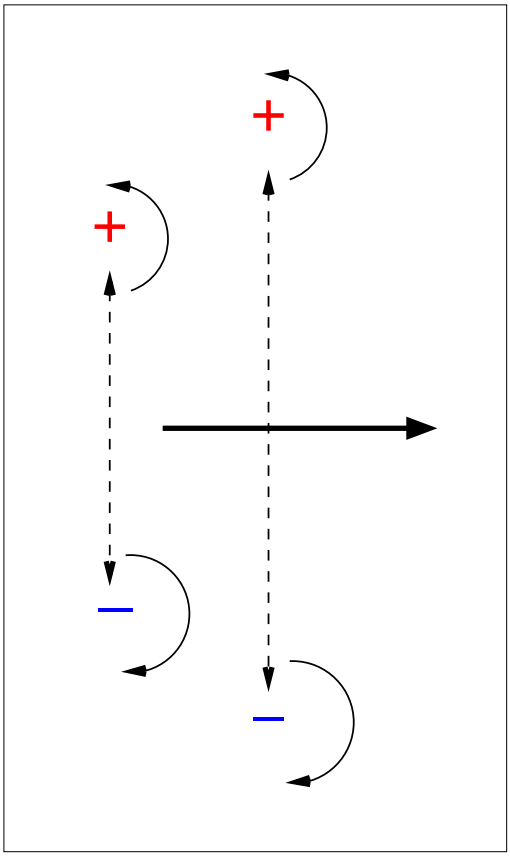

Figure 10.16: Schematic diagram of two vortex-antivortex pairs. Dashed lines show smaller and larger diameters. Solid black lines show directions of motion: translation to the right and rotational motion about each point vortex.

perform the leapfrogging motion if the parameter $\hat{\alpha}$, defined as the ratio of diameter of the smaller pair to the diameter of the larger pair, obeys the condition $\hat{\alpha} > 3 - 2\sqrt{2} \approx 0.172 = \hat{\alpha}_c$. If $\hat{\alpha} < \hat{\alpha}_c$, leapfrogging does not occur. The smaller, faster ring 'escapes' the effect of the larger, slower ring and disappears off to infinity. Acheson (Acheson, 2000) investigated the parameter $\hat{\alpha}$ numerically and extended Love's work by identifying three different regimes. When $\hat{\alpha} < 0.172$ leapfrogging does not occur. When $0.172 < \hat{\alpha} < 0.382$ leapfrogging is possible, but is unstable such that slight perturbations cause the system to develop a different type of behaviour. Acheson proves that these instabilities are not numerical. When $\hat{\alpha} > 0.382$, leapfrogging occurs without instabilities: the system is unaffected by small perturbations. Love and Acheson's work raises the question about whether there exists a critical $\hat{\alpha}$ for a system of two (initially) coplanar, coaxial rings and if so what is its value. Or, more generally, whether there is such a critical value for a system of N vortex rings. How does $\hat{\alpha}_c$ vary as N increases?

Bearing in mind that my calculation is 3D, I would like to identify which values of $\hat{\alpha}$ exhibit leapfrogging and which do not. I can distinguish between these cases by considering the rate of change of R. Leapfrogging only occurs when $\dot{R}$ is non-zero. Values of $\hat{\alpha}$ for which $\dot{R}$ drops to zero do not exhibit the leapfrogging phenomenon.

This is because, when $\dot{R} = 0$, the vortices have moved so far apart that one vortex has no effect on the other. I first translate the parameter $\hat{\alpha}$ into terms of R and a in the following way:

$$\hat{\alpha} = \frac{R-a}{R+a} = 1 - \frac{2a}{R+a}. \tag{10.4}$$

I investigate this parameter for two vortex rings using the $\dot{R} = 0$ criterion. I do this in two ways: (1) I fix R and allow a to vary, and (2) I fix a and allow R to vary. Using this criterion I calculate the range in which $(R/a)_c$, and hence $\hat{\alpha}_c$, must lie. Both methods give the same range: $3.5 < (R/a)_c < 3.75$ or, equivalently, $0.556 < \hat{\alpha}_c < 0.579$, as opposed to $\hat{\alpha}_c = 0.172$ in the point vortex case. Note also that I use a minimum $R/a = 4$ in my numerical simulations. With regard to Borner's experiment, recall (see Section 7.6) that the interpretation of Borner's results depends on his definition of D, the diameter of the macroscopic ring. If $D = 2R$, then $3.64 < R/a < 4.18$ which should sustain a leapfrogging motion, but if $D = 2R + 2a$, then $2.64 < R/a < 3.18$ which is subcritical for 2 vortex rings. Figure 10.17 shows the main result of this investigation. The red and green lines belong to the series of runs in which $a = 0.0075$ cm was kept fixed. The red line shows the values of $\dot{R}$ for $R/a = 3.5$ and the green line for $R/a = 3.75$. On the other hand, the blue and the black lines belong to the series of runs in which $R = 0.03$ cm was kept fixed. The blue line shows the values of $\dot{R}$ for $R/a = 3.5$ and the black line for $R/a = 3.75$. $\dot{R}$ drops to zero in both cases of $R/a = 3.5$ (red and blue), whereas in both cases of $R/a = 3.75$ (green and black) it jumps from negative to positive values at one point, indicating that the rings have started growing. Hence, the critical value of R/a lies between 3.5 and 3.75. Full BS Law was used, $\Delta t = 5 \cdot 10^{-5}$ seconds and $\Delta\xi = 0.00149$ cm.

In the case of three rings preliminary results show that the macroscopic ring formation collapses for $R/a = 2$ and exhibits instabilities when $R/a \geq 3$. I conclude that there is evidence for a critical value for leapfrogging of 3D vortex rings and that the critical value seems to differ for different values of N. A more rigorous study is necessary to clarify these questions, but issues of stability will be touched on in Chapter 11.

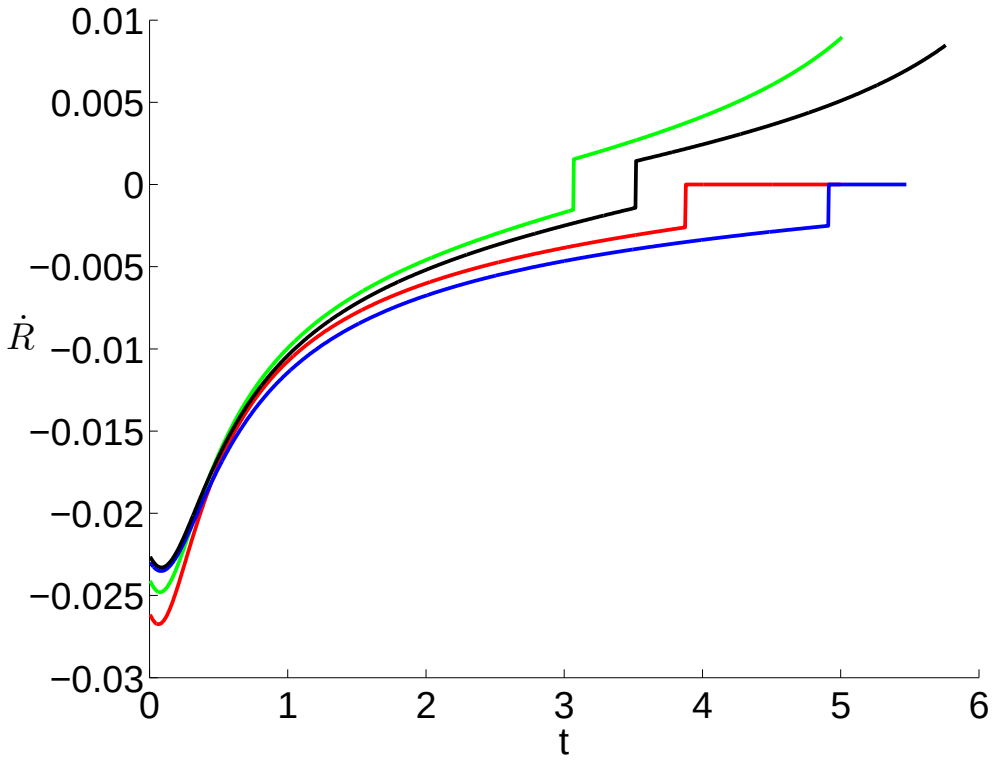

Figure 10.17: $\dot{R}$ (cms^{-1}) vs t (s). Leapfrogging fails to occur if $\dot{R}$ drops to zero. Red and blue lines represent cases in which $R/a = 3.5$ and green and black lines cases in which $R/a = 3.75$. Red and blue fail to leapfrog, the sudden jump in their curves indicating the point at which the 2 rings have moved so far apart that they no longer influence one another. Green and black successfully leapfrog, the sudden jumps in the curves indicating the switchover from shrinking to growth.

10.9 Trajectories of individual vortices

In the Section on leapfrogging (Section 10.7) I followed the motion of individual vortices as they underwent a leapfrog event by considering a planar cross-section through the macroscopic vortex ring. I now define the trajectory of an individual vortex as the path taken by the vortex in the plane containing the vortex's cross-section and in the reference frame of the centre of vorticity. In other words, I track the motion of individual vortices whilst following the centre of vorticity.

I plot the trajectories as the vortex rings cut the x-z plane. I show only the cross-section in which the circulation is positive (anticlockwise). The trajectory in the other cross-section is the mirror image of the one plotted. I mark the steps of the trajectories with blue dots and draw a red circle to illustrate how close to (or far away from) a circular route is the path described by the vortex. As mentioned above, I plot the trajectories following the reference frame of the centre of vorticity. However, since the centre of vorticity is subject to a certain amount of numerical noise and does not move smoothly, the trajectories that follow this frame of reference are subject to the same lack of smoothness. This is more noticeable in plots in which the vortex moves slowly around its trajectory, such as when ℓ is large. I plot one complete trajectory for one vortex in each case (Figures 10.18(a,c,) and 10.19(a,c)). In these plots for $N = 2$ and $N = 3$ the trajectory starts at the top of the circles and for $N = 7$ and $N = 19$ it starts at the right of the circles. I also plot a few points at the beginning of the trajectory of each vortex to show how all of the vortices start their paths (Figures 10.18(b,d) and 10.19(b,d)). The parameters for these runs are recorded in Table 10.7. I also show the approximate time taken for the vortex to return to complete its first 360 degree leapfrog. Further examples of τ_{LF} can be found in Table 11.1.

Not all vortices return exactly to their starting positions. This is particularly noticeable for $N = 3$ for lower values of $R/a \approx 4$, although for higher values of $R/a = 10$, which describe a more circular orbit, the vortices do return to their starting positions. Even for $R/a \approx 4$ the trajectory is not irregular, but seems to precess slightly. It is not clear why this occurs, nor why $N = 3$ is most susceptible to it. The stability of the leapfrogging motion in Figures 10.18 and 10.19 depends on the relative stability of the system. In Figure 10.20, subplot (a) shows the extremely regular leapfrogging motion of a vortex in an $N = 2$ system. The motion is so regular that subsequent trajectories are indistinguishable one from another. This is not the case for the $N = 19$ system shown in subplots (b-d), in which vortices are seen spiralling both inwards and outwards. Once again is is not clear why this occurs. It may be due to chaos or because particle paths differ from streamlines in time-dependent flows.

N	R (cm)	ℓ (cm)	a (cm)	R/a	$\Delta\xi$ (cm)	$\ell/(\Delta\xi)$	Δt (s)	τ_{LF} (s)
2	0.03	0.015	0.0075	4	0.0005	30	6.25×10^{-6}	9.4
3	0.03464	0.015	0.00896	3.87	0.00149	10	5×10^{-5}	3.15
7	0.0896	0.0223	0.0223	4	0.00149	15	5×10^{-5}	5.86
19	0.12	0.015	0.03	4	0.00149	10	5×10^{-5}	3.0 (outer) 2.3 (inner)

Table 10.7: Parameters used to produce trajectories in Figures 10.18 and 10.19.

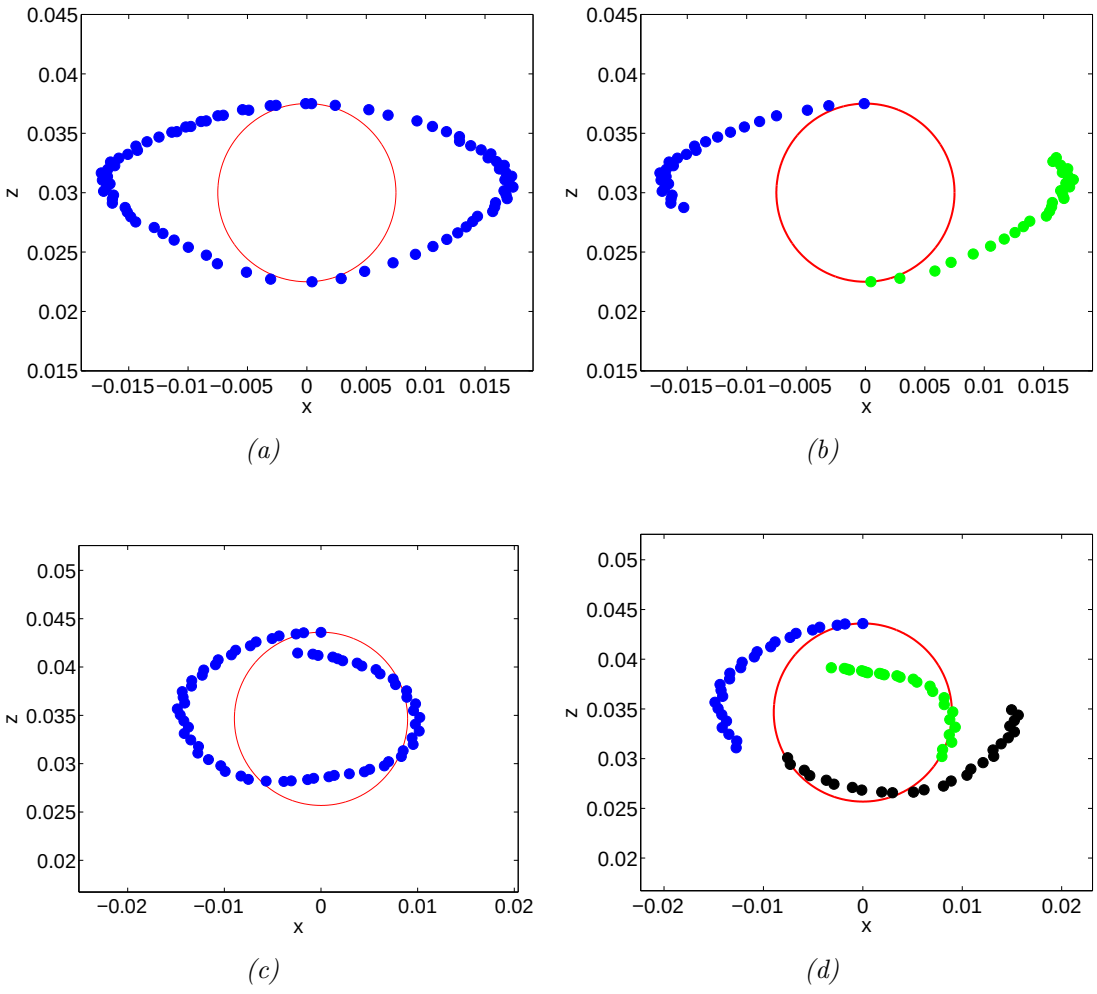

Figure 10.18: Trajectories of individual vortices in x-z plane in reference frame of centre of vorticity for (a) $N = 2$ and (c) $N = 3$, and for all vortices for (b) $N = 2$ and (d) $N = 3$. Red circles are for illustrative purposes only.

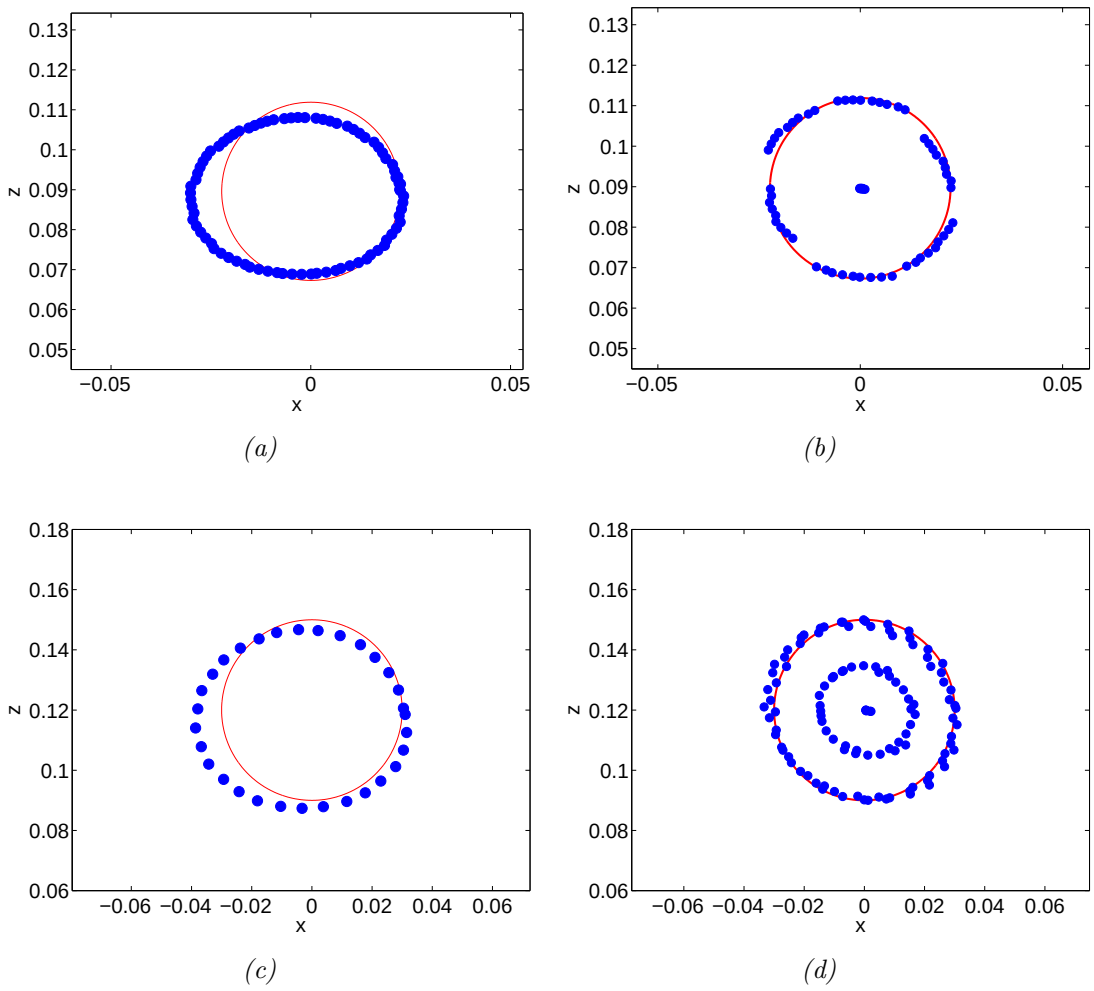

Figure 10.19: Trajectories of individual vortices in x-z plane in reference frame of centre of vorticity for (a) $N = 7$ and (c) $N = 19$, and for all vortices for (b) $N = 7$ and (d) $N = 19$. Red circles are for illustrative purposes only.

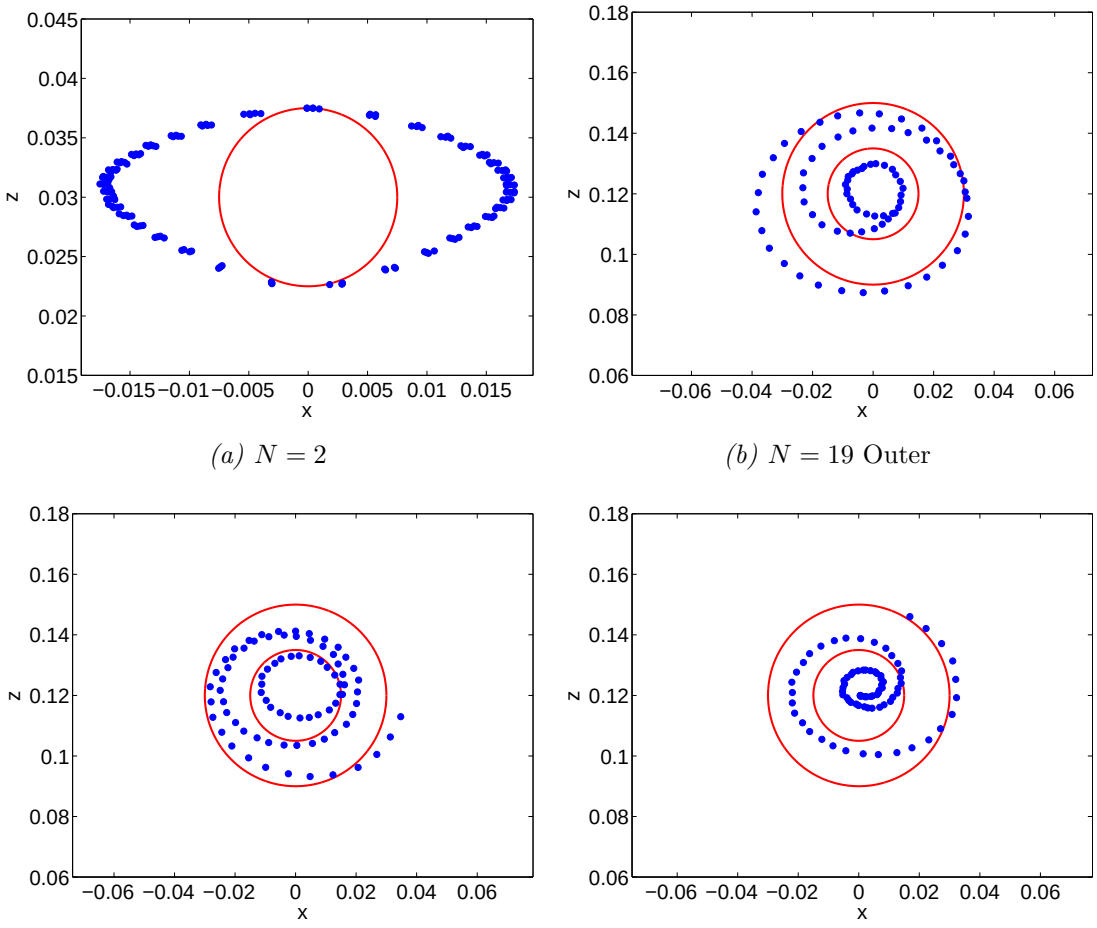

(a) $N = 2$ *(b)* $N = 19$ Outer

(c) $N = 19$ Middle *(d)* $N = 19$ Inner

Figure 10.20: Trajectories of individual vortices in x-z plane in reference frame of centre of vorticity over a period of 32 seconds for $N = 2$ and 8 seconds for $N = 19$. (a) Vortex starts at top of red circle, completes several circuits in anticlockwise direction, exhibits continued regular motion. (b) Vortex from outer layer, starts on RHS of outer circle, spirals anticlockwise inwards. (c) Vortex from middle layer, starts on RHS of inner circle, spirals anticlockwise outwards. (d) Central vortex, spirals anticlockwise outwards. Red circles are for illustrative purposes only.

10.10 Summary

In this Chapter I used the full BS law to evolve systems of rings in which $N \leq 19$. I showed the effects of finite temperature and the necessity of including a normal fluid velocity field. I also showed that the imposed field was extremely effective in prolonging the life of the macroscopic ring at finite temperatures. All systems of rings successfully travelled at least $10D$ both at T0 and at T2, in agreement with the results reported by the superfluid vortex ring experiments. I also showed that in all cases energy was conserved to within less than 1% before the onset of reconnections, but as expected it is not conserved thereafter. Leapfrogging is known to occur for two coaxial rings ($N = 2$). I showed that a generalised form of leapfrogging occurs

for $N \geq 2$ and, in analogy to Acheson's (Acheson, 2000) analysis of 2D point vortex leapfrogging, I discussed the existence of a parameter which controls leapfrogging and its critical value. I investigated the trajectories of the individual vortices in the reference frame of the centre of vorticity and showed that the shape of the trajectory varied from case to case (a fuller discussion of this is included in Chapter 11). I also showed that in some cases the trajectories were stable and repeated themselves and that in others they quickly became unstable such that the paths of individual vortices moved either inwards towards the centre of the cross section of the macroscopic vortex core or outwards away from the centre.

Chapter 11

The effects of changing the values of ℓ and R/a

11.1 Introduction

I have touched briefly (Section 10.8) on the existence of a critical value of R/a which either allows or disallows a leapfrogging motion and which controls the stability of that motion. In fact, the stability and regularity of such a complex procedure as leapfrogging can be taken as a sign of stability for the system as a whole, as will become apparent in this Chapter. I now investigate the effect on the system of changing the parameters ℓ and R/a. Recall that for centred hexagonal configurations of vortices $a = (n-1)\ell$ (also when $N = 2$, I set $a = \ell/2$ and when $N = 3$, I set $a = \ell/\sqrt{3}$). The computer code calls for inputs for R and a. In order to study R/a independently of ℓ one must fix a (and hence ℓ) and allow R to vary such that R/a takes on a suitable range of values. Conversely, in order to study ℓ independently of R/a one must fix a value for R/a and vary the inputs for both R and a (which means that ℓ also varies) such that R/a remains constant throughout. This means however that one cannot easily investigate whether a change in the velocity of the macroscopic ring is due to a change in ℓ or a change in R/a. This is because velocity depends on R. One can only compare the velocity of systems which have a common value of R, as I did, for example, to investigate the effect of temperature on the velocity. In order to investigate either ℓ or R/a, one must vary R, in which case the systems are no longer readily comparable.

Questions which must be considered include: Is the system more or less stable for larger or smaller values of ℓ or R/a? Does the macroscopic vortex ring travel faster or slower? Do the individual rings leapfrog more or less frequently (i.e. is τ_{LF} larger or smaller)? What shape do the trajectories taken by the individual vortices adopt for different values of ℓ or R/a? One can ask similar questions about the effect of ℓ on systems at finite temperature, with or without a normal fluid velocity field.

11.2 Velocity of macroscopic ring as ℓ and R/a vary

I have shown (Section 7.4) how the intervortex spacing, ℓ, can be deduced from Borner's experimental data and that several possible values of ℓ can be calculated giving a range of values such that $0.0033 \leq \ell \leq 0.0046$ cm. In general typical values of ℓ lie between 10^{-2} cm and 10^{-4} cm. I now consider the effect of varying the value of ℓ (and R/a) over several values (see Table 11.1) which cover a broad range of the possible values. I do so at $T = 0$ K using the full BS law for $N = 2$, 3 and 7 rings. For $N = 2$ rings I also investigate different two levels of discretisation along the rings ($\Delta\xi = 0.0005$ cm and $\Delta\xi = 0.00149$ cm) and two sizes of macroscopic ring ($R = 0.03$ cm and $R = 0.0896$ cm). Due to the interdependence of the parameters ℓ and R/a, my investigation of ℓ also involves changes in the value of R/a. I record all relevant parameters in Table 11.1. I then plot (Figures 11.1(a)-(e)) the distance travelled in each case over time. This allows me to compare the relative velocities for the different values of ℓ and R/a. In these images I show only the first 25 seconds of the translatory motion, which is sufficient time to identify which values of ℓ and R/a lead to faster rings. From these images it is clear that the smaller the value of ℓ and the larger the value of R/a the faster the macroscopic ring travels, irrespective of the value of N, the size of the rings R and the size of $\Delta\xi$.

Case	R (cm)	ℓ (cm)	a (cm)	R/a	$\Delta\xi$ (cm)	$\ell/(\Delta\xi)$	Δt (s)	τ_{LF} (s)
2a	0.03	0.015	0.0075	4	0.0005	30	6.25×10^{-6}	9.4
2b	0.03	0.010	0.0050	6	0.0005	20	6.25×10^{-6}	2.4
2c	0.03	0.005	0.0025	12	0.0005	10	6.25×10^{-6}	0.5
2d	0.03	0.015	0.0075	4	0.00149	10	5×10^{-5}	9.4
2e	0.03	0.010	0.0050	6	0.00149	6.66	5×10^{-5}	2.4
2f	0.03	0.005	0.0025	12	0.00149	3.33	5×10^{-5}	0.5
2g	0.0896	0.015	0.0075	11.95	0.00149	10	5×10^{-5}	4.5
2h	0.0896	0.010	0.0050	17.92	0.00149	6.66	5×10^{-5}	2.0
2i	0.0896	0.005	0.0025	35.84	0.00149	3.33	5×10^{-5}	0.5
3a	0.03464	0.015	0.00896	3.87	0.00149	10	5×10^{-5}	3.15
3b	0.03464	0.010	0.00577	6.00	0.00149	6.66	5×10^{-5}	1.25
3c	0.03464	0.005	0.00289	11.99	0.00149	3.33	5×10^{-5}	0.3
7a	0.0896	0.0223	0.0223	4	0.00149	15	5×10^{-5}	5.86
7b	0.0896	0.0149	0.0050	17.92	0.00149	10	5×10^{-5}	2.60
7c	0.0896	0.0075	0.0025	35.84	0.00149	5	5×10^{-5}	0.64
7d	0.06	0.015	0.015	4	0.00149	10	5×10^{-5}	2.55
7e	0.012	0.003	0.003	4	0.0003	10	2.5×10^{-6}	0.1

Table 11.1: Table of cases to compare different values of ℓ for similar numbers of vortex rings. $N = 2$: (2a-2c): $\ell \geq 10\Delta\xi$ for all three values of ℓ, but with reduced Δt such that $\Delta t = 0.625 \times 10^{-5}$ seconds in order to maintain stability (see Figure 11.1(a)). (2d-2f): Same as (2a-2c), but relax condition between ℓ and $\Delta\xi$ (Note that smallest length scale is actually $\Delta\xi/2$, so ℓ is 6.66 times that length scale) (see Figure 11.1(b)). (2g-2i): Same as (2d-2f), but with much larger R, so investigating much larger R/a (see Figure 11.1(c)). (3a-3c) $N = 3$ (see Figure 11.1(d)). (7a-7e) $N = 7$ (see Figure 11.1(e) for (7a-7c)).

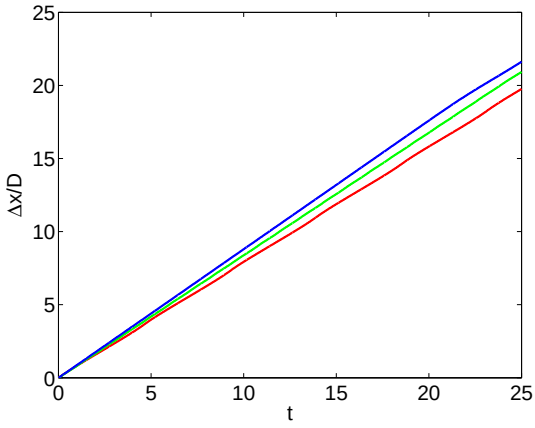

(a) Cases 2a-2c

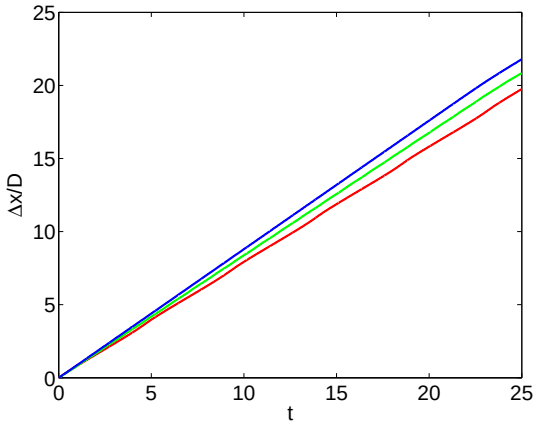

(b) Cases 2d-2f

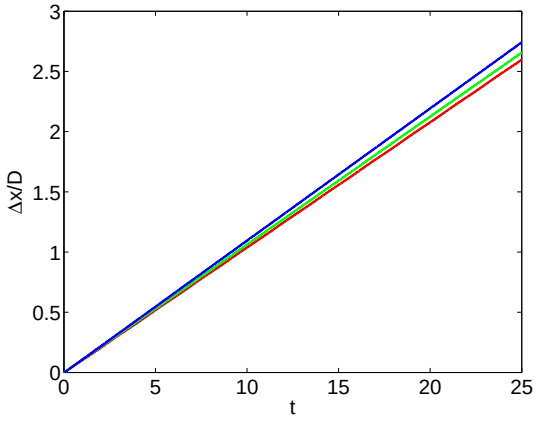

(c) Cases 2g-2i

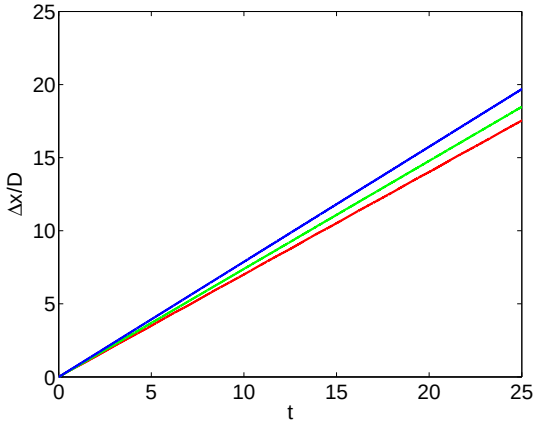

(d) Cases 3a-3c

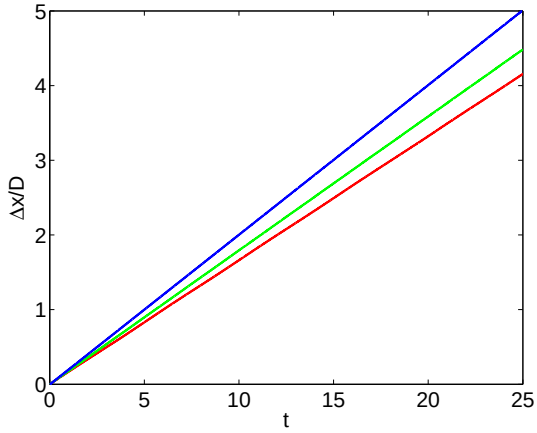

(e) Cases 7a-7c

Figure 11.1: Distance travelled by centre of vorticity $\Delta x/D$ vs t (s) for $\ell = 0.005$ cm (blue), 0.010 cm (green) and either 0.015 or 0.0223 cm (red) (see Table 11.1). Subplots: (a) $N = 2$, $R = 0.03$ cm and $\Delta\xi = 0.0005$ cm, (b) $N = 2$, $R = 0.03$ cm and $\Delta\xi = 0.00149$ cm ,(c) $N = 2$, $R = 0.0896$ cm and $\Delta\xi = 0.00149$ cm, (d) $N = 3$, $R = 0.03464$ cm and $\Delta\xi = 0.00149$ cm and (e) $N = 7$, $R = 0.0896$ cm and $\Delta\xi = 0.00149$ cm. For other parameters see Table 11.1. It is clear that the smaller the value of ℓ the faster the macroscopic ring travels, irrespective of the value of N, the size of the rings R and the size of $\Delta\xi$

11.3 Period of leapfrog, τ_{LF}, as ℓ and R/a vary

In the next series of plots (Figures 11.2 and 11.3) I plot 2 physical parameters of the macroscopic vortex ring. The first parameter is δx, where δx is the distance between the front and the back of the ring, the thickness of the ring in the x direction. The second parameter is $\ell(t)/\ell_0$, the instantaneous intervortex spacing normalised by the initial intervortex spacing. If a macroscopic ring retains the initial configuration of its cross-section, these parameters will be steady over time. On the other hand, if the cross-section of the macroscopic ring changes shape and the individual rings rearrange themselves, then these parameters will also change. Several points are immediately observable from these plots.

Firstly, the periodicity or quasi-periodicity of the values of δx is related to the period of the leapfrog, τ_{LF}, especially in the case $N = 2$ for which every second minimum indicates the completion of one entire 360 degree leapfrog. It is clear from these figures that the τ_{LF} is significantly shorter for smaller initial ℓ and larger R/a. Compare, for example, cases (2a), (2b) and (2c): the longest leapfrog period is associated with the largest intervortex spacing and smallest R/a (red), the medium leapfrog period with the medium intervortex spacing and medium R/a (green) and the shortest leapfrog period with the smallest intervortex spacing and largest R/a (blue). But which parameter causes this phenomenon? Is it the intervortex spacing alone, the ratio R/a alone or a combination of both? One is tempted to attribute this feature to the intervortex spacing, based on the behaviour of a 2D vortex-vortex pair, which rotate around each other with a shorter period the smaller the distance between them. On the one hand, if I compare cases (2c) and (2g), I find that in both cases $R/a = 12$ (approximately), but in (2c) $\ell = 0.005$ cm and in (2g) $\ell = 0.015$ cm. The period of (2c) is a small fraction of the period of (2g). On the other hand, changes in R/a also seem to effect the leapfrog period. Consider, for example, the cases (2a) and (2g). In both cases $\ell = 0.015$ cm, but in (2a) $R/a = 4$ and in (2g) $R/a \approx 12$. The period in (2a) looks about twice as long as in (2g). I conclude that both ℓ and R/a noticeably effect the period of the leapfrog.

Secondly, there is significantly more variance over time in the magnitude of both δx and $\ell(t)/\ell_0$ for larger initial values of ℓ and smaller initial values of R/a. One can see this from the amplitude of the different coloured curves: red > green > blue. Macroscopic vortex rings in which the individual vortex rings are initially close together tend to stay close together. This is not just because, the rings, being closer together, have a smaller distance to travel in order to circumvent (leapfrog) the other rings, but also because the paths taken by the individual rings are more circular for smaller ℓ or larger R/a, whereas for larger ℓ they are more elliptical. I will now show that this feature is due to large R/a, not to small ℓ.

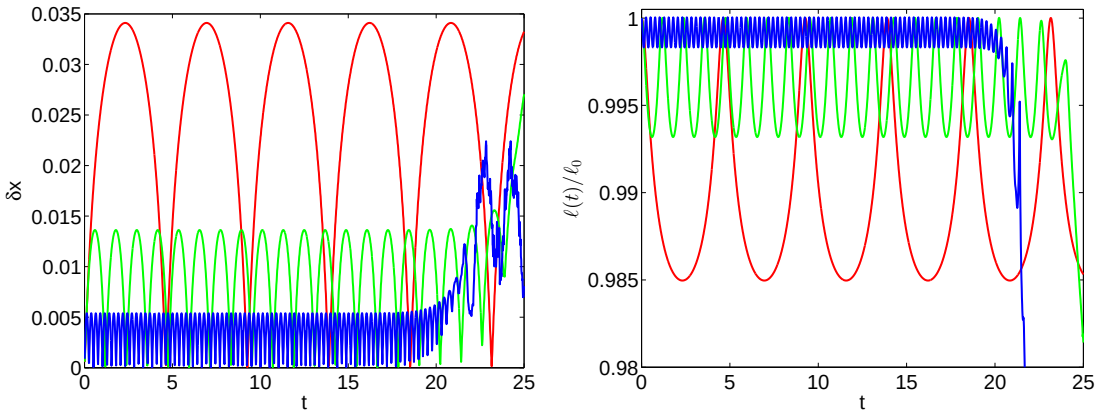

(a) Cases 2a-2c *(b)* Cases 2a-2c

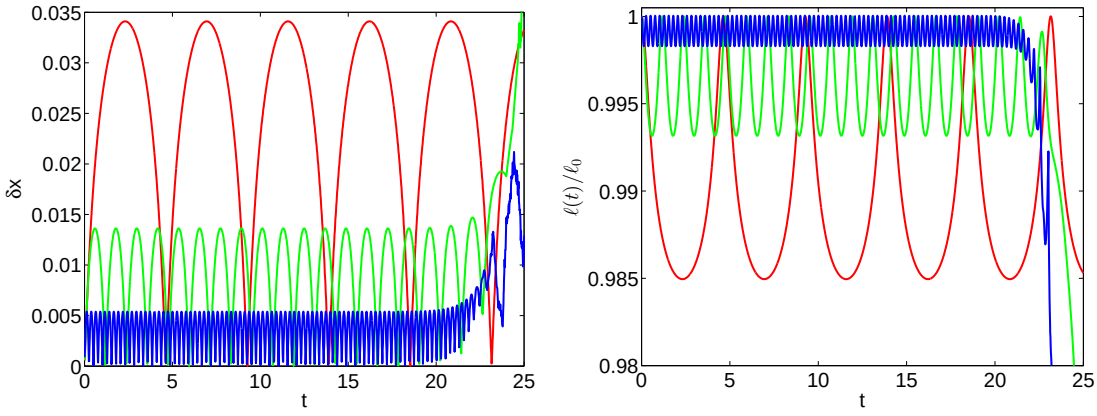

(c) Cases 2d-2f *(d)* Cases 2d-2f

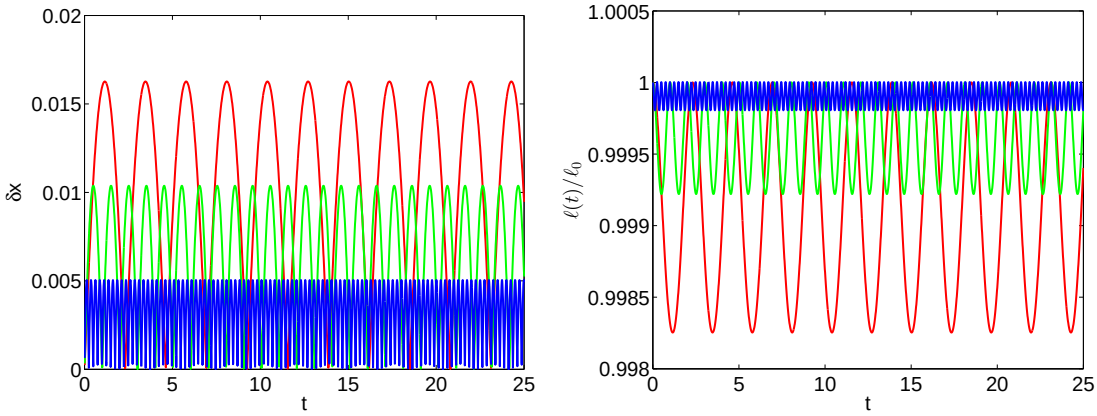

(e) Cases 2g-2i *(f)* Cases 2g-2i

Figure 11.2: Thickness of macroscopic vortex ring in x direction δx (left) and normalised intervortex spacing $\ell(t)/\ell_0$ (right) vs t (s) for $N = 2$ for $\ell = 0.005$ cm (blue), 0.010 cm (green) and either 0.015 or 0.0223 cm (red) (see Table 11.1). Subplots: (a-b) $N = 2$, $R = 0.03$ cm and $\Delta\xi = 0.0005$ cm, (c-d) $N = 2$, $R = 0.03$ cm and $\Delta\xi = 0.00149$ cm ,(e-f) $N = 2$, $R = 0.0896$ cm and $\Delta\xi = 0.00149$ cm. For other parameters see Table 11.1. It is clear that both δx and ℓ vary significantly less for smaller initial values of ℓ, irrespective of the value of N, the size of the rings R and the size of $\Delta\xi$.

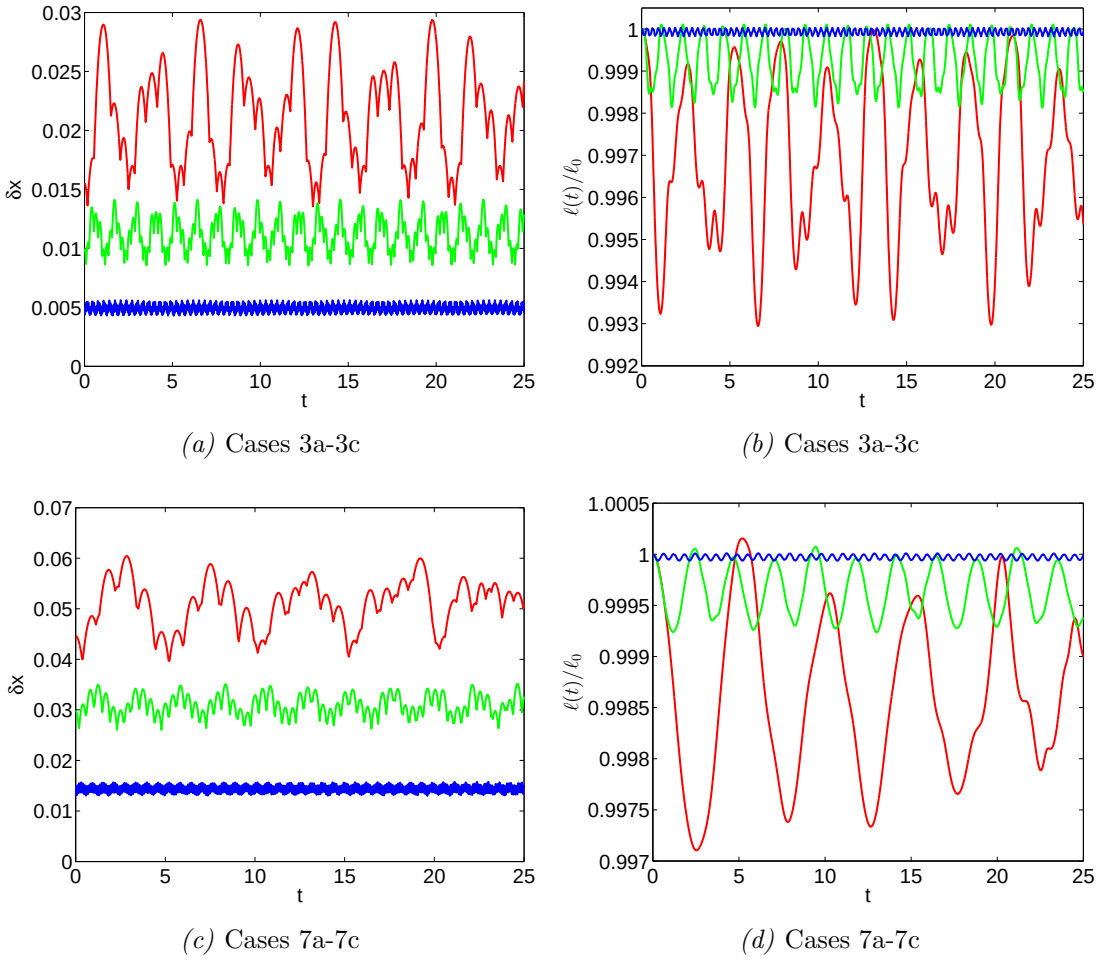

(a) Cases 3a-3c

(b) Cases 3a-3c

(c) Cases 7a-7c

(d) Cases 7a-7c

Figure 11.3: Thickness of macroscopic vortex ring in x direction δx (left) and normalised intervortex spacing $\ell(t)/\ell_0$ (right) vs t (s) for $N = 3$ and $N = 7$ for $\ell = 0.005$ cm (blue), 0.010 cm (green) and either 0.015 or 0.0223 cm (red) (see Table 11.1). Subplots: (a-b) $N = 3$, $R = 0.03464$ cm and $\Delta\xi = 0.00149$ cm, (c-d) $N = 7$, $R = 0.0896$ cm and $\Delta\xi = 0.00149$ cm. For other parameters see Table 11.1. It is clear that both δx and ℓ vary significantly less for smaller initial values of ℓ, irrespective of the value of N, the size of the rings R and the size of $\Delta\xi$.

11.4 Shape of trajectory as ℓ and R/a vary

In Section 10.9 I introduced the concept of following the trajectories of individual vortices in the reference frame of the centre of vorticity. I showed the trajectories of individual vortices in several different systems (Figures 10.18 to 10.20), consisting of $N = 2$, 3, 7 and 19 vortices. The trajectories varied considerably in the different systems. Once again I attempt to identify the reason for the different paths of the trajectories. In figure 11.4 I compare 3 pairs of cases (subplots a-b, c-d and e-f). Each pair of cases share the same value of ℓ, but have different values of R/a. Subplots 11.4(a-b) offer the clearest indication that the shape of the trajectory does depend on the value of R/a. For $R/a = 4$ the trajectory is elliptical, for $R/a = 6$ it is more circular and for $R/a > 12$ it is circular. The reason why there are more points plotted in the trajectories in subplots 11.4(c-d) than in subplots 11.4(e-f) and even more in subplots 11.4(a-b) is that when the vortices are closer together the rings leapfrog faster around each other, so there are less timesteps needed to make a complete circuit. I now consider the trajectories of cases (7a,d,e) in which $R/a = 4$, but ℓ is allowed to vary. Figure 11.5 shows that in all three cases the trajectories are similar, being somewhat elliptical. This shows that the value of ℓ is not responsible for the shape of the trajectory. One can appreciate the truth of this from the 2D analogy of point vortices. Members of a vortex-vortex pair will always describe a circular trajectory regardless of their proximity to each other. It is the relative effect of other point vortices which will alter the shape of the trajectory of the vortex-vortex pair. A measure of that effect is the ratio of the distance between the members of the vortex-vortex pair and their distance from other point vortices, in other words a ratio similar to R/a.

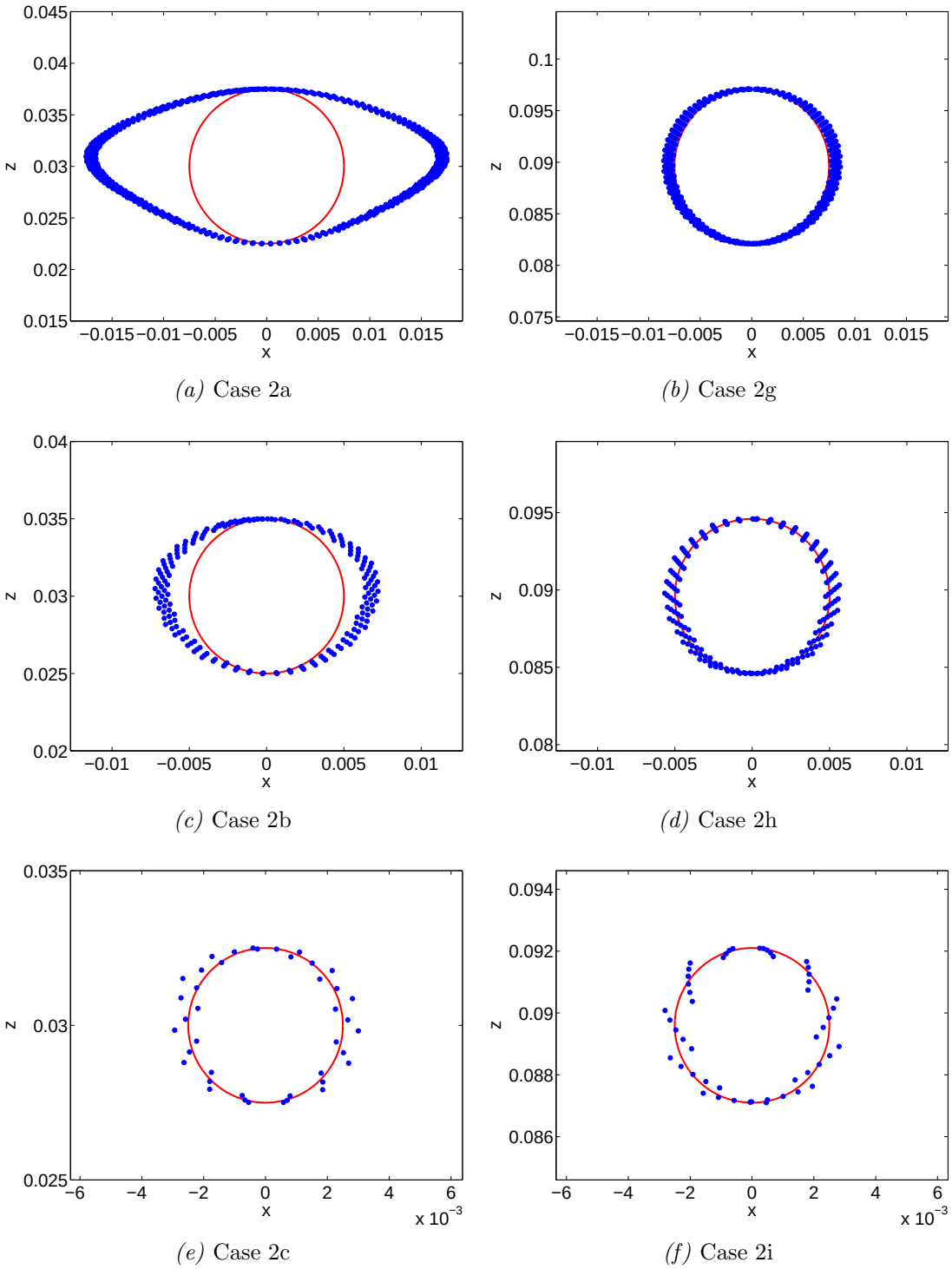

(a) Case 2a

(b) Case 2g

(c) Case 2b

(d) Case 2h

(e) Case 2c

(f) Case 2i

Figure 11.4: Trajectories in x-z plane for 3 pairs of cases with same ℓ: (a-b) $\ell = 0.015$ cm, but case 2a (left) $R/a = 4$ and case 2g (right) $R/a \approx 12$, (c-d) $\ell = 0.010$ cm, but case 2b (left) $R/a = 6$ and case 2h (right) $R/a \approx 18$, and (e-f) $\ell = 0.005$ cm, but case 2c (left) $R/a = 12$ and case 2i (right) $R/a \approx 36$. Trajectories are marked with blue dots and start from top of the red circle and move anticlockwise. Red circles are for illustrative purposes only. Shape of trajectories change for different values of R/a.

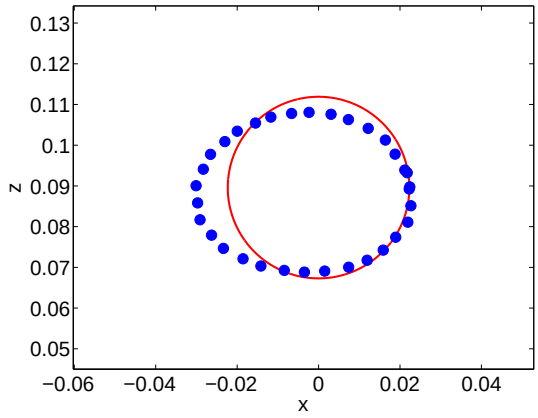

(a) Case 7a

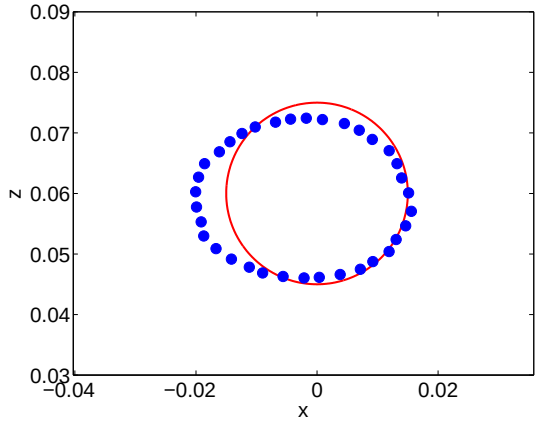

(b) Case 7d

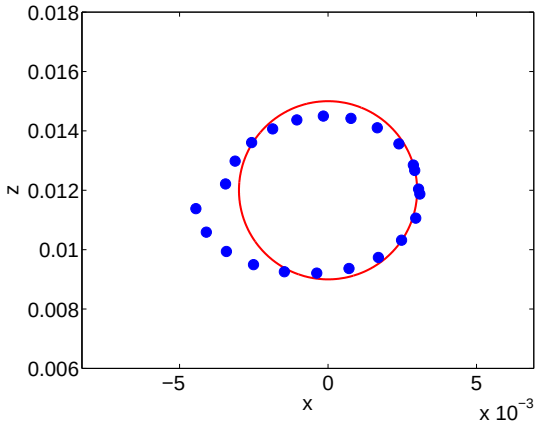

(c) Case 7e

Figure 11.5: Trajectories in x-z plane for 3 pairs of cases with same R/a: (a) $R/a = 4$ and $\ell = 0.0223$ cm, (b) $R/a = 4$ and $\ell = 0.015$ cm, and (c) $R/a = 4$ and $\ell = 0.003$ cm. Trajectories are marked with blue dots and start from right of red circle and move anticlockwise. Red circles are for illustrative purposes only. Shape of trajectories does not change for different values of ℓ. The reason for the 'jump' on the left-hand-side of subplot(c) is unknown.

11.5 Stability of macroscopic vortex ring as ℓ and R/a vary

I now consider the issue of stability. I define a stable macroscopic vortex ring as one that translates a considerable distance, such as $10D$, whilst maintaining a coherent torus-like structure in which the individual vortex lines are aligned in the plane perpendicular to the direction of motion. Any deviation from these features can be considered as the onset of turbulence. Does varying the values of ℓ or R/a affect the stability of the system? From Acheson's results for 2D (Acheson, 2000) and my own results for 3D (Section 10.8) it was made clear that increasing R/a leads to increased stability for the leapfrogging process and indeed for the whole vortex ring structure. This is borne out by comparing Figures 11.2(a-d) with Figures 11.2(e-f). In Figures 11.2(a-d) R/a varies between 4 and 12, whereas in Figures 11.2(e-f) it varies between approximately 12 and 36. The latter figures showing much more stability than the former ones.

The only way to vary ℓ whilst keeping R/a constant (for a constant number of rings) is to increase R. This means that the macroscopic rings being compared will move at different velocities. It is easy to compare rings of the same size by plotting against time. In order to compare rings of different sizes it is necessary to plot against $\Delta x/D$, numbers of diameters travelled by the ring. In Figure 11.6 I compare 3 systems each consisting of 7 rings, cases 7(a,d,e) from Table 11.1. The systems evolve at zero temperature according to the full BS Law. I show in Figure 11.6(a) the extent to which these 3 systems differ. Their different sizes induce vastly different velocities. However, Figures 11.6(b-d) show that this difference is illusionary, even though the intervortex spacing changes by a factor of $7-8$. All 3 systems develop instabilities, such as increased curvature, alignment of line length in the direction of motion and even reconnections, after travelling approximately $10D$. These figures constitute strong evidence that decreases in intervortex spacing, which are unaccompanied by increases in R/a, do not lead to a more stable system.

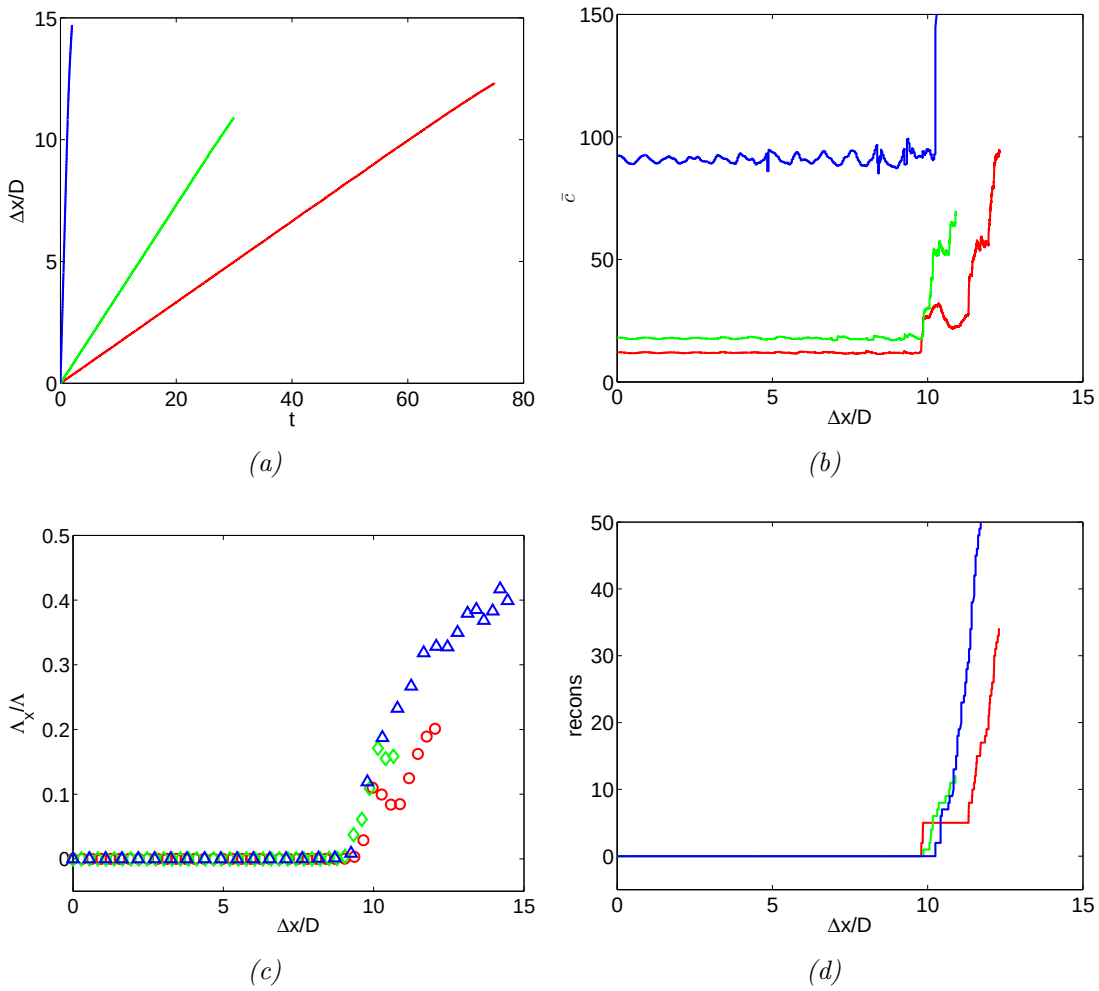

Figure 11.6: Comparison of 3 systems of $N = 7$ in which $R/a = 4$, but ℓ varies: $\ell = 0.0223$ cm (red), 0.015 cm (green) and 0.0003 cm (blue). (a) $\Delta x/D$ vs t (s), (b) average curvature $\bar{c}$ (cm^{-1}) vs $\Delta x/D$, (c) fractional line length in direction of motion Λ_x/Λ vs $\Delta x/D$, and (d) number of reconnections vs $\Delta x/D$. Although the systems move at greatly different velocities (a), all 3 become unstable at about $10D$ (b-d).

11.6 Summary

I have shown that increasing R/a and thereby decreasing ℓ leads to an increase in translational velocity. I have not been able to identify whether it is the change in R/a or ℓ that is the primary cause of this effect, or whether both are equally responsible. The period of the leapfrog depends strongly on both R/a and ℓ, but both the shape of the trajectory and the ring's stability only have a strong dependence on R/a, not on ℓ. These results are summarised in Table 11.2.

Feature	Strongly depends on R/a	Strongly depends on ℓ
Translational velocity	?	?
Period of leapfrog	Y	Y
Shape of trajectory	Y	N
Ring stability	Y	N

Table 11.2: Summary of macroscopic ring features which depend on ℓ and R/a.

Chapter 12

A comparison between mathematical and numerical models at finite temperature in the absence of a normal fluid velocity field

In this Chapter I consider briefly the predictions of the mathematical model at finite temperature without a normal fluid velocity field to sustain the superfluid vortex rings. I compare these predictions with numerical simulations. In Section 6.3 I cited equations for a single vortex ring at finite temperature in the absence of counterflow ($v_n = v_s = 0$). The equations govern the rate at which the ring shrinks (Equation 6.12)

$$\dot{R} = -\frac{\gamma}{\rho_s \kappa}\, v_{si},$$

the lifetime of the ring (i.e. how long it takes until $R \approx a_0$), τ_{ring}, (Equation 6.15),

$$\tau_{ring} = \frac{2\pi\rho_s}{\gamma \bar{L}}\, (R^2 - a_0^2),$$

where (Equation 6.13)

$$\bar{L} = ln\left(\frac{8R}{a_0}\right) - \frac{1}{2},$$

is the slowly-varying part of v_{si} which is approximated as a constant, and the distance travelled in the x direction before the ring disappears is given by (Equation 6.16)

$$\Delta x = \frac{\rho_s \kappa}{\gamma} \frac{1 - \gamma\gamma_0/\rho_s^2\kappa^2}{1 - \gamma_0'/\rho_s\kappa}\, (R - a_0).$$

Adapting Equation 6.12 to model a system of N quantised vortices of radius R and core radius a, and substituting Equation 9.2 for the self-induced velocity of the

macroscopic vortex ring, gives (after simplification)

$$\dot{R} = -\frac{\gamma \bar{L}}{4\pi R \rho_s}. \tag{12.1}$$

I do not attempt to adapt Equations 6.15 and 6.16 to model a macroscopic vortex ring. The reason is that a macroscopic ring is killed in two ways by the mutual friction. Firstly, the entire macroscopic ring formation shrinks as one unit in the same way as a single vortex ring shrinks, and, secondly, individual vortex rings escape from the structure of the macroscopic ring and are killed one by one. The leapfrogging motion of the macroscopic vortex ring which causes the smaller rings to grow again is insufficient to counter the shrinking effect of the mutual friction, such that small rings become even smaller, thereby picking up speed and becoming separated from the main body of rings. It is due to this second effect, which has no analogy in the case of a single ring, that a point is reached at which the parameters of the model are no longer valid. The net result is that the first part of the motion of the macroscopic ring can be described by this model, but the latter part of the motion may not necessarily obey the same rules. Since τ_{ring} and Δx describe the entire evolution of the ring, they will not be subject to equations such as 6.15 and 6.16. $\dot{R}$, however, is the instantaneous rate of change of the ring radius and has an analogy in a macroscopic vortex ring. I would like to qualitatively test the agreement between Equation 12.1 and my numerical results. Equation 12.1 is independent of N, has a strong $1/R$ dependence and a weak dependence on a (and hence ℓ) through $\bar{L}$. This model predicts that macroscopic rings of the same radius R will shrink slightly more slowly as a is increased (since $\log R/a$ decreases with increasing a). I record the cases that I compare in Table 12.1. All the cases consist of 7 rings and use the full BS law.

Figures 12.1(a-d) show the evolution of the macroscopic ring until its death. Subplots (c) and (d) show the change in R and a over time. In this case both R and a are the average radius of the ring and the core in the y-z plane. The rings remain entirely within this plane throughout their evolution. The relative values of $\dot{R}$ can be identified in subplot (c). As predicted by Equation 12.1, the rings with smaller values of a shrink more quickly. Thus the blue line ($a = 0.03$ cm) has the gentlest slope and the black line ($a = 0.005$ cm) has the steepest slope. It is apparent from all subplots that a transition takes place between about 6 and 7 seconds. This is probably the point at which the model ceases to be valid. The macroscopic ring can no longer be considered as a coherent entity after this time and should be treated as a loose collection of individual vortex rings. Subplot (a) shows the relative velocities of the centre of vorticity for these rings. The larger rings move more slowly in keeping with their larger core radius (as seen from subplot (c)). This is also in agreement with the results for zero temperature (see figure 11.1)

for which rings with a smaller intervortex spacing ($\ell = a$ for 7 rings) move faster. The discontinuity visible in subplot (d) is perhaps due to the ring at the front of the vortex configuration reaching a distance from the other rings such that it no longer felt the effect of the other rings. At this point the escaping ring experiences greater shrinking and acceleration, leading to the rapid increase in the value of the parameter a seen in subplot (d). On the other hand, the discontinuity in subplot (c), signifying an increase in the value of the parameter R, may be a result of the quasi-periodic growth and shrinking which take place during a leapfrogging motion.

Case	Colour	R (cm)	a (cm)	R/a
7a	blue	0.0896	0.0300	2.99
7b	green	0.0896	0.0223	4
7c	magenta	0.0896	0.0150	5.97
7d	cyan	0.0896	0.0100	8.96
7e	black	0.0896	0.0050	17.92

Table 12.1: Table of cases to investigate finite temperature effects in absence of counter flow for a range of values of a. I also include the colour of the line that will appear in Figures 12.1.

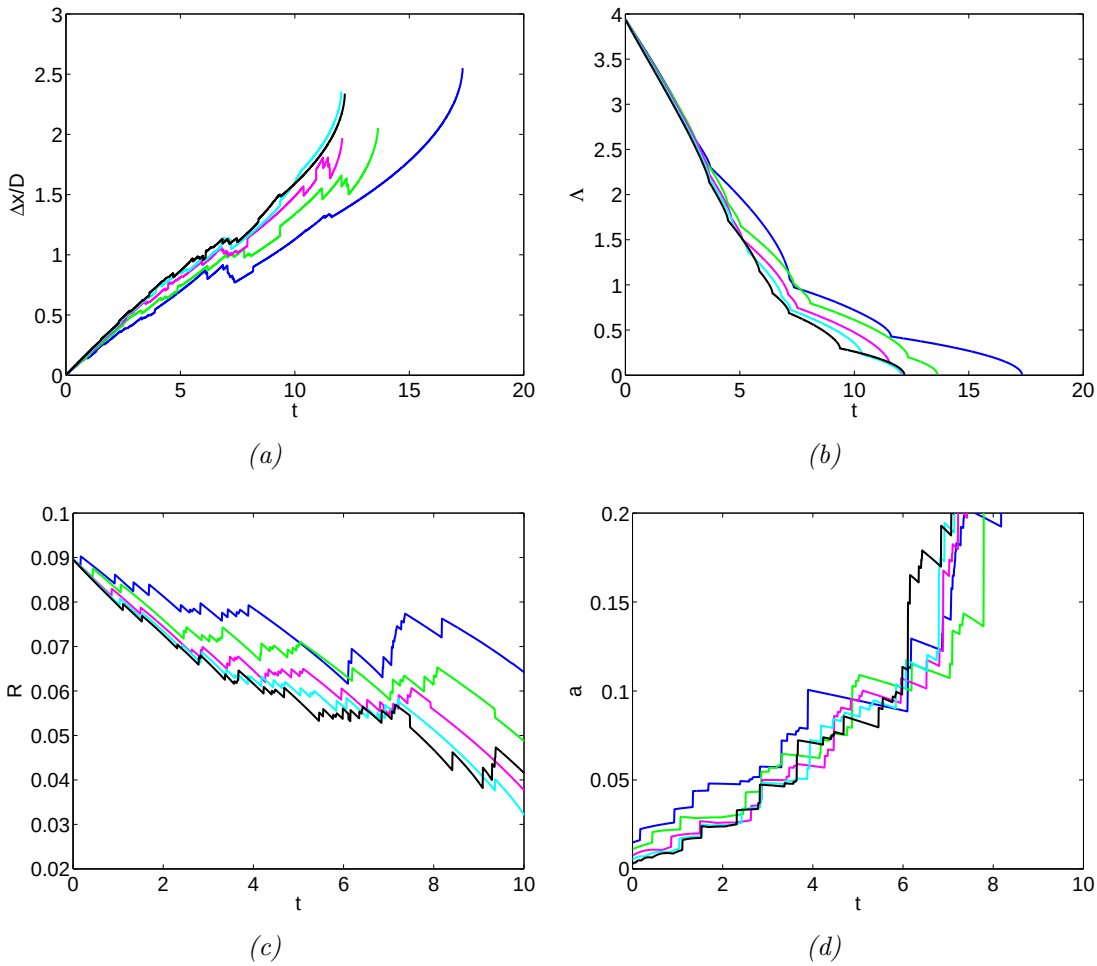

Figure 12.1: Comparison at T1 with constant N and R: (a) Distance travelled $\Delta x/D$ vs t (s), (b) total line length Λ (cm) vs t (s), (c) macroscopic ring radius R vs t (s), and (d) core radius a vs t (s) for $a = 0.03$ cm (blue), 0.0223 cm (green), 0.015 cm (magenta), 0.01 cm (cyan) and 0.005 cm (black).

12.1 Summary

In this Chapter I have looked briefly at mathematical predictions of the macroscopic ring's behaviour at finite temperature with no normal fluid velocity field. My results support the mathematical model's prediction that macroscopic rings with a smaller core radius shrink more quickly.

Chapter 13

The development of instabilities in macroscopic vortex rings

In Sections 10.4 and 10.5 I highlighted the fact that the successful robust translation by the macroscopic vortex rings consisting of 7 and 19 rings was accompanied by the development of instabilities and even reconnections. I now investigate the development of these instabilities in more detail. I begin with a 7 ring system at zero temperature (Section 13.1), then move on to the same system at finite temperature with a normal fluid velocity field (Section 13.2) and lastly consider a 19 ring system both at zero and finite temperatures (Section 13.3). In Sections 13.5 and 13.6 I revisit the 7 ring system to focus more on the phenomenon of reconnections.

13.1 Instabilities in $N = 7$ at zero temperature

In this section I concentrate on the development of instabilities at zero temperature. Vortex dynamics at this temperature are not subject to the mutual friction force, which acts to damp out small scale motions, and as such are prone to develop into a much more complicated tangle than their finite temperature counterpart. I start with a series of KnotPlot images showing side and rear views of the macroscopic vortex ring. The first images are of a still-stable ring and the last of a highly turbulent one. Due to the different sizes of the stable and unstable rings, the scaling (amplification) of the KnotPlot images must be changed to make the images more visible. The scale used to output each KnotPlot image is recorded below that image. The parameters of the rings that I show are: $R = 0.0896$ cm, $a = \ell = 0.0223$ cm (such that $R/a = 4$), $\Delta\xi = 0.00149$ cm and $\Delta t = 5 \times 10^{-5}$, using the full BS law. The radius of the cylinders in the KnotPlot images is 0.025 in arbitrary units. Rings are also coloured arbitrarily so that rings of the same colour in any 2 images are not necessarily related to each other. Table 13.1 contains data pertaining to the KnotPlot figures. The highly turbulent nature of the vortex configuration can be seen most clearly from the increase, by an order of magnitude, in the average

curvature, $\bar{c}$. It is also apparent from an approximately 50 % increase in the number of discretisation points, N_p, and the total line length, Λ.

The first visible instabilities occur after about 57 seconds. At zero temperature the unstable rings initially remain coaxial. A long wavelength perturbation distorts the shape of the ring so that it is no longer circular (see in particular Figures 13.1 and 13.2 rear views). Simultaneously to the development of long wave perturbations, the rings begin to wrap themselves through and around other rings until a reconnection event occurs, all the while maintaining their coaxiality. Due to their enduring coaxiality the type of reconnections which occur naturally at zero temperature between the individual vortex rings are 'parallel' reconnections. A more detailed study of these reconnections can be found in Section 13.5. The short wave length perturbations engendered by the reconnections remain undamped in the inviscid superfluid and in the absence of the viscous normal fluid component and by about 70 seconds have developed into a dominant feature of the ring.

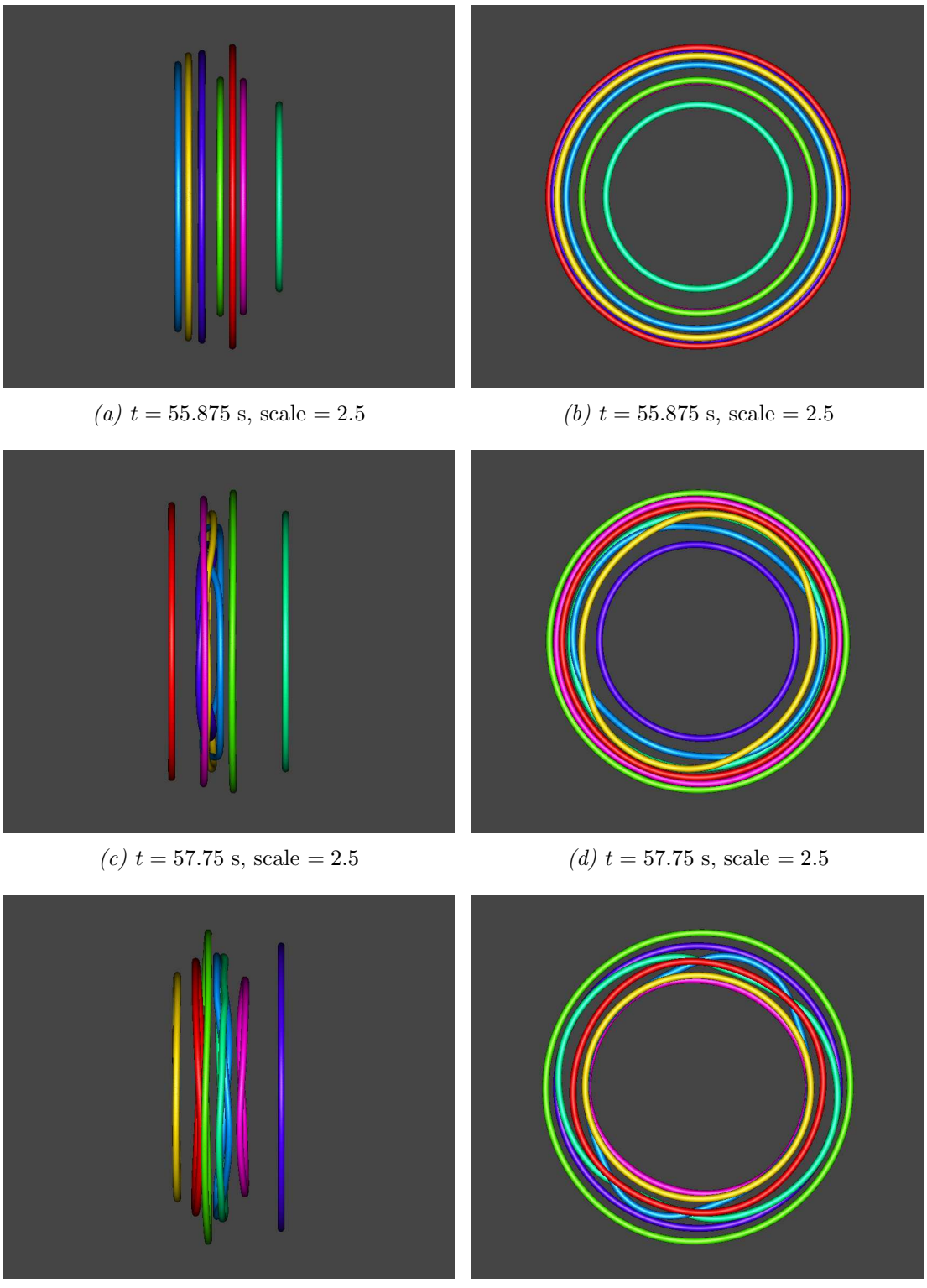

(a) $t = 55.875$ s, scale $= 2.5$

(b) $t = 55.875$ s, scale $= 2.5$

(c) $t = 57.75$ s, scale $= 2.5$

(d) $t = 57.75$ s, scale $= 2.5$

(e) $t = 58.5$ s, scale $= 2.5$

(f) $t = 58.5$ s, scale $= 2.5$

Figure 13.1: Knotplot images of development of instabilities in $N = 7$ system evolved using Biot-Savart at $T = 0$ K. Side (left panel) and rear (right panel) views.

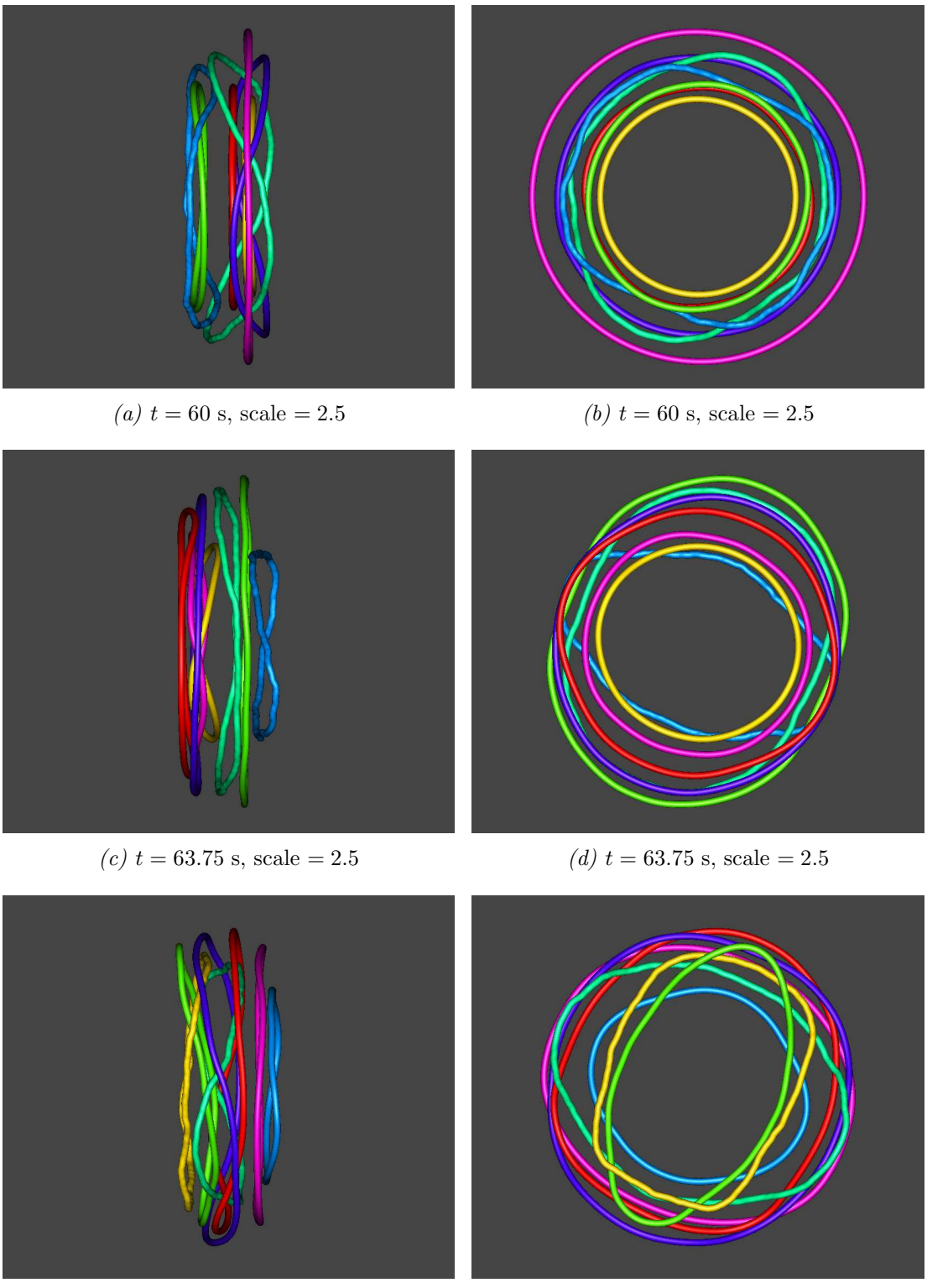

(a) $t = 60$ s, scale $= 2.5$ *(b)* $t = 60$ s, scale $= 2.5$

(c) $t = 63.75$ s, scale $= 2.5$ *(d)* $t = 63.75$ s, scale $= 2.5$

(e) $t = 67.5$ s, scale $= 2.5$ *(f)* $t = 67.5$ s, scale $= 2.5$

Figure 13.2: Knotplot images of development of instabilities in $N = 7$ system evolved using Biot-Savart at $T = 0$ K. Side (left panel) and rear (right panel) views.

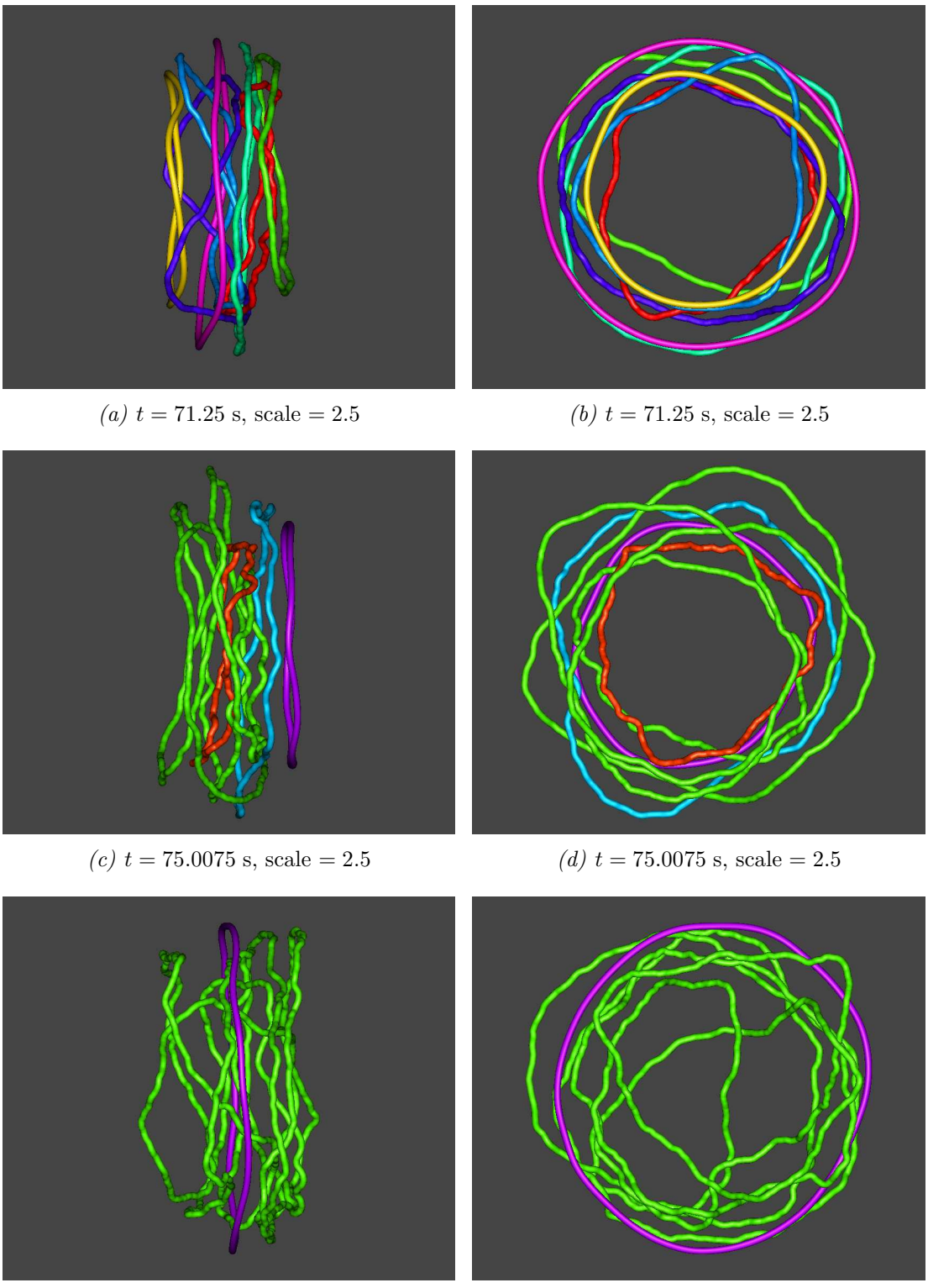

(a) $t = 71.25$ s, scale $= 2.5$

(b) $t = 71.25$ s, scale $= 2.5$

(c) $t = 75.0075$ s, scale $= 2.5$

(d) $t = 75.0075$ s, scale $= 2.5$

(e) $t = 78.75$ s, scale $= 2.5$

(f) $t = 78.75$ s, scale $= 2.5$

Figure 13.3: Knotplot images of development of instabilities in $N = 7$ system evolved using Biot-Savart at $T = 0$ K. Side (left panel) and rear (right panel) views.

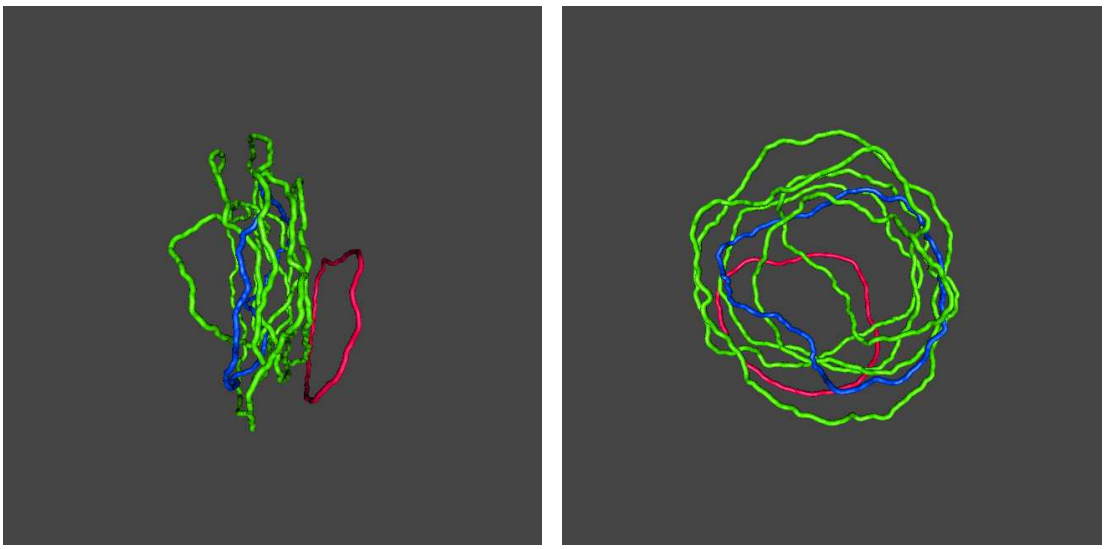

(a) $t = 82.5$ s, scale $= 1.8$ *(b)* $t = 82.5$ s, scale $= 1.8$

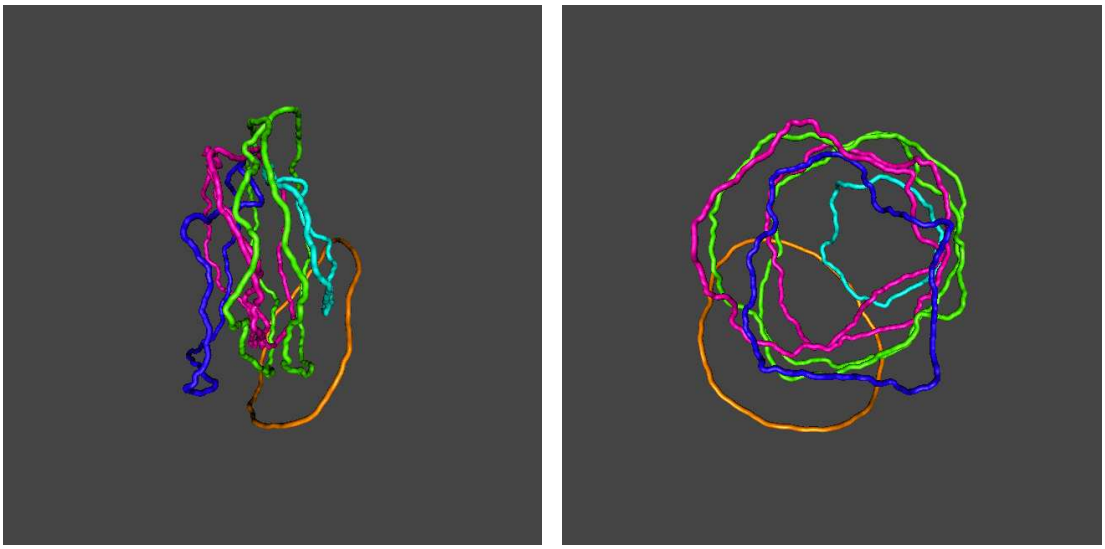

(c) $t = 86.25$ s, scale $= 1.8$ *(d)* $t = 86.25$ s, scale $= 1.8$

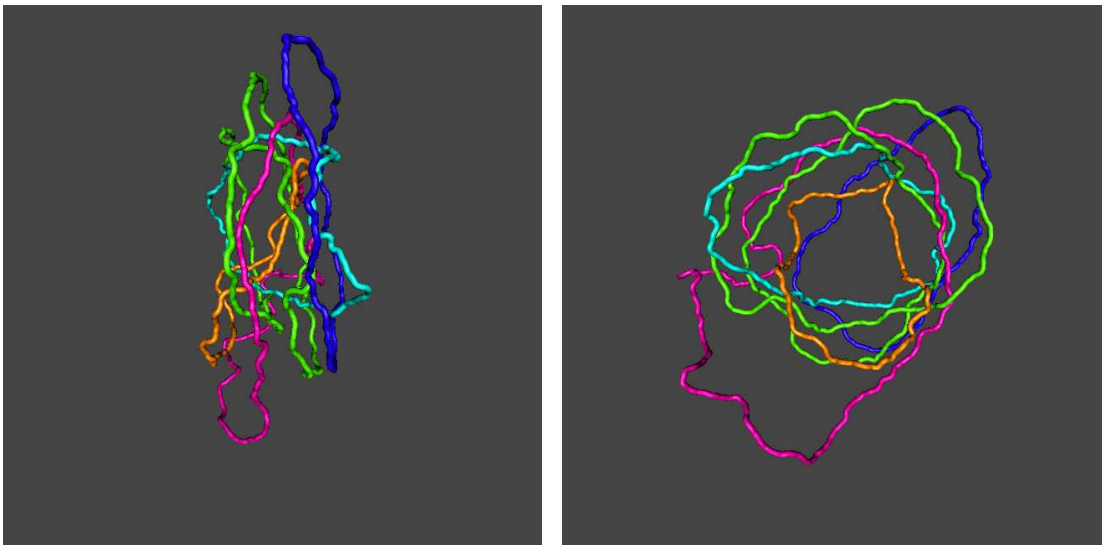

(e) $t = 90$ s, scale $= 1.8$ *(f)* $t = 90$ s, scale $= 1.8$

Figure 13.4: Knotplot images of development of instabilities in $N = 7$ system evolved using Biot-Savart at $T = 0$ K. Side (left panel) and rear (right panel) views.

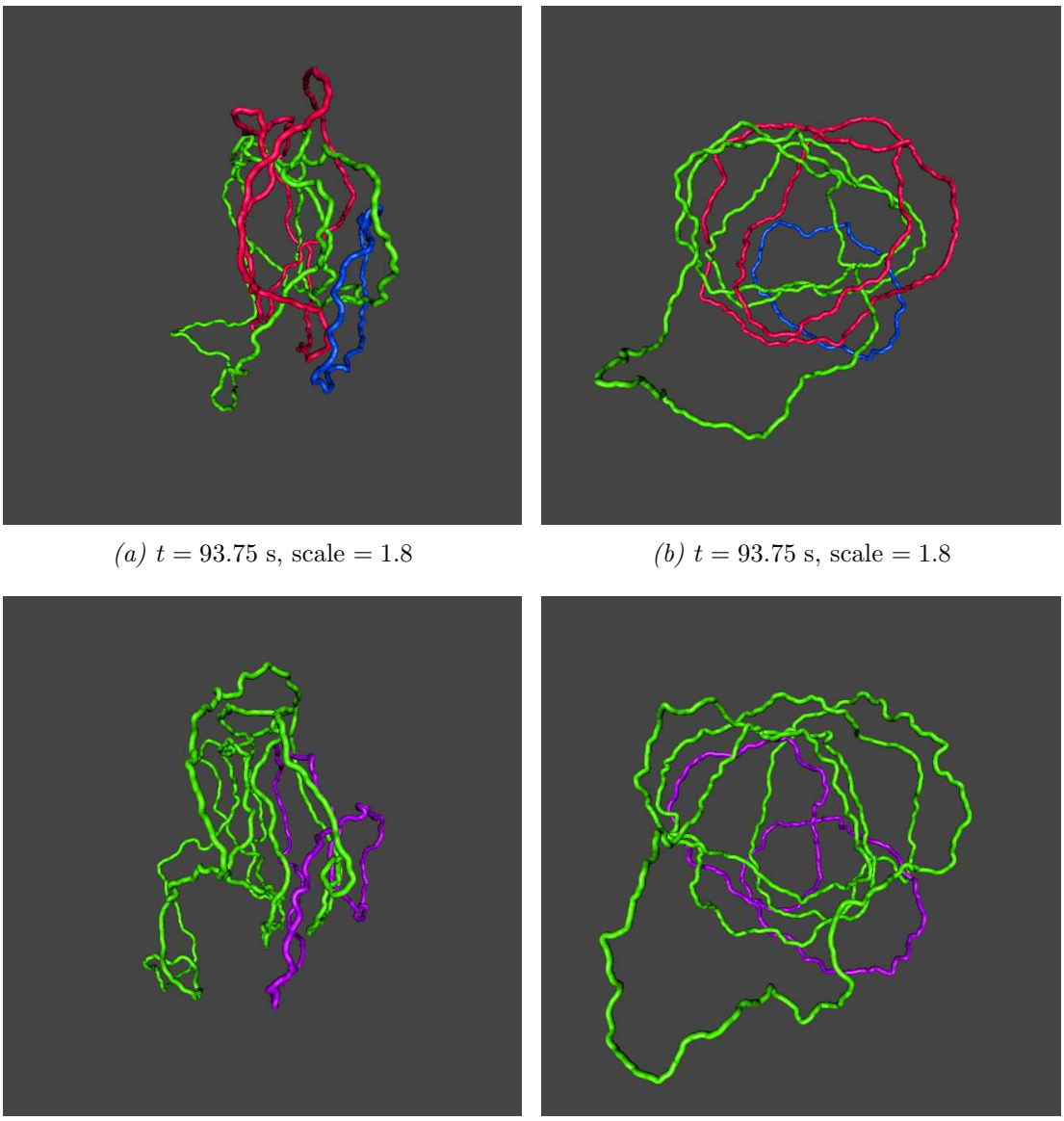

(a) $t = 93.75$ s, scale $= 1.8$ *(b)* $t = 93.75$ s, scale $= 1.8$

(c) $t = 97.5$ s, scale $= 1.8$ *(d)* $t = 97.5$ s, scale $= 1.8$

Figure 13.5: Knotplot images of development of instabilities in $N = 7$ system evolved using Biot-Savart at $T = 0$ K. Side (left panel) and rear (right panel) views.

Initially, at $t = 0$ seconds, the vortex rings are all aligned in the y-z plane such that all of their line length is perpendicular to the direction of motion. With the onset of instability a fraction of line length parallel to the direction of motion begins to develop and, as the rings become more and more unstable, this fraction grows. In an attempt to quantify the amount of instability, I measure the relative line length out of the plane of the initial rings. I define Λ_x, Λ_y and Λ_z as the projection of the total line length onto the x, y and z axes respectively. Then $\Lambda = \sum_{i=1}^{i=N_p} \sqrt{\Lambda_{x,i,i+1}^2 + \Lambda_{y,i,i+1}^2 + \Lambda_{z,i,i+1}^2}$ is the (pointwise) total line length, where $\Lambda_{x,i,i+1}$ means the projection of the line segment between point i and point $i+1$ onto the x axis. Λ_x is thus the element of line length parallel to the direction of motion and Λ_y and Λ_z are the elements perpendicular to the direction of motion. I

t (s)	N_p	recons	N	Λ (cm) (3dp)	$\bar{c}$ (cm/s^2) (2dp)	Δx (cm) (3dp)	$\Delta x/D$ (2dp)	v_x (cm/s) (4dp)
55.875	3528	0	7	3.950	12.06	1.666	9.30	0.0287
57.75	3528	0	7	3.976	11.92	1.720	9.60	0.0292
58.5	3593	0	7	3.979	11.84	1.741	9.72	0.0288
60	3747	5	7	4.017	27.04	1.786	9.97	0.0289
63.75	3714	5	7	4.026	25.77	1.895	10.57	0.0278
67.5	3925	5	7	4.087	25.66	2.003	11.18	0.0265
71.25	3944	17	7	4.207	57.32	2.108	11.76	0.0254
75.0075	4284	34	4	4.327	93.49	2.208	12.32	0.0237
78.75	4347	47	2	4.516	101.68	2.301	12.84	0.0226
82.5	4509	68	3	4.680	120.07	2.288	13.33	0.0211
86.25	4625	86	5	4.847	122.60	2.466	13.76	0.0181
90	4766	102	5	4.976	125.43	2.531	14.12	0.0152
93.75	4900	124	3	5.105	133.55	2.589	14.45	0.0141
97.5	4989	142	2	5.213	135.46	2.646	14.77	0.0134

Table 13.1: Development of instabilities in $N = 7$ system at $T = 0$ K. See Figures 13.1 to 13.5.

record their values from shortly before the onset of instability in the Table 13.2. In order to compare the different elements of line length, I normalise these elements by Λ and plot these normalised values versus time (Figure 13.6). Λ_x is seen to approach the value of Λ_y and Λ_z, showing a high degree of disorder in the system. I also show separately the increase in the total line length Λ (Figure 13.7) and in the average curvature $\bar{c}$ (Figure 13.8). It is unclear whether either is tending towards a steady state. All of the data is from runs involving an initial configuration of 7 vortex rings, $R = 0.0896$ cm, $a = 0.0223$ cm (such that $R/a = 4$), $\ell = 0.0223$ cm, $\Delta t = 5 \times 10^{-5}$ seconds and $\Delta\xi = 0.00149$ cm (such that $\ell/\Delta\xi = 15$).

t (s)	Λ_x (cm)	Λ_y (cm)	Λ_z (cm)	Λ (cm)	t (s)	Λ_x (cm)	Λ_y (cm)	Λ_z (cm)	Λ (cm)
37.51	0.00	2.51	2.51	3.94	69.38	0.67	2.55	2.56	4.11
39.38	0.00	2.51	2.51	3.95	71.26	0.80	2.56	2.62	4.21
41.26	0.00	2.51	2.51	3.94	73.13	0.86	2.64	2.63	4.28
43.13	0.00	2.52	2.52	3.96	75.01	0.92	2.66	2.67	4.33
45.01	0.00	2.52	2.52	3.95	76.88	1.09	2.72	2.63	4.44
46.88	0.00	2.49	2.49	3.91	78.76	1.16	2.74	2.67	4.52
48.76	0.00	2.50	2.50	3.93	80.63	1.22	2.65	2.78	4.58
50.63	0.00	2.54	2.54	3.98	82.51	1.39	2.66	2.83	4.68
52.51	0.00	2.51	2.51	3.94	84.38	1.49	2.77	2.77	4.76
54.38	0.00	2.48	2.48	3.89	86.26	1.61	2.83	2.73	4.85
56.26	0.01	2.52	2.52	3.96	88.13	1.75	2.84	2.69	4.91
58.13	0.11	2.54	2.52	3.98	90.01	1.78	2.81	2.82	4.98
60.01	0.44	2.53	2.51	4.02	91.88	1.88	2.73	2.89	5.03
61.88	0.40	2.53	2.55	4.04	93.76	2.00	2.74	2.87	5.10
63.76	0.34	2.53	2.57	4.03	95.63	1.97	2.82	2.92	5.17
65.63	0.34	2.56	2.54	4.03	97.51	2.08	2.93	2.78	5.21
67.51	0.51	2.60	2.54	4.09	99.38	2.15	2.90	2.82	5.25

Table 13.2: Values of total line length Λ and elements of line length Λ_x, Λ_y and Λ_z in x, y and z directions during the development of instabilities over time in an initial configuration of $N = 7$ at zero temperature using Biot-Savart law.

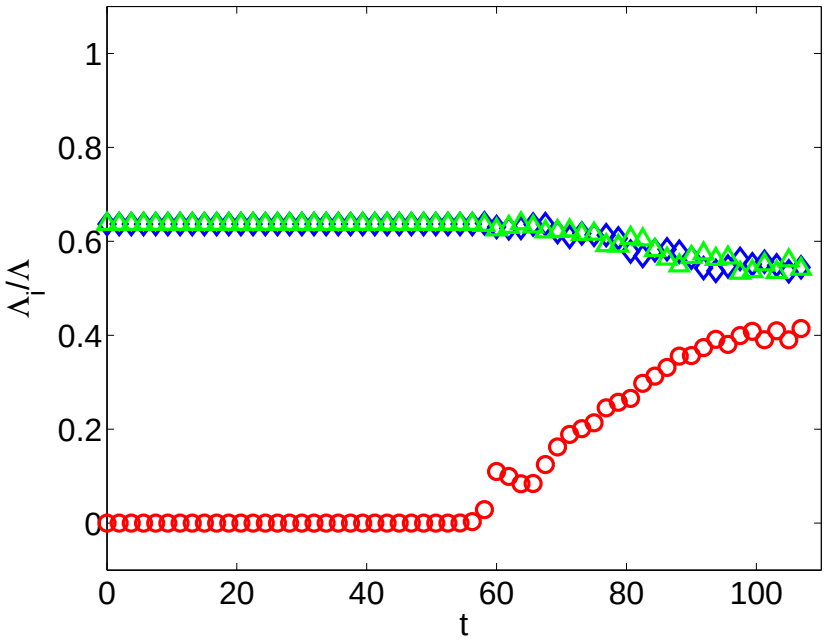

Figure 13.6: Fractional line lengths Λ_i/Λ ($i = x, y, z$) vs t (s). In particular the line length parallel to the direction of motion, Λ_x (red circles), develops from an initial configuration in which all line length was perpendicular to the direction of motion, Λ_y (blue diamonds) and Λ_z (green triangles). All elements of the line length are normalised by the total line length, Λ. Data points are plotted every 1.875 seconds between 37.5 and 97.5 seconds, a range which includes all of the KnotPlot images (13.1 to 13.5). Run parameters: $N = 7$, $R = 0.0896$ cm, $a = 0.0223$ cm (such that $R/a = 4$), $\ell = 0.0223$ cm, $\Delta t = 5 \times 10^{-5}$ seconds and $\Delta\xi = 0.00149$ cm (such that $\ell/\Delta\xi = 15$).

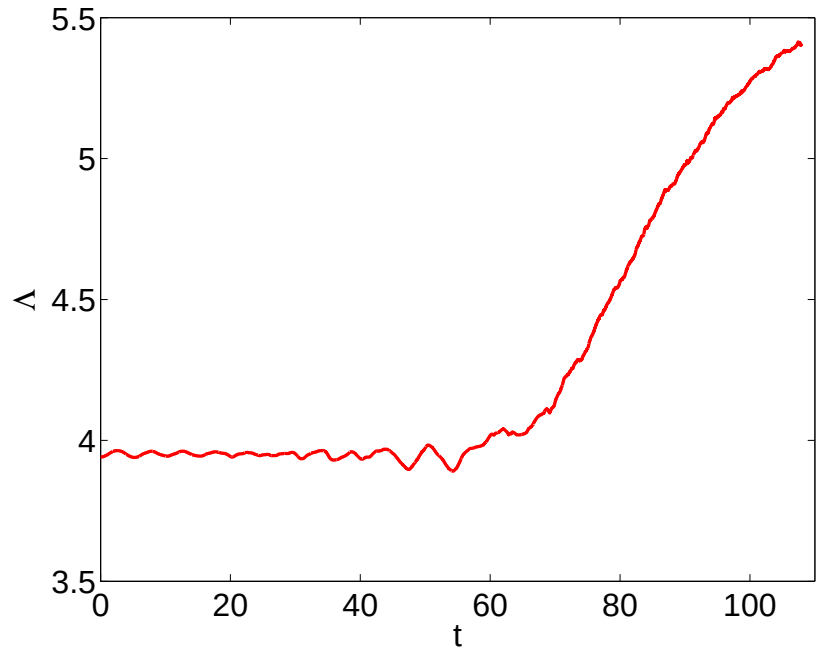

Figure 13.7: Total line length Λ vs t (s). Run parameters: $N = 7$, $R = 0.0896$ cm, $a = 0.0223$ cm (such that $R/a = 4$), $\ell = 0.0223$ cm, $\Delta t = 5 \times 10^{-5}$ seconds and $\Delta\xi = 0.00149$ cm (such that $\ell/\Delta\xi = 15$).

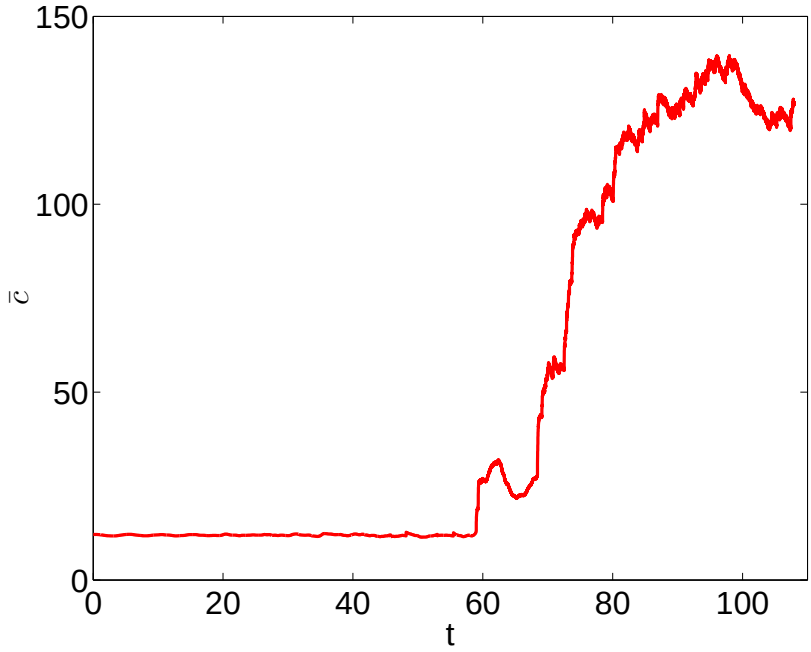

Figure 13.8: Average curvature $\bar{c}$ (cm^{-1}) vs t (s). Run parameters: $N = 7$, $R = 0.0896$ cm, $a = 0.0223$ cm (such that $R/a = 4$), $\ell = 0.0223$ cm, $\Delta t = 5 \times 10^{-5}$ seconds and $\Delta\xi = 0.00149$ cm (such that $\ell/\Delta\xi = 15$).

13.2 Instabilities in $N = 7$ at finite temperature in the presence of a normal fluid velocity field

I now consider the development of instabilities at finite temperature of the same macroscopic ring as in the previous section. The picture that emerges is quite different to that at zero temperature. I will show that the occurrence of small scale, high frequency perturbations are rare, short-lived events. The instabilities are dominated by large scale perturbations. I will furthermore show that the macroscopic ring undergoes a period of unstable development, before reaching a steady state in which it assumes the shape of an interconnected toroidal coil (see Figures 13.11(c-f)), which translates along its axis with much the same velocity as the initial bundle and is very resilient to the dissipative effects of the mutual friction. The ring's parameters are exactly the same as in the zero temperature case: 7 vortex rings, $R = 0.0896$ cm, $a = 0.0223$ cm (such that $R/a = 4$), $\ell = 0.0223$ cm, $\Delta t = 5 \times 10^{-5}$ seconds and $\Delta\xi = 0.00149$ cm (such that $\ell/\Delta\xi = 15$). Once again the vortex rings are all initially aligned in the y-z plane such that all of their line length is perpendicular to the direction of motion.

The development of the macroscopic ring's instability can be broken down into several stages:

1. There are measurable, although not visible, signs of instability from $t = 0$, such as a (tiny) non-zero fraction of line length in the direction of motion, $\Lambda_x > 0$.

2. The first visible onset of instability occurred after about 22.5 seconds. Notice that this is much earlier than the equivalent onset of visible instability in the zero temperature case, which occurred after about 57.75 seconds. The nature of the instability differs too. At zero temperature the unstable rings remain coaxial. A long wavelength perturbation distorts the shape of the ring so that it is no longer circular whilst one ring begins to wrap itself through and around another ring until a reconnection occurs. Whereas, at finite temperature, the opposite occurs: the rings begin to lose their coaxiality; they reorient themselves at a different angle, whilst retaining a circular shape. I believe that this difference is due to the interaction between the normal fluid velocity field and the superfluid vortex rings i.e. the superfluid rings reorient themselves due to the normal fluid velocity field.

3. This situation continues until differently orientated rings begin to collide with each other, giving rise to reconnections. One can distinguish between this type of reconnection, which are called 'antiparallel' reconnections, and those mentioned in the zero temperature case, which are called 'parallel' reconnections. Anti-parallel reconnections lead to the formation of small independent

rings, which in the presence of mutual friction are short-lived. What remains is a large, hollow-centred, figure-of-eight shaped ring (see Section 13.6 for further details). As this ring undergoes the leapfrog process, the relatively sharp edges left by the disappearance of the middle section of the figure-of-eight are smoothed out until an almost-unperturbed, ring-like shape is reattained.

4. The process of reconnections reduces the number of individual rings in the system (see Table 13.3). This process continues until a steady state is reached in which a single toroidal coil remains. This particular toroidal coil consists of 3 longitudinal wraps and 1 meridian wrap. It proves exceptionally resilient to the dissipative effects of mutual friction (see Figures 13.11(c-f)).

I show first the development of the instabilities in Figures 13.9, 13.10 and 13.11. Under each subplot is its time and the KnotPlot scaling (magnification). In this case all images share the same scaling, since the instabilities do not grow so much as to require a different scaling factor (unlike zero temperature). There is a conspicuous lack of small scale perturbations in these images. In fact the only small scale perturbations that occur are those accompanying a reconnection event (see Section 13.6). The last 4 images (c-f) in Figure 13.11 show the toroidal coil at times 75 seconds and 150 seconds. Besides from a rotation about itself, little seems to have changed between the 2 times. Table 13.3 contains the data pertaining to Figures 13.9 to 13.11. Although the average curvature does increase somewhat (about 10 %) it is far less than at equivalent times for zero temperature. Notice also how little the parameters change in the second 75 seconds from $t = 75$ seconds to $t = 150$ seconds, compared to how much they changed in the first 75 seconds. Table 13.4, containing data about the fraction of line length in each of the x, y and z directions, and Figure 13.12 both show that Λ_x, after a transitional period, settles down to a periodic steady state corresponding to the rotation of the toroidal coil. Figures 13.13 and 13.14 show that total line length and average curvature have also reached an approximately steady state (subject to a very slow dissipative action of the mutual friction).

In the final plot in this Section, Figure 13.15, I compare the distance travelled and velocity of the centre of vorticity in 4 cases. The blue line shows the progress of the 7 ring macroscopic vortex ring at finite temperature during its first 75 seconds. The red line shows its progress during the second 75 seconds, in other words after it transformed into a toroidal coil. The green line shows what happens to the identical coil at zero temperature. Lastly, the black line shows the progress of an $N = 3$ macroscopic ring, which is (almost) identical in radius R and number of discretisation points N_p to the toroidal coil. The toroidal coil is just slightly slower than the unconnected $N = 3$ ring. The zero temperature toroidal coil unravels and is beset by instabilities and further reconnections.

In Maggioni *et al.* (2010) Maggioni *et al.* report on the velocity, energy, and

helicity of vortex knots and unknots in an inviscid fluid (e.g. ^{4}He at $T = 0$ K). They parametrise the complexity of the vortex knots in terms of the winding number, w, which is the ratio of the number of meridian (poloidal) wraps, q, to the number of longitudinal (toroidal) wraps, p. They conclude that for $w < 1$ vortex knots and toroidal coils move faster and carry more energy than a reference vortex ring of same size and circulation, whereas for $w > 1$ knots and poloidal coils have approximately same speed and energy as the reference vortex ring. My toroidal coil has 3 longitudinal wraps and 1 meridian wrap, hence $w = 1/3$. If the same results hold at finite temperatures, I should find that the corresponding reference vortex moves more slowly with less energy.

By $t = 75$ seconds, my toroidal coil is well developed (see Figure 13.11(c-d)). At that time $N_p = 1510$ (for the entire coil) and the average distance between neighbouring points is approximately 0.001 cm. For a single ring, $2\pi R_{ref} = 1510/3 \times 10^{-3} \approx 0.517$ cm, so $R_{ref} \approx 0.0822$ cm. The velocity for this ring is then $v_x^{ref} = 0.01704$ cms^{-1} and the vortex energy (per unit density) is $E^{ref} = 7.22 \times 10^{-7}$ cm^{2}s^{-2}. The corresponding values for the toroidal coil are $v_x = 0.02085$ cms^{-1} and the vortex energy (per unit density) is $E = 2.45 \times 10^{-6}$ cm^{2}s^{-2}, which is indeed faster and more energetic than the reference ring. There is agreement between my results and Maggioni *et al.* .

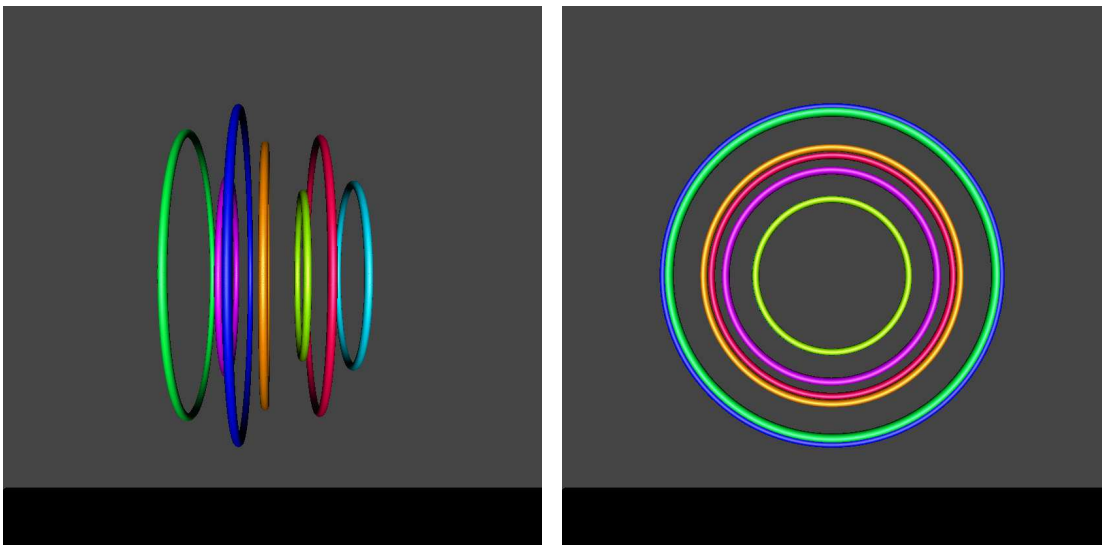

(a) $t = 15$ s, scale $= 2.5$ *(b)* $t = 15$ s, scale $= 2.5$

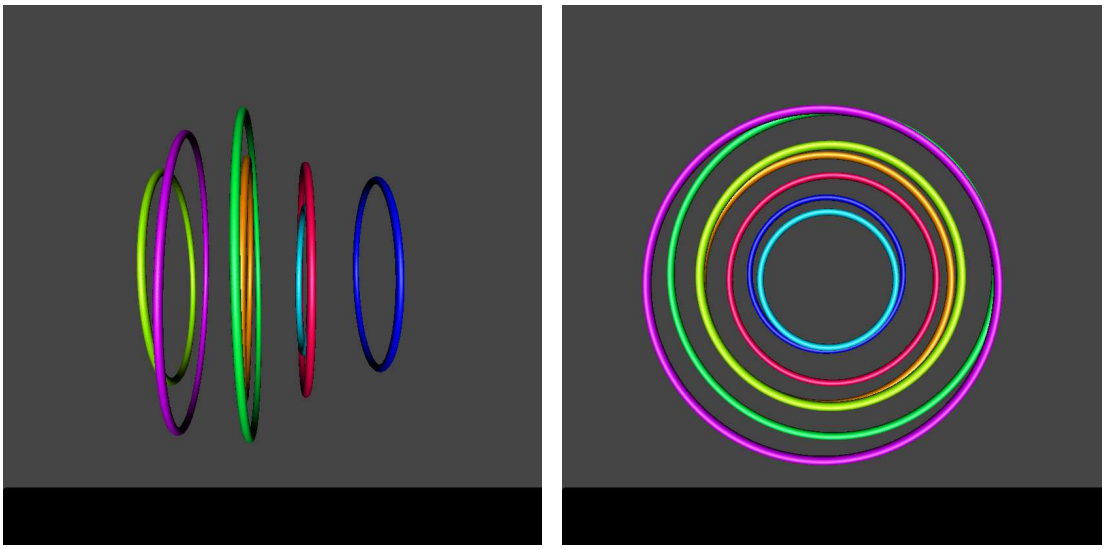

(c) $t = 30$ s, scale $= 2.5$ *(d)* $t = 30$ s, scale $= 2.5$

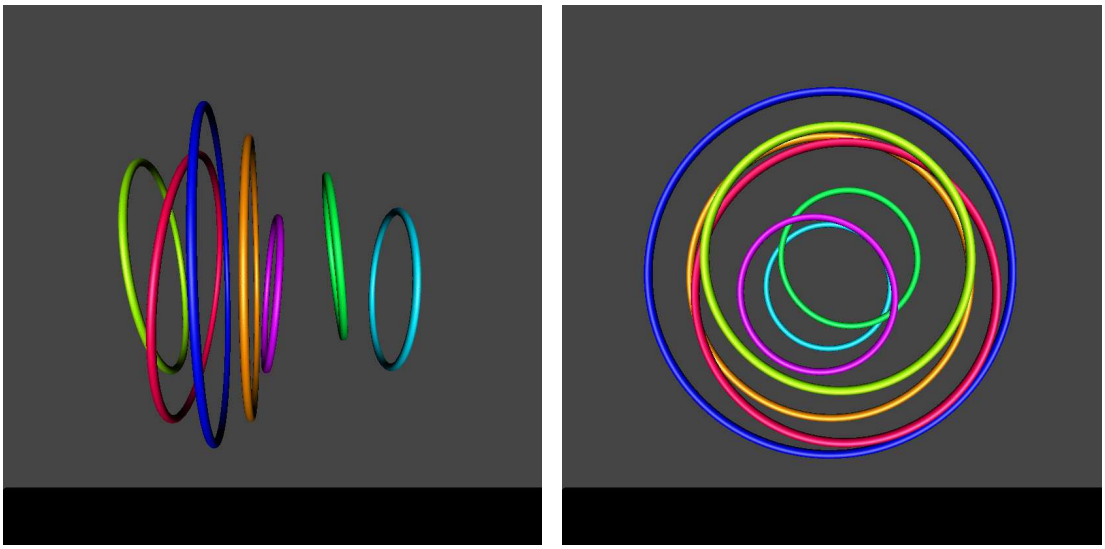

(e) $t = 37.5$ s, scale $= 2.5$ *(f)* $t = 37.5$ s, scale $= 2.5$

Figure 13.9: Knotplot images of development of instabilities in $N = 7$ system evolved using Biot-Savart at $T = 2.02$ K. Side (left panel) and rear (right panel) views.

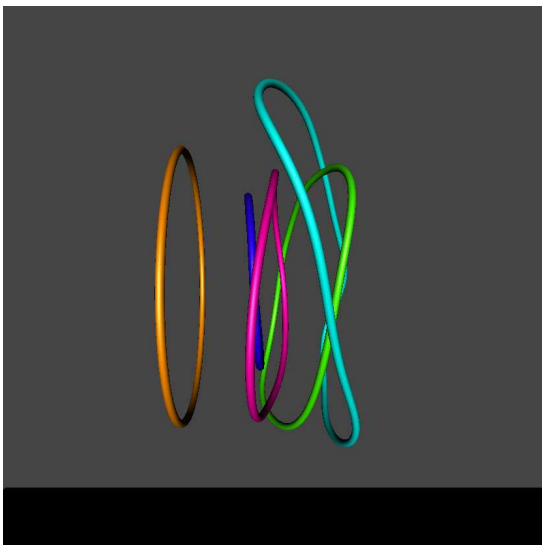

(a) $t = 45$ s, scale $= 2.5$

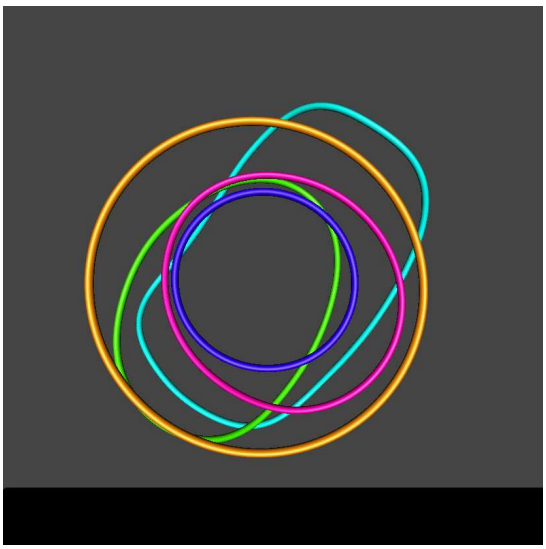

(b) $t = 45$ s, scale $= 2.5$

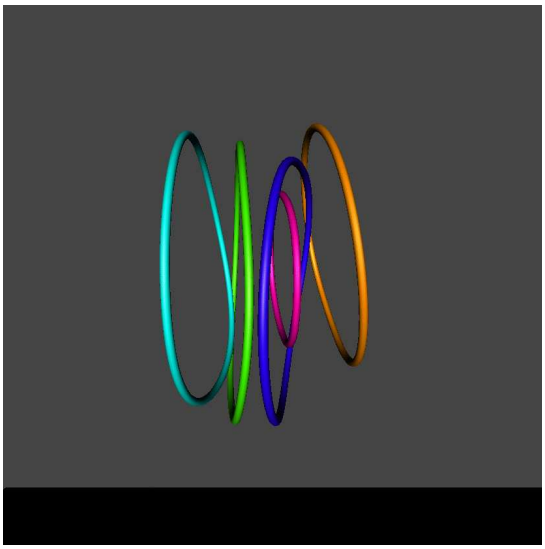

(c) $t = 52.5$ s, scale $= 2.5$

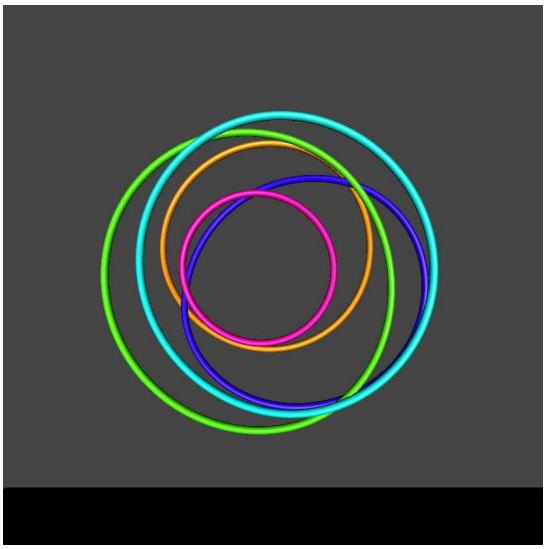

(d) $t = 52.5$ s, scale $= 2.5$

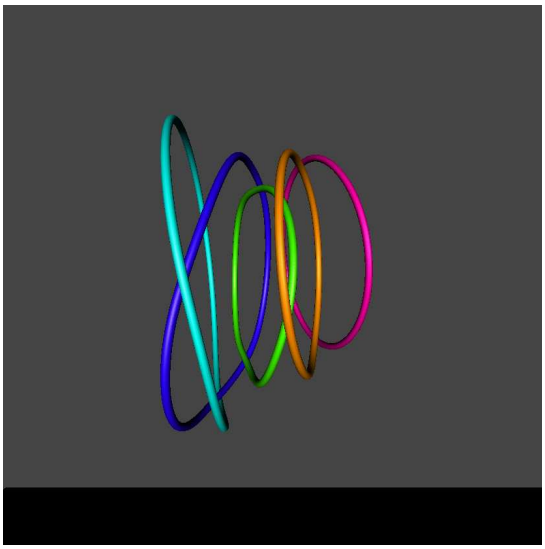

(e) $t = 60$ s, scale $= 2.5$

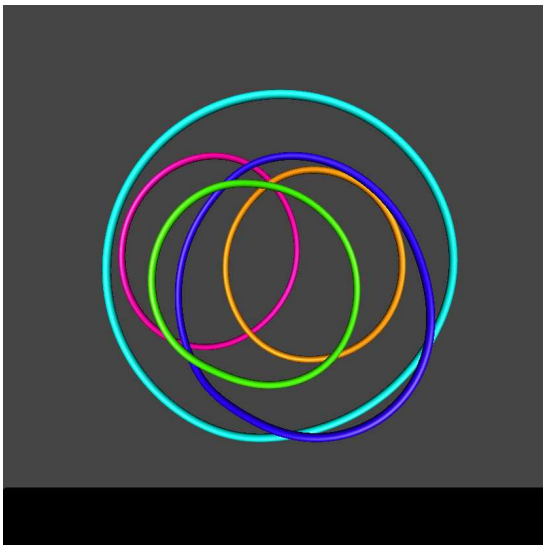

(f) $t = 60$ s, scale $= 2.5$

Figure 13.10: Knotplot images of development of instabilities in $N = 7$ system evolved using Biot-Savart at $T = 2.02$ K. Side (left panel) and rear (right panel) views.

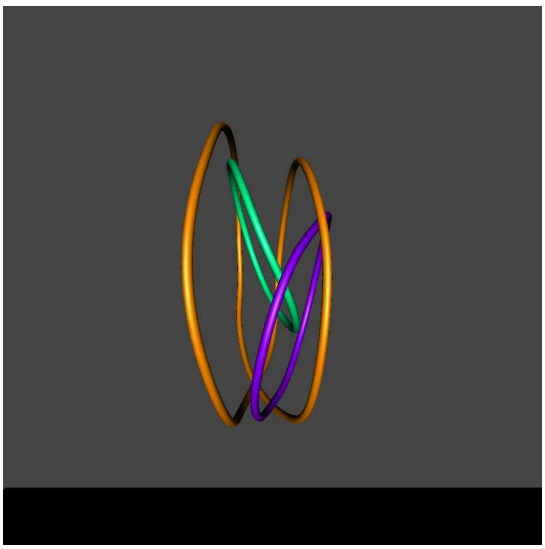

(a) $t = 67.5$ s, scale $= 2.5$

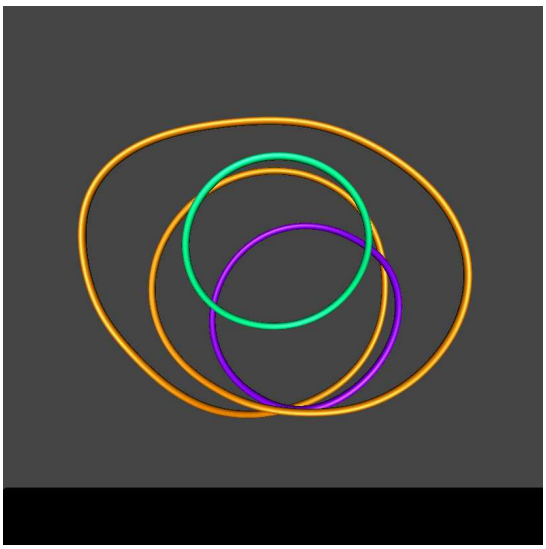

(b) $t = 67.5$ s, scale $= 2.5$

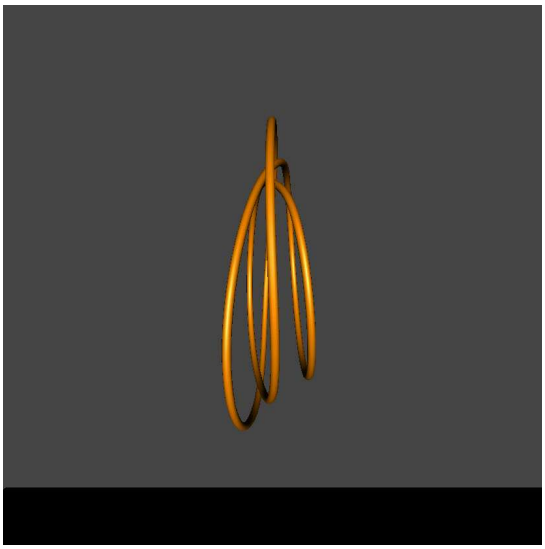

(c) $t = 75$ s, scale $= 2.5$

(d) $t = 75$ s, scale $= 2.5$

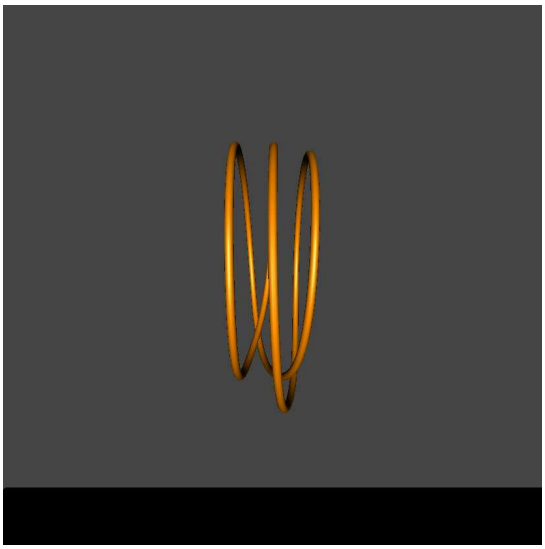

(e) $t = 150$ s, scale $= 2.5$

(f) $t = 150$ s, scale $= 2.5$

Figure 13.11: Knotplot images of development of instabilities in $N = 7$ system evolved using Biot-Savart at $T = 2.02$ K. Side (left panel) and rear (right panel) views.

t (s)	N_p	recons	N	Λ (cm) (3dp)	$\bar{c}$ (cm/s^2) (2dp)	Δx (cm) (3dp)	$\Delta x/D$ (2dp)	v_x (cm/s) (4dp)
0	3528	0	7	3.940	11.88	0	0	0.0305
15	3367	0	7	3.518	13.18	0.440	2.46	0.0277
30	3250	0	7	3.418	13.34	0.878	4.90	0.0267
37.5	2994	2	7	3.236	13.85	1.090	6.08	0.0275
45	2541	2	5	2.706	13.65	1.289	7.19	0.0209
52.5	2374	2	5	2.477	12.73	1.473	8.22	0.0231
60	2441	2	5	2.449	13.27	1.666	9.30	0.0235
67.5	1955	4	3	2.007	12.79	1.839	10.26	0.0219
75	1510	7	1	1.551	12.27	1.998	11.34	0.0209
150	1432	7	1	1.492	12.85	3.697	20.63	0.0216

Table 13.3: Development of instabilities in $N = 7$ system at $T = 2.02$ K with imposed normal fluid velocity field. 'recons' refers to visible reconnections only, not including algorithmic reconnections. See Figures 13.9 to 13.11.

t (s)	Λ_x (cm)	Λ_y (cm)	Λ_z (cm)	Λ (cm)	t (s)	Λ_x (cm)	Λ_y (cm)	Λ_z (cm)	Λ (cm)
0	0.00	2.51	2.51	3.94	75	0.14	0.98	0.98	1.55
5	0.00	2.37	2.37	3.72	80	0.15	0.96	0.95	1.51
10	0.01	2.27	2.27	3.57	85	0.11	0.96	0.95	1.51
15	0.01	2.24	2.24	3.52	90	0.10	0.95	0.94	1.49
20	0.01	2.18	2.18	3.43	95	0.12	0.94	0.94	1.48
25	0.02	2.17	2.17	3.41	100	0.15	0.94	0.94	1.49
30	0.06	2.18	2.18	3.42	105	0.12	0.95	0.94	1.49
35	0.11	2.10	2.10	3.30	110	0.10	0.95	0.94	1.49
40	0.30	2.09	2.10	3.32	115	0.10	0.94	0.94	1.48
45	0.36	1.77	1.68	2.71	120	0.14	0.94	0.93	1.48
50	0.23	1.55	1.57	2.47	125	0.13	0.95	0.94	1.49
55	0.35	1.54	1.53	2.44	130	0.10	0.95	0.94	1.49
60	0.43	1.56	1.49	2.45	135	0.10	0.94	0.94	1.48
65	0.54	1.42	1.43	2.36	140	0.14	0.94	0.94	1.48
70	0.27	1.16	1.27	1.95	145	0.14	0.95	0.94	1.49
75	0.14	0.98	0.98	1.55	150	0.10	0.95	0.94	1.49

Table 13.4: Values of total line length Λ and elements of line length Λ_x, Λ_y and Λ_z in x, y and z directions during the development of instabilities over time in an initial configuration of $N = 7$ at finite temperature using Biot-Savart law.

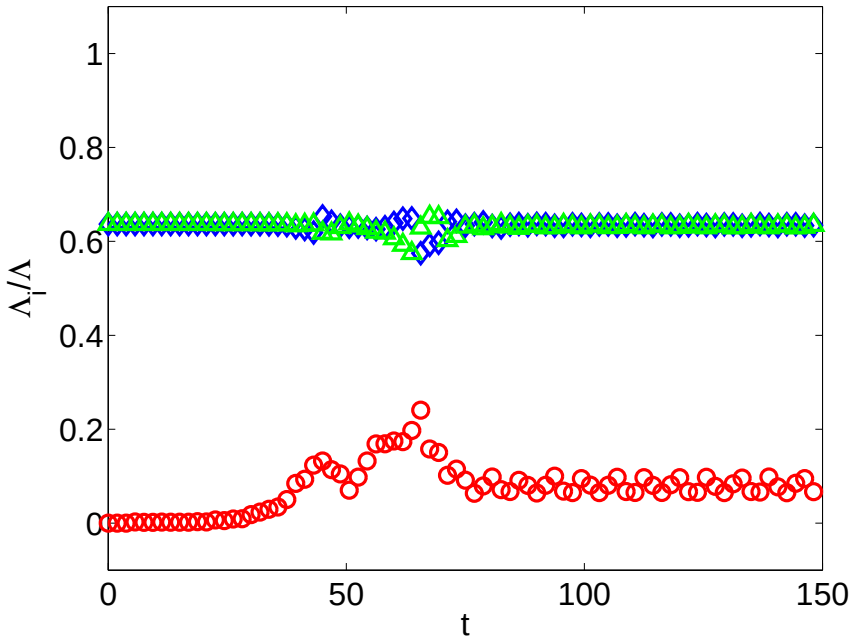

Figure 13.12: Fractional line lengths Λ_i/Λ ($i = x, y, z$) vs t (s). In particular the line length parallel to the direction of motion, Λ_x (red circles), develops from an initial configuration in which all line length was perpendicular to the direction of motion, Λ_y (blue diamonds) and Λ_z (green triangles). All elements of the line length are normalised by the total line length, Λ. Data points are plotted every 1.875 seconds. Run parameters: $N = 7$, $R = 0.0896$ cm, $a = 0.0223$ cm (such that $R/a = 4$), $\ell = 0.0223$ cm, $\Delta t = 5 \times 10^{-5}$ seconds and $\Delta\xi = 0.00149$ cm (such that $\ell/\Delta\xi = 15$). Note Λ_x is immediately non-zero, unlike at zero temperature.

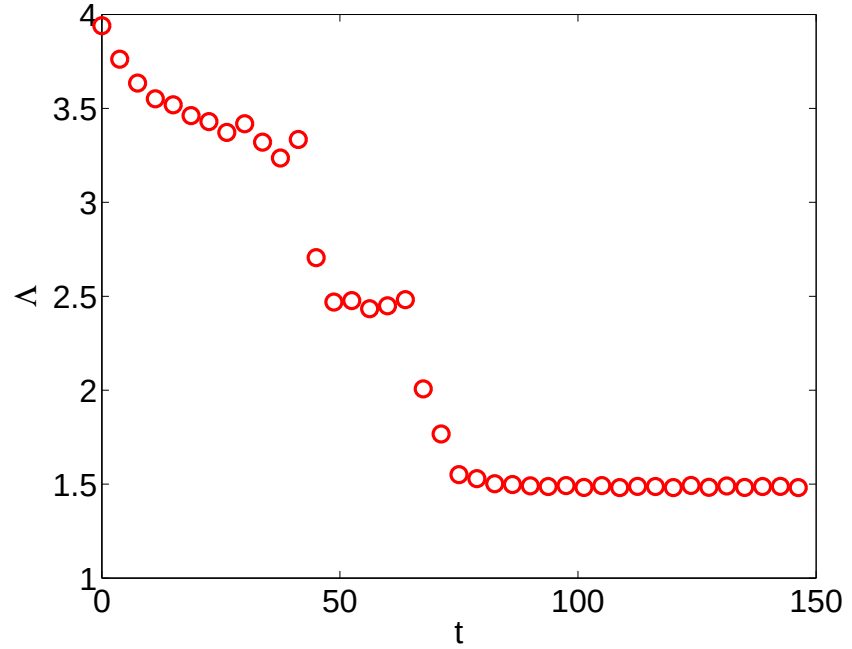

Figure 13.13: Total line length Λ vs t (s) at $T = 2.02$ K. Run parameters: $N = 7$, $R = 0.0896$ cm, $a = 0.0223$ cm (such that $R/a = 4$), $\ell = 0.0223$ cm, $\Delta t = 5 \times 10^{-5}$ seconds and $\Delta\xi = 0.00149$ cm (such that $\ell/\Delta\xi = 15$). Symbols are plotted every 3.75 seconds.

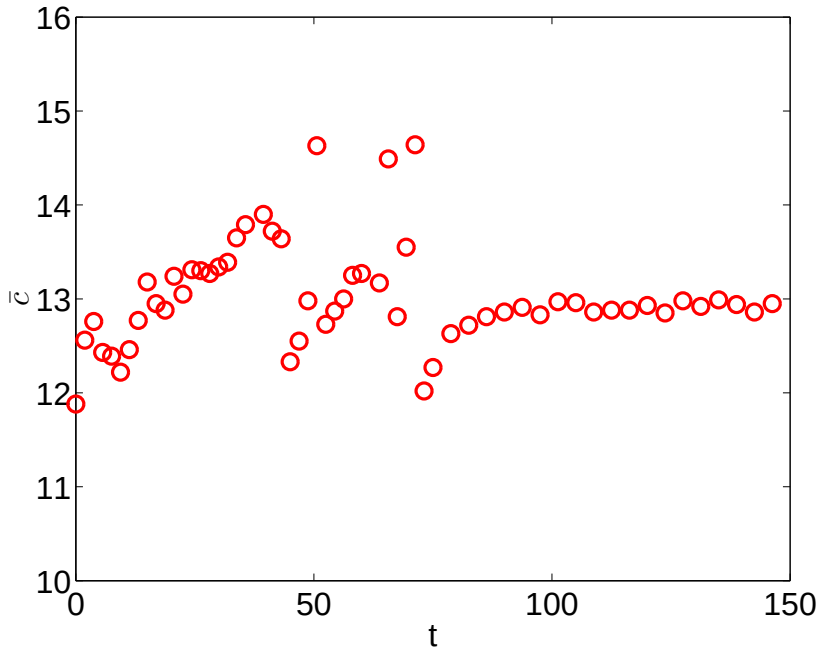

Figure 13.14: Average curvature $\bar{c}$ (cm^{-1}) vs t (s) at $T = 2.02$ K. Run parameters: $N = 7$, $R = 0.0896$ cm, $a = 0.0223$ cm (such that $R/a = 4$), $\ell = 0.0223$ cm, $\Delta t = 5 \times 10^{-5}$ seconds and $\Delta\xi = 0.00149$ cm (such that $\ell/\Delta\xi = 15$). Symbols are used due to the large amount of numerical anomalies.

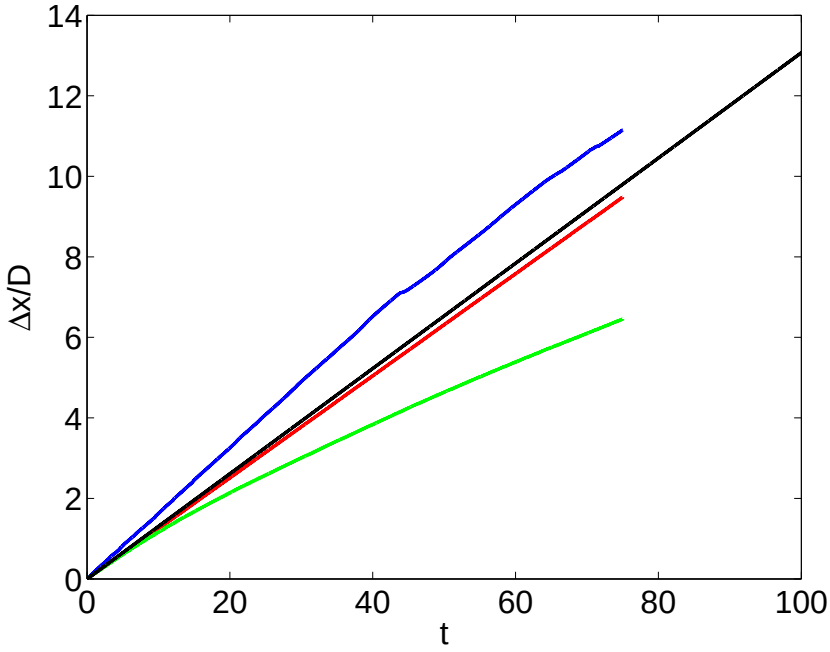

Figure 13.15: Comparison of distance travelled $\Delta x/D$ vs t (s) by (a) $N = 7$ macroscopic ring at T2 (blue), (b) toroidal coil at T2 (red), (c) toroidal coil at T0 (green), and (d) $N = 3$ macroscopic ring at T2 (black).

13.3 Instabilities in $N = 19$

I now perform an identical analysis of an $N = 19$ ring system at T0 and T2. The parameters used are: $R = 0.12$ cm, $a = 0.03$ cm (such that $R/a = 4$), $\ell = 0.015$ cm, $\Delta\xi = 0.00149$ cm and $\Delta t = 5\times10^{-5}$ seconds. Figure 13.16 shows a small selection of snapshots from the development of instabilities at T0. Long wave instabilities once again develop into short wave instabilities. Figure 13.17 shows a similar selection of snapshots from the development of instabilities at T2. Once again, as in the $N = 7$ case, the individual rings lose their coaxiality, although the macroscopic ring retains a roughly toroidal shape. The middle row shows the aftermath of a vortex reconnection. The red ring on the left-hand-side of the image is presently killed by the mutual friction. No small scale instabilities are evident. In both Figure 13.16 and Figure 13.17 the cylinder radius is 0.025 in arbitrary units and the scale (magnification) is either 2.5 or 2.25 as indicated under each subplot. Table 13.5 contains data for the development of instabilities at $T = 0$ and Table 13.6 for their development at $T = 2.02$ K. The picture that emerges from these tables is in agreement with that which emerged from the Tables 13.1 and 13.3 for the case of $N = 7$. The T0 case undergoes an increase in N_p, Λ and (especially in) $\bar{c}$, which increases by an order of magnitude. It is also notable that the number of components N in the system is steadily increasing in the 19 ring case. This is due to the emission of tiny vortex rings due to self-reconnections. Whereas the 7 ring case (see Table 13.1) does not yet show signs of increasing numbers of components. The distinction may lie in the difference in the magnitude of $\bar{c}$. In the 7 ring case $\bar{c} \approx 135$ cm^{-1}, but in the 19 ring case it is much greater $\bar{c} \approx 199$ cm^{-1}. This much higher value may be a cause of the higher level of emission of small vortex rings. The T2 case of 19 rings appears to be headed towards the approximately steady state attained in the $N = 7$ case. Tables 13.7 and 13.8 together with Figures 13.18 and 13.21 show the development of the fractional line length parallel to the direction of motion Λ_x in the T0 and T2 regimes for $N = 19$. In the T2 regime an approximately steady state appears to have been reached, similar to $N = 7$. The T0 regime also mirrors the $N = 7$ case, such that the fractional line lengths appear to be heading towards the same value. In Figures 13.19 to 13.23 I plot the development of the magnitude of the total line length and the average curvature for T0 and T2. The average curvature in the T0 regime appears to have reached a highly turbulent steady state and the T2 regime appears to have reached a steady state with low level of turbulence.

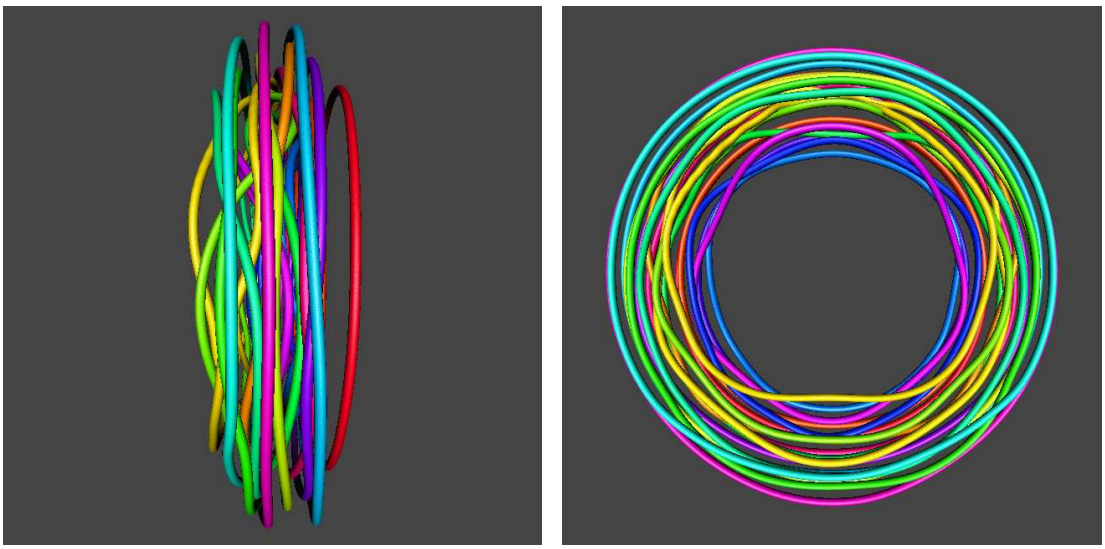

(a) $t = 20$ s, scale $= 2.5$ *(b)* $t = 20$ s, scale $= 2.5$

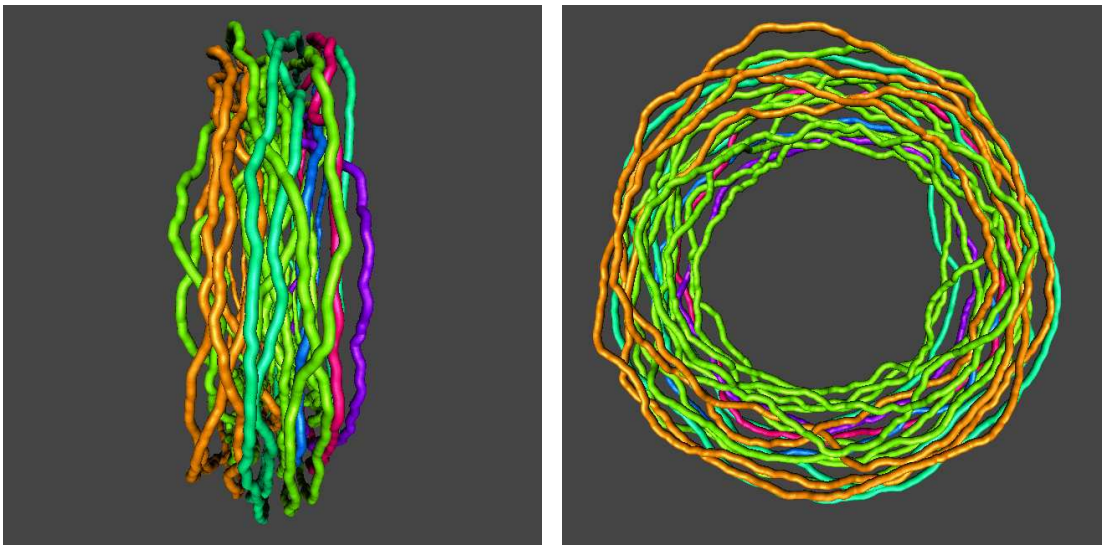

(c) $t = 30$ s, scale $= 2.5$ *(d)* $t = 30$ s, scale $= 2.5$

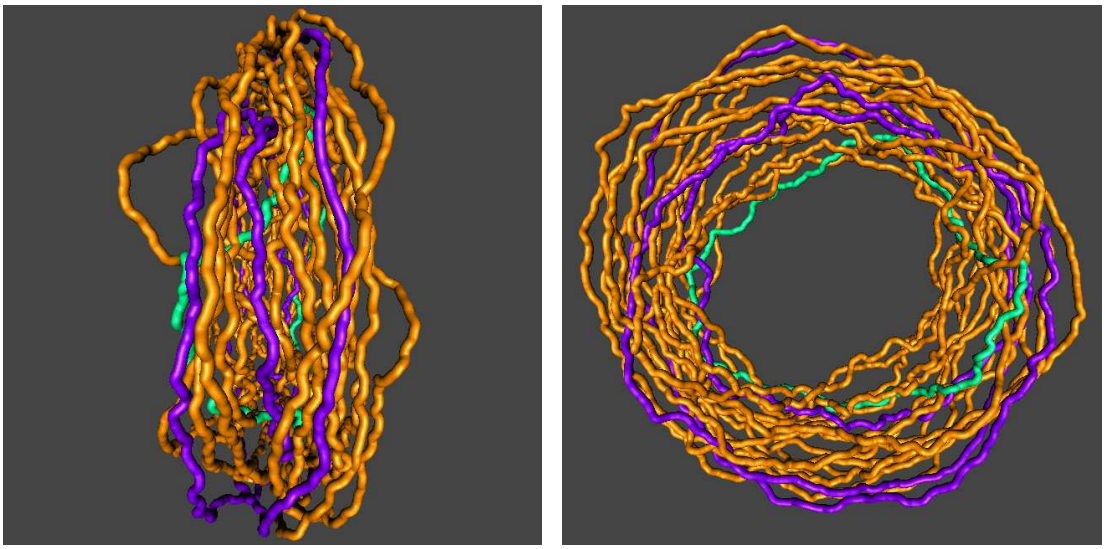

(e) $t = 40$ s, scale $= 2.5$ *(f)* $t = 40$ s, scale $= 2.5$

Figure 13.16: Selection of Knotplot images from development of instabilities in $N = 19$ system evolved using Biot-Savart at $T = 0$ K. Side (left panel) and rear (right panel) views. Top row consists of 18 components, middle row of 6 and bottom row of 3.

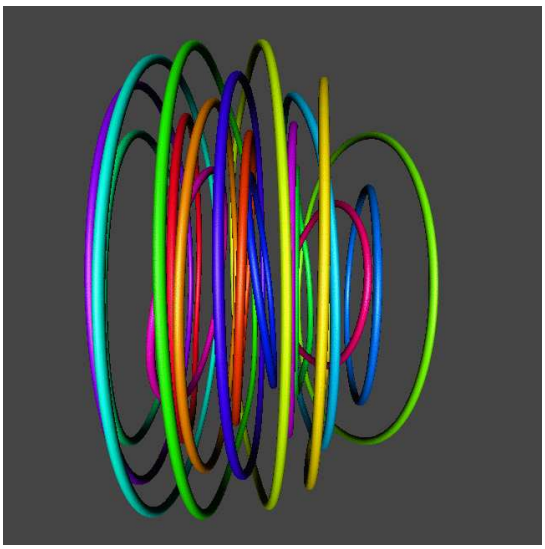

(a) $t = 40$ s, scale $= 2.5$

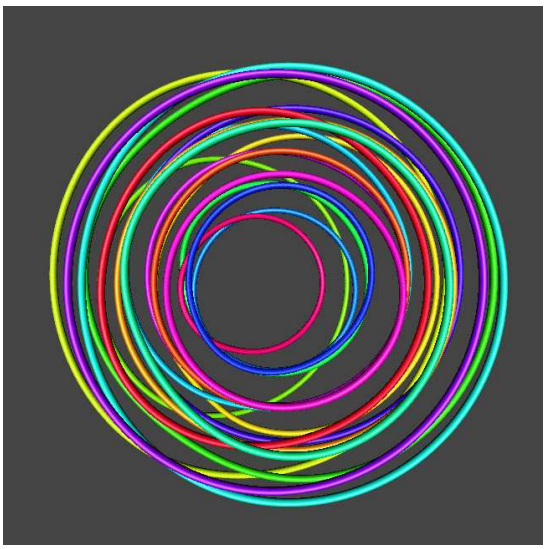

(b) $t = 40$ s, scale $= 2.5$

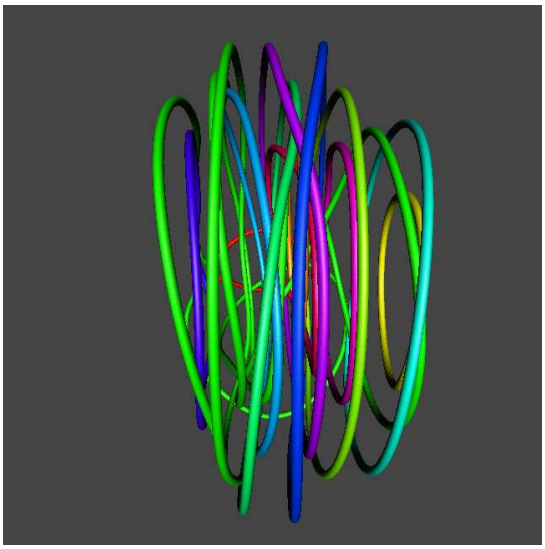

(c) $t = 60$ s, scale $= 2.25$

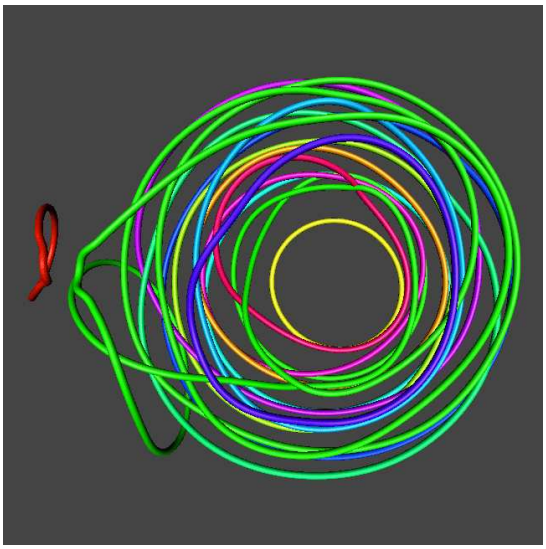

(d) $t = 60$ s, scale $= 2.25$

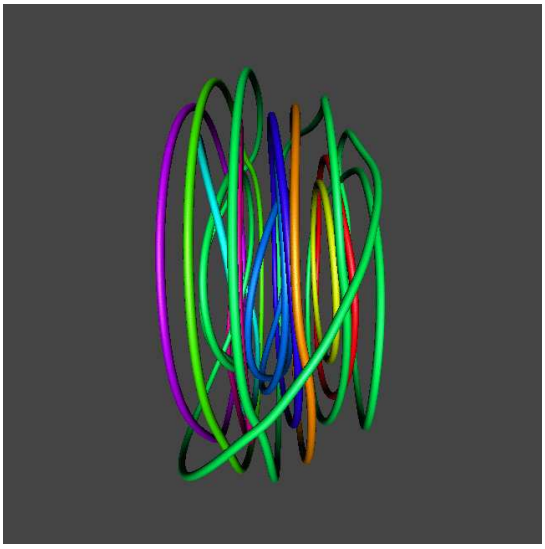

(e) $t = 80$ s, scale $= 2.25$

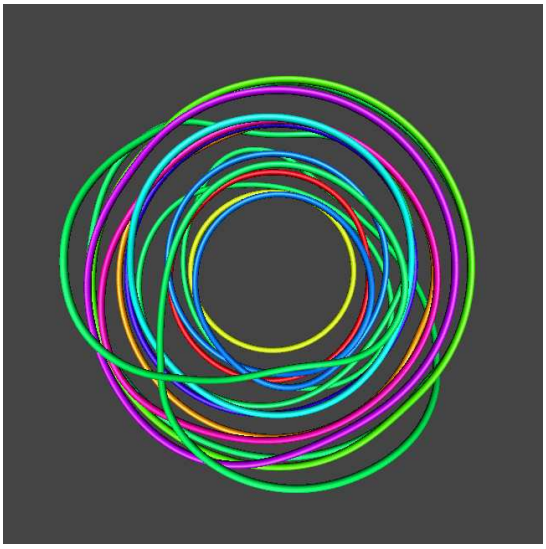

(f) $t = 80$ s, scale $= 2.25$

Figure 13.17: Selection of Knotplot images from development of instabilities in $N = 19$ system evolved using Biot-Savart at $T = 2.02$ K. Side (left panel) and rear (right panel) views. Top row consists of 18 components, middle row of 13 and bottom row of 10.

t (s)	N_p	recons	N	Λ (cm) (3dp)	$\bar{c}$ (cm/s^2) (2dp)	Δx (cm) (3dp)	$\Delta x/D$ (2dp)	v_x (cm/s) (4dp)
0	12825	0	19	14.326	10.87	0	0	0.0471
10	12825	0	19	14.371	10.58	0.463	1.93	0.0456
20	13128	1	18	14.497	13.13	0.924	3.85	0.0462
30	15177	204	6	15.713	121.65	1.372	5.72	0.0392
40	16710	967	3	17.339	174.61	1.792	7.47	0.0359
50	18759	2559	8	19.754	198.72	2.170	9.04	0.0326
60	21084	4387	15	22.451	199.54	2.490	10.38	0.0277

Table 13.5: Development of instabilities in $N = 19$ system at $T = 0$ K.

t (s)	N_p	recons	N	Λ (cm) (3dp)	$\bar{c}$ (cm/s^2) (2dp)	Δx (cm) (3dp)	$\Delta x/D$ (2dp)	v_x (cm/s) (4dp)
0	12825	0	19	14.321	10.53	0	0	0.0471
10	11713	0	19	12.724	10.37	0.424	1.77	0.0375
20	11565	0	19	12.370	10.75	0.843	3.51	0.0373
30	11719	0	19	12.241	10.84	1.258	5.24	0.0368
40	11429	0	18	11.774	10.58	1.666	6.94	0.0353
50	11552	6	16	11.788	10.74	2.070	8.63	0.0343
60	11225	17	13	11.421	11.31	2.450	10.21	0.0301
70	9861	31	13	10.154	10.66	2.814	11.73	0.0327
80	9737	36	10	9.996	10.60	3.183	13.26	0.0319
90	9677	38	12	9.984	10.34	3.555	14.81	0.0321

Table 13.6: Development of instabilities in $N = 9$ system at $T = 2.02$ K with imposed normal fluid velocity field. 'recons' refers to visible reconnections only, not including algorithmic reconnections.

t (s)	Λ_x (cm)	Λ_y (cm)	Λ_z (cm)	Λ (cm)
0	0.00	9.12	9.12	14.33
5	0.00	9.12	9.12	14.33
10	0.00	9.15	9.15	14.37
15	0.02	9.11	9.11	14.31
20	1.29	9.13	9.14	14.50
25	2.74	9.35	9.27	15.08
30	3.60	9.58	9.52	15.71
35	4.55	9.81	9.79	16.54
40	5.35	10.10	10.11	17.34
45	6.38	10.57	10.47	18.41
50	7.30	10.94	11.18	19.75
55	8.19	11.73	11.62	21.14
60	9.00	12.46	12.11	22.45

Table 13.7: Values of total line length Λ and elements of line length Λ_x, Λ_y and Λ_z in x, y and z directions during the development of instabilities over time in an initial configuration of $N = 19$ at T0 using Biot-Savart law.

t (s)	Λ_x (cm)	Λ_y (cm)	Λ_z (cm)	Λ (cm)
0	0.00	9.12	9.12	14.32
5	0.02	8.40	8.40	13.20
10	0.01	8.10	8.10	12.72
15	0.02	7.98	7.98	12.53
20	0.04	7.87	7.88	12.37
25	0.10	7.84	7.84	12.32
30	0.22	7.79	7.79	12.24
35	0.55	7.70	7.69	12.11
40	0.79	7.50	7.42	11.77
45	1.45	7.45	7.41	11.89
50	1.35	7.38	7.42	11.79
55	1.60	7.26	7.26	11.60
60	1.42	7.10	7.02	11.42
65	1.45	6.69	6.65	10.83
70	1.16	6.21	6.34	10.15
75	0.73	6.26	6.22	9.85
80	0.99	6.29	6.30	10.00
85	0.93	6.29	6.26	9.93
90	0.78	6.33	6.30	9.98

Table 13.8: Values of total line length Λ and elements of line length Λ_x, Λ_y and Λ_z in x, y and z directions during the development of instabilities over time in an initial configuration of $N = 19$ at T2 using Biot-Savart law.

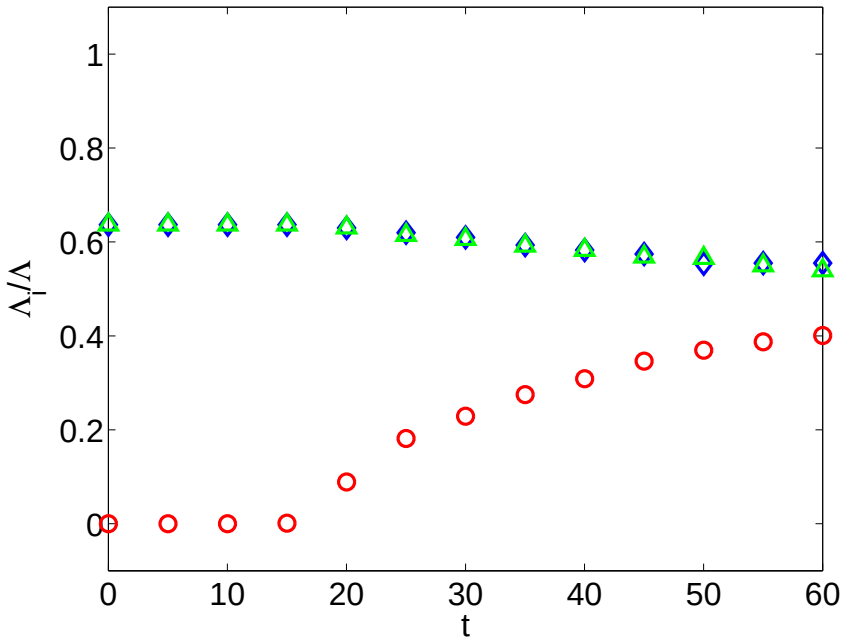

Figure 13.18: Fractional line lengths Λ_i/Λ ($i = x, y, z$) vs t (s) for $N = 19$ at T0. In particular the line length parallel to the direction of motion, Λ_x (red circles), develops from an initial configuration in which all line length was perpendicular to the direction of motion, Λ_y (blue diamonds) and Λ_z (green triangles). All elements of the line length are normalised by the total line length, Λ. Data points are plotted every 5 seconds.

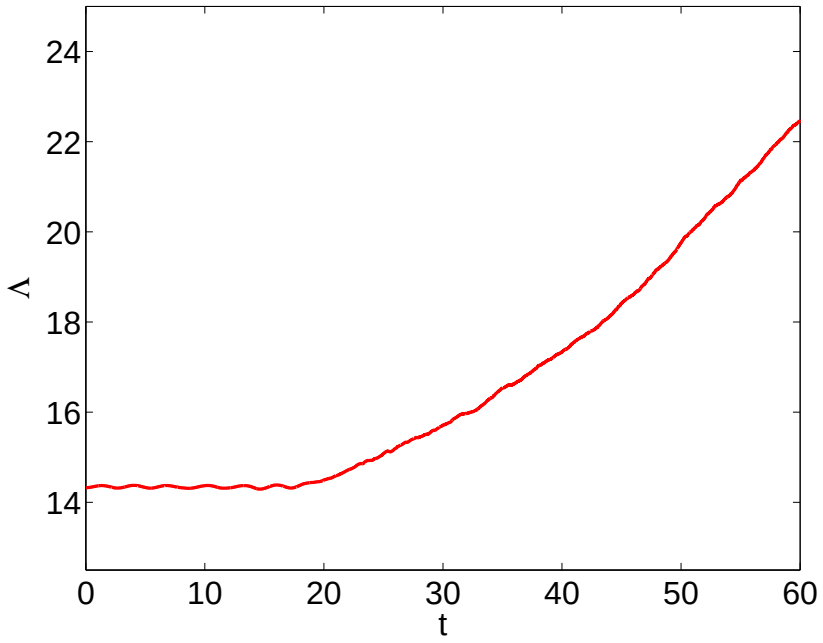

Figure 13.19: Total line length Λ vs t (s) at T0 for $N = 19$.

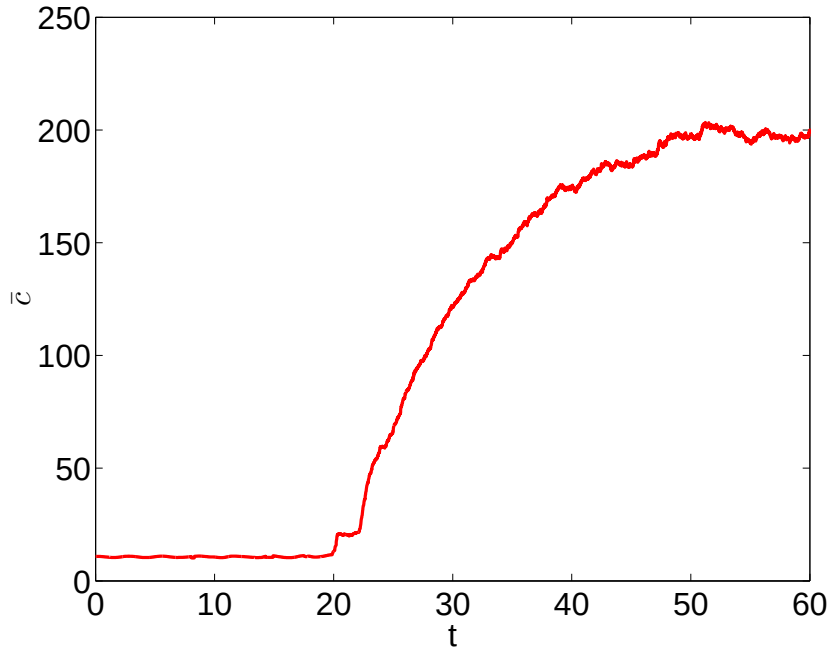

Figure 13.20: Average curvature $\bar{c}$ (cm^{-1}) vs t (s) T0 for $N = 19$.

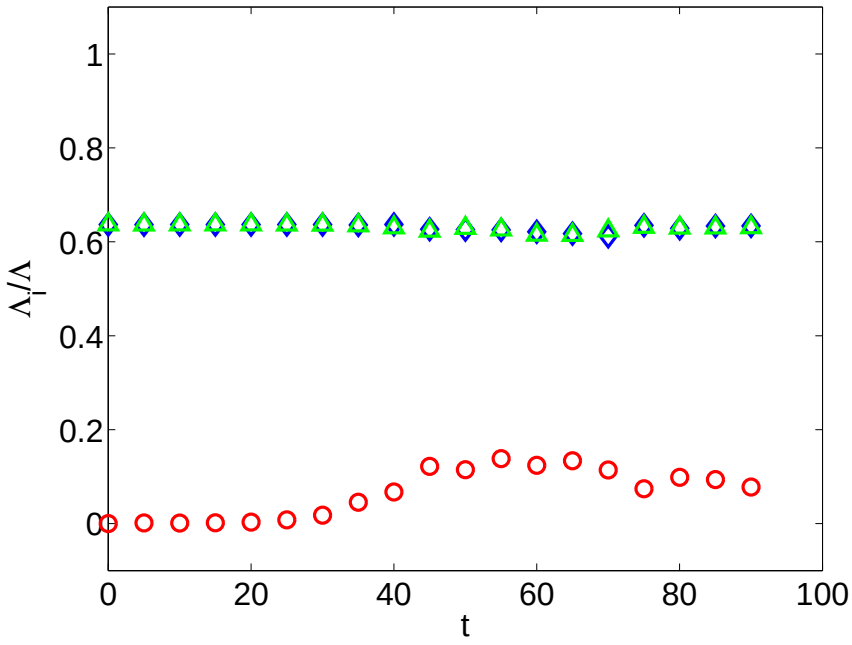

Figure 13.21: Fractional line lengths Λ_i/Λ ($i = x, y, z$) vs t (s) for $N = 19$ at T2. In particular the line length parallel to the direction of motion, Λ_x (red circles), develops from an initial configuration in which all line length was perpendicular to the direction of motion, Λ_y (blue diamonds) and Λ_z (green triangles). All elements of the line length are normalised by the total line length, Λ. Data points are plotted every 5 seconds. Note Λ_x is immediately non-zero, unlike at zero temperature.

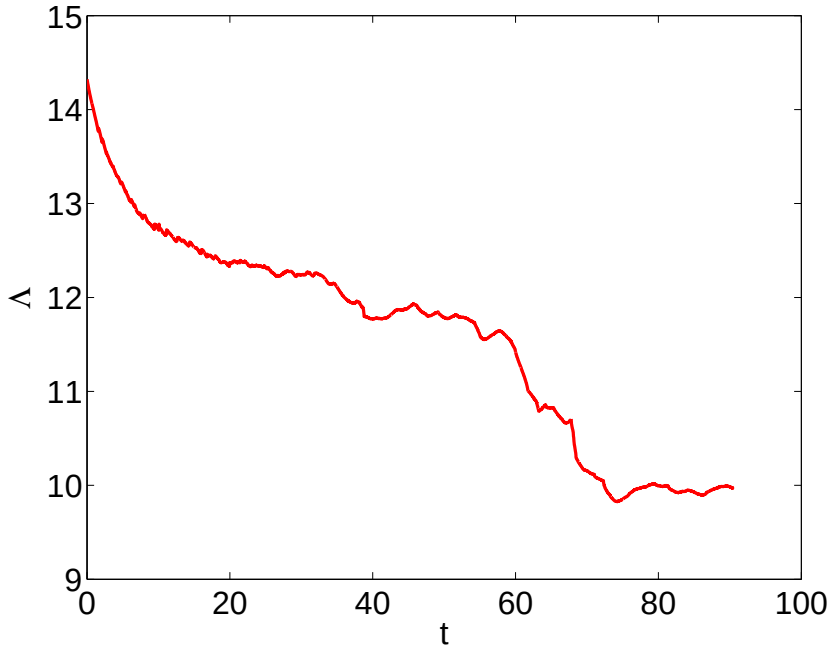

Figure 13.22: Total line length Λ vs t (s) at T2 for $N = 19$.

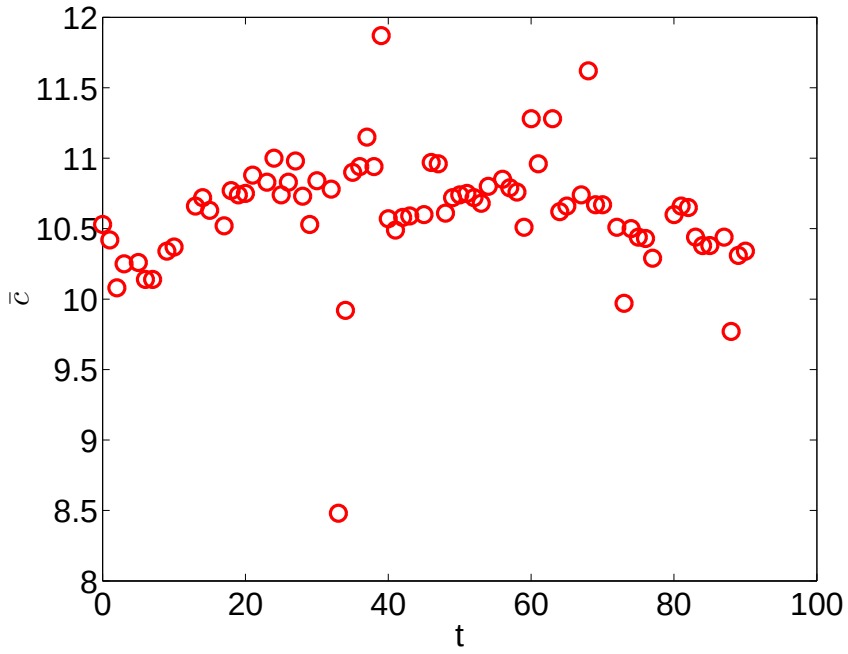

Figure 13.23: Average curvature $\bar{c}$ (cm^{-1}) vs t (s) T2 for $N = 19$. Symbols are used due to the large amount of numerical anomalies.

13.4 Parallel and antiparallel reconnections

Although all reconnections by definition must be locally nonparallel since the reconnecting vortex lines must meet at an angle in order to reconnect, there are two ways of describing the larger scale geometry of the reconnection: parallel and antiparallel. I have observed both of these types of reconnections in simulations of $N = 7$. I include schematic diagrams of a pair of vortex rings before and after each of these types of reconnections (Figure 13.24). I will describe the way in which these two types of reconnections occur in the context of vortex rings.

An antiparallel reconnection is the simpler of the two to describe. In an antiparallel reconnection 2 (or more) non-coaxial rings collide in a figure-of-eight formation (Figure 13.24(c)). This may be the result of the rings having different orientations or of one ring being smaller and hence faster than the other. The two rings reconnect at the two points of contact. This may not happen simultaneously, but within a short period of time. The result is a large, hollow-centred, figure-of-eight shaped ring with a smaller, more circular ring inside it (Figure 13.24(d)).

Parallel reconnections involve 2 rings that are possibly still coaxial, but whose geometry differs as in Figure 13.24(a). This may be the result of long wave length perturbations that change the shape of the rings. As a result of their different shapes, the red ring (at the back) 'feels' the blue ring (at the front) in different ways. The velocity field of the blue ring is positive (into the page) inside it and negative (out of the page) outside it. This means that the segments of the red ring which are in line with the inside of the blue ring will receive a positive velocity contribution from the blue ring. Whereas the segments of the red ring which are in line with the outside of the blue ring will receive a negative velocity contribution from the blue ring. The net result is that the 'inner' segments of the red ring will move faster than the 'outer' segments, such that the 'inner' segments will perform their part of the leapfrog manoeuvre whilst the 'outer' segments will trail behind. The δ symbol in Figure 13.24(a) is the distance between the segments of the blue and red rings which are closer together and the Δ symbol is the distance between the segments which are further apart ($\delta < \Delta$). Eventually the red ring collides with the blue ring and reconnections occur at the four points of contact. Once again this need not happen simultaneously.

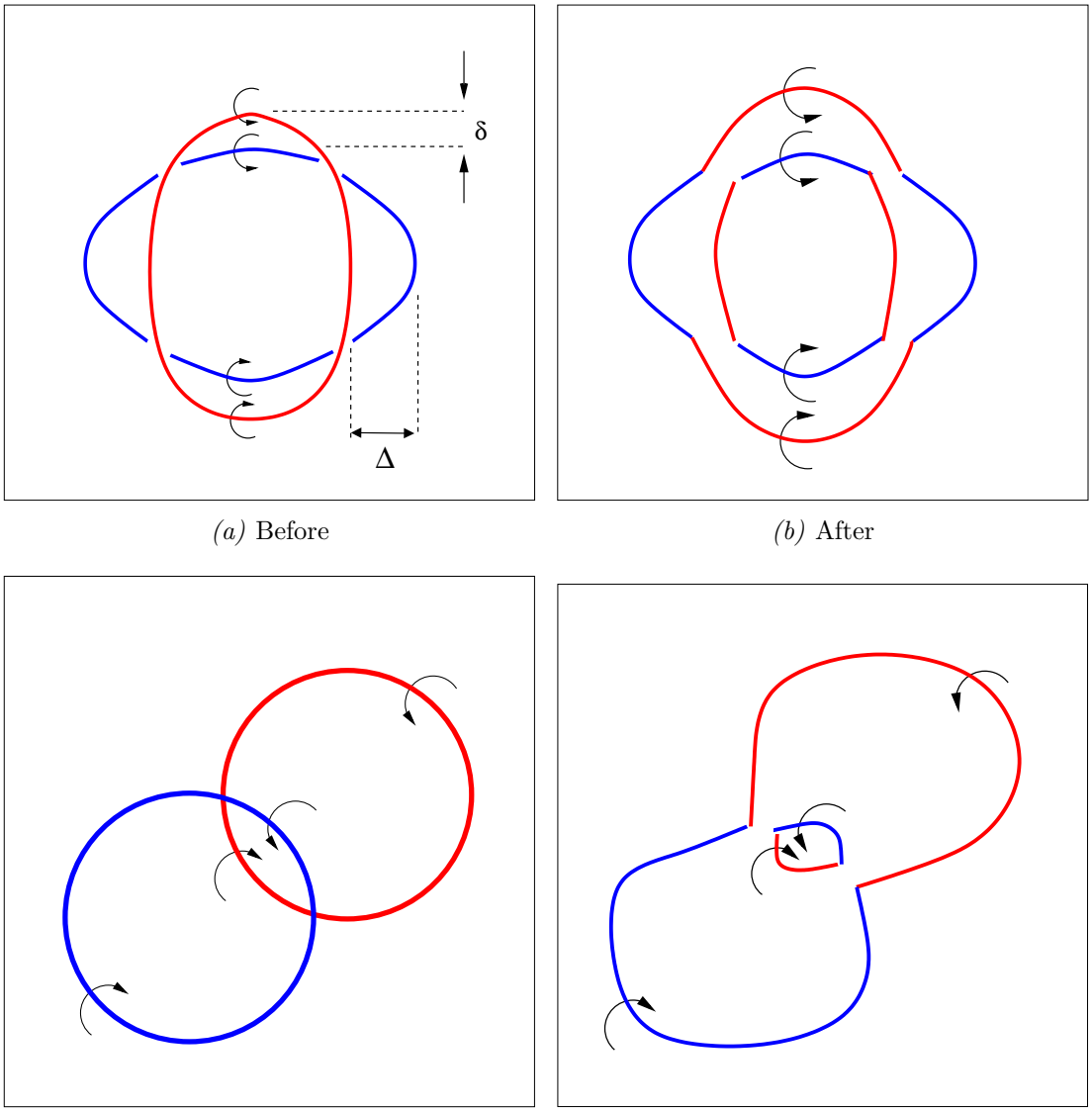

(a) Before *(b)* After

(c) Before *(d)* After

Figure 13.24: Schematic diagrams of parallel and antiparallel reconnections of two vortex rings, coloured red and blue. (a) Before and (b) after a parallel reconnection. (c) Before and (d) after an antiparallel reconnection. Arrows show the sense of the circulation.

13.5 Parallel reconnections in $N = 7$ at zero temperature

I present here 3D close-up images of a pair of parallel reconnections which occur at zero temperature. They are in fact the first reconnections to occur in this system. The first reconnection occurs at the bottom left of the vortex rings and the second, a short time later, at the top right. The two rings that reconnect are coloured light green and dark green, the light green ring being behind the dark green ring.

I firstly show three images from a distance (Figure 13.25). The first image is before the first reconnection, the second in between the two reconnections and the third after the second reconnection. In the first image (Figure 13.25(a-b)) the top and bottom of the light green ring are 'caught' on the dark green ring. In the second image (Figure 13.25(c-d)) the bottom reconnection has taken place so that the bottom of the light green ring is now in front of the bottom of the dark green ring, or, more accurately put, the light green and dark green rings have exchanged their bottom segments. In the third image (Figure 13.25(e-f)) the same has occurred at the top of the rings, so that the light green ring is now wholly in front of the dark green ring, having exchanged both bottom and top segments. The cylinders used in these images are 0.025 radius in arbitrary units and the scale (magnification) is 3.5.

I next show close-up images of the bottom reconnection (Figures 13.26 and 13.27). These images show a few slides immediately before and after the reconnection event, which takes place at $t = 58.995$ seconds. In this reconnection event both points of contact between the light green and dark green line reconnect simultaneously (or at least within 0.0075 seconds of each other). Small perturbations can be seen running along the vortex rings involved in the reconnection immediately after the reconnection takes place. In the images looking 'up' from the bottom of the ring, the top of the ring at which the second reconnection will take place is clearly visible. In the snapshot immediately after the reconnection event ($t = 59.25$ seconds) the light green ring has already moved round underneath the dark green one. This is probably due to the strength of the $1/r$ velocity field in the vicinity of the rings.

In the top reconnection (Figures 13.28 and 13.29) the reconnection takes place in two stages at the two points of contact between the light green and dark green vortices. The point of contact further away from the viewer reconnects first at $t = 59.295$ seconds and then the closer point of contact at 59.31 seconds. In the interim both rings are coloured light green. The same small perturbations can be seen travelling along the rings immediately after each reconnection event. The rings do not wrap around each other immediately after the reconnection event, as they did in the bottom reconnection.

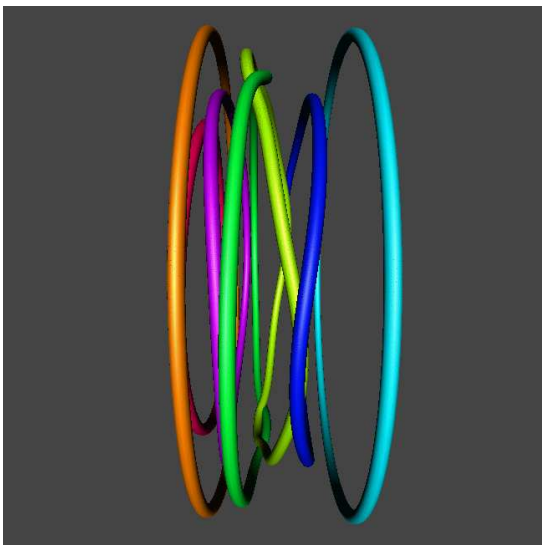

(a) 58.875 s, scale = 3.5

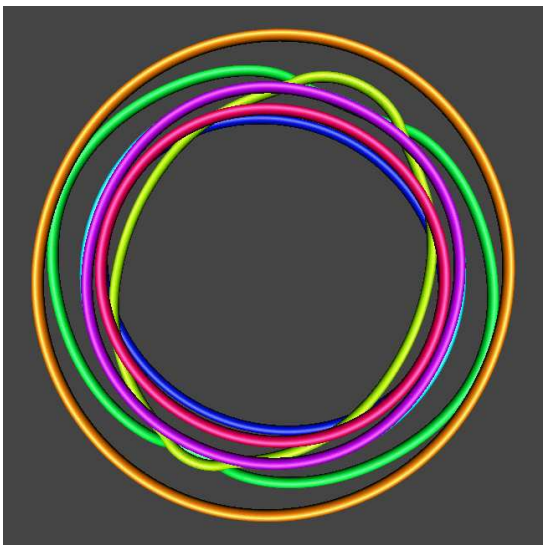

(b) 58.875 s, scale = 3.5

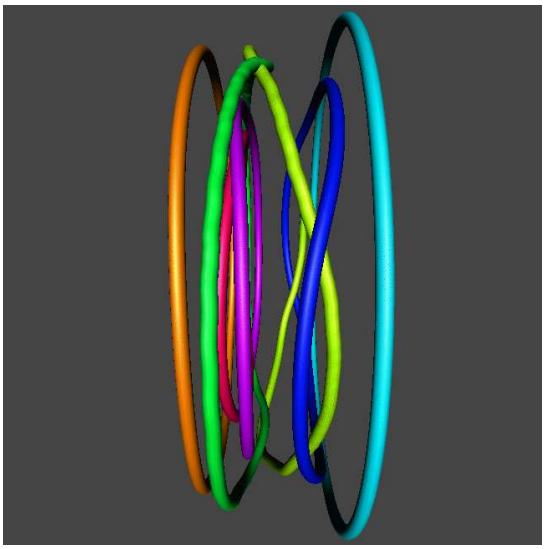

(c) 59.25 s, scale = 3.5

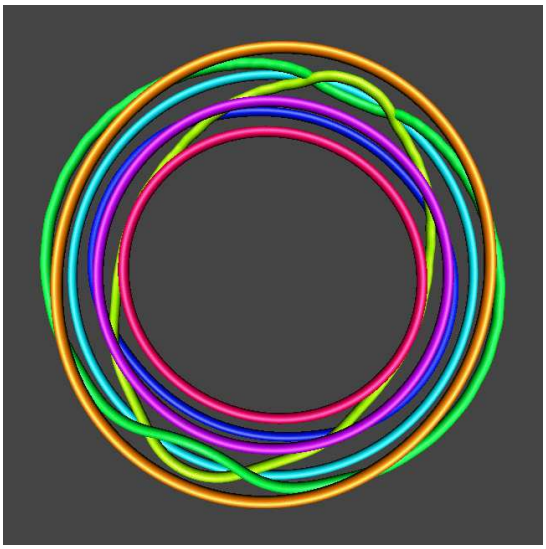

(d) 59.25 s, scale = 3.5

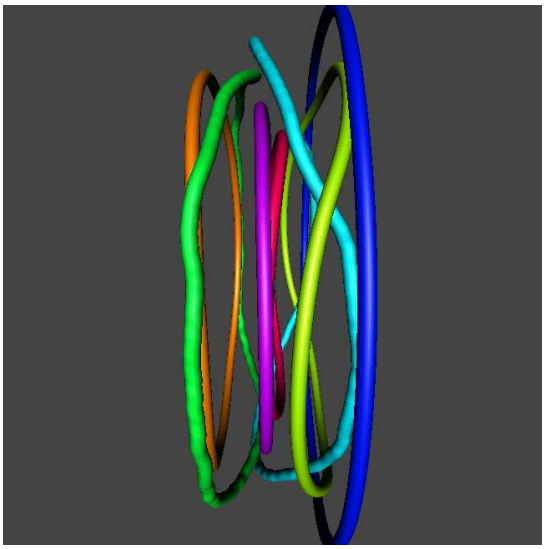

(e) 59.625 s, scale = 3.5

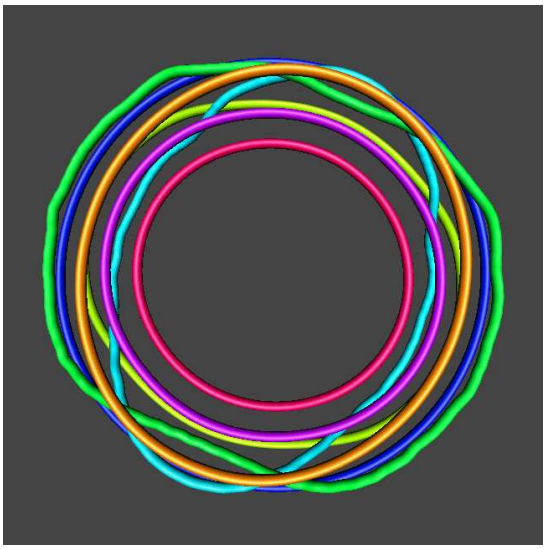

(f) 59.625 s, scale = 3.5

Figure 13.25: (a-b) Before, (c-d) in between and (e-f) after two parallel reconnection events at T0.

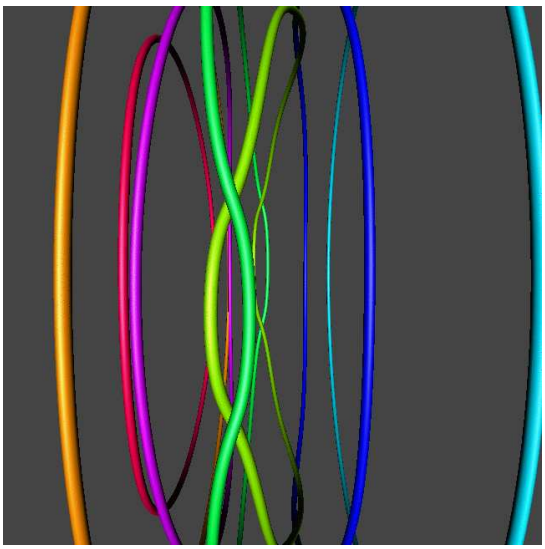

(a) 58.875 s, scale = 5

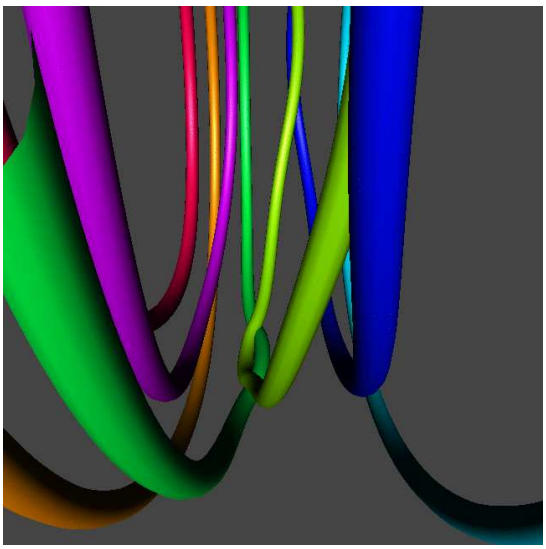

(b) 58.875 s, scale = 5

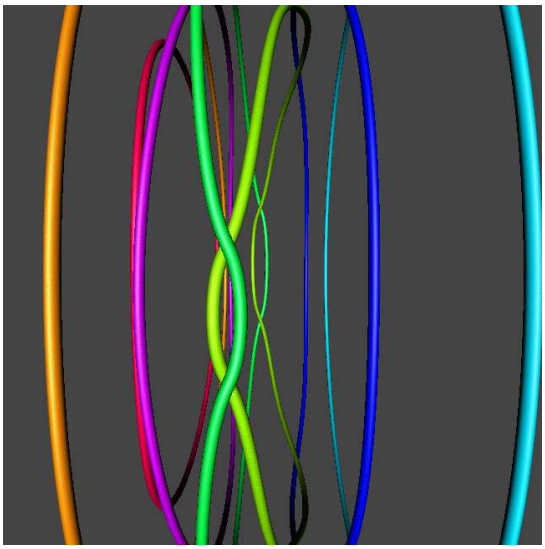

(c) 58.95 s, scale = 5

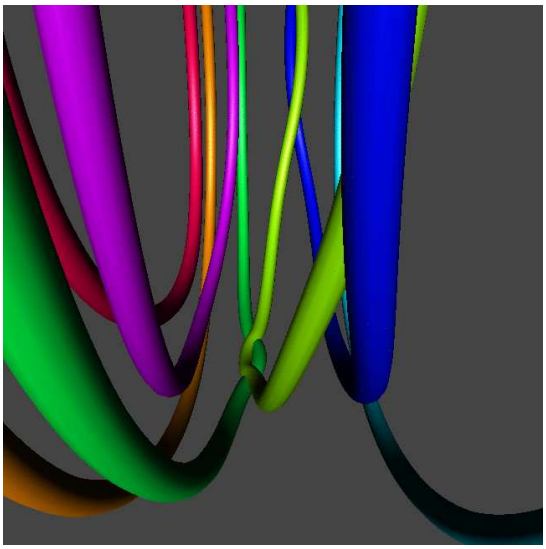

(d) 58.95 s, scale = 5

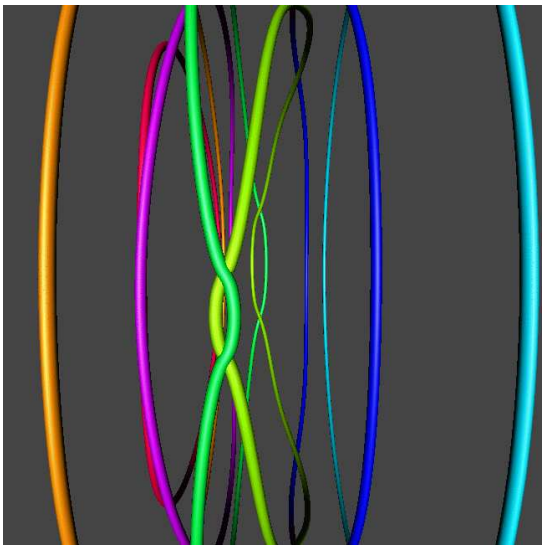

(e) 58.9875 s, scale = 5

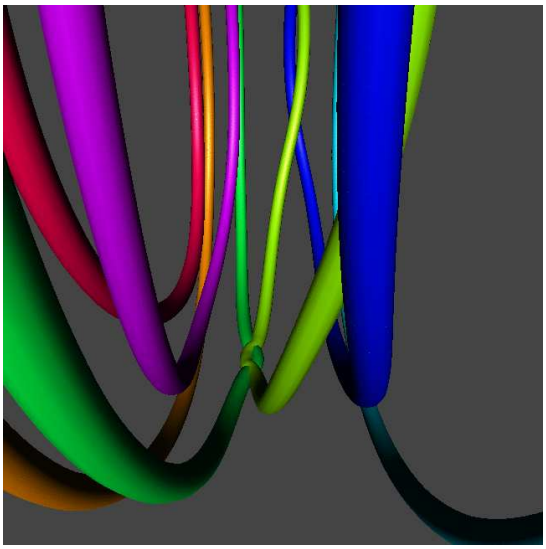

(f) 58.9875 s, scale = 5

Figure 13.26: Bottom parallel reconnection event at T0. (a,c,e) Bottom images cylinder radius 0.01. (b,d,f) Side images cylinder radius 0.025.

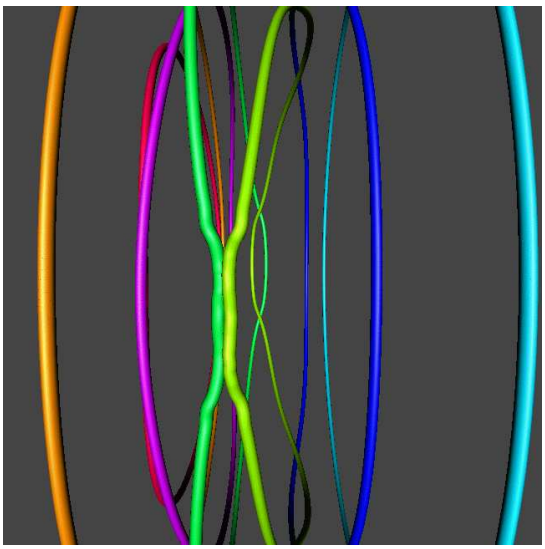

(a) 58.995 s, scale = 5

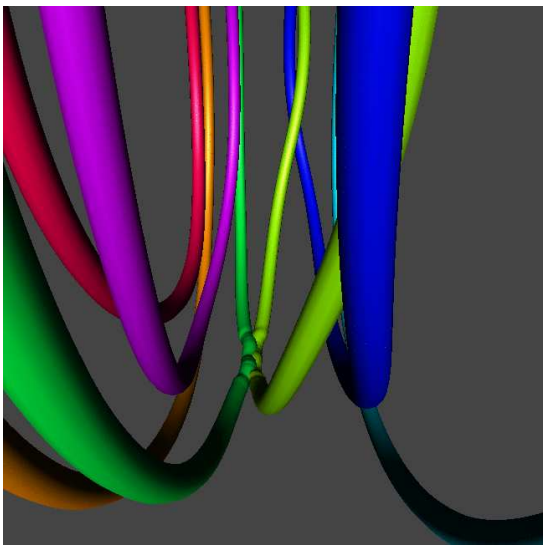

(b) 58.995 s, scale = 5

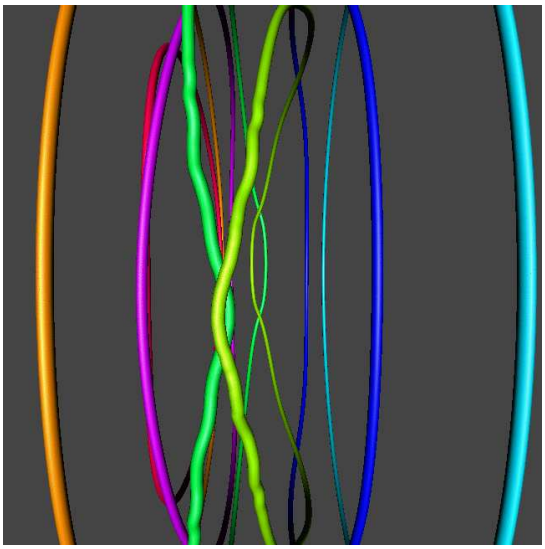

(c) 59.01 s, scale = 5

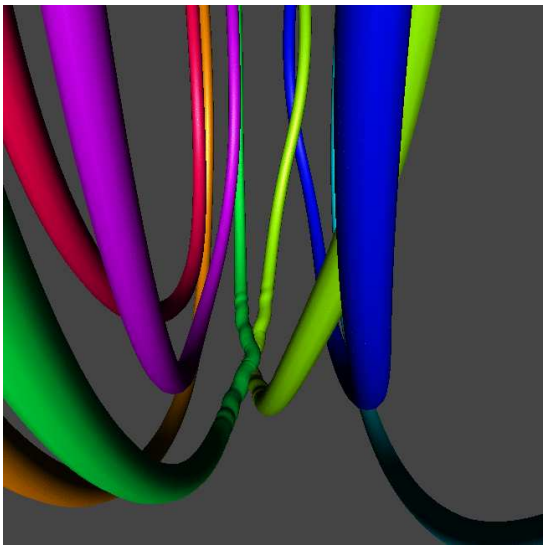

(d) 59.01 s, scale = 5

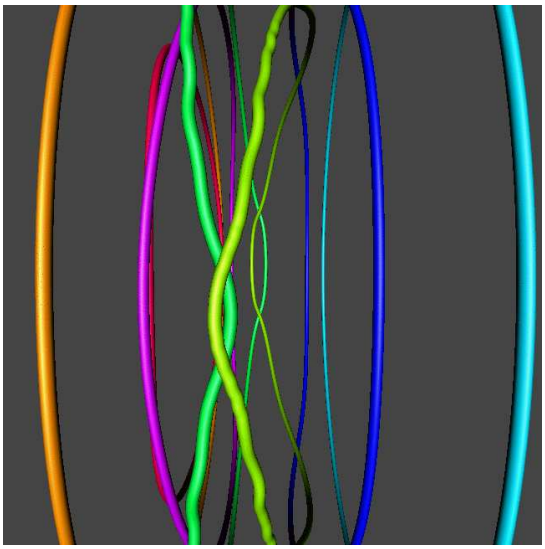

(e) 59.025 s, scale = 5

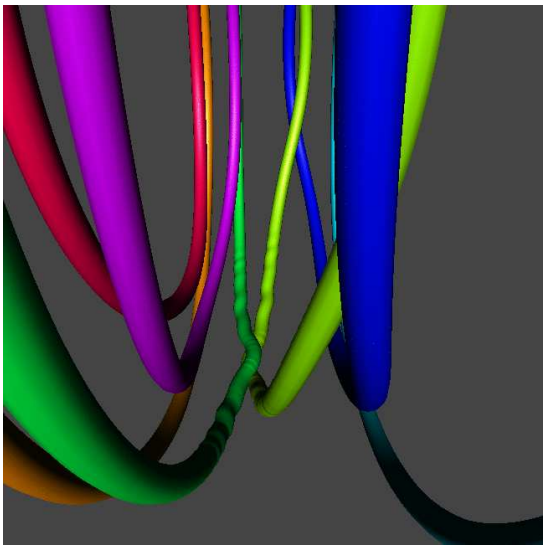

(f) 59.025 s, scale = 5

Figure 13.27: Bottom parallel reconnection event at T0. (a,c,e) Bottom images cylinder radius 0.01. (b,d,f) Side images cylinder radius 0.025.

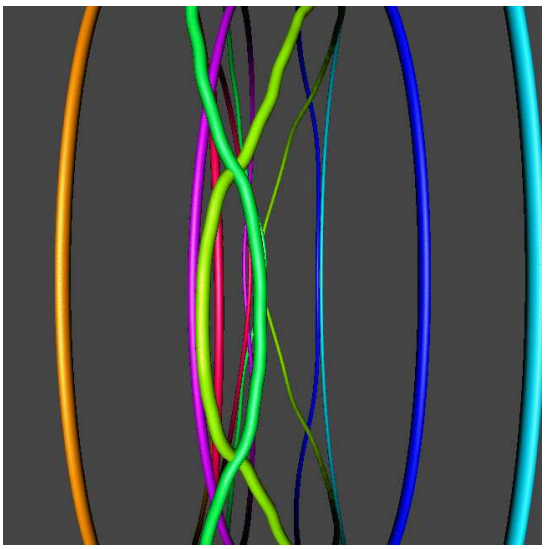

(a) 59.2875 s, scale = 5

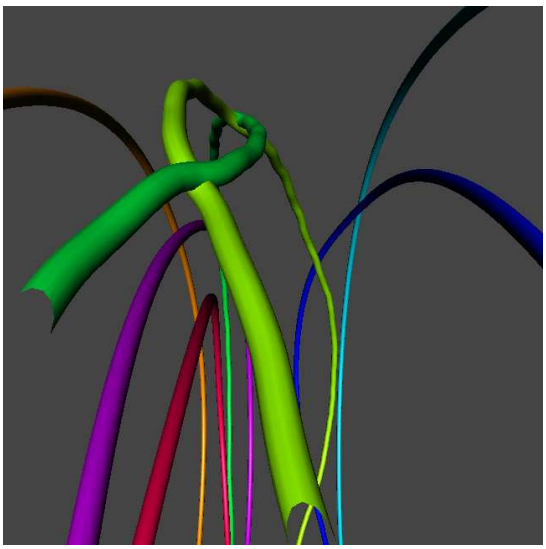

(b) 59.2875 s, scale = 5

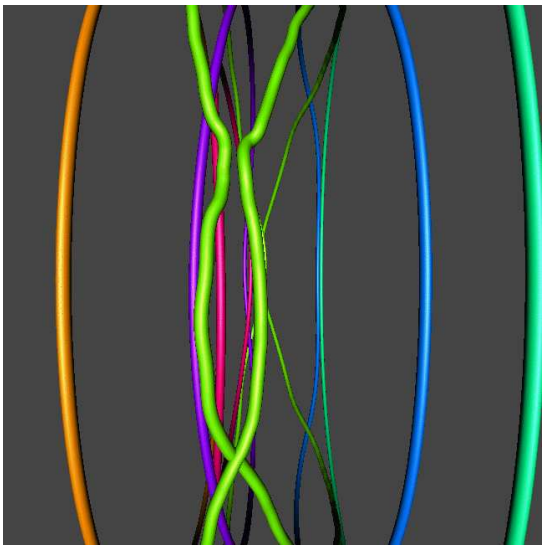

(c) 59.295 s, scale = 5

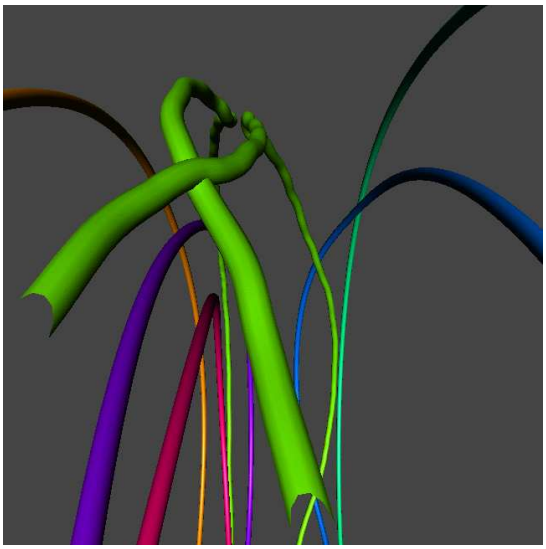

(d) 59.295 s, scale = 5

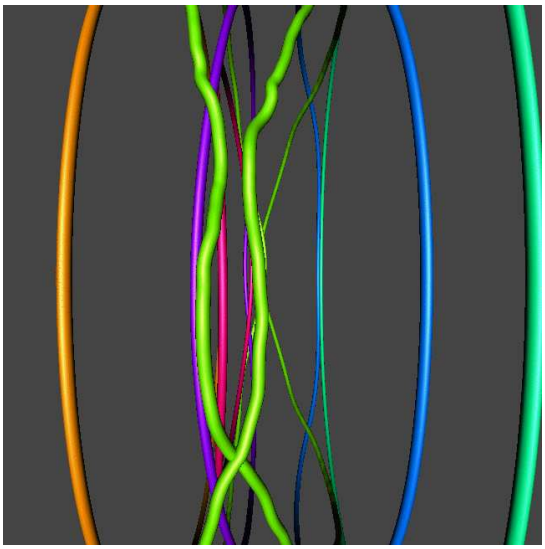

(e) 59.3025 s, scale = 5

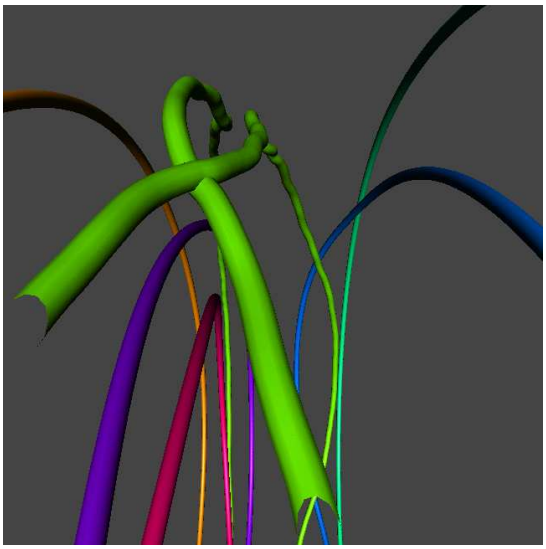

(f) 59.3025 s, scale = 5

Figure 13.28: Top parallel reconnection event at T0. (a,c,e) Top images cylinder radius 0.01. (b,d,f) Side images cylinder radius 0.01.

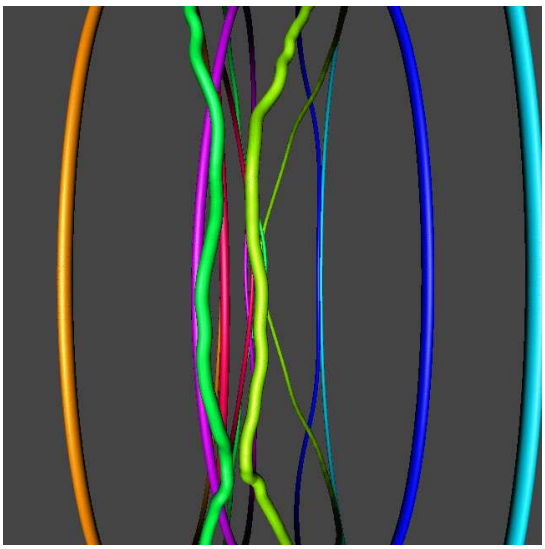

(a) 59.31 s, scale = 5

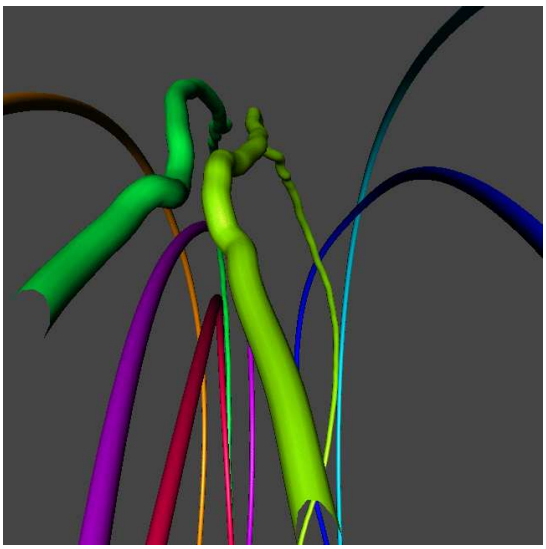

(b) 59.31 s, scale = 5

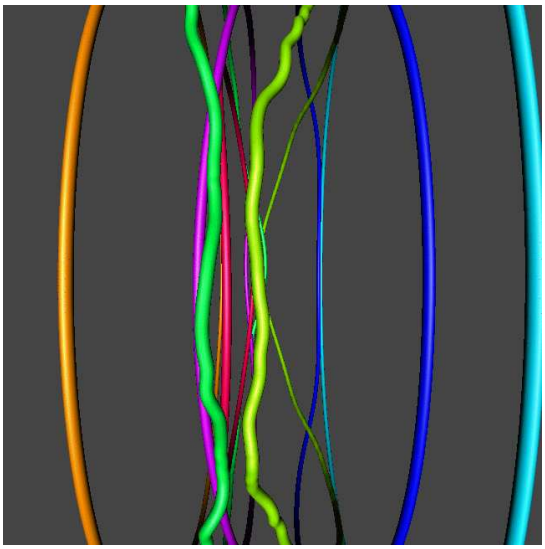

(c) 59.3175 s, scale = 5

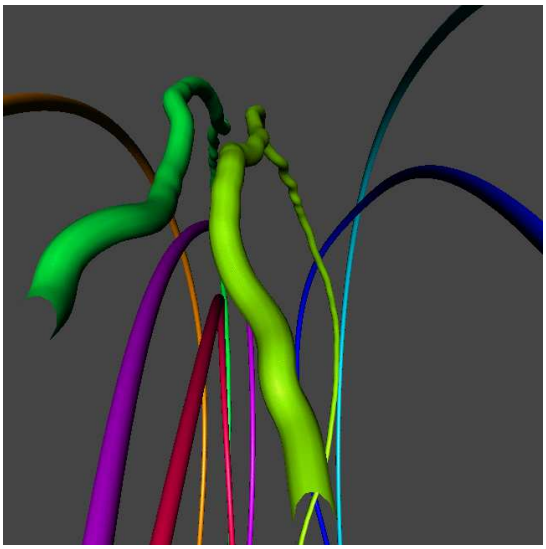

(d) 59.3175 s, scale = 5

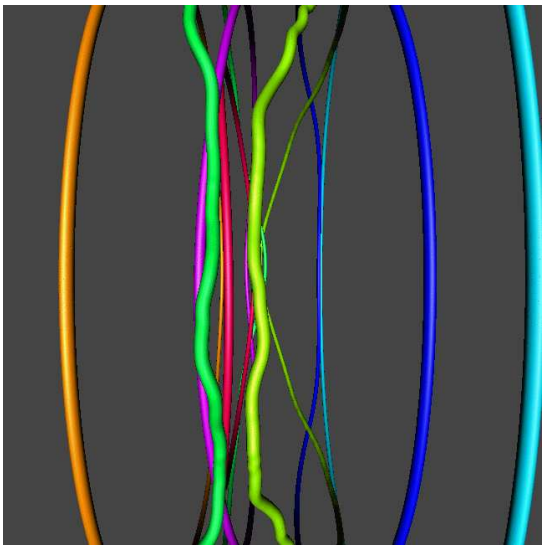

(e) 59.325 s, scale = 5

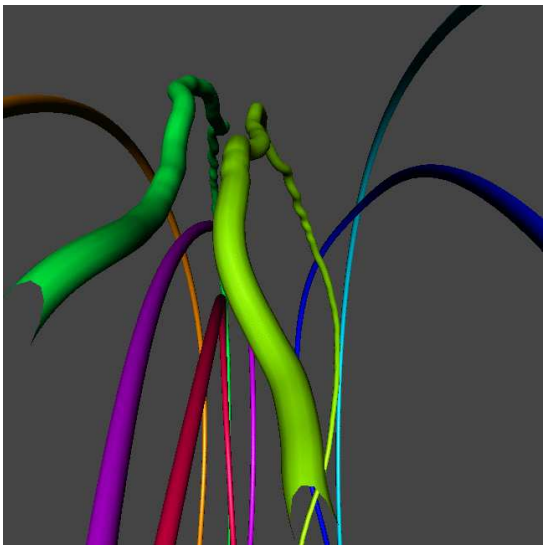

(f) 59.325 s, scale = 5

Figure 13.29: Top parallel reconnection event at T0. (a,c,e) Top images cylinder radius 0.01. (b,d,f) Side images cylinder radius 0.01.

13.6 Antiparallel reconnections in $N = 7$ at finite temperature in the presence of a normal fluid velocity field

Reconnections are not as common at finite temperature as at zero temperature. There are in fact only 7 which take place in the $N = 7$ system before the toroidal coil develops. Out of these 5 are antiparallel reconnections and 2 are parallel reconnections. I will show images of the last 2 antiparallel reconnections which occur just prior to the development of the toroidal coil. In these images (Figures 13.30 and 13.31) the blue ring collides with the copper ring from the rear. Both points of contact reconnect simultaneously. The copper ring retains a hollow figure-of-eight shape for a while until the sharp reconnection cusps soften, probably due to the action of mutual friction. The small blue ring escapes from the copper toroidal coil. It can be seen shrinking in size. By $t = 72$ seconds it has disappeared. The images use uniform cylinder radius 0.025 in arbitrary units.

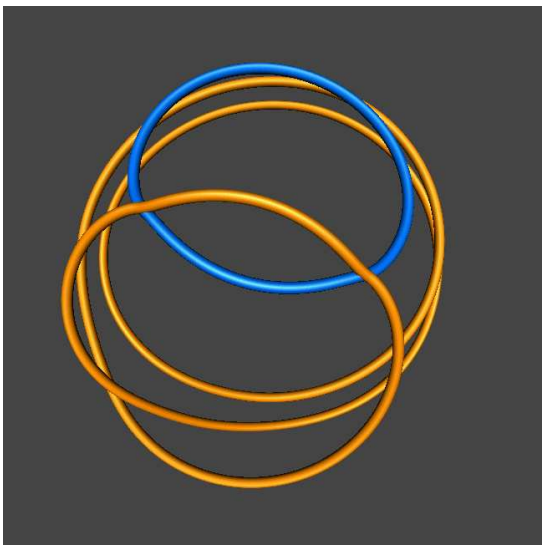

(a) 70.5 s, scale = 3.5

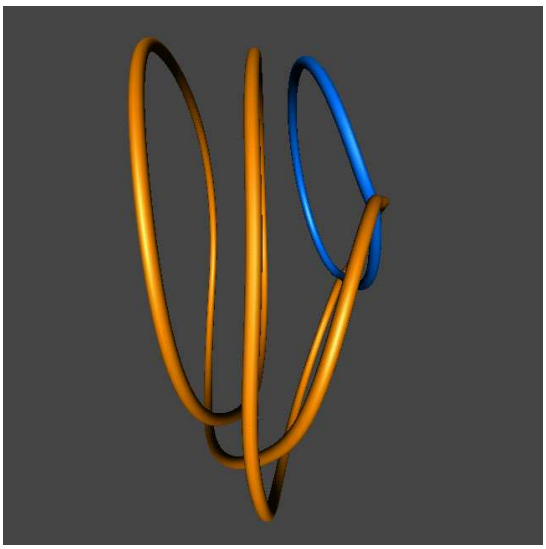

(b) 70.5 s, scale = 3.5

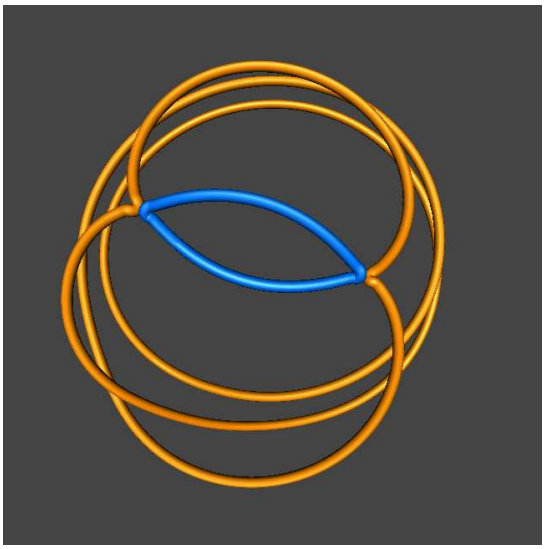

(c) 70.53 s, scale = 3.5

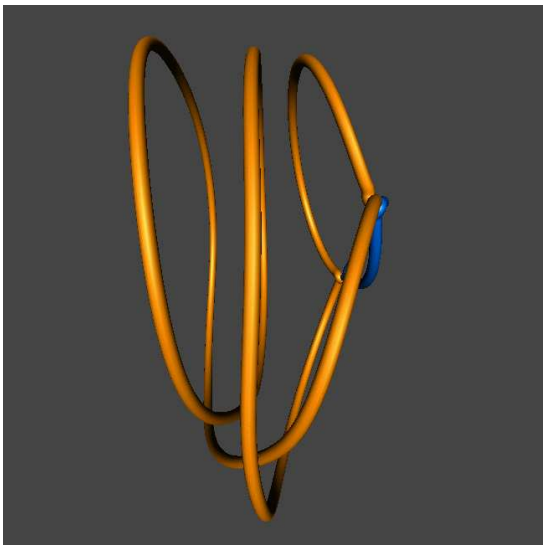

(d) 70.53 s, scale = 3.5

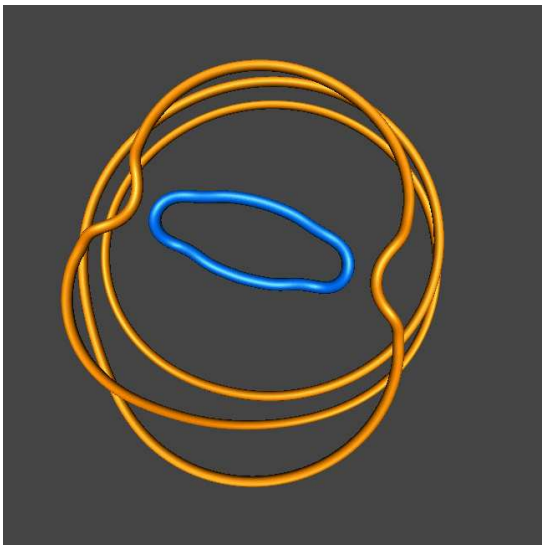

(e) 70.575 s, scale = 3.5

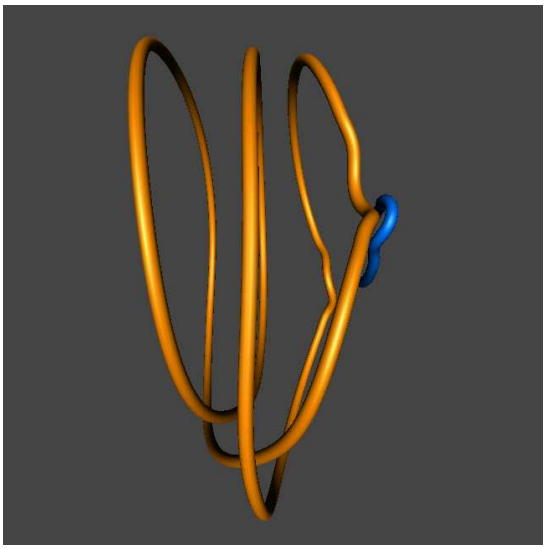

(f) 70.575 s, scale = 3.5

Figure 13.30: Antiparallel reconnection event at T2. (a,c,e) Front view and (b,d,f) side view. Cylinder radius 0.025.

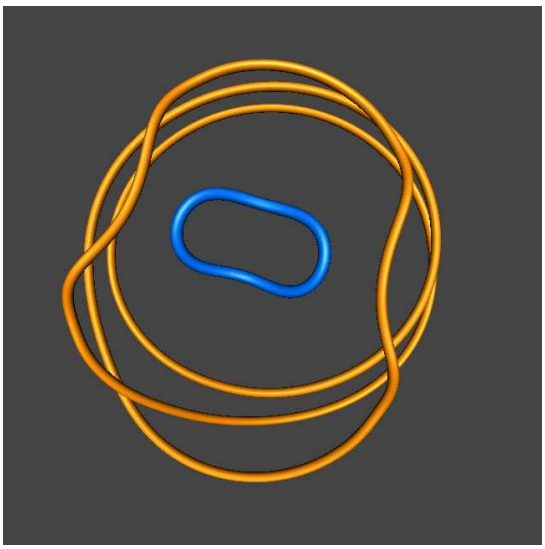

(a) 70.725 s, scale = 3.5

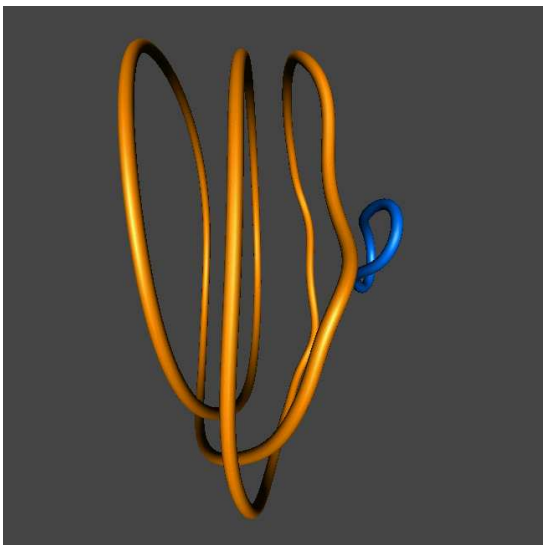

(b) 70.725 s, scale = 3.5

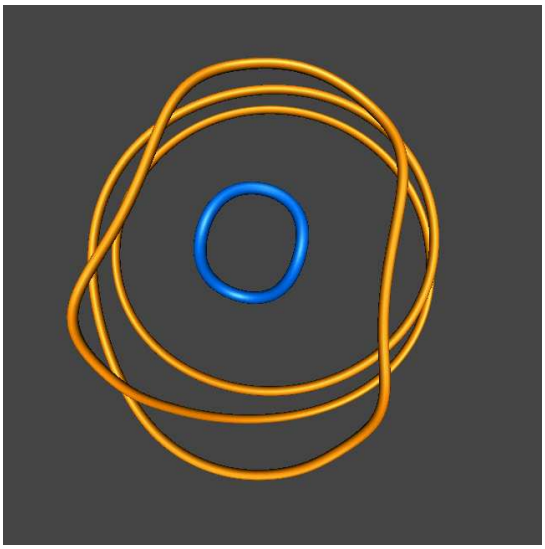

(c) 70.825 s, scale = 3.5

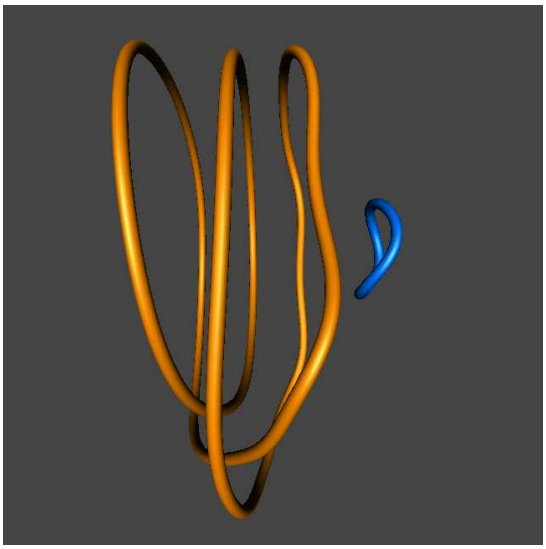

(d) 70.825 s, scale = 3.5

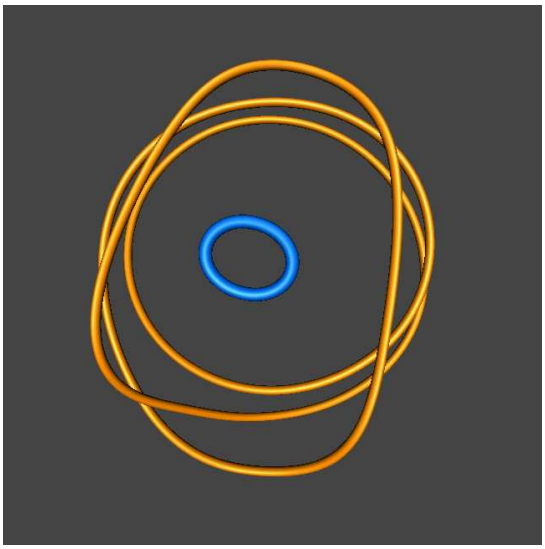

(e) 71.25 s, scale = 3.5

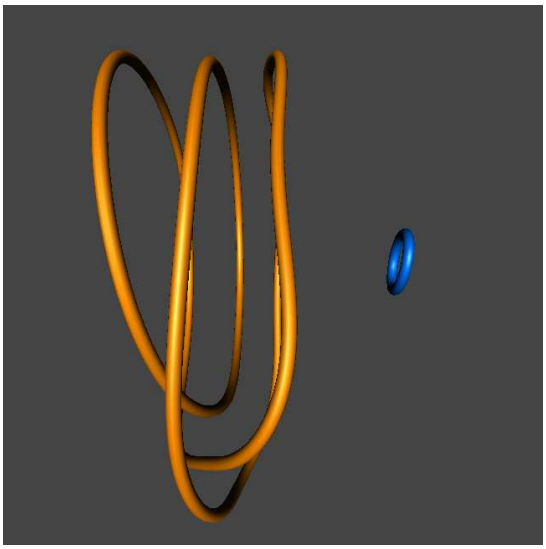

(f) 71.25 s, scale = 3.5

Figure 13.31: Antiparallel reconnection event at T2. (a,c,e) Front view and (b,d,f) side view. Cylinder radius 0.025.

13.7 Summary

In this Chapter I returned to consider the development of instabilities at zero and finite temperature for $N = 7$ and $N = 19$. At zero temperature small scale instabilities develop such that the ring became more and more turbulent leading to multiple self-reconnections and a, seemingly, ever-increasing curvature. The fraction of line length parallel to the direction of motion soon approached that of the fraction of line length perpendicular to it. At finite temperature the situation was entirely different. Although instabilities developed, the mutual friction 'ironed out' small scale perturbations. Also in contrast to zero temperature, at which reconnections seemed to encourage further instabilities, at finite temperature the system seemed to become more and more stable with each reconnection. For example, in the case of $N = 7$ after 75 seconds an almost steady state was achieved, in which the macroscopic ring was transformed into a toroidal coil, for which the level of instability (as measured by the fraction of line length parallel to the direction of motion) did not noticeably increase for the second 75 seconds. The situation was similar for $N = 19$, although the macroscopic ring had not yet transformed into single toroidal coil, the indications were that it would have done so given enough time. I examined closely the two types of reconnection that I observed during the unstable motion of the macroscopic vortex rings: parallel and antiparallel. I explained why parallel reconnections appeared more common at zero temperature and antiparallel at finite temperature.

Chapter 14

A macroscopic ring $N = O(10^2)$

It has been mentioned several times that the circulation measured by Borner (Borner *et al.*, 1983; Borner & Schmidt, 1985) is indicative of a macroscopic vortex ring consisting of $O(10^3)$ individual quantised vortex rings. It has also been pointed out that present computing power does not allow one to investigate such a system quantitatively. I have attempted to investigate it qualitatively by means of the BS law. This approach allowed me to study a macroscopic ring consisting of 19 quantised rings made up initially of 12825 discretisation points. The BS law requires N^2 operations to be carried out at each time step. In Section 8.1 I cited an alternative method, known as the Tree Algorithm which is capable of speeding up the computational process so that the number of operations per time step scales like $N\log(N)$ rather than N^2. Full details of the applicability of this algorithm to quantised vortices can be found in Baggaley & Barenghi (2012). In Appendix F I compare the CPU time required for the full BS law and for the Tree Algorithm for a range of open angles, θ (a measure of the degree of averaging employed). I also consider how well the Tree code replicates one of the main results of the full BS law, robust translation of the macroscopic ring over a distance $10D$. I compare results at $T = 0$ K with those at $T > 0$ K and conclude that the Tree Algorithm can be safely used to simulate the macroscopic vortex ring at finite temperature.

In this section I report results for a macroscopic vortex ring consisting of 91 individual quantised vortex rings. The initial configuration of the ring is hexagonally centred as described in Section 8.3, consisting of a central vortex surrounded by 5 hexagonal layers of vortices (Figure 14.1). I evolve the macroscopic ring in the presence of the normal fluid velocity field described in Section 8.4. The opening angle used is $\theta = 0.2$ radians. The other parameters used to set up initial configuration are $R = 0.06$ cm and $a = 0.015$ cm (such that $R/a = 4$), in which case $\ell = a/(n-1) = a/5 = 0.003$ cm. In order to complete this simulation within a reasonable timescale, I reduce the requirement that $\ell/\Delta\xi \geq 10$, and set $\Delta\xi = 0.00061$ cm, or approximately 5ℓ, and $\Delta t = 1\times10^{-5}$ seconds. This still leaves ℓ ten times greater than the smallest length scale, $\Delta\xi/2$.

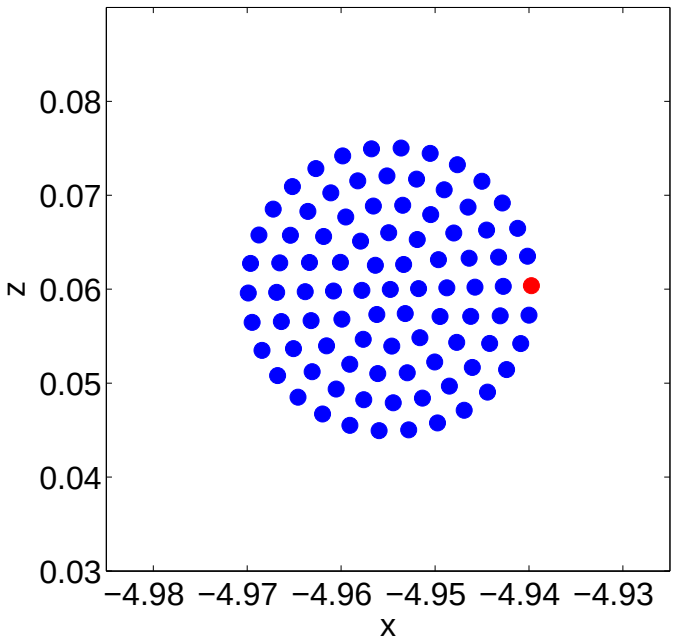

Figure 14.1: Top cross-section of initial configuration of $N = 91$.

The macroscopic ring undergoes leapfrogging (Figure 14.2) and successfully travels a distance greater than $10D = 1.2$ cm in just over 4 seconds (Figure 14.3). The development of Λ and $\bar{c}$ (Figures 14.4 and 14.5) during this period is in keeping with the results for $N = 7$ and $N = 19$ at finite temperature using the full BS law. Λ drops significantly at first. As the macroscopic vortex ring becomes more disordered (e.g. a fraction of line length parallel to the direction of motion develops), Λ stabilises somewhat. The curvature remains small in the absence of small scale perturbations.

In Table 14.1 I record data relevant to the evolution of this macroscopic ring. Notice that, in contrast to the results for $N = 7$ and $N = 19$ at T2, in which $\bar{c}$ remained about the same value, for $N = 91$ $\bar{c}$ decreases. Figures 14.6 to 14.9 show the side and front or front-angled views (as appropriate) at $t = 1$, 2, 3 and 4 seconds and Figure 14.10 shows the corresponding cross-sectional slices. At $t = 4$ seconds, 2 of the individual vortex rings (not shown) have been left trailing behind the main body of the macroscopic ring.

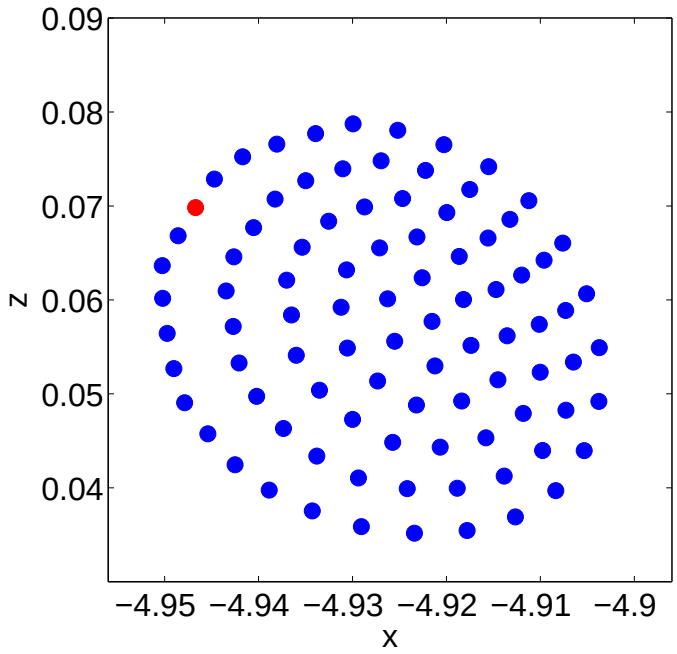

Figure 14.2: Configuration of upper cross-section after performing about half a leapfrog motion ($t = 0.075$ seconds) for $N = 91$ at T2. The ring identified by a red dot in Figure 14.1 has moved to the back of the macroscopic ring. The shape of the cross-section has become more elliptical as in the case of fewer rings (see Figure 10.15).

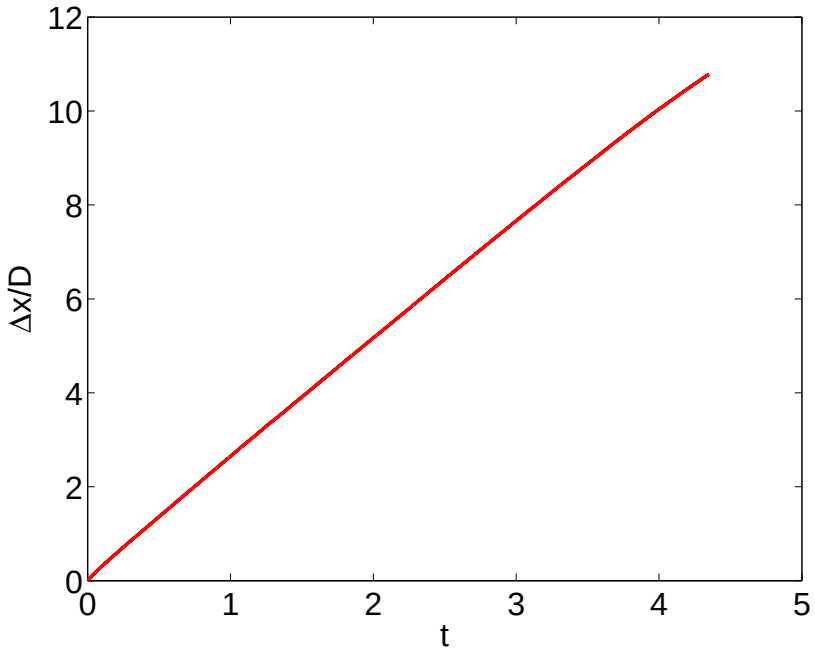

Figure 14.3: Distance travelled $\Delta x/D$ vs t (s) for $N = 91$ at T2 using Tree Algorithm.

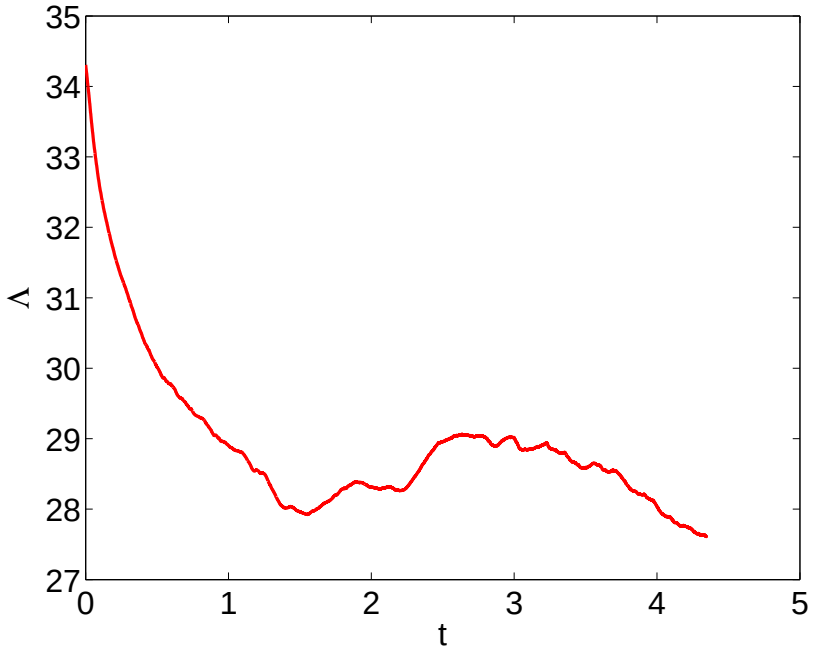

Figure 14.4: Total line length Λ (cm) vs t (s) for $N = 91$ at T2 using Tree Algorithm.

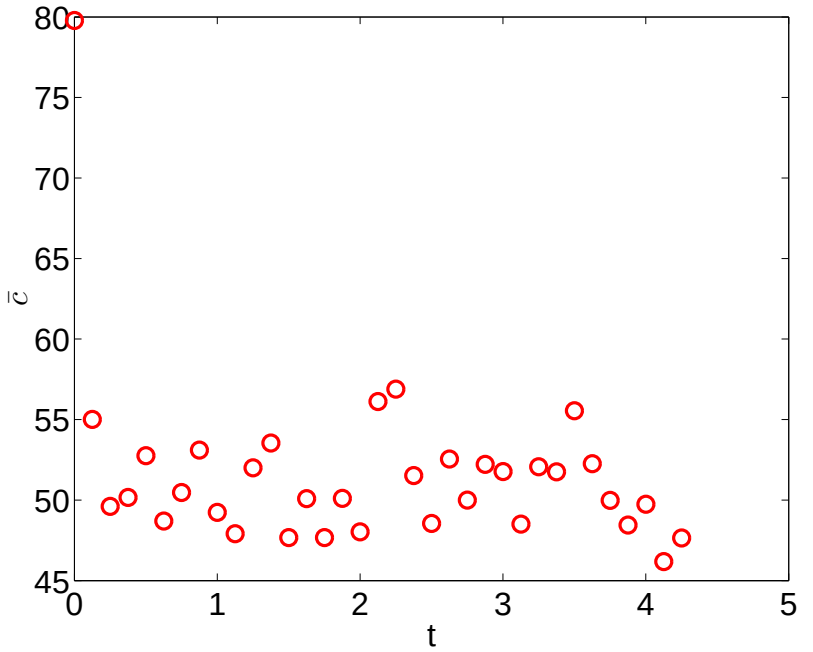

Figure 14.5: Average curvature $\bar{c}$ (cm^{-1}) vs t (s) for $N = 91$ at T2 using Tree Algorithm. Symbols are used due to the large amount of numerical anomalies.

t (s)	N_p	recons	N	Λ (cm) (3dp)	$\bar{c}$ (cm/s^2) (2dp)	Δx (cm) (3dp)	$\Delta x/D$ (2dp)	v_x (cm/s) (4dp)
0.0	75028	0	91	34.304	79.78	0.000	0.00	0.4284
0.5	68622	18	91	30.017	51.30	0.163	1.36	0.2672
1.0	66320	18	91	28.905	46.36	0.318	2.65	0.2611
1.5	64365	18	89	27.960	46.20	0.470	3.92	0.2594
2.0	66979	49	71	28.310	48.44	0.620	5.17	0.2501
2.5	68979	160	47	28.960	47.15	0.771	6.42	0.2447
3.0	69093	379	36	29.017	52.94	0.920	7.67	0.2433
3.5	68120	593	37	28.590	49.21	1.065	8.88	0.2324
4.0	67130	770	37	28.037	49.64	1.205	10.04	0.2199
4.5	64789	973	30	27.130	49.28	1.330	11.08	0.1889

Table 14.1: Development of instabilities in $N = 91$ system at T2 using Tree Algorithm. 'recons' refers to both visible and algorithmic reconnections.

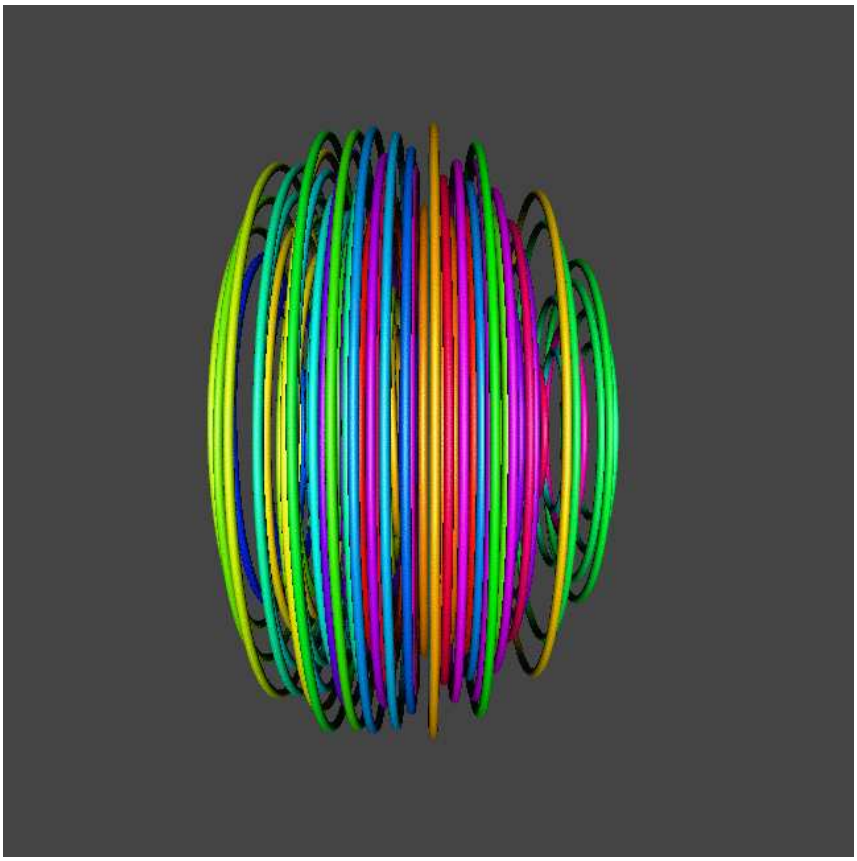

(a)

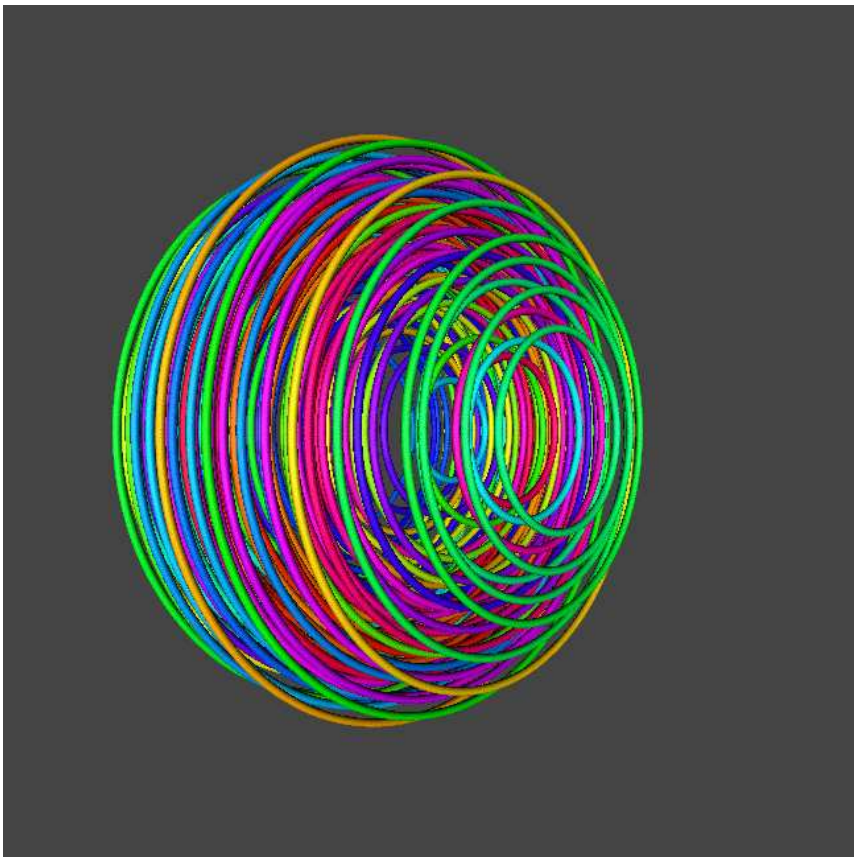

(b)

Figure 14.6: Side view (top) and front angle view (bottom) of $N = 91$ at $t = 1$ second. $\Delta x/D = 2.65$. Scale=4, cylinder radius=0.01 (arbitrary units).

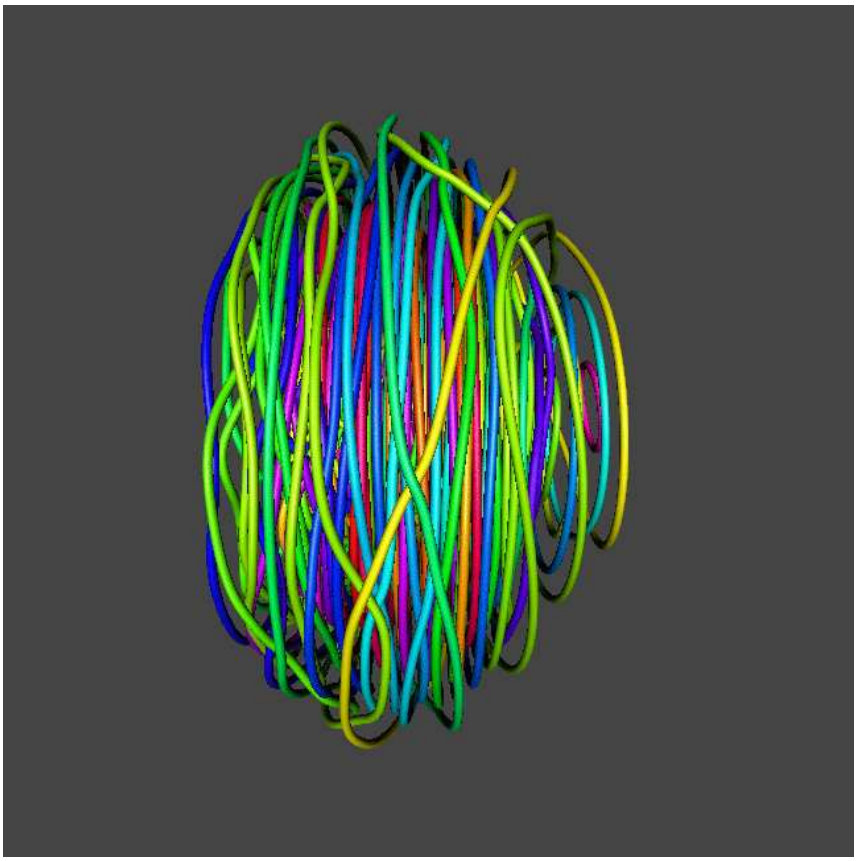

(a)

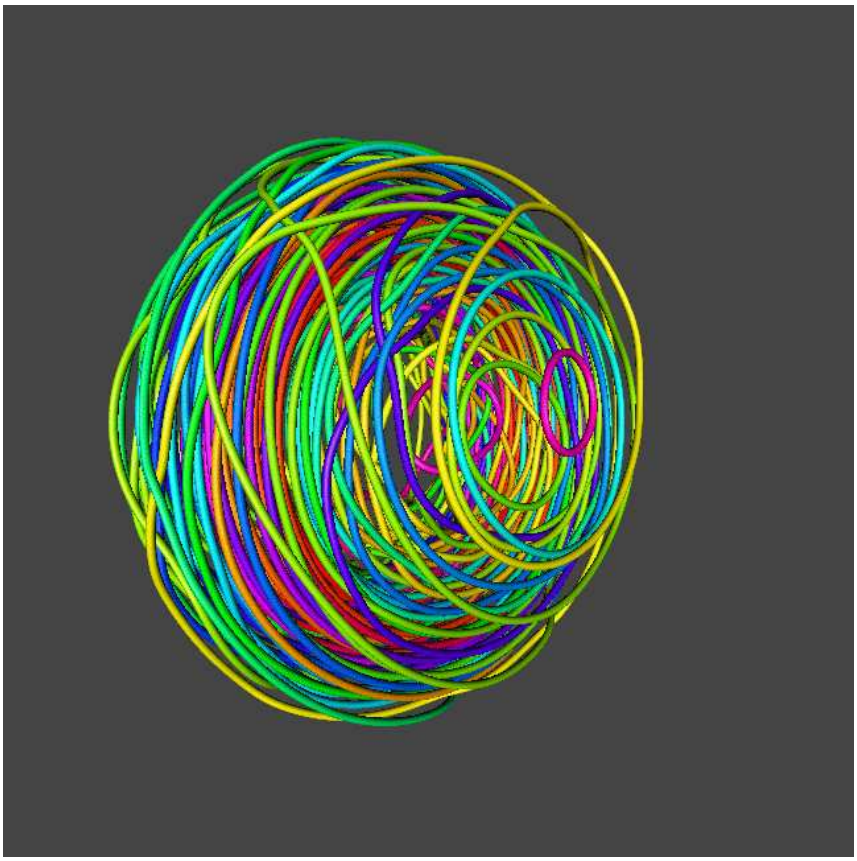

(b)

Figure 14.7: Side view (top) and front angle view (bottom) of $N = 91$ at $t = 2$ seconds. $\Delta x/D = 5.17$. Scale=4, cylinder radius=0.01 (arbitrary units).

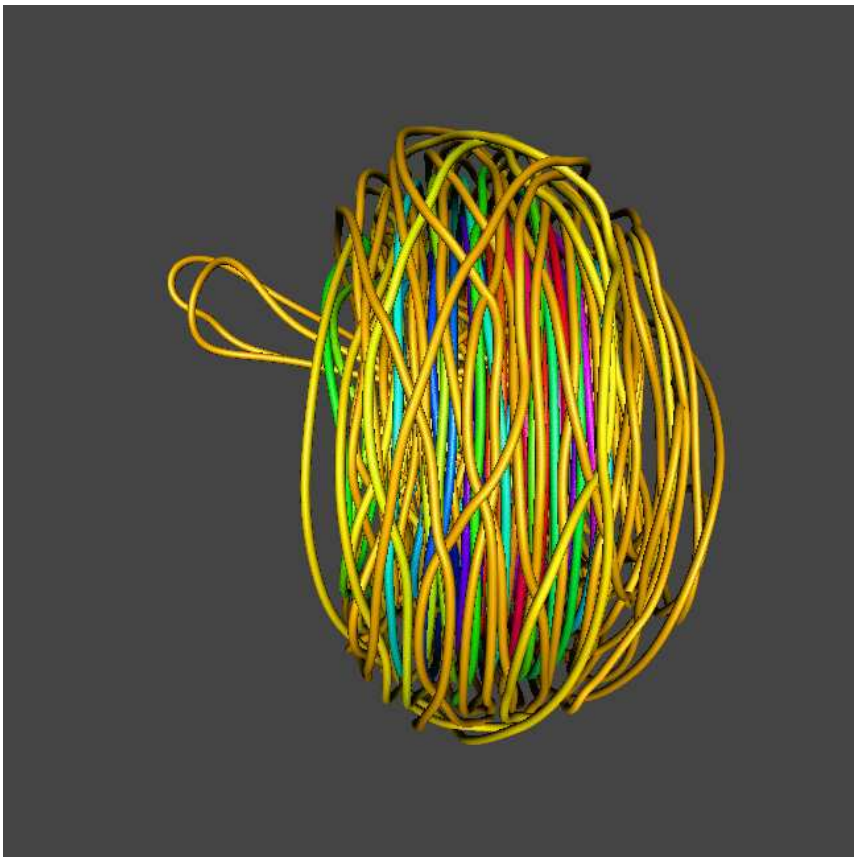

(a)

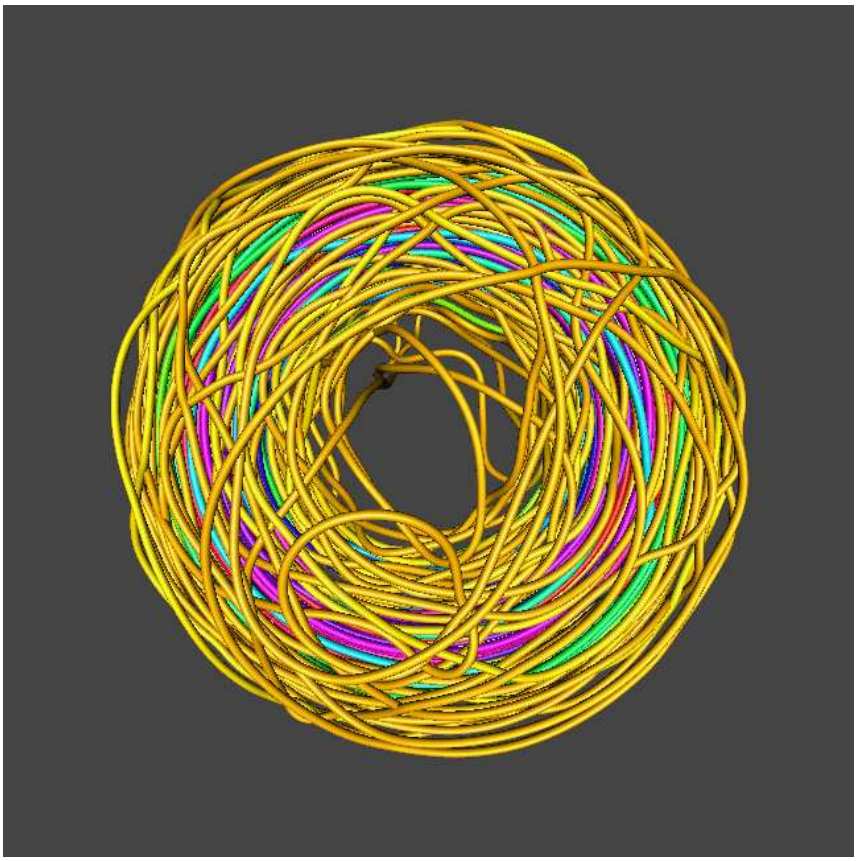

(b)

Figure 14.8: Side view (top) and front view (bottom) of $N = 91$ at $t = 3$ seconds. $\Delta x/D = 7.67$. Scale=4, cylinder radius=0.01 (arbitrary units).

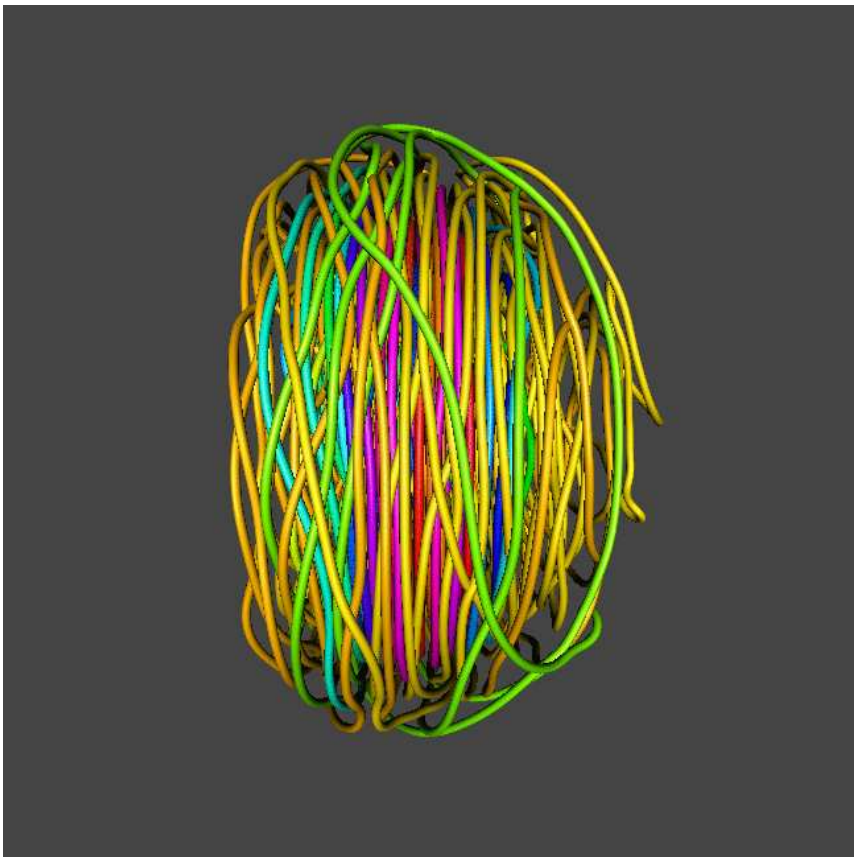

(a)

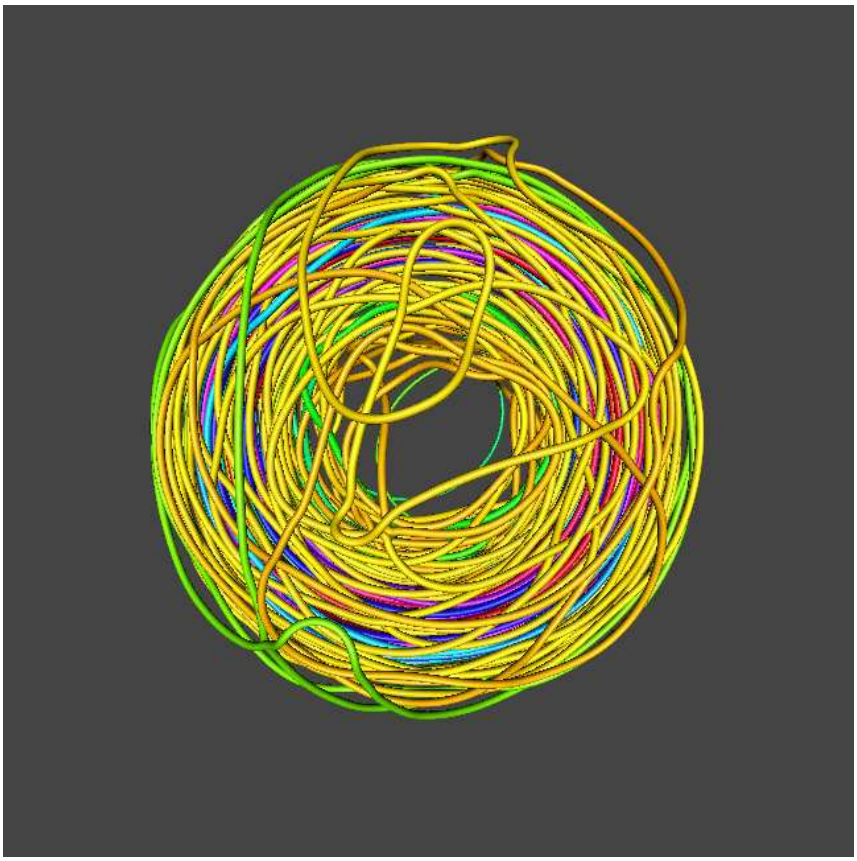

(b)

Figure 14.9: Side view (top) and front view (bottom) of $N = 91$ at $t = 4$ seconds. $\Delta x/D = 10.04$. Scale=4, cylinder radius=0.01 (arbitrary units).

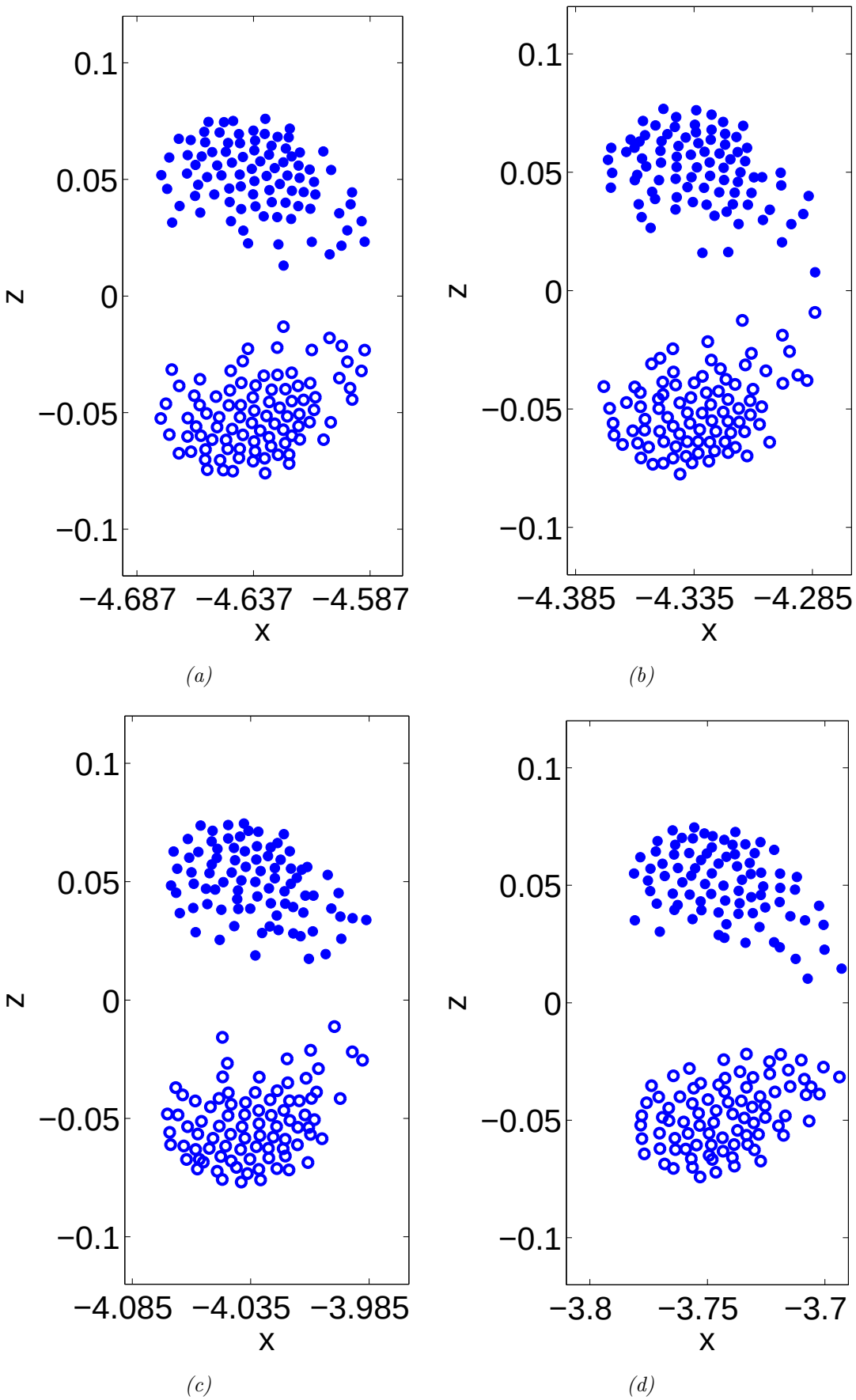

Figure 14.10: Cross-sectional slices at (a) $t = 1$, (b) 2,(c) 3 and (d) 4 seconds.

14.1 Summary

In this Chapter I introduced the use of the Tree Algorithm (the use of which for macroscopic rings is validated in Appendix F). The use of this algorithm cut down the computational cost (potentially from N_p^2 operations per time step to $N_p \log N_p$ operations per time step) and allowed the evolution of a macroscopic ring in which $N = 91$ to be studied. This macroscopic ring performed exactly as expected in light of the results for the smaller, BS-law-evolved finite temperature rings. It travelled at least $10D$ without falling apart. There were no small scale instabilities and the number of individual rings which constituted the macroscopic ring decreases as reconnections occur in the same way as they did for $N = 7$ and $N = 19$. Once again it could be expected to eventually become a single toroidal coil.

Chapter 15

Discussion and further work

After introducing the theory of thin-cored vortex rings and their equations in Chapter 6, I reviewed in Chapter 7 the small number of experiments that have been carried out to study vortex rings in superfluid helium II. The experiments were made particularly interesting due to the fact that the circulation they reported corresponds to the presence of a large number of vortex rings $N = O(10^3)$ and that this system of vortex rings, known as a macroscopic or large-scale vortex ring, was shown to have travelled a considerable distance, some 10 times the original diameter of the macroscopic ring without having undergone a turbulent transformation. Thus, in Chapter 8, I introduced Schwarz's filament method, due to the lack of suitable governing equations (as described in Chapter 1), as a means of following the evolution of the macroscopic ring. I designed an initial configuration which followed a centred hexagonal pattern and, most importantly, a prescribed normal fluid velocity field. The importance of the normal fluid velocity field cannot be understated. It is literally the 'life' of the macroscopic superfluid vortex ring, as I showed that, in its absence, the macroscopic superfluid vortex ring quickly decayed due to the mutual friction (see, for example, Table 8.1). I tested my code and the initial configuration for $N = 1$ and $N = 2$ rings and found them to behave as expected and to be independent of the choice of time and spatial discretisation.

In Chapter 9 I suggested a form for the expressions governing the self-induced velocity and vortex energy of a macroscopic vortex ring and compared the predictions of this mathematical model with those of an optimised form of the numerical macroscopic ring and with the experimental measurements. The results compared favourably with each other, with relatively small percentage errors considering the crude nature of the mathematical model and experimental errors.

In Chapter 10 I used the full BS law to evolve systems of rings in which $N \leq 19$. I showed the effects of finite temperature and the necessity of including a normal fluid velocity field. I also showed that the imposed field was extremely effective in prolonging the life of the macroscopic ring at finite temperatures. All systems of rings successfully travelled at least $10D$ both at T0 and at T2, in agreement

with the results reported by the superfluid vortex ring experiments. Leapfrogging is known to occur for two coaxial rings ($N = 2$). I showed that a generalised form of leapfrogging occurs for $N \geq 2$ and, in analogy to Acheson's (Acheson, 2000) analysis of 2D point vortex leapfrogging, I discussed the existence of a parameter which controls leapfrogging and its critical value. I investigated the trajectories of the individual vortices in the reference frame of the centre of vorticity and showed that the shape of the trajectory varied from case to case (a fuller discussion of this is included in Chapter 11). I also showed that in some cases the trajectories were stable and repeated themselves and that in others they quickly became unstable such that the paths of individual vortices moved either inwards towards the centre of the cross-section of the macroscopic vortex core or outwards away from the centre.

In Chapter 11 I investigated the dependence of translational velocity, period of leapfrog, shape of trajectory and stability of macroscopic ring on the two parameters ℓ and R/a. I found that translational velocity increased with decreasing ℓ and increasing R/a, but that it was not clear which parameter had a greater effect. The other three features all depended strongly on R/a, whereas the only feature which was demonstrably strongly dependent on ℓ was the period of the leapfrog.

In Chapter 12 I looked briefly at mathematical predictions of the macroscopic ring's behaviour at finite temperature with no normal fluid velocity field. My results supported the mathematical model's prediction that macroscopic rings with a smaller core radius shrink more quickly.

In Chapter 13 I returned to consider the development of instabilities at zero and finite temperature for $N = 7$ and $N = 19$. At zero temperature small scale instabilities develop such that the ring became more and more turbulent leading to multiple self-reconnections and a, seemingly, ever-increasing curvature. The fraction of line length parallel to the direction of motion soon approached that of the fraction of line length perpendicular to it. At finite temperature the situation was entirely different. Although instabilities developed, the mutual friction 'ironed out' small scale perturbations. Also in contrast to zero temperature, at which reconnections seemed to encourage further instabilities, at finite temperature the system seemed to become more and more stable with each reconnection. For example, in the case of $N = 7$ after 75 seconds an almost steady state was achieved, in which the macroscopic ring was transformed into a toroidal coil, for which the level of instability (as measured by the fraction of line length parallel to the direction of motion) did not noticeably increase for the subsequent 75 seconds. The situation was similar for $N = 19$, although the macroscopic ring had not yet transformed into single toroidal coil, the indications were that it would have done so given enough time. I examined closely the two types of reconnection that I observed during the unstable motion of the macroscopic vortex rings: parallel and antiparallel. I explained why parallel reconnections appeared more common at zero temperature and antiparallel at finite

temperature.

In Chapter 14 I introduced the use of the Tree Algorithm (the use of which for macroscopic rings is validated in Appendix F). The use of this algorithm cut down the computational cost (potentially from N_p^2 operations per time step to $N_p \log N_p$ operations per time step) and allowed the evolution of a macroscopic ring in which $N = 91$ to be studied. This macroscopic ring performed exactly as expected in light of the results for the smaller, BS-law-evolved finite temperature rings. It travelled at least $10D$ without falling apart. There were no small scale instabilities and the number of individual rings which constituted the macroscopic ring decreased as reconnections occured in the same way as they did for $N = 7$ and $N = 19$. Once again it could be expected to eventually become a single toroidal coil. I anticipate that with a greater level of parallelisation (i.e. `mpi` rather than `openmp`) it will become possible to model even more complex systems with the Tree Algorithm.

With hindsight it appears that the Gorter-Mellink form of the mutual friction term (Equation 3.1) may be a valid description of the mutual friction at finite temperature, since the initial laminar vortex flow is not greatly disturbed during the macroscopic ring's evolution. Alternatively, one could instead use a toroidal coil as the initial configuration of the system, since it has shown itself to be even more robust than the equivalent macroscopic ring consisting of unconnected vortex rings. Once in possession of a suitable governing equation the advantages are considerable. One may then seek steady solutions of the equation for one or more vortex rings. One can also analyse the development of instabilities. For example, the instabilities which appeared in $N = 7$ at T0 in Figures 13.1 to 13.5, in which the individual rings retained their coaxiality, but were twisted out of shape, seems to indicate a dominant $m = 2$ mode of instability. On the other hand, the instabilities which appeared in $N = 7$ at T2 in Figures 13.9 to 13.11, in which the rings lost their coaxiality, but retained their circular shape, seems to indicate a dominant $m = 1$ mode of instability.

A further topic which could be examined is the addition of tracers into the flow showing the particle paths around the macroscopic vortex formation at its different stages. One expects that in the initial laminar macroscopic vortex formation the particles would trace 2D circular paths around the core of the macroscopic vortex ring. Notice however in Figures 13.11(c-f) that the toroidal coil seems to have rotated about its axis. This seems to indicate that as the coil translates in the x direction it is also rotating about the x axis. If this is the case, particles would describe helical paths around the core of the macroscopic vortex formation.

Appendix A

List of variables and parameters used in Part I

Below are a list of most variables which are used in Part I, accompanied by a brief description. Where it is relevant I also give, in the brackets following the description, the origin of the variable (i.e. in whose papers the variable appears) and its dimensions. Complex conjugation is indicated either by an asterisk (e.g. u^*) or by a line on top of the variable (e.g. $\bar{u}$). A temporal derivative is expressed as $\dot{u}$ for some variable u. Superscripts s, n, t and c mean indicate super, normal, 'total' or 'cross term' respectively (e.g. u^s and u^n). $\Re$ and $\Im$ denote real and imaginary parts respectively.

ρ density (gcm^{-3})

$\mathbf{u}$ velocity (cms^{-1})

ω vorticity (s^{-1})

p pressure ($\mathrm{gcm}^{-1}\mathrm{s}^{-2}$)

s specific entropy

T temperature (K)

μ viscosity ($\mathrm{gcm}^{-1}\mathrm{s}^{-1}$)

ν kinematic viscosity ($\mathrm{cm}^2\mathrm{s}^{-1}$)

u_m Fourier velocity associated with shell m (cms^{-1})

k_m wavenumber associated with shell m (cm^{-1})

k_m^2 Laplacian in k-space (cm^{-2})

k_0 reference wavenumber (cm^{-1})

λ	aspect ratio
m	shell index ($1 \leq m \leq M$)
$G_m[u]$	GOY model inertial term
$c_m^{(1)}$,$c_m^{(2)}$,$c_m^{(3)}$	GOY model real constants
a,b,c	GOY model real constants
f	amplitude of external forcing
$\delta_{m,m'}$	Kronecker's delta
V	volume (cm^3)
S	simply-connected surface (cm^2)
$\mathbf{n}$	unit normal vector
E	energy ($\mathrm{cm}^2\mathrm{s}^{-2}$)
H	helicity (cms^{-2})
Q	enstrophy (s^{-2})
$E^{(1)}$,$E^{(2)}$	the two conserved quantities of the GOY shell model
α_1,α_2	generators of two conserved quantities
E_k	spectral energy ($\mathrm{cm}^3\mathrm{s}^{-2}$)
E_m	spectral energy associated with shell m ($\mathrm{cm}^3\mathrm{s}^{-2}$)
Q_m	enstrophy associated with shell m (s^{-2})
ω_m	vorticity associated with shell m (s^{-1})
τ_m	eddy turnover associated with shell m (s)
Δt	timestep (s)
δ_{err}	percentage (absolute) error, defined in text
ϵ	rate of energy transfer ($\mathrm{cm}^2\mathrm{s}^{-3}$)
ℓ	intervortex spacing (cm)
k_ℓ	wavenumber corresponding to intervortex spacing (cm^{-1})
k_η	Kolmogorov microscale (cm^{-1})
l	eddy size (cm)
τ	eddy turnover time (s)
$\mathbf{F}_{ns}$	mutual friction ($\mathrm{gcm}^{-2}\mathrm{s}^{-2}$)
F_m	mutual friction associated with shell m ($\mathrm{gcm}^{-2}\mathrm{s}^{-2}$)
L	vortex line density (cm^{-2})
κ	quantum of circulation ($\mathrm{cm}^2\mathrm{s}^{-1}$)
B	temperature dependent mutual friction coefficient
α	temperature dependent mutual friction coefficient

T_m	energy transfer rates from triadic interactions ($\mathrm{cm}^{-1}\mathrm{s}^{-3}$)
D_m	energy transfer rate due to viscous dissipation ($\mathrm{cm}^{-1}\mathrm{s}^{-3}$)
M_m	energy transfer rate due to mutual friction ($\mathrm{cm}^{-1}\mathrm{s}^{-3}$)
ϵ_{inj}	rate of influx of energy due to forcing term ($\mathrm{cm}^{-1}\mathrm{s}^{-3}$)
Π_m	energy flux at shell m
Δ_m	correlator at shell m
D	large eddy size (cm)
U	large eddy velocity (cms^{-1})
Re	Reynolds number
δ	small eddy size (cm)
T_c	critical temperature (K)
h	Planck's constant ($\mathrm{gcm}^2\mathrm{s}^{-1}$)
m_4	mass of ^{4}He atom (g)
m_3	mass of ^{3}He atom (g)

Appendix B

Extent of averaging required for two-fluids GOY shell model

I have stated (Section 2.10) that the severe oscillations (orders of magnitude) in the energy spectra necessitate time and/or ensemble averaging. An obvious question is: How much averaging is necessary to 'iron out' these oscillations, which are features of the shell models and not of Navier-Stokes turbulence itself? A simple numerical test shows that surprisingly little averaging is required. I compared the results of several averages, taken after an initial run of 500 seconds during which the initial condition evolved into fully developed turbulence. I used standard parameters $(N, \lambda, b, dt) = (18, 2, -0.5, 5 \times 10^{-6})$ at a single temperature $T = 2.157$ K with the fluids coupled by mutual friction. The averages investigated are as follows:

- Time average of 10 snapshots over a run of 500 seconds
- Time average of 10 snapshots over a run of 5000 seconds
- Time average of 100 snapshots over a run of 5000 seconds
- Ensemble average of 10, 50, 100, 250 and 500 randomly phase shifted realisations, each realisation of length 500 seconds

There does not appear to be any appreciable difference between any of the above averages. I conclude that there is no benefit in performing a lengthy process of averaging since the result of a much shorter one is demonstrably identical for the purposes of this work.

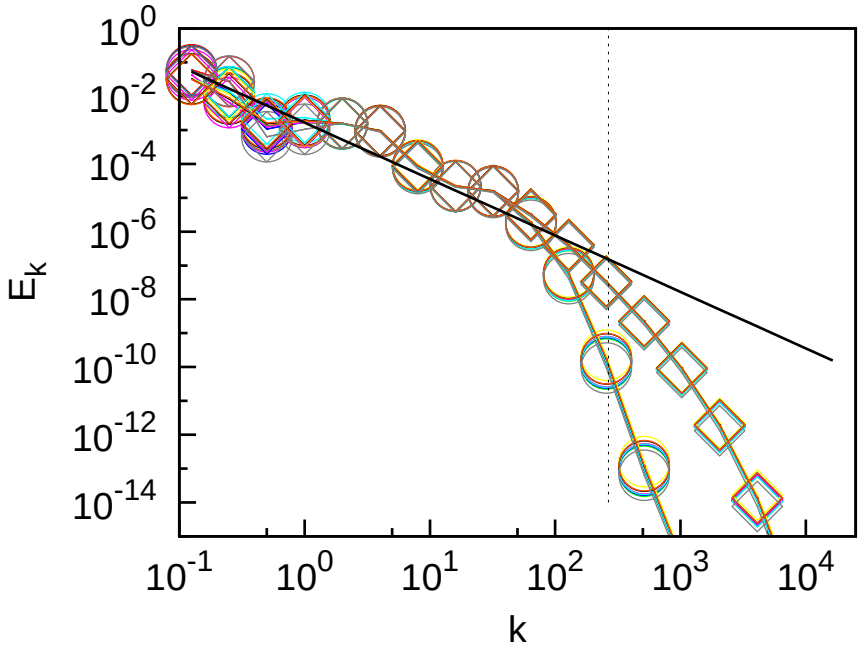

Figure B.1: Log-log plot of the energy spectra E_k ($\mathrm{cm}^2\mathrm{s}^{-2}$) vs wavenumber k (cm^{-1}) for the normal fluid (circles) and superfluids (diamonds) resulting from time averaging and ensemble averaging. Three time averages and five ensemble averages (different colours) were performed.

Appendix C

A GOY shell model to produce an arbitrary power law scaling law for the spectral energy

In Section 2.9.2 I showed that the Kolmogorov spectrum satisfies the GOY shell model evolution equation in the steady, inviscid and unforced limit. One may ask whether the parameters of the shell model can be designed in such as way so as to produce an arbitrary power-law in the steady, inviscid and unforced limit.

Write $E_k \sim k^\beta$, where β is the desired power law. Recall Equation 2.10 for the spectral energy associated with the shell m, $E(k_m) = |u_m|^2/2k_m$. Recall also that $k_m = k_0\lambda^m$. Combining these gives

$$u_m \sim k_m^{\frac{1}{2}(\beta+1)} = k_m^\gamma, \tag{C.1}$$

where $\gamma = \frac{1}{2}(\beta+1)$. Now substitute into the steady, inviscid, unforced GOY equation

$$\begin{aligned}
0 &= ak_{m+1}u_{m+1}u_{m+2} + bk_m u_{m+1}u_{m-1} + ck_{m-1}u_{m-1}u_{m-2} \\
&\sim ak_{m+1}\ (k_{m+1})^\gamma(k_{m+2})^\gamma + bk_m\ (k_{m-1})^\gamma(k_{m+1})^\gamma + ck_{m-1}\ (k_{m-1})^\gamma(k_{m+2})^\gamma \\
&= a\lambda^{m+1}\lambda^{m+1}\lambda^{m+2} + b\lambda^m\lambda^{m+1}\lambda^{m-1} + c\lambda^{m-1}\lambda^{m-1}\lambda^{m-2} \\
&= a\lambda^{1+3\gamma} + b + c\lambda^{-(1+3\gamma)}.
\end{aligned}$$

Hence the condition to fulfil is

$$0 = a^{\frac{1}{2}(5+3\beta)} + b + c^{-\frac{1}{2}(5+3\beta)} \tag{C.2}$$

such that $a + b + c = 0$.

By convention set $a = 1$, leaving $b + c = 0$ or $c = -b$. Then Equation C.2 becomes

$$\lambda^{\gamma} + b - b\lambda^{-\gamma} = 0$$

$$b\left(1 - \lambda^{-\gamma}\right) = -\lambda^{\gamma}$$
$$b = \frac{-\lambda^{\gamma}}{1 - \lambda^{-\gamma}} = \frac{\lambda^{2\gamma}}{1 - \lambda^{\gamma}}.$$

Thus choosing $a = 1$ and setting $c = -b$, then for whatever choice of power law β (in $E_k \sim k^{\beta}$) I can find a b such that energy is conserved using

$$b = \frac{\lambda^{2\gamma}}{1 - \lambda^{\gamma}}, \tag{C.3}$$

where $\gamma = \frac{1}{2}(\beta + 1)$.

For example, if I want $\beta = -3$, then I should set $c = -b = -1/12$.

Appendix D

List of variables and parameters used in Part II

Below are a list of most variables which are used in Part II, accompanied by a brief description. Where it is relevant I also give, in the brackets following the description, the origin of the variable (i.e. in whose papers the variable appears) and its dimensions. A temporal derivative is expressed as $\dot{u}$ for some variable u.

t	time (s)
Δt	time step (s)
ξ	arc length (cm)
$\Delta\xi$	discretisation along vortex lines (cm)
$\mathbf{s}$	vector along the vortex lines (cm)
$\mathbf{s}'$	first derivative with respect to arc length, $d\mathbf{s}/d\xi$
$\mathbf{s}''$	second derivative with respect to arc length, $d^2\mathbf{s}/d\xi^2$ (cm^{-1})
$\mathbf{u}$	velocity of vortex lines (cms^{-1})
E	kinetic energy per unit density of vortex lines ($\mathrm{cm}^2\mathrm{s}^{-2}$)
s	specific entropy
a_0	vortex core size (cm)
ρ_s	superfluid density (gcm^{-3})
ρ_n	normal fluid density (gcm^{-3})
n	index for centred hexagonal numbers
N	number of vortex rings
N_p	total number of points along all vortex rings
R	radius of macro-ring (cm)
a	radius of core of macro-ring (cm)
D	diameter of macro-ring (cm)
d	diameter of macro-ring core (cm)
δx	distance between the front and back rings (cm)

L	vortex line density (cm^{-2})
ℓ	inter-vortex spacing (cm)
Λ	total vortex line length (cm)
Λ_x,Λ_y,Λ_z	projection of vortex line length onto x, y and z directions (cm)
$\bar{c}$	mean curvature (cm^{-1})
$\mathbf{x}$	position of centre of vorticity (cm)
$\Delta\mathbf{x}$	distance moved by centre of vorticity (cm)
$\mathbf{v}$	velocity of centre of vorticity (cms^{-1})
v_{si}	self-induced velocity of vortex ring (cms^{-1})
T	temperature (K)
Γ	circulation (cms^{-2})
Γ_0	maximum measured circulation (cms^{-2})
Γ_1,Γ_2	circulation measured using first and second sound respectively (cms^{-2})
κ	quantum of circulation (cms^{-2})
α	and α' coefficients of mutual friction
θ	opening angle (Tree code, radians)
$\hat{\alpha}$	ratio of diameters of inner and outer co-axial, concentric rings (cf. Acheson α)
$\hat{\alpha}_c$	critical value of $\hat{\alpha}$ (cf. Acheson α_c)
τ_{LF}	period of leap-frog (s)
N_{LF}	number of leap-frogs performed
P_L	length of piston stroke (cf. Borner L_M, cm)
P_U	velocity of piston (cf. Borner U_M, cms^{-1})
P_D	diameter of piston orifice (cf. Borner D_M, cm)
U_T	translational velocity of macroscopic vortex ring (Borner, cms^{-1})
δ_{err}	percentage (absolute) error, defined in text

Appendix E

Effective use of KnotPlot to visualise vortex rings

E.1 How to produce movies using KnotPlot

E.1.1 Outline

This section includes a brief description of how to produce movies using the KnotPlot software (http://www.KnotPlot.com/). I have written it in the context of vortex rings, but it can, of course, be generalised.

The `var****.log` files which `qvort` (http://www.staff.ncl.ac.uk/a.w.baggaley/doxy/html/index.html) produces contain a list of the vortex points accompanied by their positions and velocities. The final piece of information associated with each vortex point is the identity of the vortex point next to it along the vortex filament. These vortex points are initially in the correct order (e.g. the point on line 2 is the one next to line 1), but once points are added or removed or a reconnection takes place, a reordering occurs. I use `dhw_vortex_loop_knotplot.m` to put points back into order. KnotPlot plots the points in the order that they appear in the data file. I use `dhw_vortex_loop_knotplot_anim.m` to produce multiple consecutive data files for the purpose of making a movie. This calculation can be slow as Matlab needs to sort out all of the points in each file. `dhw_vortex_loop_knotplot_anim.m` takes the arguments (start,final,skip,snapshot). 'start' and 'final are the first and last data files to be read. 'skip' means only read every ith `var` file. 'snapshot' means only write every jth vortex point to the output files.

I change the KnotPlot parameters in `kp_anim.sh` to reflect the individual requirements of the movie, such as scale, view angle etc. and use this script to produce a `kp_anim.kp` file. This file will be read by KnotPlot and used to produce the individual frames of the movie. I make sure to remove any old `kp_anim.kp` files, since `kp_anim.sh` appends to the end of the `kp_anim.kp` file.

I make sure that the `kp_anim.kp` file and all of the files to be read by KnotPlot are in the same folder. Open KnotPlot and read in the `kp_anim.kp` file. KnotPlot will now produce very large .eps files. Each .eps file can easily be larger than 10Mb, so care must be taken that sufficient memory is available to store all of the files at least temporarily. No images will appear in the KnotPlot window whilst this process is being carried out.

I use `kp_convert.sh` to convert the very large .eps files to much smaller .png files, which can be read by `makemovie` and turned into a movie.

E.1.2 Movie checklist

1. Use `dhw_vortex_loop_knotplot_anim.m` to convert `var****.log` files into format which can be read by KnotPlot.
2. If there exists an old `kp_anim.kp` file remove it.
3. Use `kp_anim.sh` to produce a `kp_anim.kp` file.
4. Open KnotPlot.
5. Type `read kp_anim.kp`. This produces .eps files.
6. Use `kp_convert.sh` to convert .eps files to .png files.
7. From Ubuntu 12.04 use the `makemovie` script to produce `output.avi` movie file.

E.1.3 Scripts

I include a copy of sample `kp_anim.sh` and `kp_convert.sh` scripts.

```
   #!/bin/bash

CYL=0.01
SCA=3
ROTATEY=37.5
ROTATEZ=0
PREFIX=var
SUFFIX=log

for file in `ls ${PREFIX}*.${SUFFIX}`; do
  cat <<EOF >> kp_anim.kp
load $file
cen
```

```
cyl=$CYL
sca=$SCA
rotate y $ROTATEY
rotate z $ROTATEZ
psmode=10
psout `basename $file .$SUFFIX`
reset all
EOF
done
```

```
   #!/bin/bash

PREFIX=var
ISUFFIX=eps
OSUFFIX=png

for file in `ls ${PREFIX}*.${ISUFFIX}`; do
  echo Converting $file...
  BASE=`basename $file .$ISUFFIX`
  convert -background grey -alpha background -alpha off $file $BASE.$OSUFFIX
done

echo Done.
```

E.2 Knotplot discretisation

When producing KnotPlot images one should be aware of 'KnotPlot discretisation', that means to say the number of points written to file to be read by KnotPlot. KnotPlot images can be very large and it may be tempting to use only some of the information available in the `var****.log` file when producing these images (i.e. to use every nth point) and thereby save time and computer resources when producing images. However care must be taken that important visual information of small scales is not lost. Below are three images of the same unstable vortex tangle (produced using the full BS Law, initially 7 rings, $T = 0$ K, $t = 78.75$ s) viewed from the rear. At this time only 2 rings remain (coloured green and purple). I show smooth tubes (tube radius 0.025) in the left panel and lines and beads (bead radius 0.025) in the right panel. The apparent small scale instabilities 'disappear' as the number of discretisation points is reduced from 4347 (top), to 436 (middle) and then to 175 (bottom).

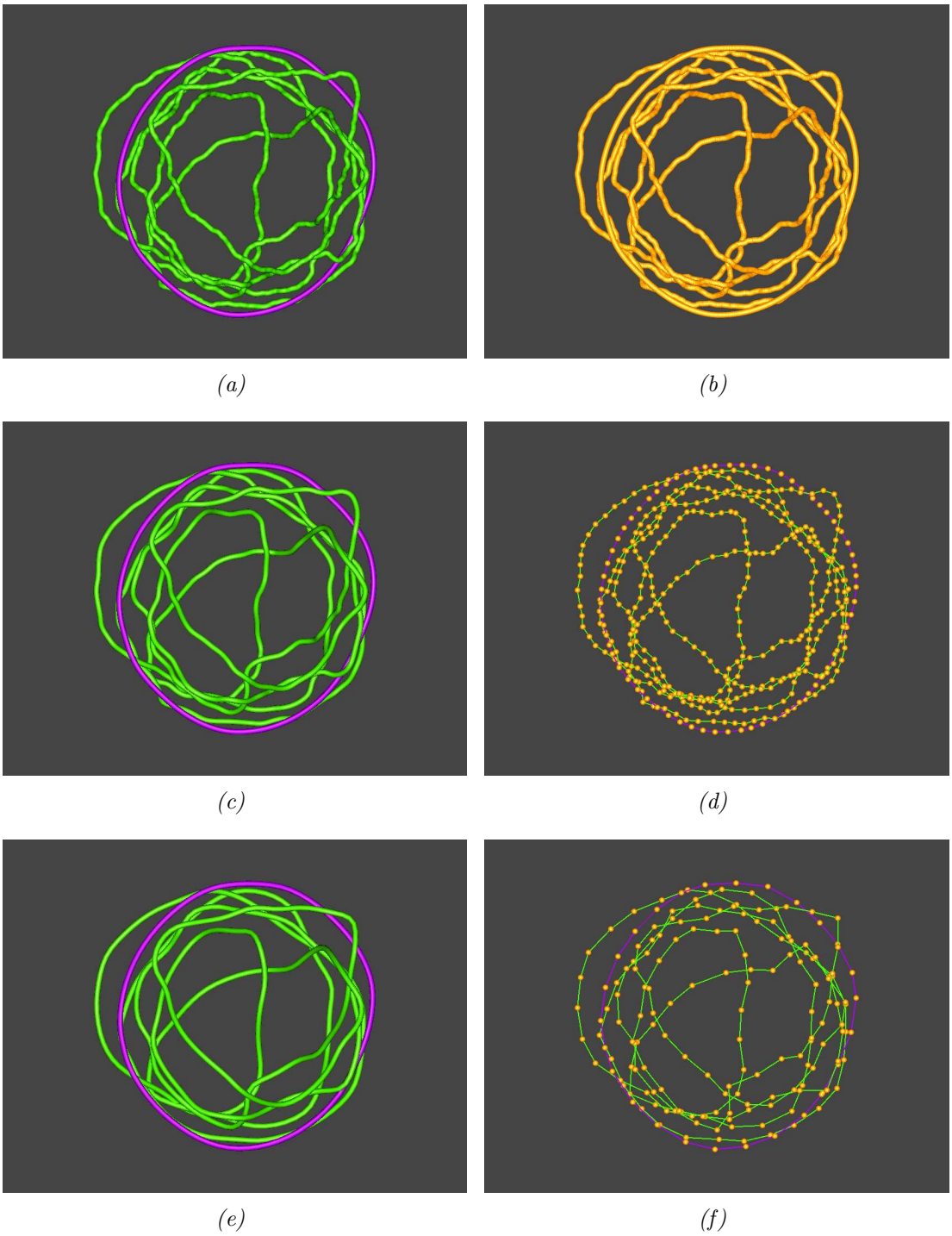

Figure E.1: Knotplot discretisation: An example of how important visual information of small scales can be lost. Here are three images of the same unstable vortex tangle (Parameters: Biot Savart law , initially $N = 7$, $T = 0$ K, $t = 78.75$ s) viewed from the rear. At this time only 2 rings remain (coloured green and purple). I show smooth cylinders (cylinders radius 0.025 in arbitrary units) in the left panel and lines and beads (bead radius 0.025 in arbitrary units) in the right panel. The small scale instabilities 'disappear' as the number of discretisation points is reduced from 4347 (top), to 436 (middle) and then to 175 (bottom). The size of cylinders and bead radii is for visualisation purposes only.

Appendix F

The applicability of the Tree Algorithm to systems of macroscopic vortex rings

Based on the pioneering work of Barnes & Hut (1986), Baggaley & Barenghi (2012) developed a version of the Tree Algorithm suitable for use in studying quantum vortex dynamics. The Tree Algorithm has the potential capability of speeding up computational time from N_p^2 to $N_p log(N_p)$, where N_p is the number of points in the system - in my case the number of vortex points which make up the vortex filaments. The gain in computational speed is balanced by a loss in accuracy: instead of a point-by-point evaluation, a degree of averaging is introduced, whereby the effect of points more distant from the point at which the evaluation is taking place is to some extent subject to averaging. This procedure is more valid in the homogeneous isotropic turbulence, which was the subject of their investigation, however a system of vortex rings is highly anisotropic, possessing a distinct shape, an axis of rotation and direction of motion. The degree of averaging is controlled by a parameter θ (in radians) known as the opening angle. $\theta = 0$ returns the full BS law. The larger the value of θ, the less evaluations that are required at each point and hence the quicker the simulation runs. Although Baggaley & Barenghi (2012) report that $\theta = 0.4$ is sufficiently small for homogeneous isotropic turbulence, this value is questionable in the case of macroscopic vortex rings. This is particularly noticeable in systems with only a few vortex rings. In other words the importance of the distant vortex points is greater when there are fewer rings. On the other hand, systems containing only a few rings can be evolved using the full BS law, as they do not contain too many discretisation points. Although it is tempting to use a larger value of θ in anticipation of a quicker running time, this argument is flawed. The error in this argument lies in the fact that the larger the value of θ, the more quickly instabilities set in. The rings develop waves, which in turn lead to reconnections and the introduction of extra points into the system, which mean more computing time even though θ is

larger.

I consider 8 cases and compare the results of the full BS law with three values of the opening angle θ: $\theta = 0.1$, 0.2 and 0.3 radians. The parameters used in the 8 cases are recorded in Table F.1. All cases are at $T = 0$ K. In the figures F.1 to F.4 I plot on the left-hand-side the CPU time (in arbitrary units) versus t (in seconds). I define the CPU time as

$$\frac{N_p(t)\,\langle Eval(t)\rangle}{N(0)\,\langle Eval(0)\rangle}, \tag{F.1}$$

where $N_p(t)$ is the number of points at time t and $\langle Eval(t)\rangle$ is the average number of evaluations per point at time t. On the right-hand-side I plot the distance travelled in units of the original diameter, $\Delta x/D$, at time t. $\theta = 0.3$ radians performs very poorly throughout. This is due to the phenomenon mentioned above that over-averaging spirals into instabilities, reconnections and a greatly increased N_p, such that the centre of vorticity fails to travel $10D$ in the time scale of the run. $\theta = 0.1$ radians performs well in all cases and $\theta = 0.2$ performs better the larger the value of N. I now consider the same 8 cases at finite temperature using the normal fluid velocity field described in Section 8.4. I plot the results in figures F.5 to F.8. The presence of the mutual friction inhibits the development of instabilities to such an extent that even when $\theta = 0.3$ radians the Tree Algorithm faithfully reproduces the results of the full BS law.

I conclude that the results of the Tree Algorithm can be used as an accurate representation of the results of the full BS law, especially at finite temperatures which inhibit the development of instabilities.

Case	N	R (cm)	a (cm)	R/a
1	1	0.0896	-	-
2	2	0.0896	0.0075	11.94
3	3	0.0896	0.00896	10
4	7	0.0896	0.0223	4
5	1	0.0896	-	-
6	2	0.03	0.0075	4
7	3	0.03464	0.0896	4
8	7	0.0896	0.0223	4

Table F.1: Cases for which compare full BS law and Tree Algorithm. Cases 1-4 have fixed $R = 0.0896$ cm and cases 5-8 have fixed $R/a = 4$.

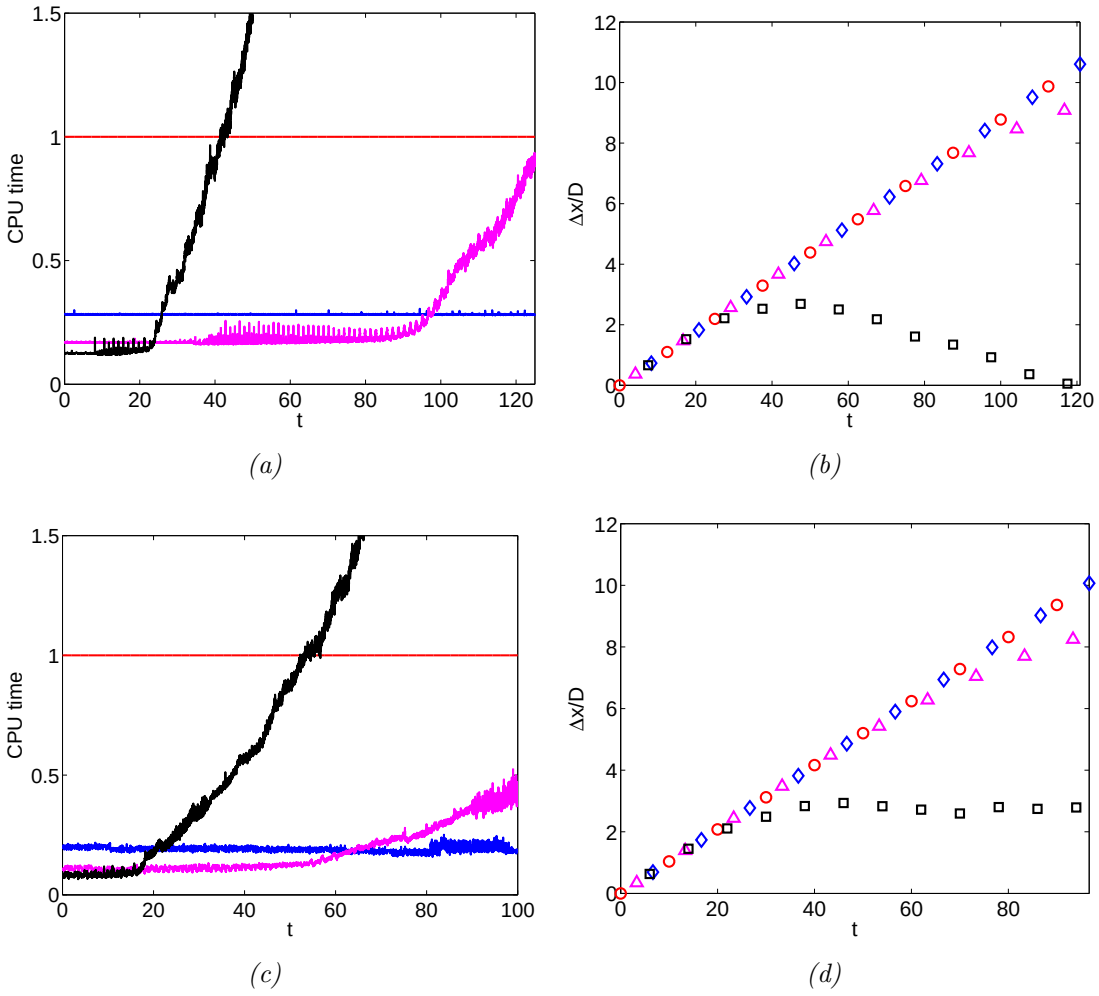

Figure F.1: $T = 0$ K: (left) CPU time vs t (s) and (right) $\Delta x/D$ vs t (s) for full BS law (red) and Tree Algorithm with $\theta = 0.1$ (blue), 0.2 (magenta) and 0.3 (black) radians. (a-b) $N = 1$ and (c-d) $N = 2$ with same initial $R = 0.0896$ cm.

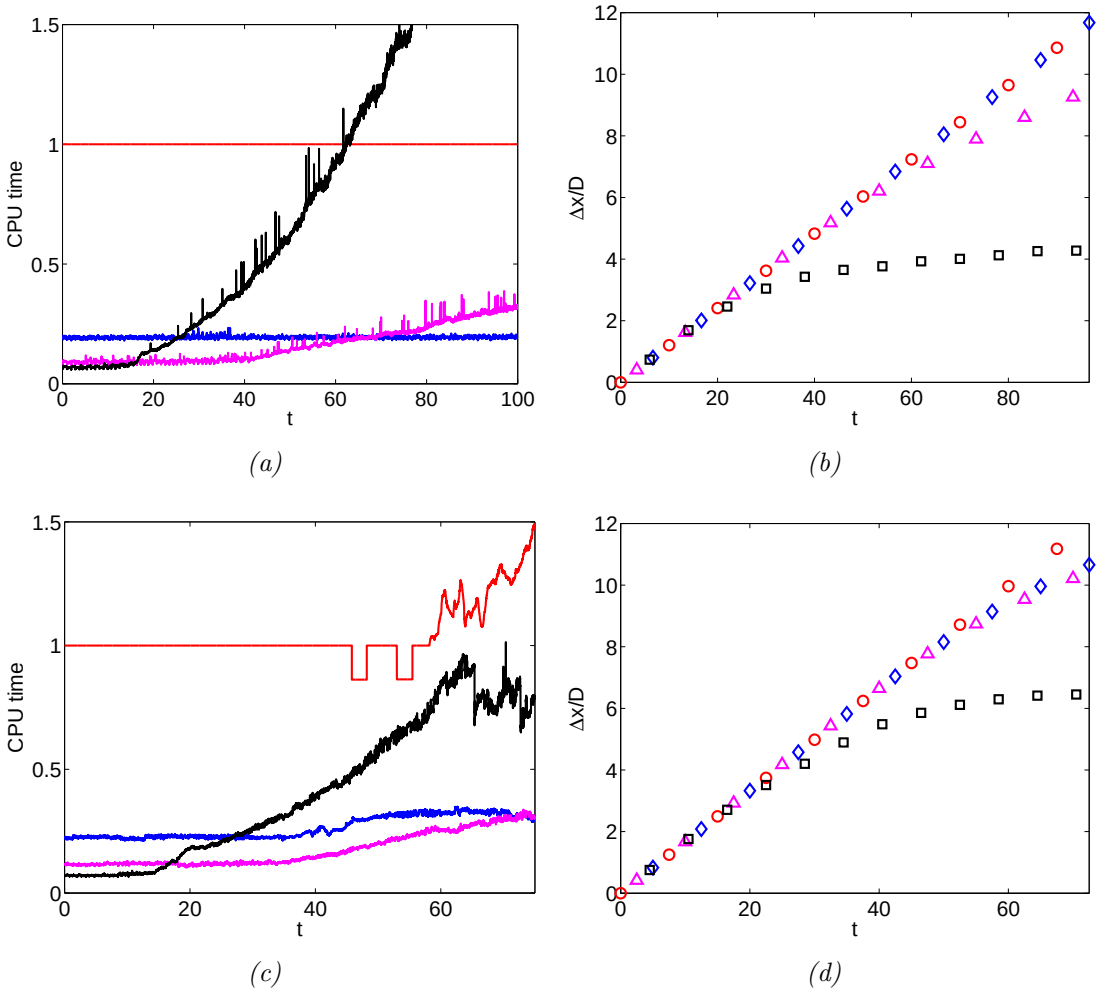

Figure F.2: $T = 0$ K: (left) CPU time vs t (s) and (right) $\Delta x/D$ vs t (s) for full BS law (red) and Tree Algorithm with $\theta = 0.1$ (blue), 0.2 (magenta) and 0.3 (black) radians. (a-b) $N = 3$ and (c-d) $N = 7$ with same initial $R = 0.0896$ cm.

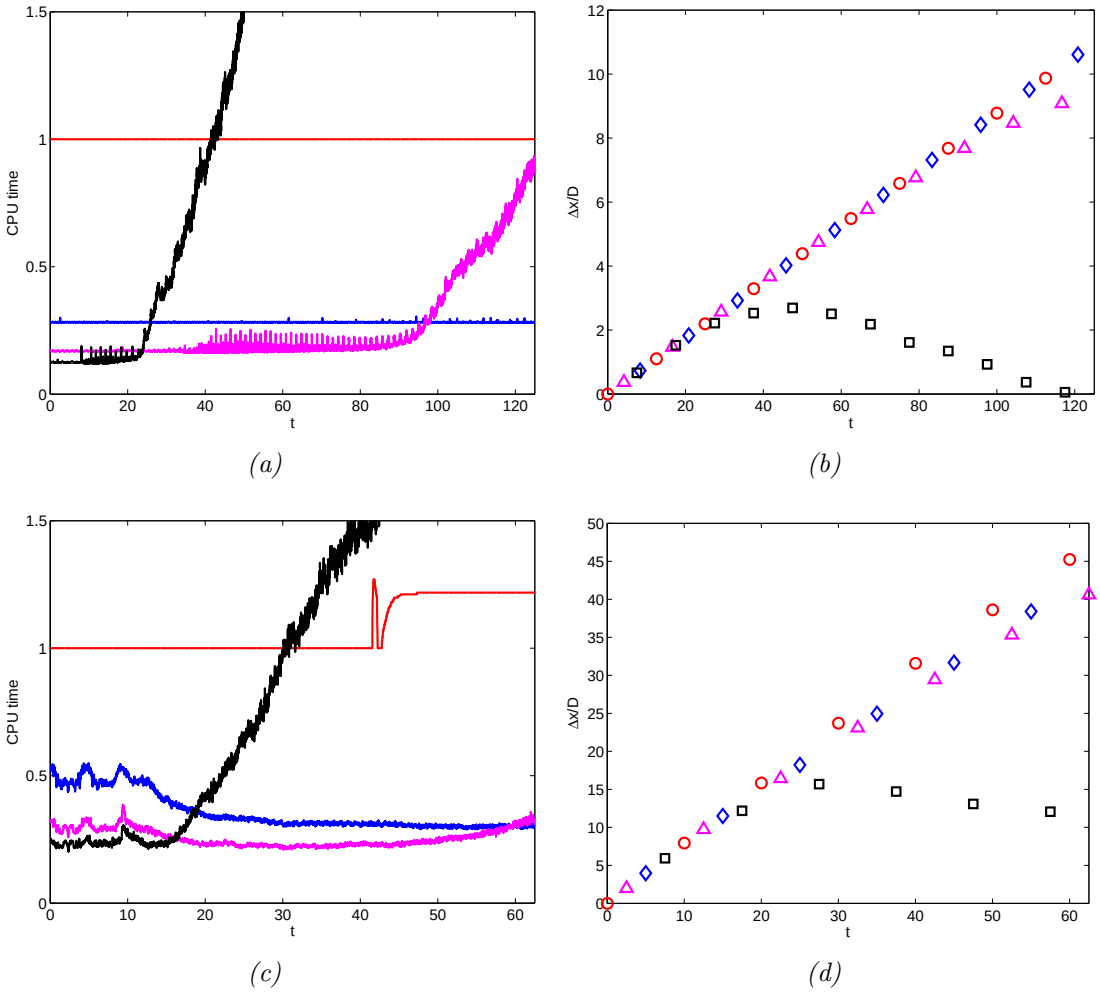

(a) *(b)* *(c)* *(d)*

Figure F.3: $T = 0$ K: (left) CPU time vs t (s) and (right) $\Delta x/D$ vs t (s) for full BS law (red) and Tree Algorithm with $\theta = 0.1$ (blue), 0.2 (magenta) and 0.3 (black) radians. (a-b) $N = 1$ and (c-d) $N = 2$ with same initial $R/a = 4$.

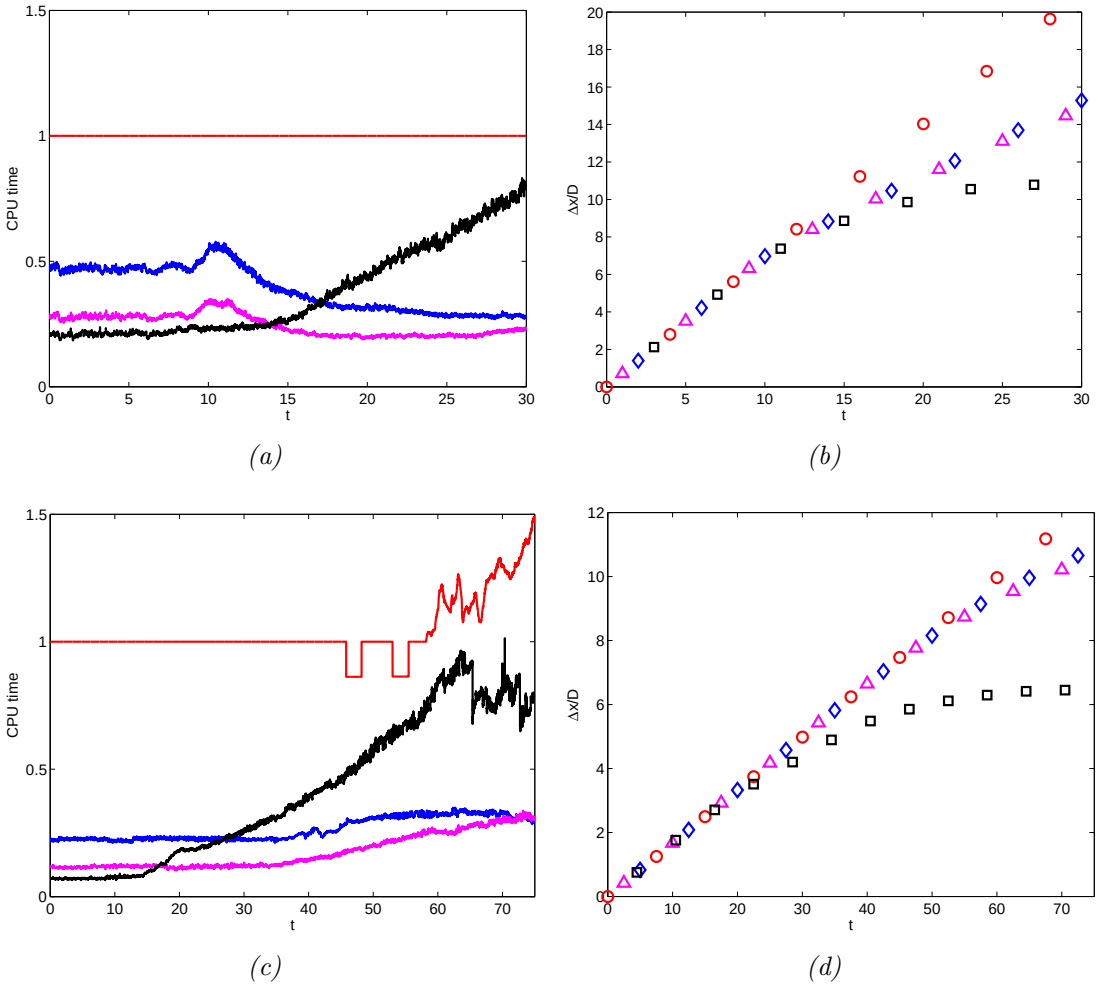

(a) *(b)* *(c)* *(d)*

Figure F.4: $T = 0$ K: (left) CPU time vs t (s) and (right) $\Delta x/D$ vs t (s) for full BS law (red) and Tree Algorithm with $\theta = 0.1$ (blue), 0.2 (magenta) and 0.3 (black) radians. (a-b) $N = 3$ and (c-d) $N = 7$ with same initial $R/a = 4$.

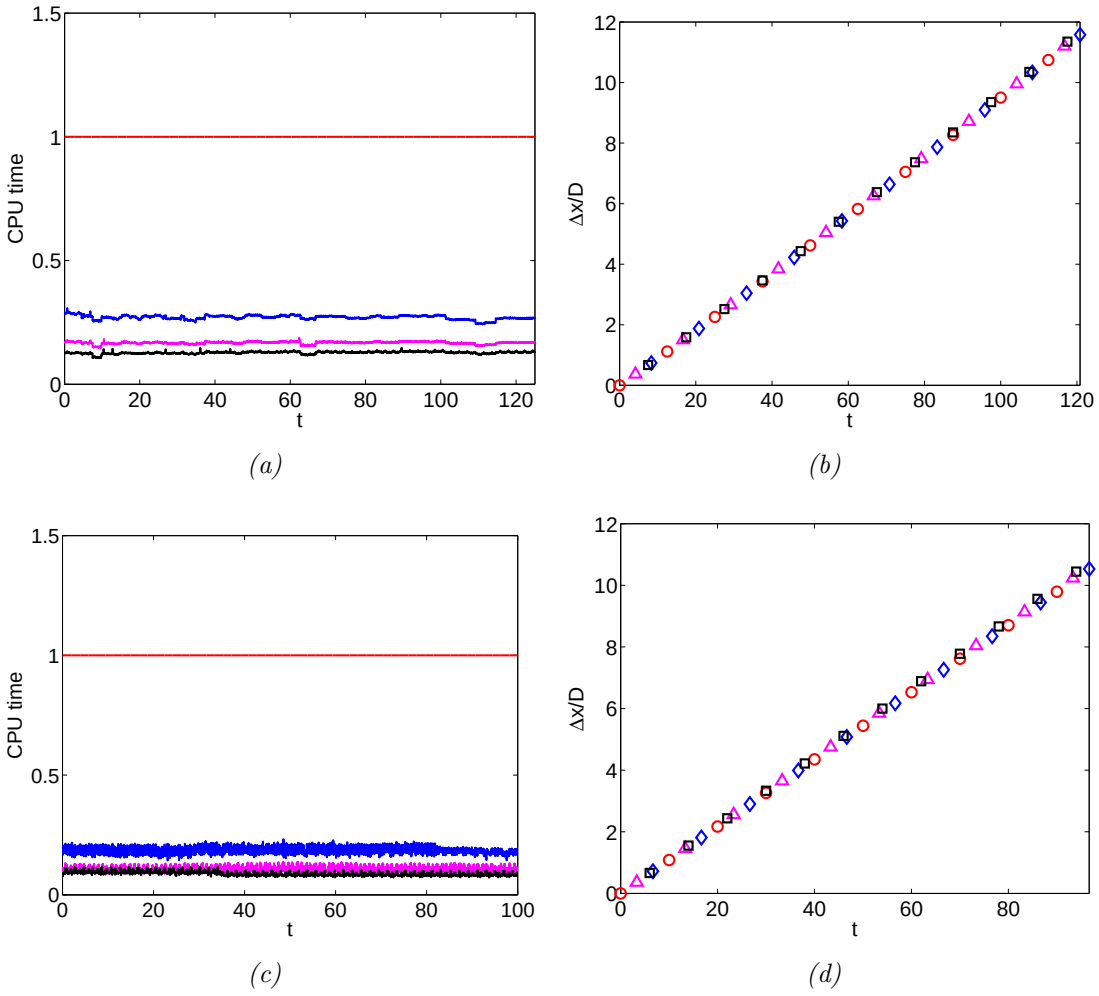

(a) *(b)* *(c)* *(d)*

Figure F.5: $T = 2.02$ K with normal fluid velocity field: (left) CPU time vs t (s) and (right) $\Delta x/D$ vs t (s) for full BS law (red) and Tree Algorithm with $\theta = 0.1$ (blue), 0.2 (magenta) and 0.3 (black) radians. (a-b) $N = 1$ and (c-d) $N = 2$ with same initial $R = 0.0896$ cm.

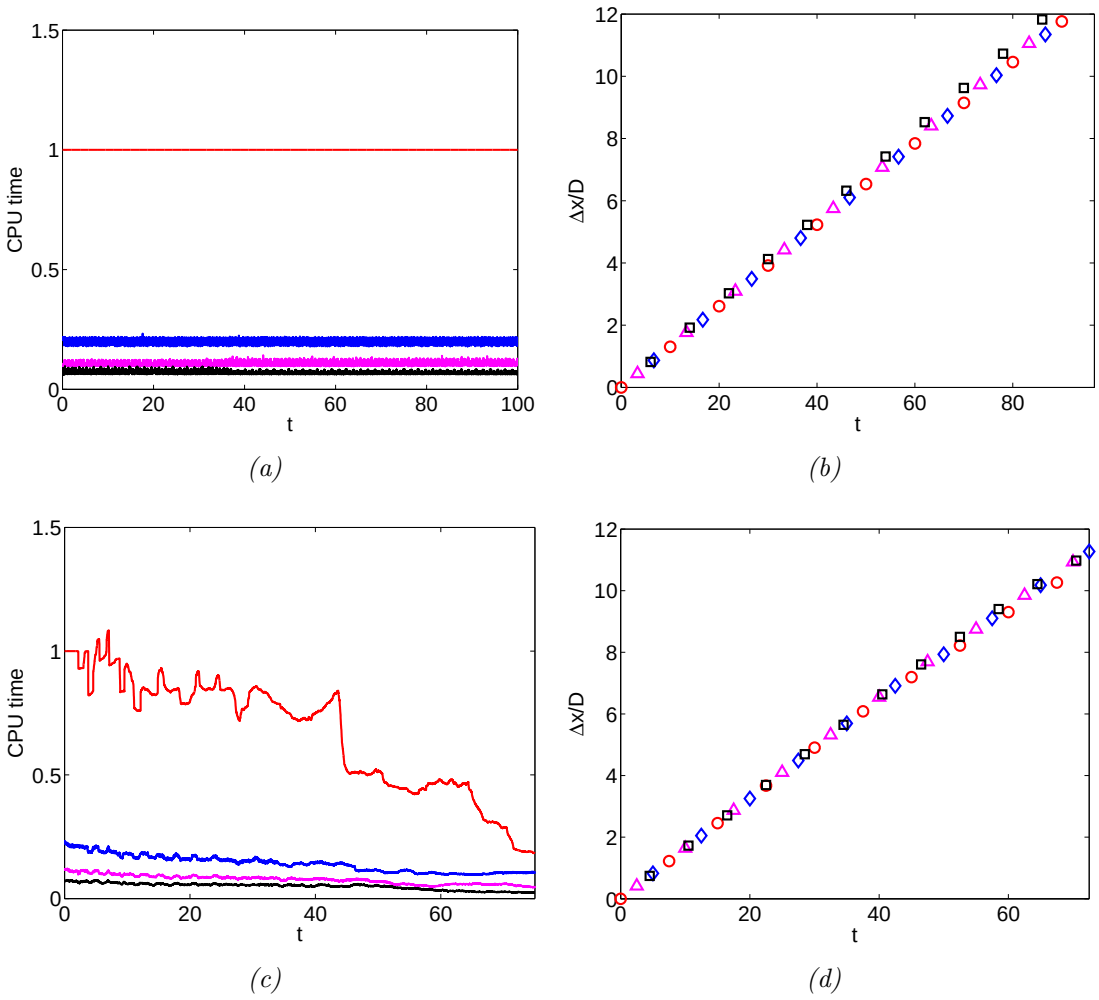

Figure F.6: $T = 2.02$ K with normal fluid velocity field: (left) CPU time vs t (s) and (right) $\Delta x/D$ vs t (s) for full BS law (red) and Tree Algorithm with $\theta = 0.1$ (blue), 0.2 (magenta) and 0.3 (black) radians. (a-b) $N = 3$ and (c-d) $N = 7$ with same initial $R = 0.0896$ cm.

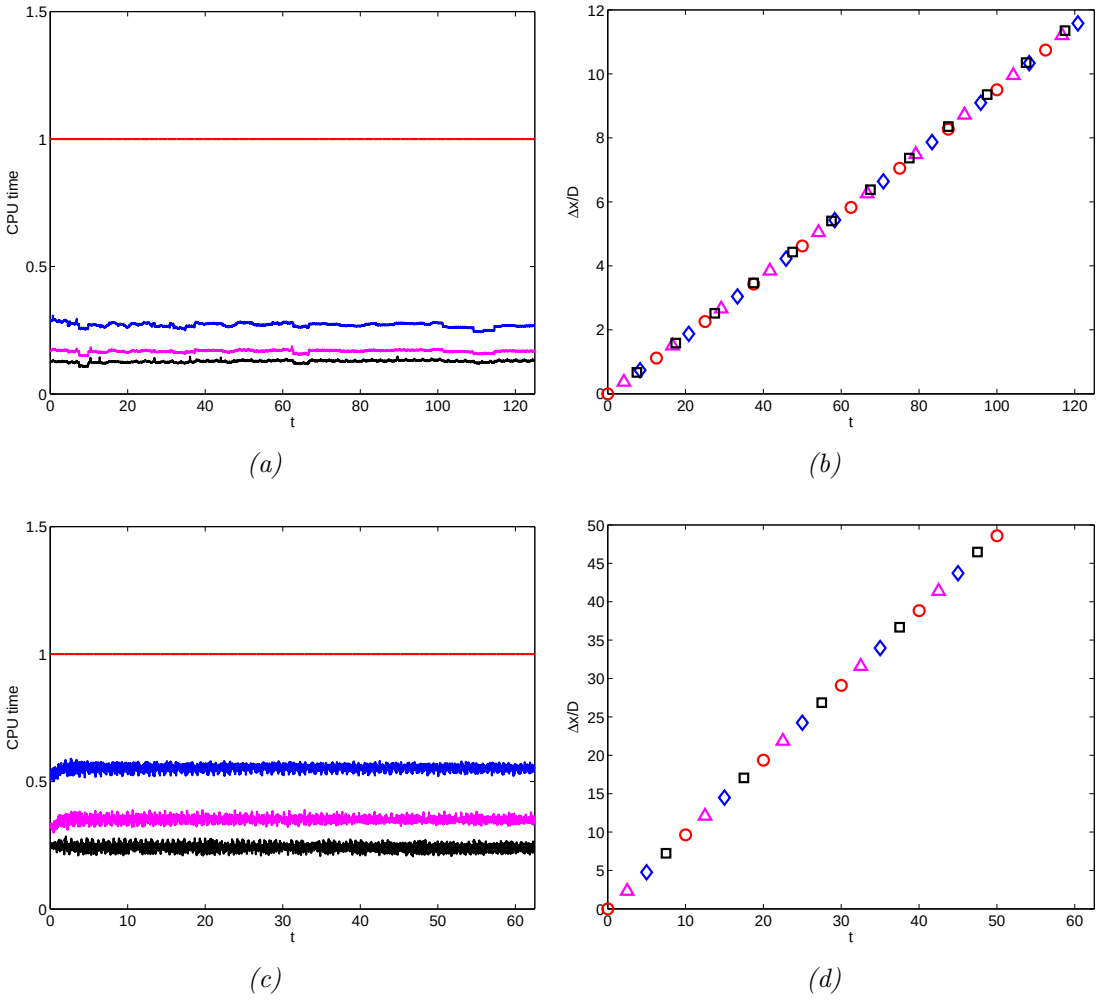

(a) *(b)* *(c)* *(d)*

Figure F.7: $T = 2.02$ K with normal fluid velocity field: (left) CPU time vs t (s) and (right) $\Delta x/D$ vs t (s) for full BS law (red) and Tree Algorithm with $\theta = 0.1$ (blue), 0.2 (magenta) and 0.3 (black) radians. (a-b) $N = 1$ and (c-d) $N = 2$ with same initial $R/a = 4$.

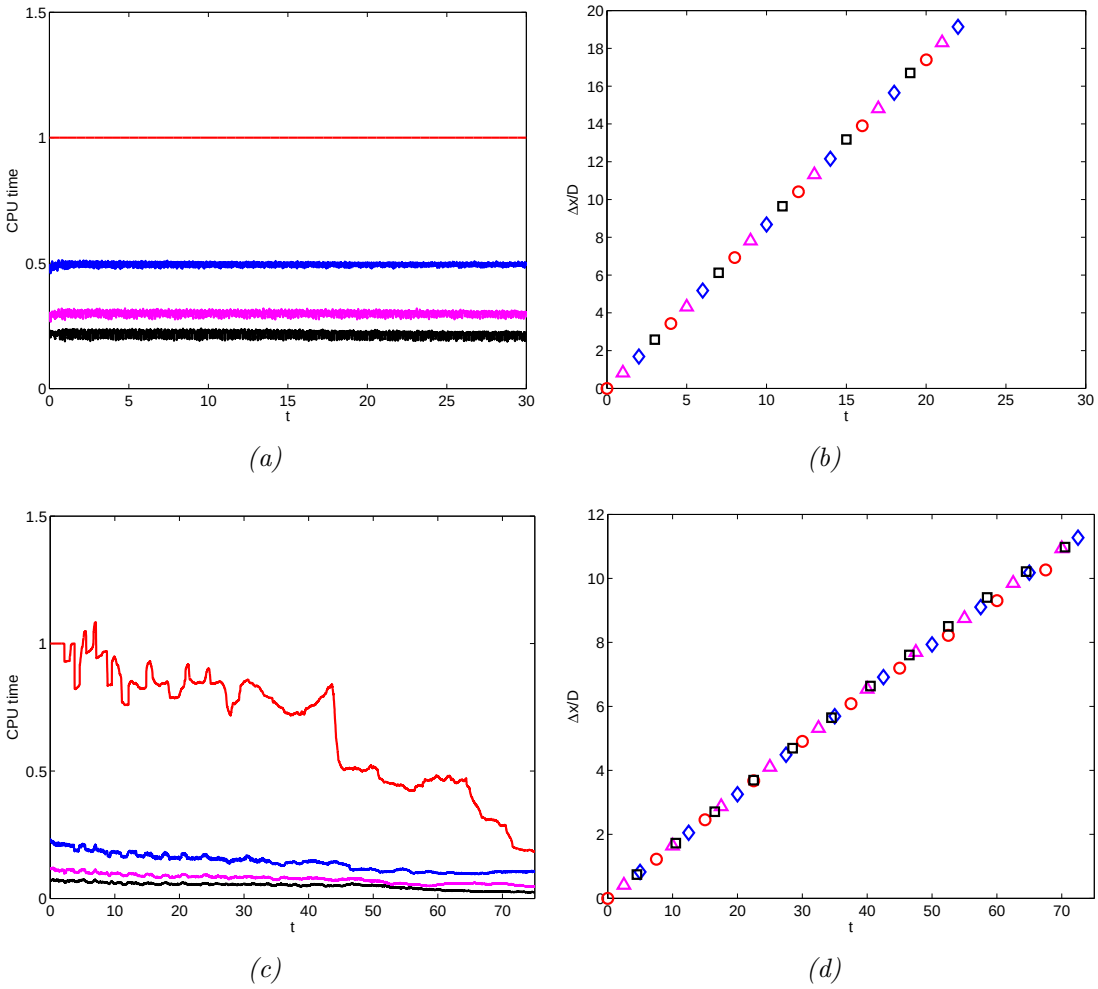

(a) *(b)* *(c)* *(d)*

Figure F.8: $T = 2.02$ K with normal fluid velocity field:(left) CPU time vs t (s) and (right) $\Delta x/D$ vs t (s) for full BS law (red) and Tree Algorithm with $\theta = 0.1$ (blue), 0.2 (magenta) and 0.3 (black) radians. (a-b) $N = 3$ and (c-d) $N = 7$ with same initial $R/a = 4$.

Bibliography

Acheson, D. 2000 Instability of vortex leapfrogging. *Eur. J. Phys.* **21**, 269273.

Adachi, H., Fujiyama, S. & Tsubota, M. 2010 Steady state counterflow quantum turbulence: simulation of vortex filaments using the full Biot-Savart law. *Phys. Rev. B* **81**, 104511.

Adzhemyan, L., Hnatich, M., D., H. & Stehlik, M. 1998 Calculation of spectra of turbulence in the energy-containing and inertial ranges. *Phys. Rev. E* **58**, 4511.

Allen, J. & Auvity, B. 2002 Interaction of a vortex ring with a piston vortex. *J. Fluid Mech.* **465**, 353–378.

Aurell, E., Boffetta, G., Crisanti, A., Frick, P., Paladin, G. & Vulpiani, A. 1994 Statistical mechanics of shell models for two-dimensional turbulence. *Phys. Rev. E* **50** (6), 4705–4715.

Baggaley, A. 2012 The Sensitivity of the Vortex Filament Method to Different Reconnection Models. *J. Low Temp. Phys.* **168**, 18–30.

Baggaley, A. & Barenghi, C. 2011*a* Spectrum of turbulent Kelvin-waves cascade in superfluid helium. *Phys. Rev. B* **83**, 134509.

Baggaley, A. & Barenghi, C. 2011*b* Vortex-density fluctuations in quantum turbulence. *Phys. Rev. B* **84**, 020504.

Baggaley, A. & Barenghi, C. 2012 Tree Method for Quantum Vortex Dynamics. *J. Low Temp. Phys.* **166**, 3–20.

Barenghi, C. 1992 Vortices and the Couette flow of He II. *Phys. Rev. B* **45**, 2290.

Barenghi, C., Donnelly, R. & Vinen, W. 1983 Friction on quantized vortices in helium ii. a review. *Journal of Low Temperature Physics* **52**, 189–247, 10.1007/BF00682247.

Barnes, J. & Hut, P. 1986 A hierarchical $O(NlogN)$ force-calculation algorithm. *Nature* **324**, 446–449.

Bewley, G. & Sreenivasan, K. 2009 The Decay of a Quantized Vortex Ring and the Influence of Tracer Particles. *Journal of Low Temperature Physics* **156**, 84–94.

Biferale, L. 2003 Shell models of energy cascade in turbulence. *Ann. Rev. Fluid Mechanics* **35**, 441.

Biferale, L., Lambert, A., Lima, R. & Paladi, G. 1995 Transition to chaos in a shell model of turbulence. *Physica D: Nonlinear Phenomena* **80**, 105–119.

Borner, H., Schmeling, T. & Schmidt, D. 1981 Experimental investigation of the circulation of large scale vortex rings in He II. *Physica B+C* **108**, 1123–1125.

Borner, H., Schmeling, T. & Schmidt, D. 1983 Experiments on the circulation and propagation of large-scale vortex rings in he ii. *Physics of Fluids* **26** (6), 1410–1416.

Borner, H. & Schmidt, D. 1985 Investigation of large-scale vortex rings in he ii by acoustic measurements of circulation. In *Flow of Real Fluids* (ed. G. Meier & F. Obermeier), *Lecture Notes in Physics*, vol. 235, pp. 135–146. Springer, Berlin / Heidelberg.

Boue, L., L'vov, V., Pomyalov, A. & Procaccia, I. 2012 . *Phys. Rev. B* **85**, 104502.

Careri, G., Cunsolo, S. & Mazzoldi, P. 1964 Periodic Discontinuities in the Drift Velocity of Ions in Liquid Helium II. *Phys. Rev.* .

C.F. Barenghi, C., Hulton, S. & Samuels, D. 2002 Polarisation of superfluid turbulence. *Phys. Rev. Lett.* **89**, 275301.

Crow, S. 1970 Stability theory for a pair of trailing vortices. *AIAA J.* **8**, 2172–2179.

Didden, N. 1979 On the formation of vortex rings: rolling-up and production of circulation. *Z. Angew. Math. Phys.* **30**, 101–116.

Ditlevsen, P. D. & Mogensen, I. A. 1996 Cascades and statistical equilibrium in shell models of turbulence. *Phys. Rev. E* **53** (5), 4785–4793.

Donnelly, R. 1991 Quantized Vortices in Helium II. In *Cambridge Studies in Low Temperature Physics*. Cambridge University Press, Cambridge.

Donnelly, R. & Barenghi, C. 1998 The observed properties of liquid helium at the saturated vapor pressure. *J. Phys. Chem. Ref. Data* **27**, 1217.

van Dyke, M. 1982 *An Album of Fluid Motion*. Parabolic, Stanford.

Dyson, F. 1893 The potential of an anchor ring. Part II. *Phil. Trans. R. Soc. Lond.* **A184**, 10411106.

Fiszdon, W., Peradzynski, Z. & Poppe, W. 1985 The evolution of axisymmetric vortex systems in liquid He II. *Phys. Fluids* **28**, 3525–3533.

Frisch, U. 1995 *Turbulence: The legacy of A.N. Kolmogorov*. Cambridge University Press,Cambridge.

Gledzer, E. 1973 System of hydrodynamic type admitting two quadratic integrals of motion. *Phys. Dokl.* **18**, 216.

Gorter, C. & Mellink, J. 1949 On the irreversible processes in liquid helium II. *Physica* **15**, 285.

Hall, H. & Vinen, W. 1956*a* The Rotation of Liquid Helium II. I. Experiments on the Propagation of Second Sound in Uniformly Rotating Helium II . *Proc. Roy. Soc A* **238**, 204.

Hall, H. & Vinen, W. 1956*b* The Rotation of Liquid Helium II. II. The Theory of Mutual Friction in Uniformly Rotating Helium II . *Proc. Roy. Soc A* **238**, 215.

Helmholtz, H. 1858 Uber integrale der hydrodynamischen gleichungen welche den wirbelbewegungen entsprechen. *Celles J.* **55**, 25–55.

Hicks, W. 1885 Researches on the theory of vortex rings - part II. *Phil. Trans. Roy. Soc.* **A176**, 725–80.

Hicks, W. 1922 On the mutual threading of vortex rings. *Proc. R. Soc. Lond.* **A102**, 111131.

Hill, M. 1894 On a spherical vortex. *Phil. Trans. R. Soc. Lond.* **A185**, 213245.

Kadanoff, L., Lohse, D., Wang, J. & Benzi, R. 1995 Scaling and dissipation in the goy shell model. *Physics of Fluids* **7** (3), 617–629.

Kelvin, L. 1867 The translatory velocity of a circular vortex ring. *Phil. Mag.* **33**, 511–512.

Kivotides, D., Barenghi, C. & Samuels, D. 2000 Triple Vortex Ring Structure in Superfluid Helium II. *Science* **290**, 777–779.

Kivotides, D., Vassilicos, J., Samuels, D. & Barenghi, C. 2001 Kelvin Waves Cascade in Superfluid Turbulence. *Phys. Rev. Lett.* **86**, 3080–3083.

Koenigsberger, L. 1906 *Hermann von Helmholtz (With a preface by Lord Kelvin)*. Clarendon, Oxford.

Kolmogorov, A. 1941 The local structure of turbulence in incompressible viscous fluid for very large Reynolds numbers. *C. R. Acad. Sci. USSR* **30**, 299–303.

Krstulovic, G. 2012 Kelvin-wave cascade and dissipation in low-temperature superfluid vortices. *Phys. Rev. E* **86**, 055301.

Lamb, H. 1895 *Hydrodynamics. 2nd edn.*. Cambridge University Press, Cambridge.

Landau, L. & Lifshitz, E. 1987 *Fluid Mechanics*. Pergamon Press, New York.

Lim, T. & Nickels, T. 1992 Instability and reconnection in the head-on collision of two vortex rings. *Nature* **357**, 225–227.

Love, A. 1894 n the motion of paired vortices with a common axis. *Proc. Lond. Math. Soc.* **25**, 185194.

L'vov, V., Nazarenko, S. & Skrbek, L. 2006 Energy Spectra of Developed Turbulence in Helium Superfluids. *J. Low Temp. Phys.* **145**, 125.

L'vov, V., Nazarenko, S. & Volovik, G. 2004 Energy spectra of developed superfluid turbulence. *JETP Lett.* **80**, 535.

L'vov, V., Podivilov, E., Pomyalov, A., Procaccia, I. & Vandembroucq, D. 1998 Improved shell model of turbulence. *Phys. Rev. E* **58**, 1811.

Maggioni, F., Alamri, S., Barenghi, C. & Ricca, R. 2010 Velocity, energy, and helicity of vortex knots and unknots. *Phys. Rev. E* **82**, 026309.

Maurer, J. & Tabeling, P. 1998 Local investigation of superfluid turbulence. *Europhys. Lett.* **43**, 29.

Meleshko, V. 2010 Coaxial axisymmetric vortex rings: 150 years after Helmholtz. *Theor. Comput. Fluid Dyn.* **24**, 403431.

Melotte, D. & Barenghi, C. 1998 Transition to Normal Fluid Turbulence in Helium II. *Phys. Rev. Lett.* **80**, 4181.

Merahi, L., Sagaut, P. & Abidat, M. 2006 A closed differential model for large-scale motion in HVBK fluids . *Europhys. Lett.* **75**, 757.

Moffatt, H. 1969 The degree of knottedness of tangled vortex lines. *J. Fluid Mech.* **35**, 117–129.

Morton, T. 2004 The velocity field within a vortex ring with a large elliptical cross-section. *J. Fluid Mech.* **503**, 247271.

Murakami, M., Hanada, M. & Yamazaki, T. 1987 Flow Visualization Study on Large-Scale Vortex Ring in He II : I. Quantum Liquids and Solids : Superfluid Flow. *Japanese journal of applied physics. Supplement* **26** (3), 107–108.

Nitshce, M. & Krasny, R. 1994 A numerical study of vortex ring formation at the edge of a circular tube. *J. Fluid Mech.* **276**, 139–161.

Okkels, F. 2001 Temporal structures in shell models. *Phys. Rev. E* **63** (5), 056214–+.

Pisarenko, D., Biferale, L., Courvoisier, D., Frisch, U. & Vergassola, M. 1993 Further Results on Multifractality in Shell Models. *Physics of Fluids A-Fluid Dynamics* **5** (10), 2533–2538.

Rayfield, G. W. & Reif, F. 1964 Quantized vortex rings in superfluid helium. *Phys. Rev.* **136**, A1194–A1208.

Roberts, P. H. & Donnelly, R. J. 1970 Dynamics of vortex rings. *Physics Letters A* **31**, 137–138.

Roche, P.-E., Barenghi, C. & Leveque, E. 2009 Quantum turbulence at finite temperature: the two-fluids cascade. *Europhys. Lett.* **87**, 54006.

Roche, P.-E., Diribarne, P. & Didelot, T. 2007 Vortex density spectrum of quantum turbulence. *Europhys. Lett.* **77**, 66002.

Rogers, W. 1858 On the formation of rotating rings by air and liquids under certain conditions of discharge. *Am. J. Sci.* **26**, 246258.

Saffman, P. 1981 Dynamics of vorticity. *J. Fluid Mech.* **106**, 4958.

Salort, J., Baudet, C., Castaing, B., Chabaud, B., Daviaud, F., Didelot, T., Diribarne, P., Dubrulle, B., Gagne, Y., Gauthier, F., Girad, A., Hebral, B., Rousset, B., Thibault, P. & Roche, P.-E. 2010 Turbulent velocity spectra in superfluid flows. *Phys. of Fluids* **22**, 125102.

Salort, J., Roche, P.-E. & Leveque, E. 2011 Mesoscale equipartition of kinetic energy in quantum turbulence. *Europhys. Lett.* **94**, 24001.

Schmoranzer, D., Kralova, M., Pilcova, V., Vinen, W. & Skrbek, L. 2010 Experiments relating to the flow induced by a vibrating quartz tuning fork and similar structures in a classical fluid. *Phys. Rev. E* **81**, 066316.

Schwarz, K. 1985 Three-dimensional vortex dynamics in supefluid He4: lineline and lineboundary interaction. *Phys. Rev. B* **31**, 57825804.

Schwarz, K. 1988 Three-dimensional vortex dynamics in superfluid He4: homogeneous superfluid turbulence. *Phys. Rev. B* **38**, 23982417.

Shariff, K. & Leonard, A. 1992 Vortex rings. *Ann. Rev. Fluid Mech.* **24**, 235279.

Skrbek, L., Niemela, J. & Donnelly, R. 2000 Four Regimes of Decaying Turbulence in a Finite Channel. *Phys. Rev. Lett.* **85**, 2973.

Smith, M., Donnelly, R., N., G. & Vinen, W. 1993 Decay of vorticity in homogeneous turbulence. *Phys. Rev. Lett.* **71**, 2583.

Smith, M., Hilton, D. & van Sciver, S. 1999 Observed drag crisis on a sphere in flowing HeI and HeII. *Phys. of Fluids* **11**, 751.

Sommerfeld, A. 1950 Mechanics of Deformable Bodies. In *Lectures on Theoretical Physics*. Academic, New York.

Southerland, K., Porter, J., Dahm, W. & Buch, K. 1991 An experimental study of the molecular mixing process in an axisymmetric laminar vortex ring. *Phys. Fluids* **3**, 1385–1392.

Stalp, S., Skrbek, L. & Donnelly, R. 1999 Decay of Grid Turbulence in a Finite Channel. *Phys. Rev. Lett.* **82**, 4831.

Stamm, G., Bielert, F., Fiszdon, W. & Piechna, J. 1994*a* Counterflow-induced macroscopic vortex rings in superfluid helium: visualization and numerical simulation. *Physica B* **193**, 188–194.

Stamm, G., Bielert, F., Fiszdon, W. & Piechna, J. 1994*b* On the existence of counterflow induced macroscopic vortex rings in he ii. *Physica B* **194-196**, 589–590.

Tait, P. 1867 Translation of 'On integrals of the hydrodynamical equations which express vortex-motion' by H. Helmholtz. *Phil. Mag.* **33**, 485–512.

Tait, P. 1876 *Lectures on Some Recent Advances in Physical Science, with a Special Lecture on Force. 2nd edn.*. Macmillan, London.

Thomson, J. & Newall, H. 1885 On the formation of vortex rings by drops falling into liquids, and some allied phenomena. *Proc.R. Soc. Lond.* **39**, 417–436.

Tough, J. 1982 Superfluid turbulence. In *Progress in Low Temperature Physics* (ed. D. Brewer), *Progress in Low Temperature Physics*, vol. 8.

Vinen, W. 2005 Theory of quantum grid turbulence in superfluid ^{3}He-B. *Phys. Rev. B* **71**, 024513.

Vinen, W. & Niemela, J. 2002 Quantum turbulence. *J. Low Temp. Phys.* **128**, 167.

Walmsley, P., Golov, A., Hall, H., Levchenko, A. & Vinen, W. 2007 Dissipation of Quantum Turbulence in the Zero Temperature Limit. *Phys. Rev. Lett.* **99**, 265302.

Walmsley, P., Golov, A., Hall, H., Vinen, W. & Levchenko, A. 2008 Decay of Turbulence Generated by Spin-Down to Rest in Superfluid ^{4}He. *J. Low Temp. Phys.* **153**, 127.

Walstrom, P., Weisend, J., Maddocks, J. & van Sciver, S. 1988 Turbulent flow pressure drops in various He II transfer system components. *Cryogenics* **28**, 101.

Winiecki, T. & Adams, C. 2000 Motion of an object through a quantum fluid. *Europhys. Lett.* **52**, 257–263.

Yamada, H. & Matsui, T. 1978 Preliminary study of mutual slip-through of a pair of vortices. *Phys. Fluids* **21**, 292294.

Yamada, M. & Ohkitani, K. 1987 Lyapunov Spectrum of a Chaotic Model of 3-Dimensional Turbulence. *Journal of the Physical Society of Japan* **56** (12), 4210–4213.

Yamada, M. & Ohkitani, K. 1988 The Inertial Subrange and Non-Positive Lyapunov Exponents in Fully-Developed Turbulence. *Progress of Theoretical Physics* **79** (6), 1265–1268.

Yoon, S. & Heister, S. 2004 Analytical formulas for the velocity field induced by an infnitely thin vortex ring. *Int. J. Numer. Meth. Fluids* **44**, 665672.